DIAGNOSIS AND ESTIMATION OF CRYOSPHERE CHANGES IN CENTRAL ASIA

A Dissertation

Presented in Partial Fulfillment of the Requirements for the

Degree of Doctor of Philosophy

with a

Major in Geography

in the

College of Graduate Studies

University of Idaho

by

Hang ZHOU

Major Professor: Vladimir B. Aizen, Ph.D.

Committee Members: Karen Humes, Ph.D.; Raymond Dezzani, Ph.D.; Elena Aizen, Ph.D.

Department Administrator: Mickey Gunter, Ph.D.

August 2016

Authorization to Submit Dissertation

This dissertation of Hang ZHOU, submitted for the degree of Doctor of Philosophy with a Major in Geography and titled “DIAGNOSIS AND ESTIMATION OF CRYOSPHERE CHANGES IN CENTRAL ASIA”, has been reviewed in final form. Permission, as indicated by the signatures and dates give below, is now granted to submit final copies to the College of Graduate Studies for approval.

Major Professor _____ Date _____
Vladimir B. Aizen, Ph.D.

Committee Members _____ Date _____
Karen Humes, Ph.D.

_____ Date _____
Raymond Dezzani, Ph.D.

_____ Date _____
Elena Aizen, Ph.D.

Department administrator _____ Date _____
Mickey Gunter, Ph.D.

Abstract

This study aimed at quantifying the cryosphere changes in central Asia (CA) for the past ~20 to 40 years as consequences of regional climate changes using remote sensing and in-situ observation data.

A comprehensive climate dataset for CA was compiled from several sources. A gridded monthly climate dataset for 1951 - 2010 was created. CA experienced a climate regime change of increasing air temperature in 1976 / 1977. Stronger increase of air temperature happened in lower elevation and higher northern latitude. High elevation areas in Tien Shan and Pamir experienced a much smaller increase of temperature than other regions. Changes of precipitation vary across CA, with Pamir experienced increase of precipitation, mainly in winter, while decreases of precipitation occurred in the alpine regions of Tien Shan, especially in summer.

A series of long-term snow cover datasets at different temporal scales (daily / 8-day) and processing levels (original / gap-filled / adjusted) were developed from AVHRR and MODIS data. Statistics describing seasonal snow cover extent and timing in 1986 – 2008 have been calculated from AVHRR snow product. Long-term mean snow cover distribution, and effects of determining factors (elevation, latitude, and relative location to major mountains) were quantified. Trends of change of duration, onset date, and melt date of snow cover were analyzed using Theil-Sen regression. Decrease of snow cover duration was observed in mountains of Altai, Tien Shan and Pamir, and vast areas surrounding the Aral Sea, associated mainly with earlier melt date and significant increase of spring air temperature.

Databases of glacier extent and surface elevation were developed for two representative massifs, the Fedchenko Glacier Massif (FGM) and the Inylchek Glacier Massif (IGM). Both massifs experienced continuous glacier area loss in the period of 1975/1976 to 2000 and 2000 to 2007, with larger glaciers tend to experience less area loss, and stronger area loss rate in the latter period. The magnitude of glacier surface elevation lowering in the ablation zone in the IGM was much stronger than in the FGM, which can be attributed to the more favorable climate conditions for glaciers in the FGM.

Acknowledgements

On my journey to PhD I met a lot of wonderful people who generously shared with me their knowledge and passion for geoscience and their fascination for high mountains in central Asia. I am grateful to them for their valuable support.

First and foremost, I would like to express my gratitude to my advisor, Dr. Vladimir Aizen. I appreciate all his contribution of time, idea, and funding to make my PhD experience productive and stimulating. His understanding of central Asia provided vital intellectual guidance for my studies, while his enthusiasm for high mountain studies was motivational for me, especially during tough times in the PhD pursuit.

I am also indebted to Elena Aizen, Karen Humes, Raymond Dezzani, and other faculty at the University of Idaho, who taught me Geographic Information System, Remote Sensing, and statistics. Their expertise greatly helped my PhD studies, providing me the right tools and the right perspectives for solving problems.

Furthermore, I would like to thank Dr. Tandong Yao at the Institute of Tibetan Plateau Research, for introducing me to the exciting field of glaciology. He also showed me an excellent example of how one developed outstanding scientific studies from his enthusiasm for high mountains and glaciers.

Many friends and fellow researchers shared programs, code, data, or thoughts with me during my studies, which I sincerely appreciate. I would like to thank Arzhan Surazakov, for his help at the time when I started my PhD, as well as the procedures he developed and shared with me for processing various types of satellite images. I also want to thank Konstantin Khlopenkov in NASA Langley Research Center for sharing the SAPS software, Abror

Gafurov in GFZ Potsdam for sharing code for satellite snow cover product gap-filling, and Xiangning Chu in UCLA for discussions about statistical methods for processing time series.

This work is made possible by generous grants provided by NASA (NNXO8AL686) and NSF (AGS-1304898). Moreover, I would like to thank agencies which provide open access to precious satellite and in-situ observation data, including NASA, NOAA, USGS, NSIDC, and RIHMI.

Lastly I would like to thank my parents for their love, encouragement, and faithful support.

Table of Contents

List of Tables

List of Figures

Chapter 1 Introduction

1 Introduction

Central Asia (CA), as a large semi-arid and arid region located in the center of the Eurasian Continent, is characterized by a highly continental climate (**Lydolph, 1977; Lioubimtseva et al., 2009**). In CA, while low elevation plains receive little precipitation, high mountains, including Altai, Tien Shan, and Pamir, block the movement of moisture-bearing westerlies (**Aizen et al. 2005; Aizen et al., 2009; Caves et al., 2015**), capture large amount of solid precipitation, and store water as seasonal snow or glaciers. Meltwater from seasonal snow and glaciers in high mountain headwater catchments serve as vital water resources for major rivers in CA (**Barnet et al., 2005; Immerzeel et al., 2010**). Those rivers direct water from the sparsely populated mountainous areas to highly populated low reaches, sustaining human communities, as well as local eco-systems.

CA is home to a large and fast growing population. The five Former Soviet Union (FSU) Central Asian Republics (CARs) has a total population of 63 million in 2000 (**World Bank, 2015**) while the Xinjiang Autonomous Region in China has a population of 21 million in 2000 (**National Bureau of Statistics China, 2015**). Most of the population in CA concentrate in fertile oases, in areas along the major rivers, or in areas with water diverted from major rivers by canals. The population in CA is growing fast, with some studies even predicting a possible doubling of the total population by the end of the year 2100 (**Lutz et al., 2008**). The increase of population will lead to the increase of water demand. Irrigated agriculture, as a major section of the economy and the major provider of food (via wheat, rice, fruit, and vegetable production) and cash (via cotton production) in CA, is the main user of

water resources, accounting for 85 – 97% of water withdrawals in CARs (**FAO, 2015**). Fast development of the oil and gas industry in many CA countries will require much more water than before. Countries controlling high mountainous headwater catchments are planning construction of dams for electricity generation to accommodate the increasing demand for energy (**Antipova et al., 2002; Schluter et al., 2005**). The increasing demand of water, as a result of the fast growing population, might lead to more water conflicts in the water scarce CA (**Bernauer and Siegfried, 2012; Siegfried et al., 2012**).

Estimation of the water resources changes in CA are hampered by the lack of knowledge about climate changes and changes of the cryosphere in CA. There does not exist a general quantification of the historical climate changes throughout CA, while most existing studies only relies on in-situ observations in a small subset of stations in the existing station network, or depends on re-analysis data which might not be correct for high mountainous areas in CA (**Böhner, 2006; You et al., 2012**). The general regime and historical changes of seasonal snow cover, which is a major component of the cryosphere and the main contributor of surface runoff in CA, have not been studied in a systematic way after the collapse of the FSU. There also exist great uncertainties about glacier changes in CA, which is also a major component of the cryosphere and a stable contributor of surface runoff in CA. Most existing works about glaciers in CA focused on Tien Shan and Altai, and relies on only data about glacier extent (**Unger-Shayesteh et al., 2013**). Information about the changes of glacier extent, surface elevation and ice volume, which is vital for estimating and assessing water resources changes in CA, especially in Pamir, generally do not exist.

This dissertation aims to quantify the general regime and historical changes of climate, seasonal snow cover and glaciers in CA. Since CA is a data-scarce region, large

efforts were spent on developing the suitable datasets for CA from both remote sensing data and in-situ observations. The developed datasets and the knowledge gained from those datasets will serve as a solid basis for future estimation of water resources changes in CA.

The main objectives of this dissertation are listed below:

1. Develop a comprehensive climate dataset for CA, synthesizing in-situ observation data from different sources.
2. Analyze and quantify the general regime and historical changes of the climate in CA.
3. Develop a series of snow cover products at different temporal scales for CA from AVHRR and MODIS satellite images.
4. Analyze and quantify the general regime, determining factors and historical changes of seasonal snow cover in CA.
5. Develop databases of glacier extent and surface elevation at different time periods for two representative glacier massifs in Pamir (the Fedchenko Glacier Massif) and Tien Shan (the Inylchek Glacier Massif).
6. Quantify and compare the general spatial distribution and historical changes of glaciers in the Fedchenko Glacier Massif and the Inylchek Glacier Massif.

2 Region of interest

2. 1 Definition of the region

In this dissertation, central Asia (CA) is defined as the geographical area in the center of the Eurasian Continent, extending from 51 °E to 113 °E, and from 32 °N to 56 °N (**Figure**

1.01). The Caspian Sea is located in the west and the Mongolian Steppes and the Gobi Desert are in the east. The Western Siberia and the Altai-Sayan Mountains are situated in the north, while the Karakum and Taklamakan deserts are to the south. The definition of the extent of CA is designed from a physical geography perspective, to include major high mountains in the interior of Asia (Altai-Sayan, Tien Shan, and Pamir), as well as low elevation plains in the basins of major rivers that originate from those high mountains (Amu Dar'ya, Syr Dar'ya, Tarim, and others). The term 'central Asia' is picked up specifically to distinguish from the term 'Central Asia', which is more frequently used but mainly as a geopolitical term. In recent English publications, 'Central Asia' is mainly used to refer to the five Central Asian Republics (CARs, Kazakhstan, Kyrgyzstan, Tajikistan, Uzbekistan, and Turkmenistan) of the FSU. Sometimes 'Central Asia' is used to refer to a larger area, with or without Afghanistan, Western China (Xinjiang, Tibet, Inner Mongolia, and Qinghai), and Mongolia (**Cowan, 2007**).

2.2 General characteristics

The total area of CA, as defined in this dissertation, is ~6.3×10^6 km^2. Most of CA is low elevation plains, with ~73% of the total area of CA is below 1000 m and with a slope less than 5°. CA is also home to high mountains, reaching 6000 - 7000 m above sea level (a.s.l.) in the Altai-Sayan, Tien Shan, and Pamir mountains. The highest point is the Kongur Peak in Eastern Pamir at 7719 m a.s.l., and the lowest point is the Turfan Depression in Eastern Tien Shan at -154 m below sea level (b.s.l.).

The Pamir, Tien Shan, and Altai-Sayan mountains extend for more than 5000 km from southwest to northeast, controlling moisture distribution and the atmospheric pressure of the mid to low latitudes of Asia (**Lydolph,1977; Bryson, 1986**). Those high mountains serve

as 'water tower' (**Immerzeel et al., 2010**), capturing and storing solid precipitation in winter as seasonal snow cover. The high amount of solid precipitation in high mountains also sustains large glacierizations. The areas of glaciers for the Pamir, Tien Shan, and Altai-Sayan mountains are ~13643, ~13254, and ~1562 km^2 in 2000 (**Surazakov, 2008**), respectively.

Several large endorheic basins are situated in CA, including the Caspian Sea in its west, which is the largest saline inland sea in the world. The Aral Sea, with water contributed mainly from the Amu Dar'ya River and the Syr Dar'ya River, has been suffering from desiccation problem since the 1960s due to water diversion for agriculture (**Micklin, 2007**). The Tarim River, as the largest and longest inland river in China, flows through the Taklamakan Desert. Lake Balkhash-Ili River and Lake Issyk Kul are also large closed-drainage basins in CA. As the major rivers in these basins originate in high mountains, melt water from seasonal snow cover and glaciers in high elevation provide vital water resources to arid or semi-arid plains in the lower reaches, and help to sustain the natural ecosystems and the local human societies.

The most conspicuous climatic feature of CA mountain ranges, especially the Tien Shan, Altai and Kunlun mountain ranges, is the occurrence of maximum precipitation during the warm season, because in the cold season the Siberian High (SH) controls the regional climate strongly. According to Panagiotopoulos et al. (**2005**), significant teleconnections exist as well between the SH and the westerly jet streams on one hand, and with the winter East Asian Monsoon on the other hand (**Takaya and Nakamura, 2005**). In the Pamir Mountains, however, maximum precipitation occurs in winter and spring because of the lesser impact of the Siberian / Tibetan highs. Local precipitation occurs during winter and early spring in the Pamir when depressions, developing over the Eastern Mediterranean, subsequently move along a northeast

trajectory where they may even replenish moisture over the Caspian Sea (**Lioubimtseva, 2002**). Therefore, in these mountains, summer and autumn are dry seasons, with occasional intrusions of the Indian monsoon into the southeastern part of the Pamir Mountains (**Aizen et al., 2009**). Tibetan highs strongly affect the eastern and southeastern regions of CA, whereas southeastern monsoon activity in these regions are very weak and may be observed only at the most eastern extension of the Kunlun mountain ridges, in the Qilian Shan.

2.3 Sub-regions of CA

To better understand the spatial variability of seasonal snow cover and its changing patterns, we further subdivide CA into several climatic regions, according to certain climatic considerations and topographical features (**Aizen et al., in preparation**).

2.3.1 Plains

Vast plain areas (~50 °E to ~80 °E) were separated into two climatic regions: the Kazakh Steppe (KS) in the north and the Aral-Caspian Desert (AD) in the south, approximately following the boundary of the Aral Sea Basin. The AD is consisted of low elevation plains of the Aral Sea and the Caspian Sea basins, hosting large deserts like the Kyzylkum Desert and the Karakum Desert. The KS, as named by the largest steppe in CA, extends for more than 2200 km from west to east. The KS borders southern Siberia to its north, Ural River to its west, and Altai Mountains to its east.

2.3.2 Altai and surrounding areas

The Altai-Sayan Mountains geographically define the continental northern periphery of the CA mountain systems and southern periphery of the Asian Arctic Basin (**Aizen et al., 2005**). It acts as the initial barrier in CA to the intrusion of cold air masses from the Arctic.

During winter it is impacted strongly by the Siberian High which prevents the entrance of moisture-bearing air mass from the west, resulting in low winter precipitation. More precipitation happens in summer due to northwestern cyclones and local convections (**Aizen et al., 2005; Surazakov et al., 2007**).

Areas surrounding the Altai-Sayan Mountains have been separated into two climatic regions approximately following the major ranges of Altai-Sayan: Siberian Altai-Sayan (SA) situated on the northwestern slope and Mongolian Altai (MA) on the southeastern slope, with SA having more precipitation than MA.

2.3.3 Tien Shan and surrounding areas

The Tien Shan Mountain is one of the major mountain systems in Asia, locating at the region from 69 °E to 95 °E and 39 °N to 46 °N and stretching for more than 2000 km from west to east. It can be further divided to into western outer ranges, inner ranges and eastern outer ranges (**Ryazanceva, 1965; Aizen et al., 1995**). Continentality is the major climate characteristic for Tien Shan and its surrounding areas. Another major climate characteristic is that the maximum amount of precipitation happens in the warm season, with Siberian High controlling the region during the cold season, preventing intrusion of moisture bearing air mass (**Aizen et al., 1995**). The areas surrounding the Tien Shan Mountain were further divided into several climatic regions, including Western Tien Shan (WT), Inner Tien Shan (IT), Northern Tien Shan (NT), Eastern Tien Shan (ET), Tarim (TR), Central Tien Shan (CT) and Issyk Kul (IK) as in clock-wise order.

WT is defined as the areas surrounding the southern part of the western outer ranges of Tien Shan, including Fergana, Pskem, Chatkal and Gissar ranges. This region is under a

relatively weak influence of Siberian anticyclonic circulation in winter and spring, as well as a moderate influence of southwest cyclonic circulation which brings warm moist air masses (**Aizen et al., 1995**), resulting in more winter precipitation compared with other climatic regions in Tien Shan.

The IT climatic region is defined as the areas bounded by high mountains in the western part of the inner range of Tien Shan, with Meridionalniy Range to the east, Fergana Range to the west, Kok-Shaal Too to the south, Terskey, Kirgizskiy, and Talasskiy Alatoo to the north. Those high mountains prevent the intrusion of moisture-bearing air mass, resulting in smaller precipitation compared with its neighboring climatic regions.

NT is defined as the areas surrounding the northern part of the western outer range of Tien Shan, including the Talasskiy, Kirgizskiy and Kungei Alatoo, Zailiyskiy and Djungarskiy Alatoo. Its northern location leads to a stronger influence of the Siberian anticyclonic circulation during winter, which decreases its winter precipitation (**Aizen et al., 1995**).

ET is defined as the areas surrounding the mountains in the eastern outer range, from Khan Tengry massif in the west, Borohoro and Bogdo Mountains in the middle, to Tomurty Mountains in the east. It consists of Jungar Basin in the north, and Turfan Basin in the south. This region mainly experiences maximum precipitation in June to July, with winter precipitation only observed in high mountains (**Aizen et al., 1995**).

TR is in defined as the contributing area of Tarim River, which the longest inland river in China, excluding areas of head water in high mountains. It is a very sensitive arid region, with most of its area occupied by Taklamakan Desert.

The eastern part of the inner range and surrounding areas is defined as CT, separating from its western neighbor of IT approximately along the Meridionalniy Range. It is home to the highest peaks including Peak Tumour and Peak Khan-Tengri in Tien Shan, as well as the large Inylchek Glacier. This region also mainly sees precipitation in summer, with maximum precipitation happens in June and July (**Aizen et al., 2004**).

The IK climatic region, which is defined as the basin of Lake Issyk Kul, is specifically cut out due to its special climate characteristics. It is much warmer than places with similar latitude and elevation in Tien Shan thanks to the protection of surrounding high mountains and the existence of the deep lake (702 m depth) that never freezes. The eastern part of this region sees much more precipitation with denser river network, compared with the western part of the IK basin.

2.3.4 Pamir and surrounding areas

The Pamir Mountain is one of the largest and highest mountain systems in CA, extending from 65 °E to 75 °E and 36 °N to 40 °N. The influence of Siberian High in Pamir is weaker compared with Tien Shan, allowing the influx of moisture-bearing westerlies in winter, resulting in more precipitation in the cold season. There is also evidence suggesting intrusion of Indian Monsoon to the southern and eastern Pamir, probably to the central Pamir occasionally as individual two-to-three day events (**Schiemann et al., 2007; Aizen et al., 2009**). In general, Pamir sees maximum precipitation in winter and spring, with summer and autumn as relatively dry seasons. Pamir and surrounding areas were divided into four climatic regions: Western Pamir (WP), Central Pamir (CP), Eastern Pamir (EP), and Pamiro-Alay (PA). The climatic regions of WP, CP and EP were defined approximately following Rototaeva (**1983**), while the Alay valley is cut out as the Pamiro-Alay (PA) climatic region.

PA is a transition zone between Tien Shan and Pamir. It consists of two major mountain ranges – the Alaiskii and Zaalaiskii ranges stretching from east to west between ~66 °E and ~74 °E, occupying an area over 150,000 km^2. Its elongated shape with an open entrance in the west facilitates the easy influx of moist bearing air mass from the west, resulting in an increasing gradient of precipitation from west to east.

The WP climatic region is located to the south of PA, bordering AD to the west and CP to the east. It receives the highest amount of precipitation in the four Pamir climatic regions, with annual precipitation up to 2000 - 2500 mm.

CP consists of high elevation mountains surrounding by other three climatic regions in Pamir. Annual precipitation varies between 800 and 1500 mm, with more precipitation in the western facing slopes. It is home to large glacierized massifs with large dendrite glaciers, including the Fedchenko Glacier, which is the largest alpine glacier in the world.

EP is a distinct high elevation plateau, with most of its areas having elevation higher than 4000 m. It has an extremely arid climate with annual precipitation between 50 and 150 mm, similar to the Tibetan Plateau.

3 Outline of the dissertation

This dissertation contains six chapters. This chapter (Chapter 1) introduces the research topics of this dissertation and provides a general description of the research area. Chapter 2 presents the work of building a comprehensive climate database for CA, characterizes the climate regime, and analyzes historical climate changes in CA. Chapter 3 describes the work of constructing a long-term snow cover remote sensing products from

historical AVHRR and MODIS satellite sensors. Chapter 4 characterizes the spatial distribution and determining factors of seasonal snow cover in CA, and analyzes the historical changes of seasonal snow cover, based on the long-term snow cover remote sensing products. Chapter 5 describes the work of developing glacier databases with information about glacier extent and surface elevation for two representative glacier massifs in CA (the Fedchenko Glacier Massif and the Inylchek Glacier Massif), and analyzes the glacier distribution regimes and historical changes of glacier extent, surface elevation and ice volume in these two massifs. Chapter 6 summarizes and concludes this dissertation.

Figures

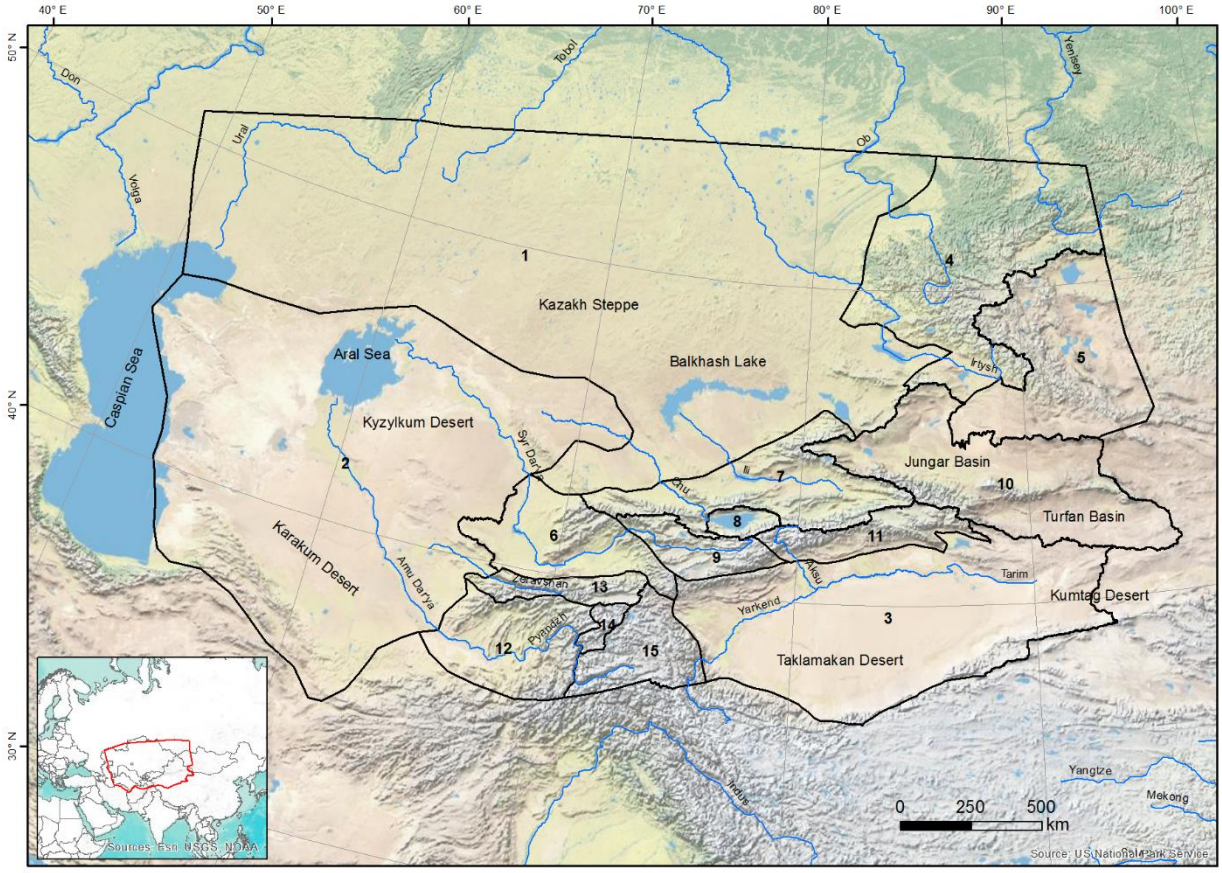

Figure 1.01-1 Map of central Asia (CA) study area

Main map shows 15 sub-regions of CA

1: Kazakh Steppe (KS), 2: Aral-Caspian Desert (AD), 3: Tarim (TR); 4: Siberian Altai-Sayan (SA), 5: Mongolian Altai (MA); 6: Western Tien Shan (WT), 7: Northern Tien Shan (NT), 8: Issyk Kul (IK), 9: Inner Tien Shan (IT), 10: Eastern Tien Shan (ET), 11: Central Tien Shan (CT); 12: Western Pamir (WP), 13: Pamiro-Alai (PA), 14: Central Pamir (CP), 15: Eastern Pamir (EP)

Inset map shows the location CA in Eurasia

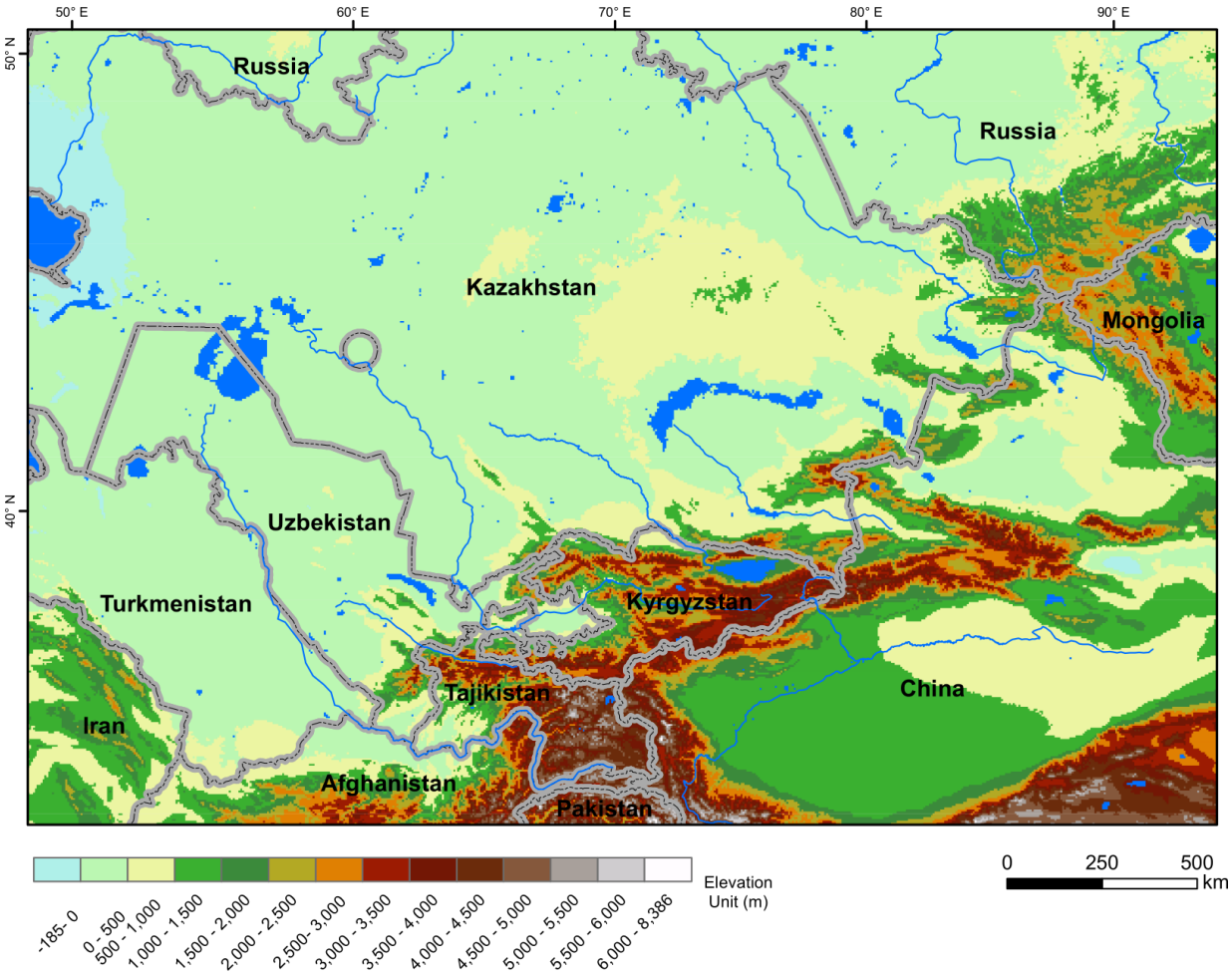

Figure 1.01-2 Digital Elevation Model of central Asia (CA) study area

Grey polygons show country boundaries in CA

References

Aizen, V. B., Aizen, E. M., & Melack, J. M. (1995). Climate, snow cover, glaciers, and runoff in the Tien Shan, Central Asia. Water Resources Bulletin, 31(6), 1113–1129.

Aizen, V. B. (2004). Association between atmospheric circulation patterns and firn-ice core records from the Inilchek glacierized area, central Tien Shan, Asia. Journal of Geophysical Research, 109(D8). http://doi.org/10.1029/2003JD003894

Aizen, V. B., Mayewski, P. a., Aizen, E. M., Joswiak, D. R., Surazakov, A. B., Kaspari, S., … Finaev, A. (2009). Stable-isotope and trace element time series from Fedchenko glacier (Pamirs) snow/firn cores. Journal of Glaciology, 55(190), 275–291. http://doi.org/10.3189/002214309788608787

Aizen, V. B., Aizen, E., Fujita, K., Nikitin, S. A., Kreutz, K. J., & Takeuchi, L. N. (2005). Stable-isotope time series and precipitation origin from firn-core and snow samples, Altai glaciers, Siberia. Journal of Glaciology, 51(175), 637–654. http://doi.org/doi:10.3189/172756505781829034

Aizen, V. B., Aizen, E., ZHOU, H., in preparation. Climate changes in CA during the 20th century

Antipova, E., Zyryanov, A., Kyrgyzenergo, J. S. C., & Republic, K. (2002). Optimization of Syr Darya Water and Energy Uses. Water International, 27(4), 504–516. http://doi.org/10.1080/02508060308691694

Barnett, T. P., Adam, J. C., & Lettenmaier, D. P. (2005). Potential impacts of a warming climate on water availability in snow-dominated regions. Nature, 438(7066), 303–9. http://doi.org/10.1038/nature04141

Böhner, J. (2006). General climatic controls and topoclimatic variations in Central and High Asia. Boreas., 35(2), 279–295. http://doi.org/10.1080/03009480500456073

Bryson, R. (1986). Airstream Climatology of Asia. In Y. Xu (Ed.), Proceedings of International Symposium on the Qinghai-Xizang Plateau and Mountain Meteorology SE - 36 (pp. 604–619). American Meteorological Society. http://doi.org/10.1007/978-1-935704-19-5_36

Cowan, P. J. (2007). Geographic usage of the terms Middle Asia and Central Asia. Journal of Arid Environments, 69(2), 359–363. http://doi.org/10.1016/j.jaridenv.2006.09.013

FAO. (2015). AQUASTAT Database. Food and Agriculture Organization of the United Nations. Retrieved December 20, 2015, from http://www.fao.org/nr/water/aquastat/data/query/ index.html

Immerzeel, W. W., van Beek, L. P. H., & Bierkens, M. F. P. (2010). Climate change will affect the Asian water towers. Science (New York, N.Y.), 328(5984), 1382–5. http://doi.org/10.1126/science.1183188

Lioubimtseva, E. (2002). Arid environments. In M. Shahgedanova (Ed.), Physical Geography of Northern Eurasia (p. 571). Oxford, England: Oxford University Press.

Lioubimtseva, E., & Henebry, G. M. (2009). Climate and environmental change in arid Central Asia: Impacts, vulnerability, and adaptations. Journal of Arid Environments, 73(11), 963–977. http://doi.org/10.1016/j.jaridenv.2009.04.022

Lutz, W., Sanderson, W., & Scherbov, S. (2008). IIASA's 2007 probabilistic world population projections. Retrieved from http://www.iiasa.ac.at/Research/POP/proj07/index.html?sb=6

Lydolph, P. E. (1977). Climates of the Soviet Union. Amsterdam [etc.]: Elsevier.

Micklin, P. (2007). The Aral Sea Disaster. Annual Review of Earth and Planetary Sciences, 35(1), 47–72. http://doi.org/10.1146/annurev.earth.35.031306.140120

National Bureau of Statistics China. (2015). The Fifth National Population Census of the People's Republic of China. Retrieved December 20, 2015, from http://www.stats.gov.cn/tjsj/pcsj/rkpc/dwcrkpc/

Panagiotopoulos, F., Shahgedanova, M., Hannachi, A., & Stephenson, D. B. (2005). Observed trends and teleconnections of the Siberian high: A recently declining center of action. Journal of Climate, 18(9), 1411–1422. http://doi.org/10.1175/JCLI3352.1

Rototaeva, O. V. (1983). Glaciologicheskoe raionirovanie Pamira (The Pamir glaciological zoning) (in Russian). Data of Glaciological Studies, 46, 39–51.

Ryazanceva, Z. A. (1965). Climate of Kirgizskoy SSR (in Russian). Frunze, USSR: Ilim Publishing.

Schiemann, R., Glazirina, M. G., & Schär, C. (2007). On the relationship between the Indian summer monsoon and river flow in the Aral Sea basin. Geophysical Research Letters, 34(5), L05706. http://doi.org/10.1029/2006GL028926

Schluter, M., Savitsky, A. G., McKinney, D. C., & Lieth, H. (2005). Optimizing long-term water allocation in the Amudarya River delta: A water management model for ecological impact assessment. Environmental Modelling and Software, 20(5), 529–545. http://doi.org/10.1016/j.envsoft.2004.03.005

Siegfried, T., Bernauer, T., Guiennet, R., Sellars, S., Robertson, A. W., Mankin, J., … Yakovlev, A. (2012). Will climate change exacerbate water stress in Central Asia? Climatic Change, 112, 881–899. http://doi.org/10.1007/s10584-011-0253-z

Surazakov, a B., Aizen, V. B., Aizen, E. M., & Nikitin, S. a. (2007). Glacier changes in the Siberian Altai Mountains, Ob river basin, (1952–2006) estimated with high resolution imagery. Environmental Research Letters, 2(4), 045017. http://doi.org/10.1088/1748-9326/2/4/045017

Surazakov, A. B. (2008). Application of Remote Sensing and GIS in Glacier Monitoring: Glacier Variability in Central Asia (Tienshan and Altai) During the Last 30-60 Years. PhD Dissertation. Department of Geography, University of Idaho.

Takaya, K., & Nakamura, H. (2005). Mechanisms of intraseasonal amplification of the cold Siberian high. Journal of the Atmospheric Sciences, 62(12), 4423–4440. http://doi.org/10.1175/JAS3629.1

World Bank. (2015). The World Bank Open Data. Population. Retrieved October 31, 2015, from http://data.worldbank.org/

You, Q., Fraedrich, K., Ren, G., Ye, B., Meng, X., & Kang, S. (2012). Inconsistencies of precipitation in the eastern and central Tibetan Plateau between surface adjusted data and reanalysis. Theoretical and Applied Climatology, 109(3-4), 485–496. http://doi.org/10.1007/s00704-012-0594-1

Chapter 2 Climate changes in central Asia from 1951 to 2010

1 Introduction

In central Asia (CA), which is a semi-arid / arid region, the fast growing population and the increasing demand of water resources for irrigated agriculture and energy generation (**Unger-Shayesteh et al., 2013**) have exacerbated the problem of water stress (**Siegfried et al. 2012**). From ancient times, the periodical drying of CA due to climate change is a well-known phenomenon (**Boroffka, 2010**). At the end of the 20th and the beginning of the 21st century, CA oases suffered from serious droughts (**Agrawala, et al., 2001**), and the most remarkable example is the Aral Sea desiccation (**Micklin, 2007**). Changes in air temperature and precipitation affect both fragile arid lowlands and glaciers as water storages in the highlands. An evaluation of climate changes in CA has become a crucial issue in the context of water resources change, for community planning, climate change adaptation and sustainable development.

Many studies about climate changes over CA have been published, presenting analysis over some parts of CA, e.g., mountains: the Tien Shan (**Aizen et al., 1997**), or state: Tajikistan (**Finaev, 2005**), or part of a state: North China (**Xu, 2001**). These investigations are limited by using climatic parameters at a subset of the station network before the 1990s (**Unger-Shayesteh et al., 2013**). Almost all studies revealed positive trends in annual / warm season air temperatures (**Aizen et al., 1997; Konovalov, 2003; Finaev, 2005**). The estimated magnitudes of changes vary across different studies because of different methods utilized and different time periods under examination, but in general fit well within the range of land surface air temperature changes reported globally (**Trenberth et al., 2007**). Investigations on precipitation changes did not reveal conformity in their estimations. Yatagai and Yasunari (**1994**) and Xu

(**2001**) revealed a negative trend of precipitation over the Southeastern Mongolia and Northern China, respectively, while Aizen et al. (**1997**), Konovalov (**2003**) and Finaev (**2005**) declared positive trends of precipitation though not so steady as for air temperature. Unger-Shayesteh et al. (**2013**) reviewed various studies concerning climate, cryosphere and hydrological changes in Central Asia, suggesting the existence of research gaps in precipitation changes, climate variability changes, and spatial patterns of climate changes. There is a lack of generalized knowledge about climate changes in CA, how both air temperature and precipitation changed over the entire CA and sub-regions of CA, and how changes happened in different elevations.

Such research gaps come from the lack of a comprehensive dataset of in-situ observations. As a region with scarce data, there exist only a few stations with long-term records of more than 100 years in CA while most stations are located in low-elevation plains or foothills of the mountains (**Unger-Shayesteh et al., 2013**). The station network degraded significantly after the collapse of the Former Soviet Union (FSU). And inhomogeneities may exist in climate time-series as a result of changes of instruments, station re-location, or land use change of stations' surrounding areas. Even though various efforts have been spent on collecting, correcting, and compiling in-situ observation data from stations across CA, most of the existing investigations of climate changes in CA used only data from 4 to 32 stations. Considering the large area of CA (~ 6.3×10^6 km^2 as defined in this study, including both plains and high mountains), which is approximately the same area of the continental United States (**Figure 2.01**), a comprehensive dataset is required for quantifying climate changes and the spatial patterns of climate changes in CA.

In this chapter, in-situ monthly climate data from various data sources were collected, corrected, and compiled together to a unified comprehensive dataset. Long-term average

climate regimes and climate changes at the regional scale for the last five decades of the 20th century and the first decade of the 21st century over CA were quantified and analyzed.

2 Study area

In this study, central Asia (CA) is defined as the center of the Eurasian continent, spanning from the Caspian Sea in the west to the Mongolian Steppes and the Gobi Desert in the east, from western Siberia and the Altai-Sayan mountains in the north to the Karakum and Taklamakan deserts to the south (**Figure 2.01**). The major terrain type for CA is plains (**Figure 2.05-a**) while it is also home to the high mountains of Altai-Sayan, Tien Shan, and Pamir, reaching 6000 m - 7000 m above sea level (a.s.l.). Those high mountains extend from northeast to southwest for more than 5000 km, controlling moisture distribution and atmospheric pressure in the mid to low latitudes of Asia (**Lydolph, 1977; Bryson, 1986; Aizen et al., 1997**).

The most conspicuous feature of CA mountain ranges, especially the Tien Shan and Altai mountain ranges, is the occurrence of maximum precipitation during the warm season, because in the cold season the Siberian High (SH) strongly controls the regional climate and blocks the entrance of moisture-bearing westerlies (**Aizen et al., in preparation**). Significant teleconnections exist between the SH and the westerlies (**Panagiotopoulos et al. 2005**), and between the SH and the East Asian Monsoon (**Takaya and Nakamura, 2004**). Various studies show a decreasing trend of the SH intensity from the 1960s with a record low SH intensity in the early 1990s (**Mokhov & Petukhov, 1999; Sahsamanoglou et al., 1991; Panagiotopoulos et al., 2005**) while recent publications (**Jeong et al. 2011; Cohen, et al., 2012; Zhang et al., 2012**) suggest a recovery of the SH intensity since the mid-1990s.

In contrast, in Pamir, maximum precipitation occurs in winter and spring because of the weaker influence of the Siberian / Tibetan highs. Local precipitation occurs during winter and early spring in Pamir when depressions develop over the Eastern Mediterranean and move subsequently over the Caspian Sea, where they may replenish moisture, and into Pamir (**Lioubimtseva, 2002**). Therefore, in mountainous areas in Pamir, summer and autumn are dry seasons, with occasional intrusions of the Indian Monsoon into the southeastern part of the Pamir Plateau (**Aizen et al., 2009**). The Tibetan High strongly affects the eastern and southeastern parts of CA, whereas southeastern monsoon activity in these regions is weak and can only be observed at the most eastern extension of the Kunlun Mountains.

To better understand the spatially varied long-term average climate regime and historical climate changes, CA was further separated into 15 climatic regions (**Figure 2.01 and Figure 2.05-d**), based on meso-climatic regimes and local topography (**Aizen et al., 2007a; Aizen et al., in preparation**). The 15 climatic regions are listed here: 1) Kazakh Steppe (KS), 2) Aral-Caspian Desert (AD), 3) Tarim (TR); 4) Siberian Altai-Sayan (SA), 5) Mongolian Altai (MA); 6) Western Tien Shan (WT), 7) Northern Tien Shan (NT), 8) Issyk Kul (IK), 9) Inner Tien Shan (IT), 10) Eastern Tien Shan (ET), 11) Central Tien Shan (CT); 12) Western Pamir (WP), 13) Pamiro-Alai (PA), 14) Central Pamir (CP), 15) Eastern Pamir (EP). Details about the segmentation of CA are presented in Chapter 1 of this dissertation.

3 Data sources

To evaluate the long-term average climate patterns and climate changes in CA since the 1950s, records of monthly average air temperature and accumulated precipitation were collected from several sources.

3.1 NSIDC monthly temperature and precipitation observation data in CA

The NSIDC dataset (**Williams and Konovalov, 2008**) contains monthly temperature and precipitation data in Central Asian countries, focusing on the Northern Tien Shan and Pamir Mountain ranges. It is primarily compiled from meteorological measurements conducted by the National Hydrometeorological Services (NHMS) of the Former Soviet Union (FSU) and the independent Central Asian Republics (CAR, including Kazakhstan, Kyrgyzstan, Tajikistan, Uzbekistan and Turkmenistan). There are records from 298 stations, with the earliest records taken in 1879 and the latest records taken in 2003. A sharp reduction of the number of stations happened during the period from 1990 to 1995. The dataset has been homogenized and quality controlled, using methods which are consistent with those used by the Global Historical Climate Network (GHCN) (**Peterson and Vose, 1997**). Station history information is also provided in this dataset.

3.2 Central Asia Database (CADB) Meteorological station data in FSU

The CADB dataset (*http://www.webpages.uidaho.edu/cae/data/*), collected by the University of Idaho cryosphere research group, contains monthly temperature and precipitation data in 227 stations in the CAR. A subset of this dataset with 77 stations has been shared openly online. The temporal range of this dataset is from 1832 to 2005, with most of the stations having data in the period from the 1950s to the 1990s. Comparison between this dataset with the NSIDC dataset suggests that both of them have a very similar, if not exactly the same origin, and a similar set of methods has been utilized for homogenization.

3.3 Monthly temperature data in GHCNv3

The GHCNv3 (**Lawrimore et al., 2011**) dataset contains 130 stations in the CAR, Western Mongolia, and Southern Russia. It covers a temporal range from 1883 to 2012, with

most of the stations having valid data in the period from the 1950s to the 1990s. Data records in this dataset have gone through rigid quality assurance and homogeneity adjustment procedures.

3.4 RIHMI Monthly meteorological station observations in Russia

The Russian Institute of Hydrometeological Information (RIHMI) dataset (*http://meteo.ru/english/data/*) contains monthly temperature and precipitation data for 40 stations in Siberian Altai-Sayan. The temporal coverage for each station varies, with the most recent records taken in 2012, and the earliest records taken in 1839. Most stations have valid data in the period from the 1950s to the 2000s. As the companion document about methods and station history suggests, the data has been quality controlled and homogenized.

4 Methods

All collected datasets went through the data preprocessing step first, including transforming to common plain text formats, fixing various types of errors and going through several quality control procedures. During the data merging step, which is the second step, data from different sources were cross compared and merged, then quality controlled again. Gaps in the merged climate dataset were filled using the iterative-PCA gap-filling method. Then various climate statistics were calculated from the gap-filled dataset, and further interpolated to spatial grids using Geographically Weighted Regression (GWR) based methods (**Figure 2.02**).

4.1 Data preprocessing

Data files obtained from different sources were reformatted to common plain text based formats. Monthly records were saved as tab-separated text files, with each line

containing the year and records in the corresponding 12 months. Air temperature data was all converted to degree centigrade while precipitation data was converted to millimeter. The value -999.0 was used as the representation for NoData. Station information was saved as YAML plain text files (*www.yaml.org*), with fields of longitude, latitude, altitude, country code and station code. Original data files, including the station meta-data, actual records, and station history documents when available, were archived for future references.

During the conversion and reformatting step, obvious errors, including typological errors, inconsistency of NoData mask and mislabeling of time in station meta-data and records were detected and corrected using automatic scripts. The resulting files were further manually checked. In addition, the location information of stations was double checked and corrected when necessary by consulting local collaborators or searching manually in high resolution satellite images in Google Earth.

All converted data files were quality controlled at the single station level with a set of four procedures, which is designed roughly following the procedures used by the GHCN version 2 (**Peterson and Vose, 1997**).

1. Physically impossible values

Monthly temperature values which are higher than 60 °C or lower than -60 °C, and monthly precipitation values outside the range of 0 mm to 2500 mm, are considered possibly wrong values and reported.

2. Duplicated Series

Years with the exact same recorded values are reported as duplicated series, which may be caused by errors in original data transmission or processing.

3. Streaks

Streaks are defined as records with four consecutive months, which have the exactly same values, except they are precipitation records with a value of 0 mm in summer months (June, July, and August) in known desert regions.

4. Climatological Outliers

Climatological outliers were examined using z-score based method (**Menne et al., 2009**). The formulas for calculating z-score are shown below:

$$Z = \frac{V_i - \bar{V}}{\sigma_V} \qquad \textbf{Equation 2.1}$$

where V_i is the value of the record under examination, $\bar{V}$ is the long-term monthly mean, and σ_V is the long-term standard deviation. For precipitation data, the value is first square-root transformed before calculating the z-score. Records with z-score outside the range of -5 to 5 are reported as climatological outliers.

4.2 Data merging

4.2.1 Comparing meta-data and matching stations

It is not uncommon for a meteorological station to have different names or different location information in different data sources. The differences of names may be due to various ways of translating the station name from Russian or local languages to English, or from the practice of replacing geographical names in Russian with names in local languages after the

independence of Central Asian Republics. Station code cannot be used as the unique identifier neither since it is possible for two nearby stations sharing the same station code with different internal extension codes, which may not be included in the meta-data documentation provided by the data source.

The first step in merging dataset from different sources is to identify the matching stations. Two stations in different data sources were marked as likely being the same station if they met one of the following rules:

1. They have the same station code, and their extension codes are also the same if available.
2. They have exactly the same station name or similar names by pronunciation as suggested by the New York State Identification and Intelligence System (NYSIIS) algorithm (**Taft, 1970**).
3. Their location information suggests that the distance between them is shorter than 5000 m, and the elevation difference is less than 100 m.

The meta-data and the actual data records of stations that have been identified as possibly the same station were further checked manually to identify matching stations in different data sources.

4.2.2 Comparing and merging of data records

Data records for a matched station in two different data sources were compared in the overlapped time periods. If no differences exist in the overlapped time periods, records from different sources for this station are combined to form a longer time series. If there is any difference in the data of the overlapped time periods, the discrepancies were further examined

semi-automatically before decisions were made for how to combine different sources together.

Most of the time, the differences between values in different sources are quite small, less than 0.5 °C for temperature or less than 10 mm for precipitation. These discrepancies may be the result of 1) different ways for averaging and rounding data; 2) different homogenization / correction methods used by different scientists. It is often not possible to know which value is correct since in general no information about how the processing has been done was provided in the companion document. Instead, a realistic though somehow arbitrary method was developed to determine which value should be picked up based on empirical evidence of the data quality of different data sources. If the data for one station in a given month from one data source has been marked as possibly having problems during the quality control step while data from another source does not have problems, then the data value with no problems was selected. If both sources were marked as problematic or both did not have any problem, then a priority rule was used. For each data source, a trustworthiness rate was calculated as:

$$R_t = 1 - \frac{N_{typos} + N_{inconsistency}}{N_{total}} \qquad \textbf{Equation 2.2}$$

where R_t is the trustworthiness rate, N_{typos} is the number of typos, $N_{inconsistency}$ is the number of records that have been marked as possibly inconsistent, and N_{total} is the total number of records in the corresponding data source. The value from the data source with higher R_t would be selected.

When the differences between values are bigger than the aforementioned criteria, it is considered that significant differences exist between the data records for this station in the

data sources being compared. Under such circumstances, the time series with longer records would be selected.

4.2.3 Quality control of merged dataset

Quality control at the single station level was performed on the merged dataset using the same four procedures described in section 4.1. Then a spatial inconsistency check was conducted using a local linear regression based method (**Song et al., 2004**). For each station, its 50 nearest neighbors were picked up and further filtered with the criterion that remaining stations should have a positive correlation with the station for the month being examined. Then linear regression models were created between the station and its selected neighbors. A series of estimated values for the record, as well as 95% confidence intervals, were calculated from those linear models. If the value of this record is outside the range of estimated confidence intervals, then it was marked as spatially inconsistent.

4.2.4 Summary of merged station data

After data merging, there are 457 stations in CA (**Figure 2.03**), spanning from 35.28 °N to 50.25 ° N in latitude, from 50.40 °E to 91.98 °E in longitude, and from -135 m b.s.l. to 4169 m a.s.l. in altitude. The record's precision is 0.1 °C for monthly temperature and 1 mm for precipitation. All values marked as not trustworthy in the quality control steps were replaced with NoData marks. The earliest records were taken in 1832 while the latest were taken in 2014. Data availability analysis (**Figure 2.04**) shows that during the period from 1961 to 2000, the number of available stations is always greater than 300. The maximum number of stations was reached in the mid-1980s but then went down quickly after the collapse of the FSU. After 2000, the number of stations with available data continued going down quickly due to either discontinuation of observation or restrictions on data sharing.

More information about station location and temporal coverage of monthly temperature and precipitation records can be found in **Appendix A Table 1**.

The period from 1951 to 2010 were designated as the research period for further data processing and analysis. Stations with a valid data rate higher than 80% in a core sub-period (1961 – 2000) were selected, resulting in 369 and 381 stations for monthly temperature and precipitation, respectively (**Figure 2.03 and Figure 2.04**). Most stations are located in areas below 1000 m. For the elevation range above 4000 m, there are only 6 and 4 stations for monthly air temperature and precipitation, respectively (**Figure 2.05-b**). The densities of stations for the elevation ranges below 1000 m and above 4000 m are around 40 stations per 10^6 km^2, sparser than other elevation ranges with densities in the range from 85 to 120 per 10^6 km^2 (**Figure 2.05-c**). The relatively denser network in the mid to upper elevation ranges is in accordance with the more complex climate variable spatial distribution. Analysis of the station distribution by different climatic regions shows that the climatic regions with mainly plains (KS, AD, and TR) have a lower density of stations even though the numbers of stations in those climatic regions are higher than many other regions. Mountainous climatic regions, including WT, NT, IK, and IT in Tien Shan and WP, PA, and CP in Pamir, have denser station networks (**Figure 2.05-e and Figure 2.05-f)**. It should be noticed that the elevation range above 4000 m, and climatic regions like SA and MA in Altai, ET and CT in Tien Shan, and EP in Pamir have sparser station distribution though their mountainous terrains are complex.

4.3 Iterative-PCA gap-filling method

A gap-filling method was developed based on the Principal Component Analysis (PCA) method. PCA is a widely used dimensionality reduction method to find a new set of

variables as linear combinations of the original variables, capturing most of the observed variance in the original data (**Storch and Zwiers, 2002**). It has been used in various climate studies for decomposing dominant mode (**Storch and Zwiers, 2002**) and time-series gap-filling (**Beckers and Rixen, 2003; Kondrashov et al., 2014**).

The algorithm developed for gap-filling in this study is described below:

1. Step 1, initial guess
    - For each station, its 50 nearest neighbors were selected.
    - For each NoData record, its neighbors having a positive correlation with the station under examination in that month were selected.
    - Simple linear models were constructed between the station and its neighbors selected in the previous sub-step.
    - An initial guess was calculated as the weighted mean of estimated values from the simple linear models. The weight is defined as $\frac{R_i^2}{\sum_{i=1}^{i=k} R_i^2}$, where the R_i is the correlation between the station under examination and its i^{th} neighboring station in that month, k is the total number of neighbors that have been selected.
    - If a weighted mean initial guess cannot be calculated, either because no linear model can be built, or no valid values in nearby stations exist, the long-term monthly mean value was used as the initial guess.
2. Step 2, optional, data transformation
    - For precipitation, the values were first transformed as deviations from the long-term monthly mean.
3. Step 3, PCA and inverse PCA

- Truncated PCA was performed on the temperature or precipitation data set, preserving a defined percentage of variance.
- Inverse PCA was performed on the resultant values of PCA, to create a generalized representation of the input dataset.

4. Step 4, optional, inversed data transformation
   - For precipitation, the values were transformed back from deviation from the long-term monthly mean to actual values, and negative estimated values were replaced by 0.
5. Step 5, replacement of values
   - For a NoData record which has not been marked as filled, if the difference between its previous estimate and the current estimate is less than a certain critical value, store the current estimate and mark this record as filled.
   - Iteratively run step 2 to step 5 until all gaps were filled.

Cross-validation was used within the iterative-PCA gap-filling method to provide a scheme for assessing the uncertainty of the gap-filled results. Before conducting the gap-filling, 5 valid values in each station were randomly selected and removed. The gap-filling method was run for 30 times, then root mean squared error (RMSE) was calculated for each station and for the whole station set from the filled values and the removed values, providing a quantification of the performance of the gap-filling method. Cross-validation results with selected parameters (**Table 2.1**) suggest that the gap-filled monthly temperatures have a mean RMSE of 0.03 °C, with a maximum value of 0.13 °C and only 2 stations have RMSE values greater than 0.1 °C. For monthly precipitation, the cross-validation procedure shows a mean

RMSE of 0.60 mm, with a maximum value of 1.99 mm and 50 stations having RMSE values greater than 1 mm (**Table 2.2**).

4.4 Calculation climatic characteristics at stations

4.4.1 Break year of mean temperature changes in CA

CA has experienced a change from a cold period to a warm period around the 1970s (**Giese, 2007**). The Bernaola-Galvan Heuristic Segmentation (BGHS) method (**Bernaola-Galvan et al., 2001**) was used to find a general break year for this change.

The BGHS method is a method to split a non-stationary time series into a set of stationary segments. At each time point, a T-test statistic is calculated by comparing the mean values before and after this time point. The maximum T-test statistic value and the corresponding time are picked up. Then the probability of observing a maximum T-test statistic less than the observed maximum T-test value in a randomly drawn time series is calculated using an approximation function generated from Monte-Carlo experimentation. If the probability is greater than a given criterion (PROB), the time series are split at this time point. The BGHS method will further process each time series subset until the length of the subset is less than a given criterion (MIN_LEN). When working on a time series subset, additional T-tests with a significant level of ALPHA would be conducted at a proposed splitting time point, comparing the separated subset with its former and latter neighboring subsets separated in the previous recursion. If any of the T-tests were not significant, the proposed split would be rejected. The BGHS method can be used to split non-stationary time series, and the formulation of its statistical test assures it is stricter than other T-test based change detection method, for example, moving window T-test. It has been widely used to

analyze biophysical and physiological data (**Fukuda et al., 2004**), financial time series (**Tóth et al., 2010**), and geophysical time series (**Feng et al., 2008**).

The BGHS method was applied on annual mean air temperature and accumulated precipitation records calculated from gap-filled monthly temperature and precipitation, with the following parameters: PROB = 0.95, MIN_LEN = 25 and ALPHA = 0.05. The results suggest 1976 / 1977 as the break year for air temperature in CA, with 113 out of 369 stations having statistically significant shifts of mean annual temperature in the 1970s, and 69 stations witnessed such a change during 1976 / 1977 (**Figure 2.06-1**). Distribution of stations with a significant break of mean air temperature does not have specific spatial patterns. At the same time, there does not exist a general break year for precipitation (**Figure 2.06-2**). As a result, the research period was cut into two sub-periods in the year 1976 / 1977.

4.4.2 Climate characteristics

Annual and seasonal mean air temperatures and accumulative precipitations were calculated from gap-filled monthly temperature and precipitation data at each station. Average and standard deviation of those variables were calculated at each station for the whole research period and the two separated sub-periods (1951 -1976 and 1977 - 2010) for describing the general patterns of climate, while differences between averages of the two sub-periods (as the average in the latter period minus the average in the former period) and corresponding Student's t-test statistics, as well as differences between the standard deviations of the two sub-periods (as the standard deviation in the latter period minus the standard deviation in the former period) and the corresponding Levene's test (**Levene, 1960**) statistics were calculated to represent the changes of the climate (**Table 2.3**).

4.5 Spatial interpolation with GWR

The Geographically Weighted Regression (GWR) method was used to interpolate climate characteristics at station level to spatial grids, generating both the interpolated value and the standard error estimation at each grid point. It is a localized regression based method widely used for spatial interpolation, accounting for the spatial inhomogeneity with spatially varying slopes and intercepts. At each prediction location, the GWR picks up nearby training data points and constructs a weighted linear regression model of the dependent variable based on explanatory variables. There exists a set of options for determining whether a training point is included and its corresponding weight for constructing the linear model at a prediction location (**Fotheringham et al., 2002**). In general, the weight for a training data point is determined by a function of the distance from the training data point to the prediction point, with points closer to the prediction point having stronger weights.

In this study, the station level climate characteristics were used as the dependent variables while the elevation at 10 km spatial resolution was used as the explanatory variable, utilizing the well-known dependency of temperature and precipitation on elevation (**Daly et al., 1994**). For climate characteristics other than mean precipitation, the adaptive bandwidth method was used to determine whether a training point would be included by picking up a defined number of nearby nearest stations at a prediction location, with the number estimated using the AICc method. The Gaussian kernel method was used to calculate the weight of each station for each prediction location. The whole procedure was constructed using functionalities provided in ESRI ArcGIS (*http://www.esri.com/software/arcgis*).

For mean precipitation, a customized GWR method was developed with a topographical facet based method for picking up neighboring stations at each prediction

location. A series of topographical facets are generated at different scale levels, following the methodology described by **Daly et al. (1994)**. At each prediction location, the customized GWR tries to first select stations sitting in the same facet at the finest level. If the number of selected stations does not meet the requirement of a minimum number of stations (MIN_STA), the algorithm goes to the upper-level facet and selects stations sitting in the same facet, until fulfilling the requirement. Considering topographical facet in the procedure of selecting neighboring stations helps to utilize the dependency of precipitation on topographical features (**Daly et al., 1994**). The whole algorithm was implemented in cython (*www.cython.org*) with Gnu Scientific Library (GSL) (*http://www.gnu.org/software/gsl/*).

4.6 Calculation of regional level climate characteristics

Regional mean value of each climatic characteristics was calculated for each climatic region (CR), elevation range (ER), and elevation range within a climatic region (ERCR) as the simple arithmetic mean of all interpolated values within the calculation region. Considering only spatial autocorrelation between two grid points within a calculation region, the uncertainty of the calculated regional mean was estimated using a simplified method based on uncertainty propagation with the following formula:

$$SE = \frac{\sqrt{\sum_{i=1}^{N} se_i^2 + \sum_{i,j} 2 * \rho_{i,j} * se_i * se_j}}{N} \qquad \textbf{Equation 2.3}$$

where SE stands for the standard error estimation for the regional mean, se_i is the standard error for the interpolated value at the ith grid point, $\rho_{i,j}$ is the correlation between the ith and the jth grid point, and N is the total number of grid points within the calculation region.

Three different types of estimation were provided based on different ways of treating the spatial autocorrelation term ($\sum_{i,j} 2 * \rho_{i,j} * se_i * se_j$) in the **Equation 2.3**.

1. A lower bound estimation

Assuming no spatial autocorrelation between values in different grids, then the **Equation 2.3** can be simplified as $SE = \frac{\sqrt{\sum_{i=1}^{N} se_i^2}}{N}$. This provides a quick but underestimated standard error of the regional mean.

2. An upper bound estimation

Assuming the spatial autocorrelation between two grid points within a calculation region is always 1.0, the **Equation 2.3** can be used to calculate an upper bound estimation of the uncertainty.

3. An approximate general estimation

Assuming decreasing autocorrelation with increasing distance between grid points, which is described by a spherical function of distance (**Hengl, 2009**), the correlation between two grid points can be calculated based on the distance between them. Then the formula 3 can be used to calculate the standard error of the regional mean as a general approximation of the uncertainty.

Notice that the uncertainty of the regional mean calculated here only accounts for the uncertainty happened during the spatial interpolation procedure. The uncertainties in the measurement, in the PCA gap-filling, and in the DEM generation were not taken into consideration.

5 Results

5.1 Long-term average and variability of air temperature in 1951 - 2010

The spatially interpolated long-term average annual air temperature (T_{ann}) in CA during 1951 - 2010 has an area-weighted mean of 5.76 °C, ranging from -19 °C to 18°C. High values of T_{ann} (> 15 °C) are observed in the Karakorum Desert, spanning from the southeastern part of the AD to the southwestern part of the WP while low values (< -15 °C) are observed in the mountains of Altai, Tien Shan and Pamir (**Figure 2.07**). The distribution of air temperatures depends on both elevation and latitude, with colder air temperature in higher elevation and farther north latitude. High elevation areas have mean T_{ann} of –2.22 °C and –7.22 °C for elevation ranges of 3000 – 4000 m and > 4000 m, respectively; while areas below 1000 m have mean T_{ann} of 7.32 °C (**Figure 2.12**). Climatic regions in the southern latitudes have higher T_{ann} compared with climatic regions in northern latitudes at the similar elevation ranges (**Figure 2.13 and Figure 2.14**). Annual and seasonal long-term average air temperatures have similar spatial distribution patterns (**Figure 2.07 to Figure 2.11**).

The standard deviation of annual temperature (σT_{ann}) has a range between 0.31 °C and 1.24 °C, with an area-weighted mean of 0.80 °C (**Figure 2.15**). High values of σT_{ann} are observed in mountainous areas, especially in Tien Shan and Altai while low values are mainly observed in northern plain areas of the KS. Winter is the season with most variable air temperature with a mean value of σT_{win} at 2.20 °C, while summer is the least variable season regarding air temperature with mean σT_{sum} at 0.88 °C (**Figure 2.16 and Figure 2.17**). The σT goes down with increasing elevation in general, with the highest mean σT_{ann} of 0.98 °C observed in the elevation range < 1000 m (**Figure 2.18**) and the lowest mean σT_{ann} of

0.60 °C observed in the elevation range 3000 – 4000 m. Higher latitude areas have greater variability of air temperature than lower latitudes, for example, the KS always have larger σT than the AD in the same elevation ranges (**Figure 2.15 to Figure 2.17**). High elevation areas above 3000 m in Tien Shan have less variability of air temperature than areas in Pamir and Altai in the same elevation range (**Figure 2.19 and Figure 2.20**).

The spatial patterns of σT vary across different seasons. Comparisons among seasonal long-term standard deviations show that high elevation areas have more stable σT across different seasons than in low elevation plains, indicated by lower values of difference between winter and summer long-term standard deviation ($\sigma T_{win} - \sigma T_{sum}$) (**Figure 2.21**). The highest mean value of $\sigma T_{win} - \sigma T_{sum}$ (1.90 °C) is observed in the elevation range < 1000 m. The KS and the AD have high values (> 1.5 °C) of $\sigma T_{win} - \sigma T_{sum}$, especially in the northeastern KS (> 2 °C). And the lowest mean value (0.61 °C) occurred in the elevation range 3000 - 4000 m, with mountainous areas in Altai, Tien Shan, and Pamir having low values of $\sigma T_{win} - \sigma T_{sum}$ below 0.5 °C. The elevation range above 4000 m has a mean difference of 0.91 °C, mainly due to the high values of difference (1.5 °C to 1.75 °C) in the southern part of the EP.

5.2 Changes of average and variability of air temperature between 1951 - 1976 and 1977 – 2010

Significant increases of long-term mean annual air temperature between the two sub-periods were found at 250 stations out of 345 stations sitting within the boundary of the 15 climatic regions, accounting for 73% of the stations under examination while no station has experienced a statistically significant decrease of annual air temperature (**Table 2.4**). Spatially interpolated differences of long-term average annual temperatures in CA between the two

sub-periods (ΔT_{ann}) have an area-weighted mean of 0.70 °C, ranging from -0.41 °C to 1.13 °C (**Figure 2.22**). The difference has a negative relationship with increasing elevation (**Figure 2.23 and Figure 2.25**), with the largest mean increase of 0.82 °C observed in the elevation range < 1000 m, and the smallest mean increase of 0.13 °C in the elevation range > 4000 m. The KS and the SA are the two climatic regions with the strongest increase of air temperature, with ΔT_{ann} of 0.90 °C and 0.89 °C, respectively (**Figure 2.24**).

Vast plain areas in the northern part of CA, spanning from areas surrounding the Aral Sea in the southwest to the Altai-Sayan Mountains in the northeast, accounting for 56% of the total area in CA, are the main areas experiencing high values of ΔT_{ann} (> 0.7 °C), with a distinct main center of increase located in the boundary areas between the northeastern KS and the SA with ΔT_{ann} greater than 1 °C (**Figure 2.22**). The high increase of annual air temperature in this region is mainly associated with strong increases of air temperature in winter, which is greater than 1.5 °C (**Figure 2.26**) while in spring and autumn the increases of temperature are greater than 1°C (**Figure 2.27 and Figure 2.29**). Another main center of increasing air temperature is located in areas surrounding the Aral Sea, with ΔT_{ann} in the range of 0.7 - 1 °C. The increase of air temperature in this region is mainly caused by the increase in spring and summer when the differences of long-term average temperature are higher than 1 °C (**Figure 2.27 and Figure 2.28**). Moderate increases of temperature with ΔT_{ann} ranging from 0.2 - 0.7 °C can be found in other plain areas, for example, southern AD and the TR.

Climatic regions with mostly high elevation areas in Tien Shan and Pamir are regions seeing the least increase of air temperatures, with the EP and the CP having the lowest mean values of ΔT_{ann} at 0.16 °C (**Figure 2.24**), as well as the smallest proportion of stations seeing

significant increase of annual air temperature (**Figure 2.22**). High elevation (> 4000 m) regions in the ET and part of the CT even experienced decreases of T_{ann} between two sub-periods, though related high elevation stations did not show statistically significant decreases (**Figure 2.22 and Figure 2.28**). The increases of air temperatures in Tien Shan and Pamir are mainly contributed by the increases in summer, with ΔT_{sum} in the range of 0.2 – 0.5 °C (**Figure 2.28**), while in winter for Pamir, and in winter and spring for Tien Shan, the air temperatures have much smaller increases or even decreases in high elevation mountains (**Figure 2.26 and Figure 2.27**).

The variability of annual air temperatures does not change strongly in CA, indicated by the small area-weighted mean of $\Delta\sigma T_{ann}$ at -0.03 °C (**Figure 2.30**). There are 20 stations with significant increases of σT_{ann} and 47 stations with significant decreases (**Table 2.4**). The $\Delta\sigma T_{ann}$ goes up with increasing elevation, with the strongest decrease of -0.05 °C happened in the elevation range below 1000 m while the elevation range 3000 – 4000 m witnessed an increase of 0.06 °C between the two sub-periods (**Figure 2.31**). Stations with significantly decreased σT_{ann} can mainly be observed in a zone spanning from the WP and the WT to the eastern part of the AD and the KS, with $\Delta\sigma T_{ann}$ in the range from -0.35 °C to -0.1 °C (**Figure 2.30**), mainly associated with the decrease of temperature variability in winter (**Figure 2.32**). The SA and the MA experienced increases of variability for annual temperature, mainly associated with increases of variability in summer (**Figure 2.30, Figure 2.32, and Figure 2.33**). Mountainous regions in the EP, IT, CT, and the boundary areas between the CT and the ET also have experienced increased variability for annual temperature, mainly associated with increases of σT_{sum}, though most of the stations there only see not statistically significant increase of σT_{ann} (**Figure 2.30 and Figure 2.33**).

5.3 Long-term average and variability precipitation in 1951 - 2010

The area-weighted mean of spatially interpolated long-term average annual precipitation in 1951 – 2010 (P_{ann}) for CA is 267 mm, with a range from 15 mm to 1470 mm. High P_{ann} (600 – 1470 mm) can be observed at major mountains of Altai, Tien Shan, and Pamir while low P_{ann} (15 - 200 mm) can be observed in deserts (e.g. the Karakorum Desert, the Taklamakan Desert and the Kumtag Desert) and rain shadows of major mountains (**Figure 2.34**). Precipitation has a positive relationship with elevation, with the highest mean P_{ann} of 398 mm and 376 mm occurred in the elevation ranges 3000 – 4000 m and > 4000m, respectively; while the lowest mean P_{ann} of 249 mm occurred in the elevation range below 1000 m (**Figure 2.35**). Tarim is the climatic region with the lowest regional mean P_{ann} (81 mm), as most of its area are taken up by the Taklamakan Desert while the ET and the AD also have low P_{ann} as home to major deserts. The CP is the climatic region with the highest regional mean P_{ann} (629 mm) while other climatic regions with a large portion of high elevation mountains also have high values of regional mean P_{ann} (**Figure 2.36**).

Spring and summer are the two seasons with the largest share of precipitation, with the area-weighted means of long-term average seasonal share of 29.7% and 28.9%, respectively (**Figure 2.37-1**). The seasonal distribution of precipitation varies a lot across different climatic regions (**Figure 2.38 to Figure 2.41**). The KS (**Figure 2.37-2**), Altai climatic regions (**Figure 2.37-5 and Figure 2.37-6**), and Tien Shan climatic regions except the WT (**Figure 2.37 -8 to Figure 2.37-12**) have summer dominated precipitation, as summer precipitation is the largest in four seasons and accounts for more than 35% of annual total precipitation. In contrast, the AD (**Figure 2.37-3**), the WT (**Figure 2.37-7**), and climatic regions in Pamir (**Figure 2.37-13 to Figure 2.37-16**) have most precipitation happened in spring and winter, as

precipitation in these two seasons accounts for more than 34% and 23% of annual total precipitation in those climatic regions, respectively. Climatic regions with summer dominated precipitation are located in higher northern latitudes compared with climatic regions with winter / spring dominated precipitation. This location difference leads to the stronger influence of the Siberian High on these higher northern latitude climatic regions compared with lower latitude climatic regions, blocking the moisture bearing air masses from westerlies, resulting in less precipitation in winter and spring (**Lydolph, 1977; Aizen et al., 1997**).

The area-weighted mean of spatially interpolated long-term standard deviation of annual precipitation (σP_{ann}) in CA is 63 mm, ranging from 26 mm to 251 mm (**Figure 2.42**). Deserts in the AD, TR, and ET are areas witnessing small variability of annual precipitation (< 50 mm), with TR as the climatic region having the lowest regional mean of σP_{ann} (39 mm). Mountainous regions in Altai, Tien Shan, and Pamir, especially in Tien Shan, and Pamir, witnessed large variability of annual precipitation (> 150 mm), with the PA as the climatic region having the highest regional mean of σP_{ann} (120 mm) (**Figure 2.44**). The spatial distribution pattern of σP_{ann} is similar as the long-term average annual precipitation, as areas with more precipitation tend to have higher variability of precipitation (**Figure 2.34 and Figure 2.42**). There also exists a positive relationship between σP_{ann} and elevation, as the lowest mean value of 60 mm can be observed in the elevation range below 1000 m and the highest values of 88 mm and 87 mm happened in elevation ranges 3000 – 4000 m and > 4000 m, respectively (**Figure 2.43**).

Spring and summer have larger variability of precipitation than autumn and winter, as the area-weighted mean values in CA for σP_{spr} and σP_{sum} are both 31 mm, compared with the mean values of 23 mm and 21 mm for σP_{aut} and σP_{win}, respectively. Autumn is the

season with the least variability of precipitation, as all climatic regions having area-weighted mean of long-term standard deviation of autumn precipitation less than 40 mm (**Figure 2.45**). Climatic regions have higher variability of precipitation in the season with larger share of precipitation. For example, spring is the season with the largest variability of precipitation in the PA and the WP, with regional mean values of σP_{spr} greater than 60 mm; while summer is the season with the largest variability of precipitation in the NT and the IT, as regional mean values of σP_{sum} are 50 mm (**Figure 2.45).**

5.4 Changes of average and variability of precipitation between 1951 – 1976 and 1977 – 2010

In CA, significant increases of average annual precipitation between two sub-periods can be observed in 33 stations while significant decreases occurred in 18 stations (**Table 2.4**). Spatially interpolated difference of long-term average annual precipitation (ΔP_{ann}) has a range from -80 mm to 45 mm. The interpolated result of ΔP_{ann} shows more areas with an absolute increase of average annual precipitation (67.2% area in CA with ΔP_{ann} greater than 0), resulting in a positive area-weighted mean of ΔP_{ann} for the whole CA at 3 mm (**Figure 2.46**). In most climatic regions, ΔP_{ann} decreased with increasing elevation, with negative values in areas above 2000 m; while WP, PA, and CP have positive regional mean ΔP_{ann} for all elevation ranges (**Figure 2.47**).

Strong decreases of annual precipitation (ΔP_{ann} < -30 mm) were mainly observed in CT and IT, while mountains in the northeastern part of the WT, the southern part of the Northern Tien Shan (NT) and the western part of the ET also experienced decreases of annual precipitation in the range from -30 mm to -10 mm. Such decreases of precipitation were

mainly associated with decreases of summer precipitation (**Figure 2.50**). Strong increases of annual precipitation (ΔP_{ann} > 30 mm) were mainly observed in PA, WP, and CP. Increases of precipitation in these areas happened in winter, summer and autumn (**Figure 2.48, Figure 2.50, and Figure 2.51**). The northwestern part of the AD and the eastern part of TR also witnessed increases of annual precipitation in the range from 10 mm to 30 mm, associated with increases of precipitation in spring, autumn, and summer (**Figure 2.49, Figure 2.50, and Figure 2.51**).

The spatially interpolated difference of long-term annual standard deviation ($\Delta\sigma P_{ann}$) has an area-weighted mean of -1 mm, ranging from -47 mm to 95 mm. Most areas (79.5% of the total area in CA) have $\Delta\sigma P_{ann}$ in the range between -10 mm and 10 mm while two main clusters of change can be observed (**Figure 2.52**). One cluster with significant increases of annual precipitation variability ($\Delta\sigma P_{ann}$ > 20 mm) is located in the Tien Shan Mountains, spanning from the western part of the NT, the IK, and the eastern part of the IT to CT and the western part of the ET (Figure 52). Increases of the variability of annual precipitation in these areas are mainly associated with increases of summer precipitation variability (**Figure 2.54**). Another cluster with significant decreases of annual precipitation variability ($\Delta\sigma P_{ann}$ < -20 mm) can be observed in the areas spanning from WT and the western part of IT to WP, the eastern part of PA, and CP (**Figure 2.52**). Such decreases of annual precipitation variability were mainly associated with decreases of precipitation variability in winter (**Figure 2.53**).

6 Discussion

6.1 Data compilation and interpolation

6.1.1 Data availability

High elevation meteorological stations with long-term observation are extremely sparse. For example, in the GHCNv3 world database (**Lawrimore et al., 2011**), there are only 191 out of 7297 (3%) stations located at areas above 2000 m, and 54 (0.7%) stations with elevation greater than 3000 m (**MRI, 2015**). In this data collection for CA, there are 84 out of 369 stations (22.8%) and 74 out of 381 stations (19.4%) for air temperature and precipitation for areas with elevation above 2000 m, resulting in denser station network in the elevation ranges 2000 m – 3000 m and 3000 m – 4000 m than the general situation in the world (**Figure 2.5**). It should be noticed that the number of stations in this dataset for the elevation range greater than 4000 m is much smaller than other elevation ranges. In this extremely high elevation range, stations were either simply not existed, or existed but with only short-term observations, or with long-term observations only in selected seasons (e.g. summer). Some recent initiatives, for example, the Global Cryosphere Watch (**WMO, 2015**) and the Mountain Research Initiative (**MRI, 2015**), propose schemes for constructing and maintaining new long-term meteorological stations in high elevation areas, which may help to alleviate the lack of data problem in high elevation in the future. The climate dataset presented in this study, as a rich archive of monthly air temperature and precipitation data in CA, can help better illustrate the long-term regime and historical changes of climate in CA than previous researches, though current results derived for this elevation range (> 4000 m) should be interpreted with extra caution.

6.1.2 Spatial interpolation method

In this study, the GWR method with different sets of dependent variables, including elevation, slope and aspect was first experimented for interpolating climate variables from station points to grids. Different set of options and parameters for transforming variables and determining weights for local interpolation have also been tested. Experiments with the GWR show that for this dataset in CA, slope and aspect do not provide additional prediction power. In addition, data transformation is not necessary for monthly temperature and precipitation data. For temperature related variables, the GWR method with the adaptive kernel using a fixed number of neighbors estimated by the AICc method can provide trustworthy results, indicated by high general R^2 and local R^2 values, low RMSE values during cross-validation procedure and reasonable visual appearances. For precipitation-related variables, the GWR method failed to capture the orographic effect in high mountain ranges. Comparisons of interpolated long-term mean annual and seasonal precipitation in selected locations with long-term mean precipitation information provided in literatures (**Aizen et al., 1996; Kotlyakov, 1997; Aizen et al., 2007c**) show that the GWR method constantly underestimates precipitation in high elevation locations. In certain climatic regions in Tien Shan and Pamir, the long-term mean precipitation interpolated by the GWR method even show a decreasing trend with elevation, which is not realistic.

The customized GWR method with topographical facet was developed to solve the problem, by adopting the idea of restricting participating stations for interpolation based on topographical facet from the widely used PRISM method (**Daly et al., 1994**), to better capture the orographic dependence of precipitation. For temperature related variables, the customized GWR provides similar results as the GWR method, with lower general R^2 and local R^2, as

well as larger RMSE values. For precipitation related variables, though the results of the customized GWR method have lower general R^2 and local R^2 compared with results generated by the GWR, the orographic effect has been better captured, with more realistic values in high elevation, as indicated by qualitative comparison between interpolated long-term mean precipitations with long-term mean precipitation information in high elevation locations. As a result, it is decided to use the GWR method for interpolating temperature related climate variables while using the customized GWR method for interpolating precipitation related climate variables.

6.2 Change of temperature

To analyze the relationship between changes of air temperature and long-term average temperature, mean Δ_T at each 5 °C range of long-term average air temperature was calculated (**Figure 2.55**). The results show that strong increase of annual air temperature occurred around the 0 °C isotherm, with the strongest increase of annual air temperature of 0.86 °C happened in the long-term average T_{ann} range 0 to 5 °C (**Figure 2.55-a**). Similar associations between the difference of temperature between two sub-periods and long-term average temperature also exist for spring and autumn (**Figure 2.55-c and Figure 2.55-e**), which are seasons of snow melting and snow accumulation, respectively. Such associations suggest that the existence of a link between snow cover albedo and air temperature (**Pepin & Lundquist, 2008; Rangwala & Miller, 2012**) in CA, as increasing air temperature leads to less snow cover, and decreased surface albedo, increased surface absorption of insolation and further increased air temperature in consequences. One explanation for the negative relationship between Δ_T and elevation is that low elevation areas are more probable to be trapped in this

kind of positive feedback loop then high elevation areas where air temperature may increase but still stay below freezing.

6.3 Change of precipitation

The total amount of precipitation increased slightly but not significantly over central Asia, indicated by the area-weighted mean of ΔP_{ann} of 3 mm between 1951 – 1976 and 1977 - 2010. Precipitation increased in Pamir and low elevation plains while decreases of precipitation can be observed in alpine regions of IT, CT, and ET. These changes in the distribution of precipitation may be the result of increasing relative humidity, which caused the lowering of condensation level (**Aizen et. al., in preparation**) and more precipitation distributed in low plains and Pamir, which are closer to the moisture sources.

Relative humidity has increased in the plain / desert regions of CA, especially in the Aral-Caspian areas (**Kadukin & Klige, 1991**). One possible source of additional moisture is the evaporation from irrigated fields. The intensive development of irrigation systems since the mid-1970s leads to expansion of irrigated farmlands, with lower albedo in comparison with previously deserts and steppes and more water available for evaporation (**Shibuo et al., 2007**). Another moisture source for increasing relative humidity in plain and desert areas in CA may be the increased re-evaporated moisture from the Caspian Sea, as a result of the rise of the water level and increase of surface area of the Caspian Sea since 1979 (**Kadukin & Klige, 1991**).

The increased precipitation observed in CA deserts is in accordance with the decreasing frequency and intensity of dust storms. Results from 154 Chinese stations show that the maximum frequency of dust weather in the mid-1960s and decreased by 80% to the lowest recorded level in the 1990s (**Sun et al., 2001; Qian et al. 2004**).

6.4 Indication for water resources

Considering the possible increase of evaporation caused by the increased air temperature, the small increase of precipitation in plain / deserts may not help to alleviate water resources problems in CA. Most semi-arid / arid areas in CA are nourished by major rivers with most of their fresh water provided by seasonal snow cover and glaciers in high alpine areas in Altai, Tien Shan and Pamir mountains. Increasing air temperature in summer in high alpine areas would cause stronger ablation in glaciers, releasing more water in summer for now before a significant shrinkage of glacier area happened. Accompanied by simultaneous decreasing precipitation in all season, all Tien Shan glaciers are retreating quickly (**Aizen et. al, 2007b; Narama et al., 2010; Farinotti et al., 2015**), which may lead to lack of water resources in the future (**Aizen et al., 2007a**). Seasonal snow cover extent would also decrease due to the increase of air temperature. In addition, with the increasing spring temperature, the seasonal snow cover may melt and release fresh water earlier in the future, changing the timing scheme of stream runoff in central Asian rivers.

7 Conclusion

To assess the climate changes throughout central Asia (CA), monthly temperature and precipitation observation data was collected from several sources. The resultant data collection contains 457 stations, with elevation ranging from -135 m below sea level to 4169 m above sea level, covering the entire territory of CA, including Kazakhstan, Kyrgyzstan, Tajikistan, Uzbekistan, Turkmenistan and Xinjiang (PR of China). All station data was pre-processed, quality-controlled then merged into a single dataset, which was further processed with the iterative PCA method to fill gaps in station time series from 1951

to 2010, resulting in gap filled time series in 369 and 381 stations for air temperature and precipitation, respectively. Significant change of mean annual air temperature was found at 280 stations, with 84 stations witnessed such a change in 1976-1977. A series of climate characteristics were calculated from the gap filled dataset to quantify long-term mean climate and changes of climate in CA. The Geographically Weighted Regression method was used to evaluate regional spatial and temporal changes in air temperatures and precipitation from 1951 to 2010.

Significant increases of annual air temperatures were found in 73% stations in CA. Spatially interpolated ΔT_{ann} between 1951 – 1976 and 1977 – 2010 has a range from -0.41°C to 1.13°C, with an area-weighted mean increase of 0.70°C for the whole CA. Stronger increase of air temperature happened in lower elevation area, with the largest regional mean increase of 0.82 °C occurred in the elevation range below 1000 m, and the smallest regional mean increase of 0.13 °C occurred in the elevation range above 4000 m. Areas in higher northern latitudes tend to have stronger increase of air temperature compared with areas in similar elevation ranges. Two main centers of increasing air temperature up to 1 °C can be observed in areas surrounding the Aral Sea and in the northeastern part of the Kazakh Steppe, associated mainly with increases of winter and summer air temperatures, respectively. High elevation areas in Tien Shan and Pamir experienced a much smaller increase of annual air temperature than other regions, or even a slight decrease of air temperature though not significant. In summer, air temperature increased nearly everywhere in CA. In contrast, in winter the elevation range below 2000 m witnessed the strongest increase of air temperature while high elevation areas in Tien Shan and Pamir experienced a much smaller increase of even a slight decrease of air temperature.

The annual precipitation did not change significantly throughout CA, with a small area-weighted mean of 3 mm and a range from -80 mm to 45 mm for the difference between average annual precipitations in the two sub-periods. Spatial interpolation results show that there are more areas (67.2% of area in CA) with increasing precipitation. Strong increases of precipitation greater than 30 mm mainly occurred in Pamiro-Alai, Western Pamir and Central Pamir, associated with increases of winter precipitation. Low elevation plains in the Aral-Caspian Desert, and Tarim also experienced increases of annual precipitation in the range of 10 to 30 mm, mainly related to increases of spring precipitation. The most significant decreases of precipitation occurred in the alpine regions of Tien Shan, especially in Central Tien Shan and Inner Tien Shan during summer, causing increased glacier ablation and shrinkage.

Tables

Table 2.1 Parameters used in Iterative-PCA Gap-filling

Parameter	Description	Value
PCN_T	Percentage of variance kept during truncated PCA for temperature, selected by CV.	0.995
PCN_P	Percentage of variance kept during truncated PCA for precipitation, selected by CV.	0.99
DEL_T	Critical value for difference between estimates in two iterations for temperature for temperature, determined as 1 / 3 of the record precision.	0.033
DEL_P	Critical value for difference between estimates in two iterations for temperature for precipitation, determined as 1 / 3 of the record precision.	0.33

Table 2.2 Results of cross validation for Iterative-PCA Gap-filling

variable type	Count	RMSE						
		mean	std	min	25%	50%	75%	max
T	369	0.03	0.02	0.01	0.02	0.03	0.04	0.13
P	381	0.60	0.35	0.10	0.35	0.51	0.74	1.99

Table 2.3 Statistics calculated for different variable, season and calculation period

variable	season	calculation period	statistics
temperature, precipitation	Annual (ann) Winter (win) Spring (spr) Summer (sum) Autumn (aut)	period 1 (p1)	T_{p1}, P_{p1} σT_{p1}, σP_{p1}
		period 2 (p2)	T_{p2}, P_{p2} σT_{p2}, σP_{p2}
		whole period (pa)	T_{pa}, P_{pa} σT_{pa}, σP_{pa} Δ_T, Δ_P $\Delta_{\sigma T}$, $\Delta_{\sigma P}$

Table 2.4 Number of stations with different types of changes

variable	season	increase (significant)	increase (not significant)	decrease (significant)	decrease (not significant)
long-term normal air temperature	annual	250	81	0	14
	winter	136	183	0	26
	spring	85	211	0	49
	summer	155	142	5	43
	autumn	218	106	0	21
long-term standard deviation of air temperature	annual	20	99	47	179
	winter	13	74	58	200
	spring	35	141	16	153
	summer	22	120	29	174
	autumn	17	137	33	158
long-term normal precipitation	annual	33	186	18	139
	winter	46	206	9	115
	spring	9	136	21	210
	summer	43	187	14	132
	autumn	14	239	5	118
long-term standard deviation of precipitation	annual	26	134	18	198
	winter	21	141	28	186
	spring	13	122	38	203
	summer	49	163	29	135
	autumn	19	174	22	161

Figures

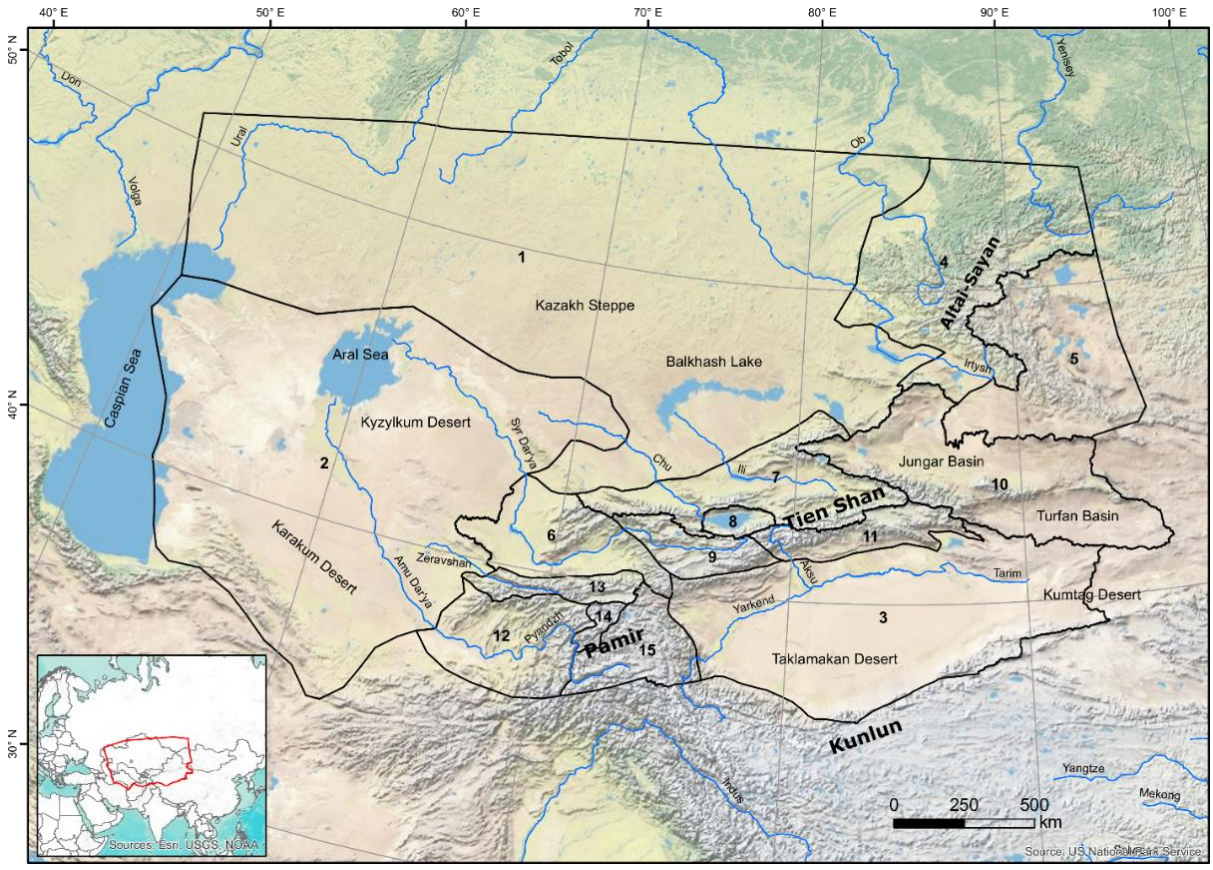

Figure 2.01 Map of central Asia study area and climatic regions

Inset map shows the location of study area as red polygon in Eurasia continent

1: Kazakh Steppe (KS), 2: Aral-Caspian Desert (AD), 3: Tarim (TR); 4: Siberian Altai-Sayan (SA), 5: Mongolian Altai (MA); 6: Western Tien Shan (WT), 7: Northern Tien Shan (NT), 8: Issyk Kul (IK), 9: Inner Tien Shan (IT), 10: Eastern Tien Shan (ET), 11: Central Tien Shan (CT); 12: Western Pamir (WP), 13: Pamiro-Alai (PA), 14: Central Pamir (CP), 15: Eastern Pamir (EP)

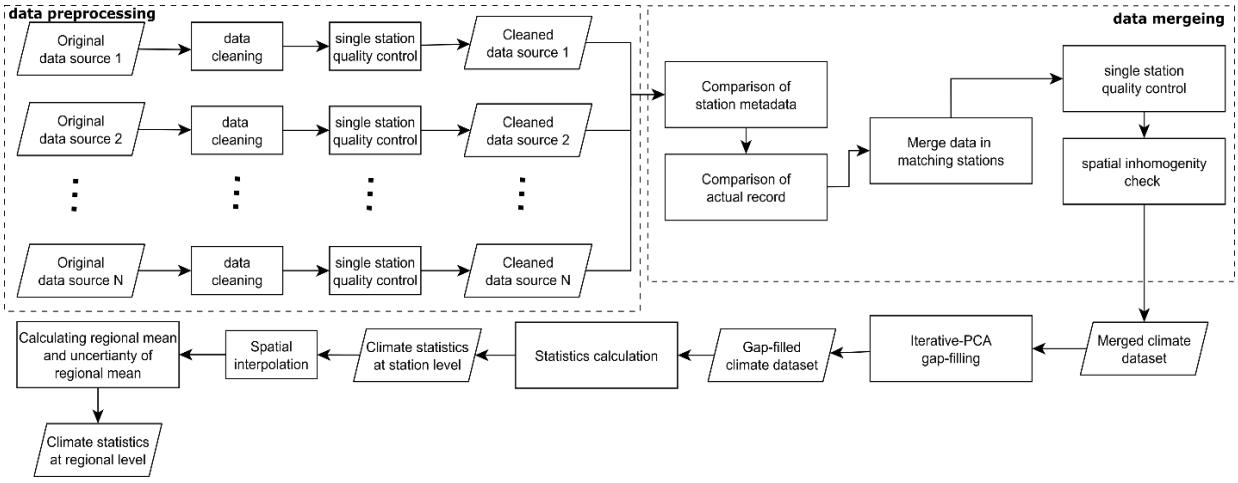

Figure 2.02 Flowchart for methodology used to process and analyze climate data in CA

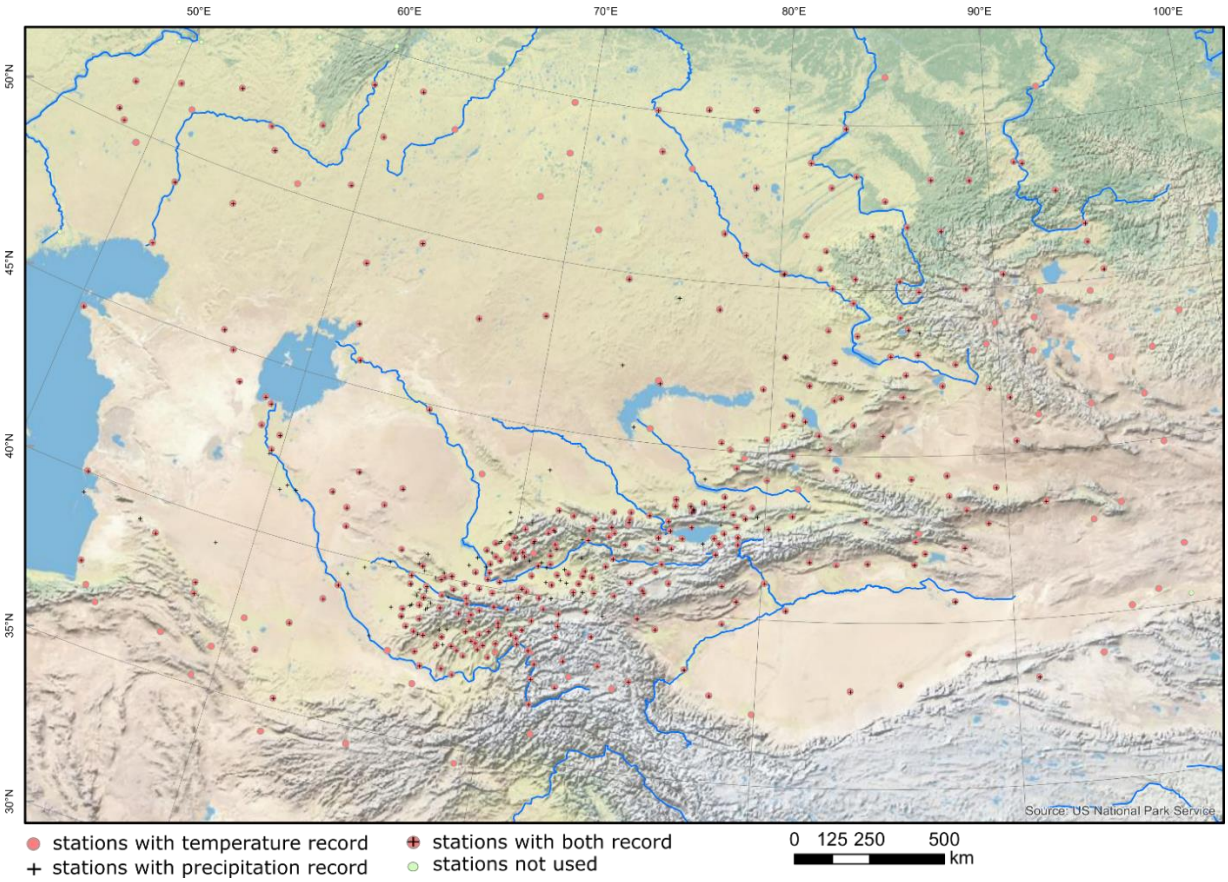

Figure 2.03 Station location after data merging

Red circles show stations selected for further analysis of monthly temperature

Black crosses show stations selected for further analysis of monthly precipitation

Yellow circles show stations not being selected for further analysis

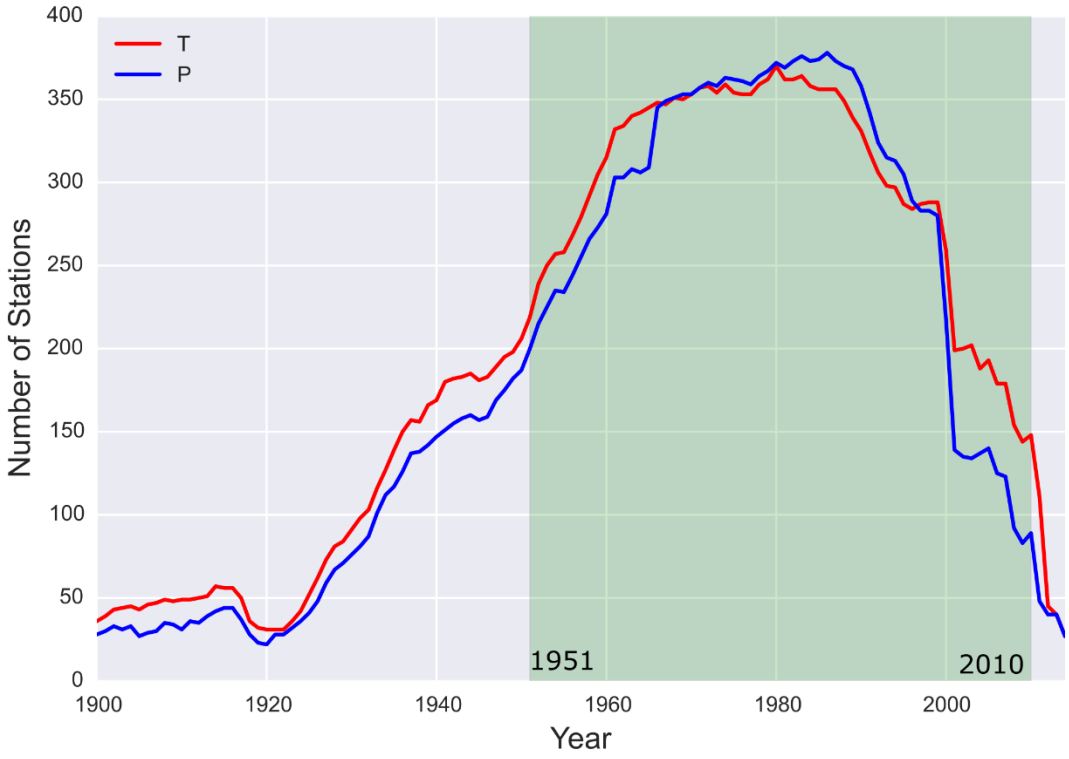

Figure 2.04 Station availability from 1900 to 2010

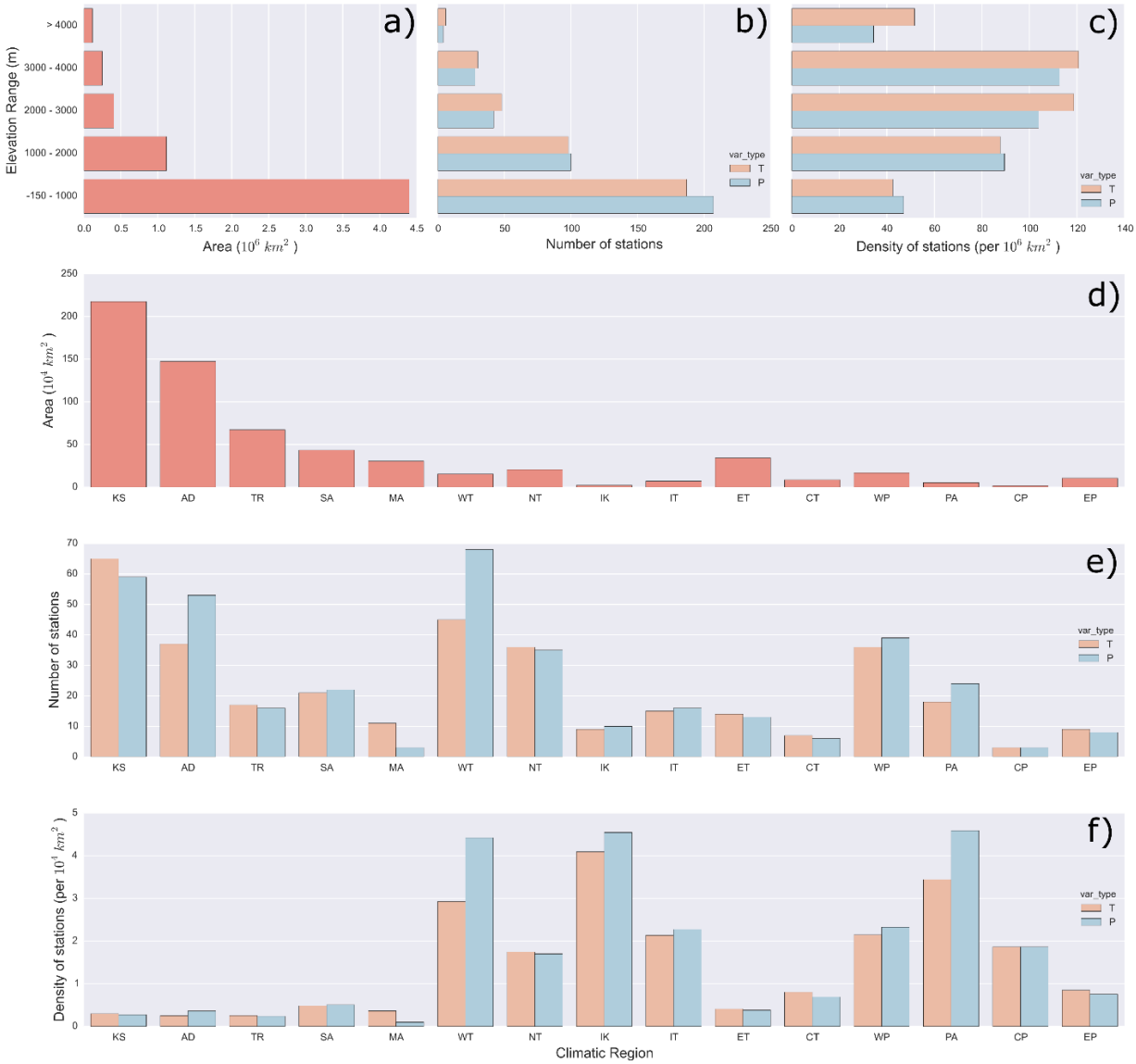

Figure 2.05 Characteristics of the station network in central Asia (CA)

Distribution of area (a, d), number of stations (b, e) and density of stations (c, f) by elevation range (a – c) and climatic region (d – f)

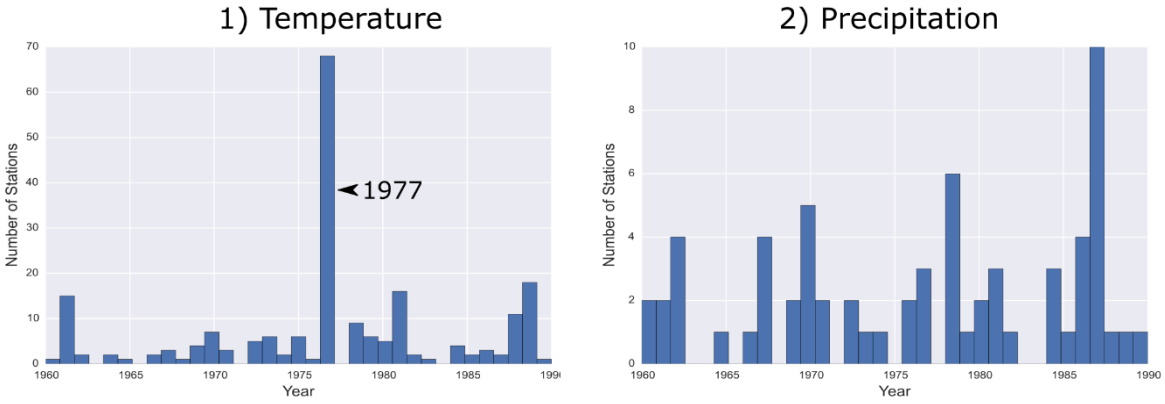

Figure 2.06 Number of stations exhibiting significant break of mean values for temperature and precipitation

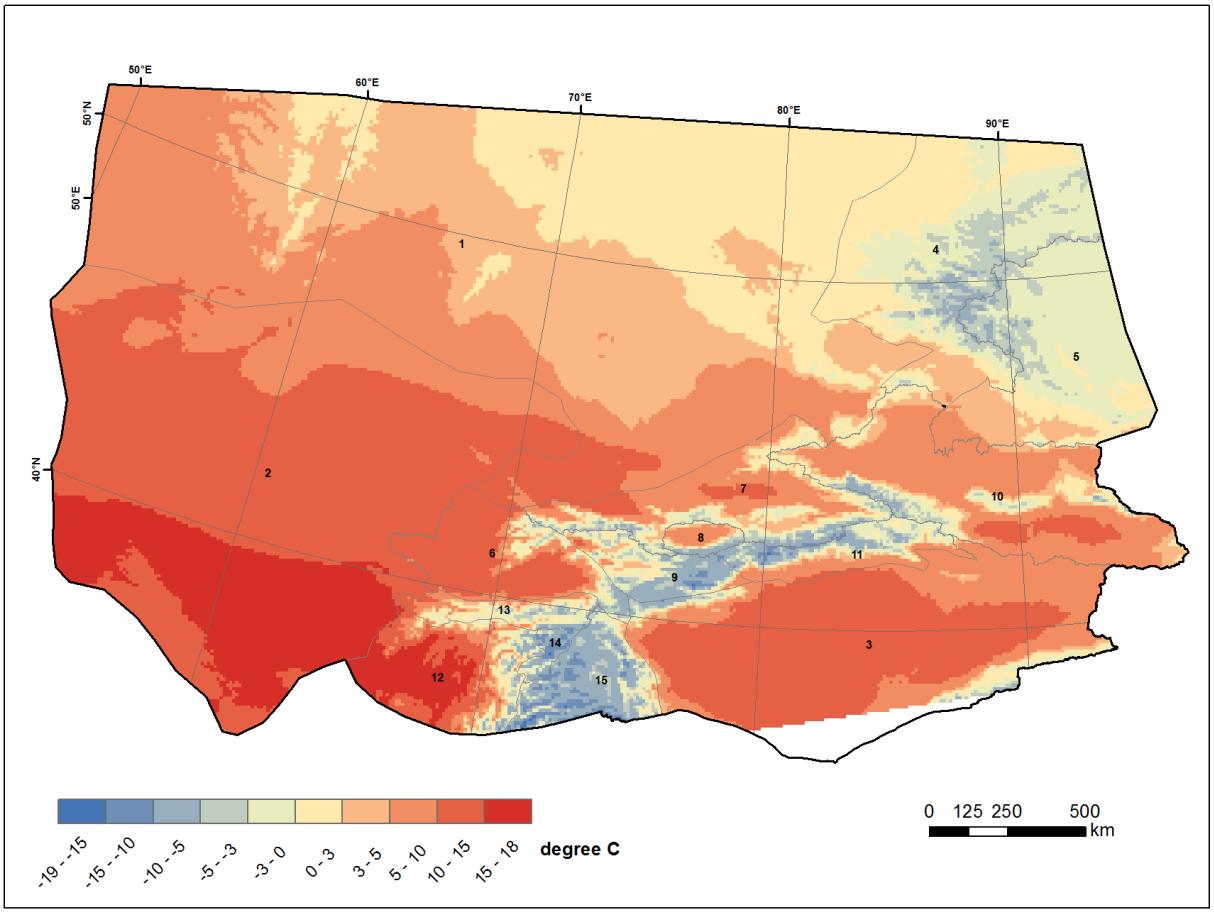

Figure 2.07 Long-term normal annual air temperature in CA from 1951 to 2010

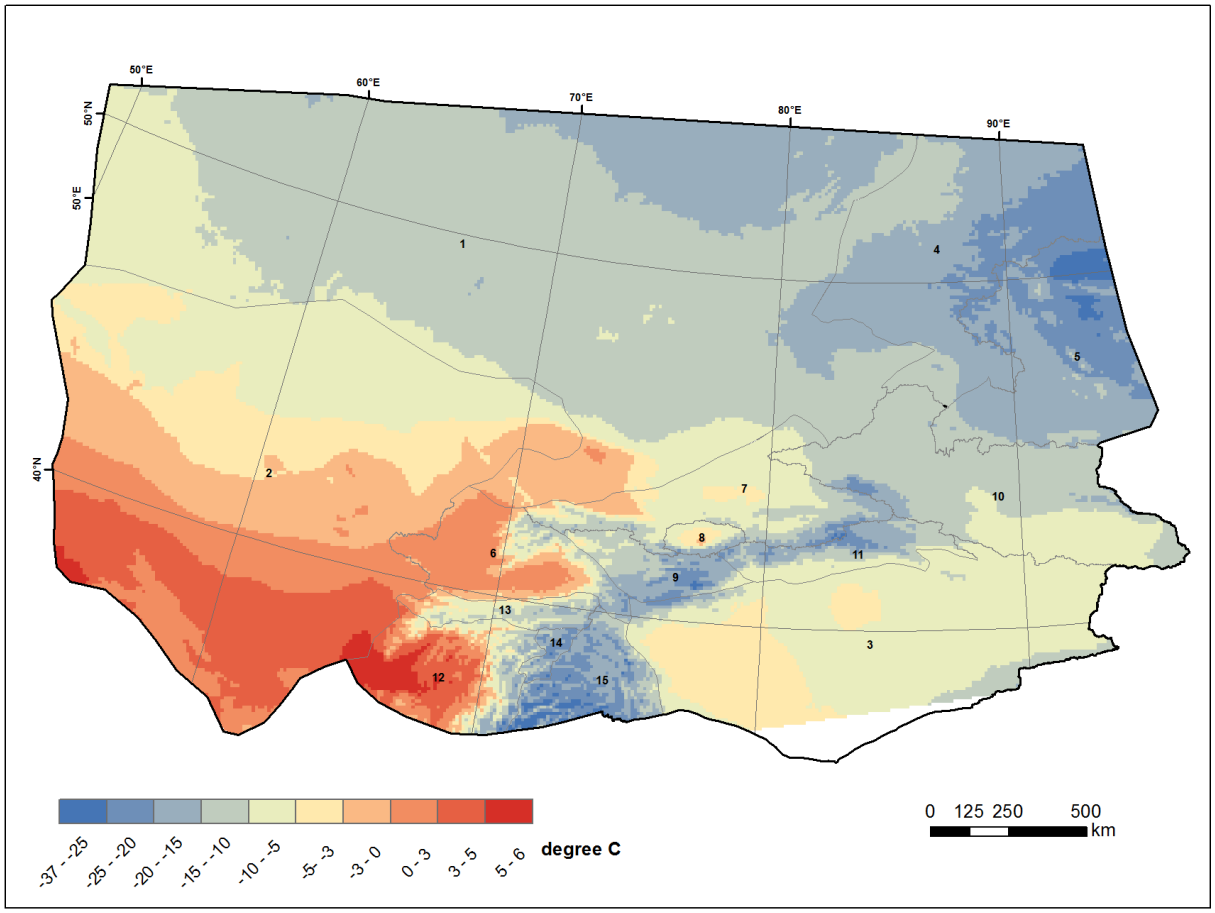

Figure 2.08 Long-term normal winter air temperature in CA from 1951 to 2010

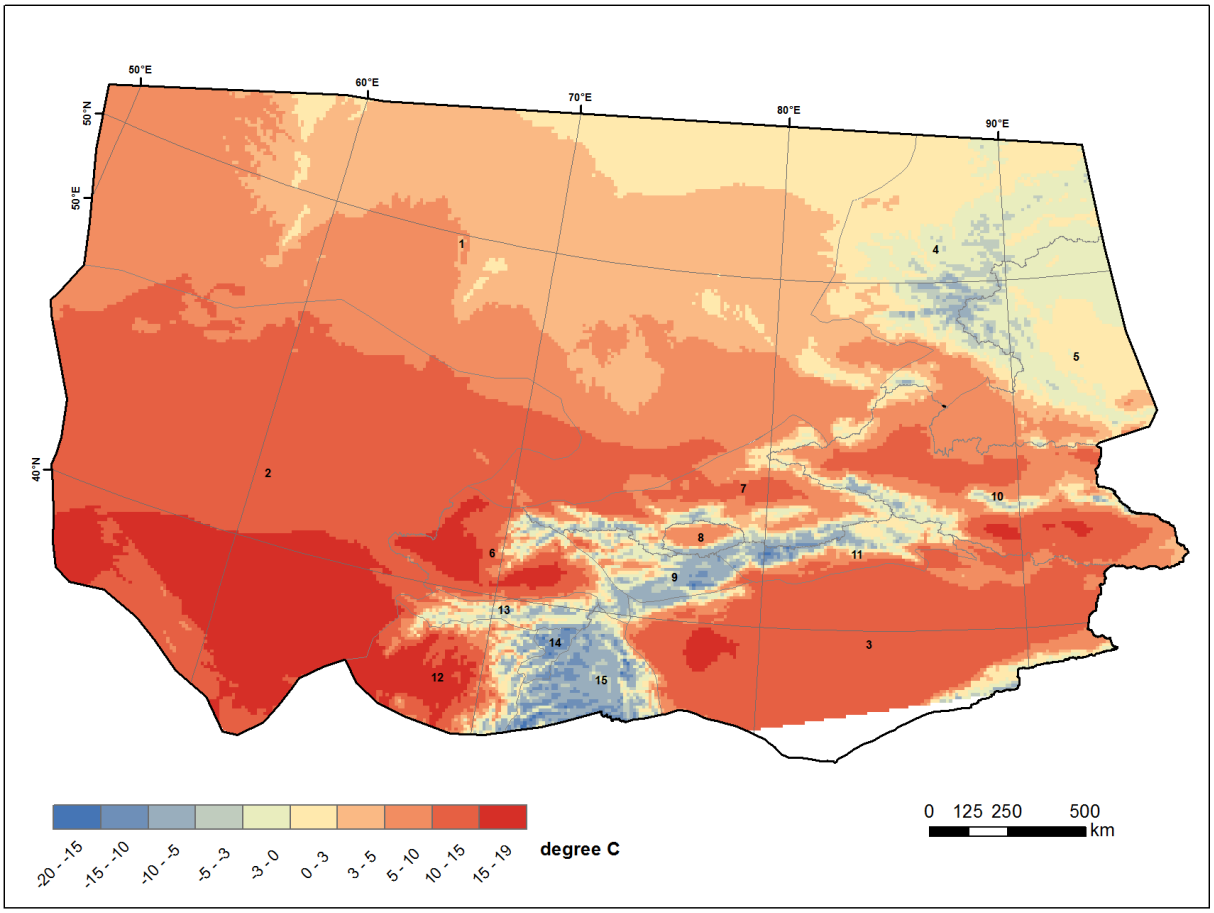

Figure 2.09 Long-term normal spring air temperature in CA from 1951 to 2010

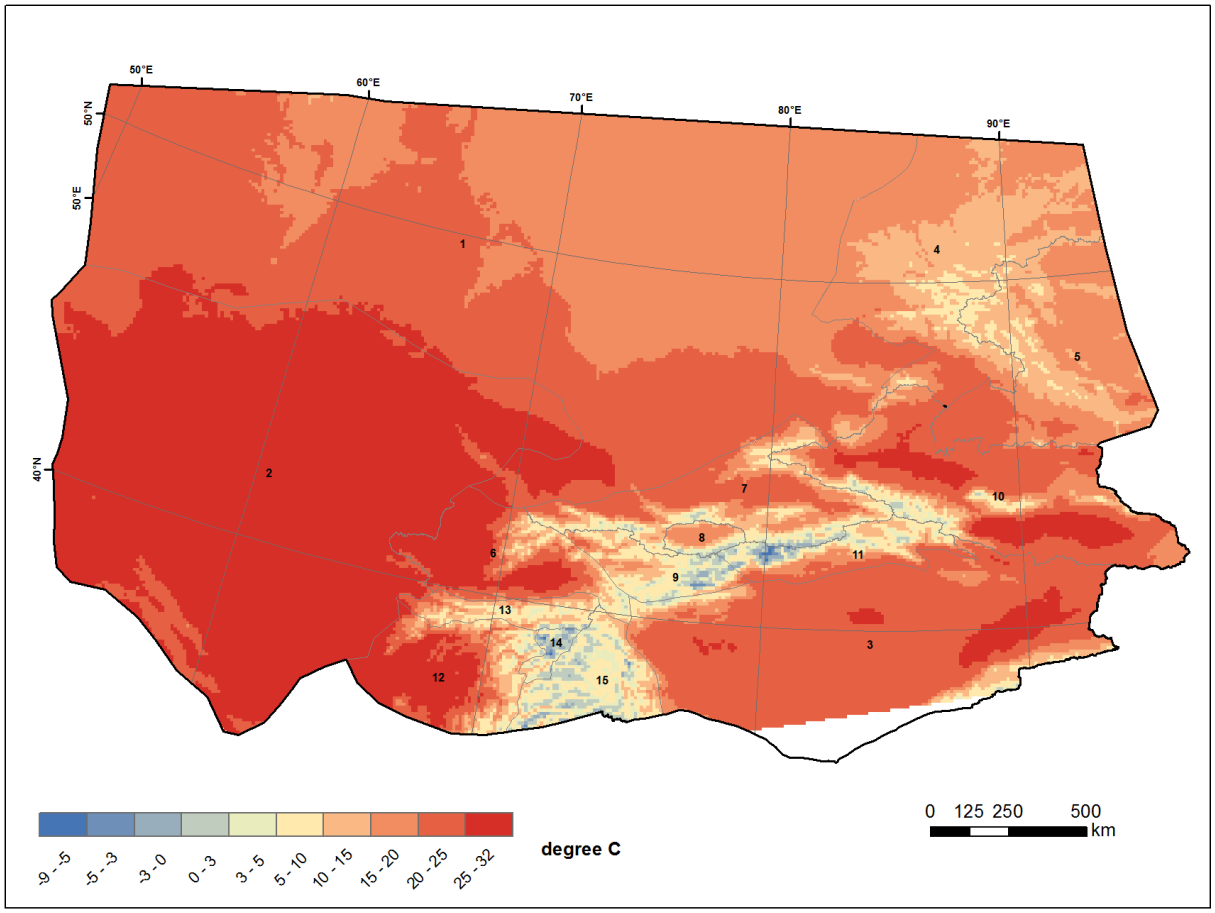

Figure 2.10 Long-term normal summer air temperature in CA from 1951 to 2010

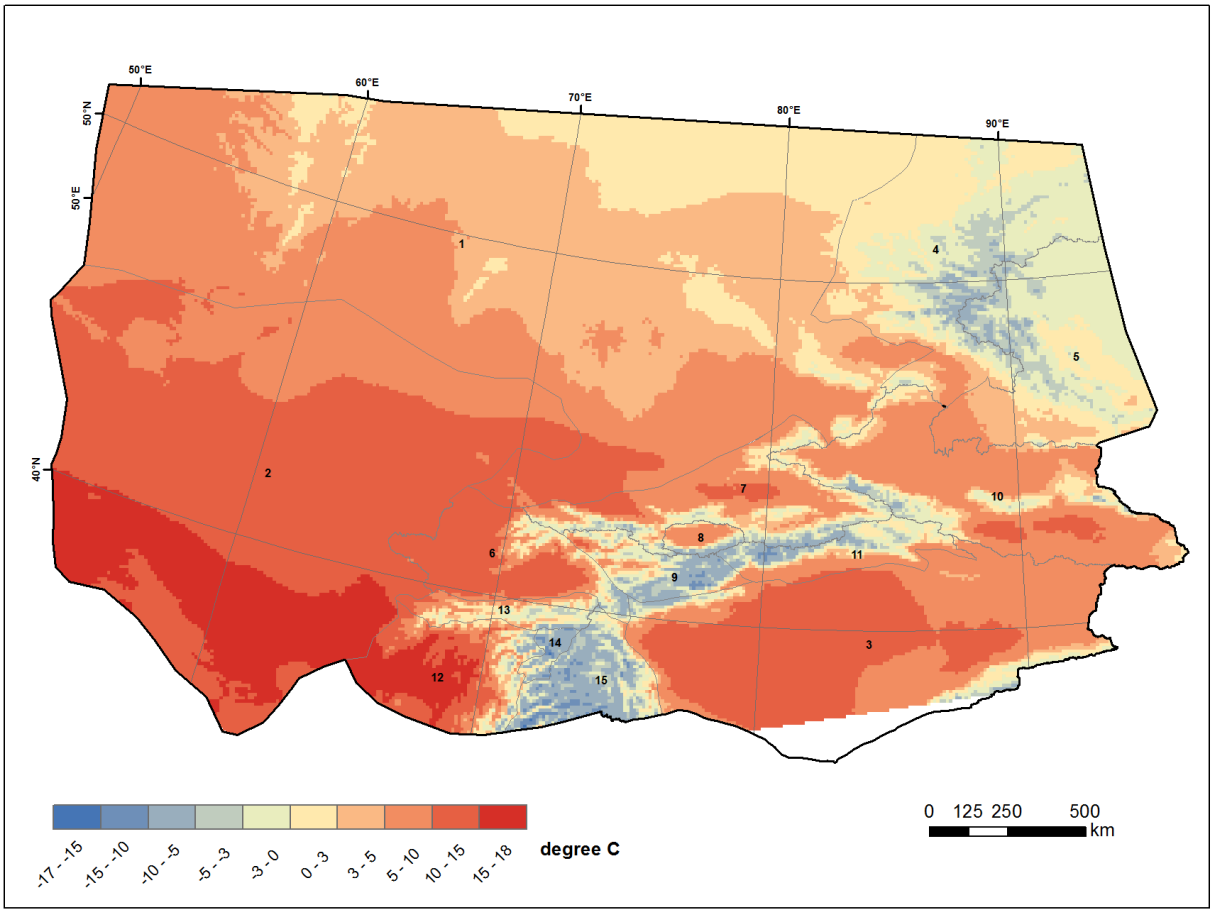

Figure 2.11 Long-term normal autumn air temperature in CA from 1951 to 2010

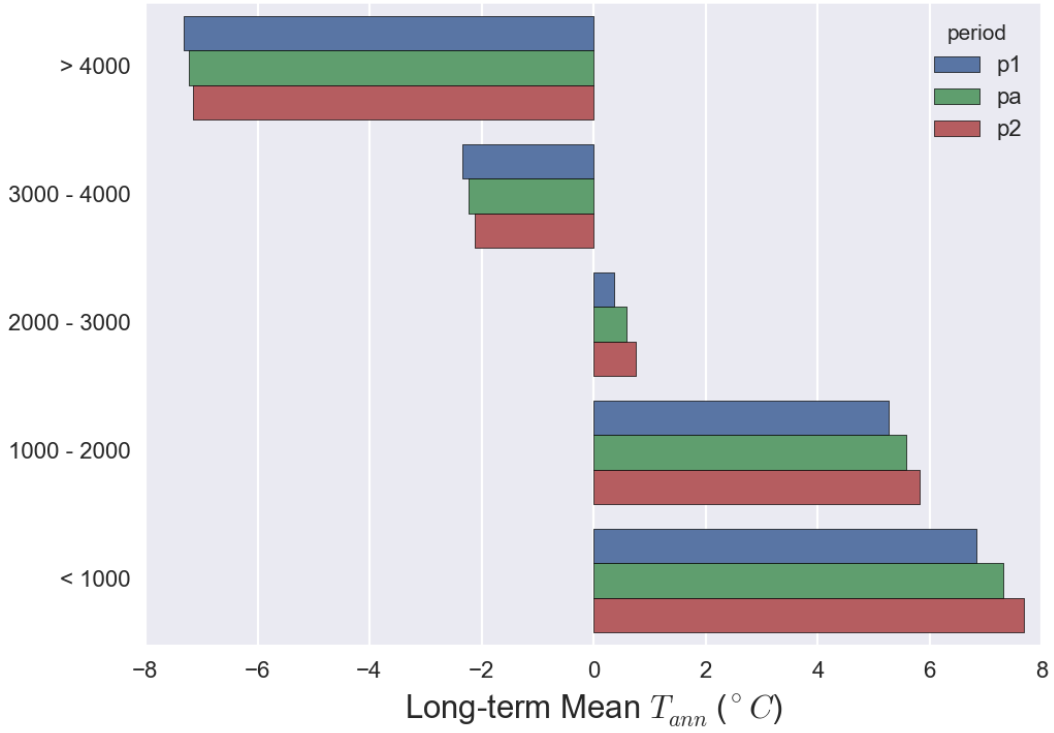

Figure 2.12 Long-term normal annual air temperature in different elevation ranges

P1: 1951 – 1976, P2: 1977 – 2010, Pa: 1951 - 2010

Figure 2.13 Long-term normal annual air temperature in different climatic regions

P1: 1951 – 1976, P2: 1977 – 2010, Pa: 1951 - 2010

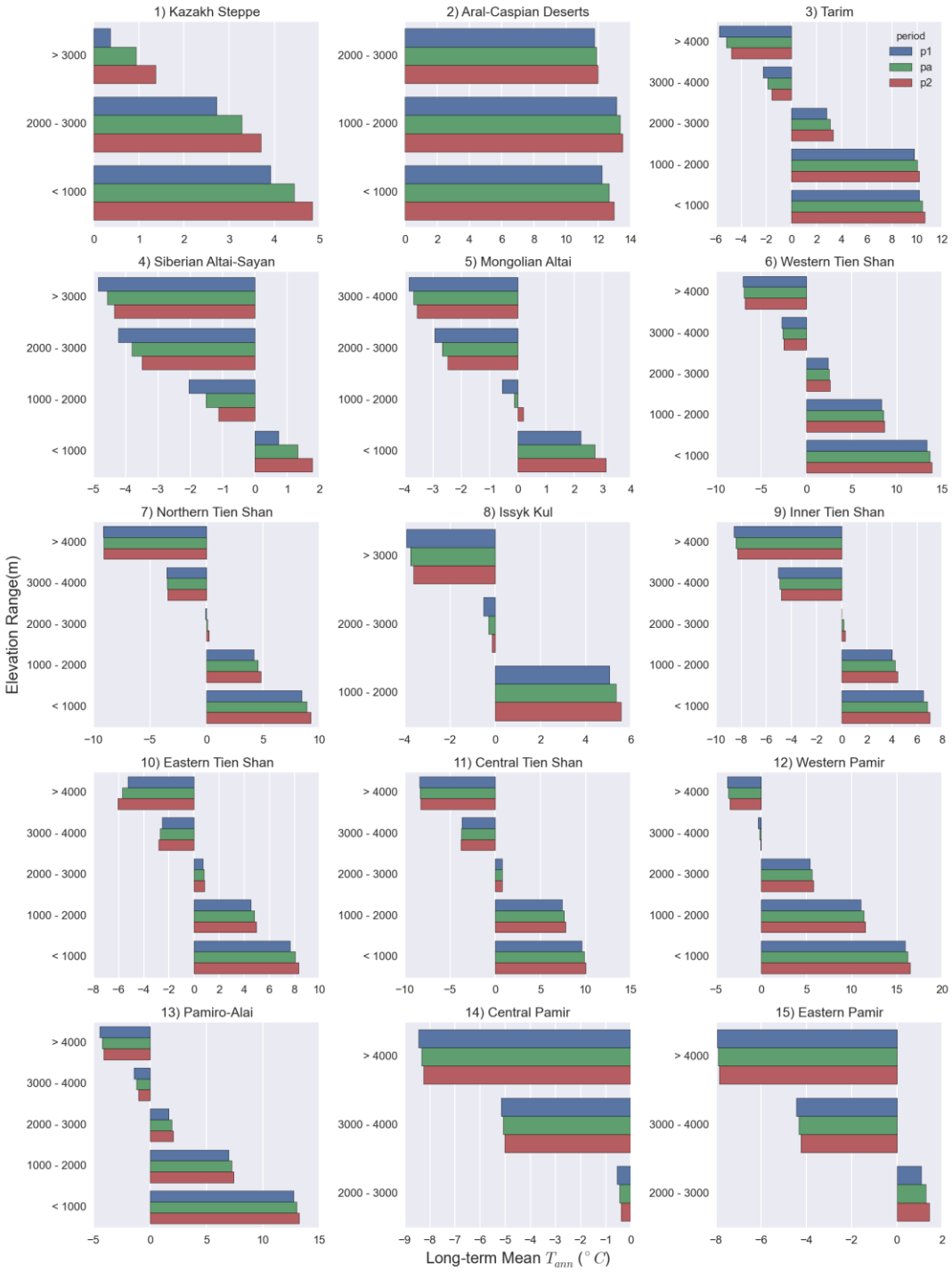

Figure 2.14 Long-term normal annual air temperature in different elevation ranges within climatic regions

P1: 1951 – 1976, P2: 1977 – 2010, Pa: 1951 – 2010

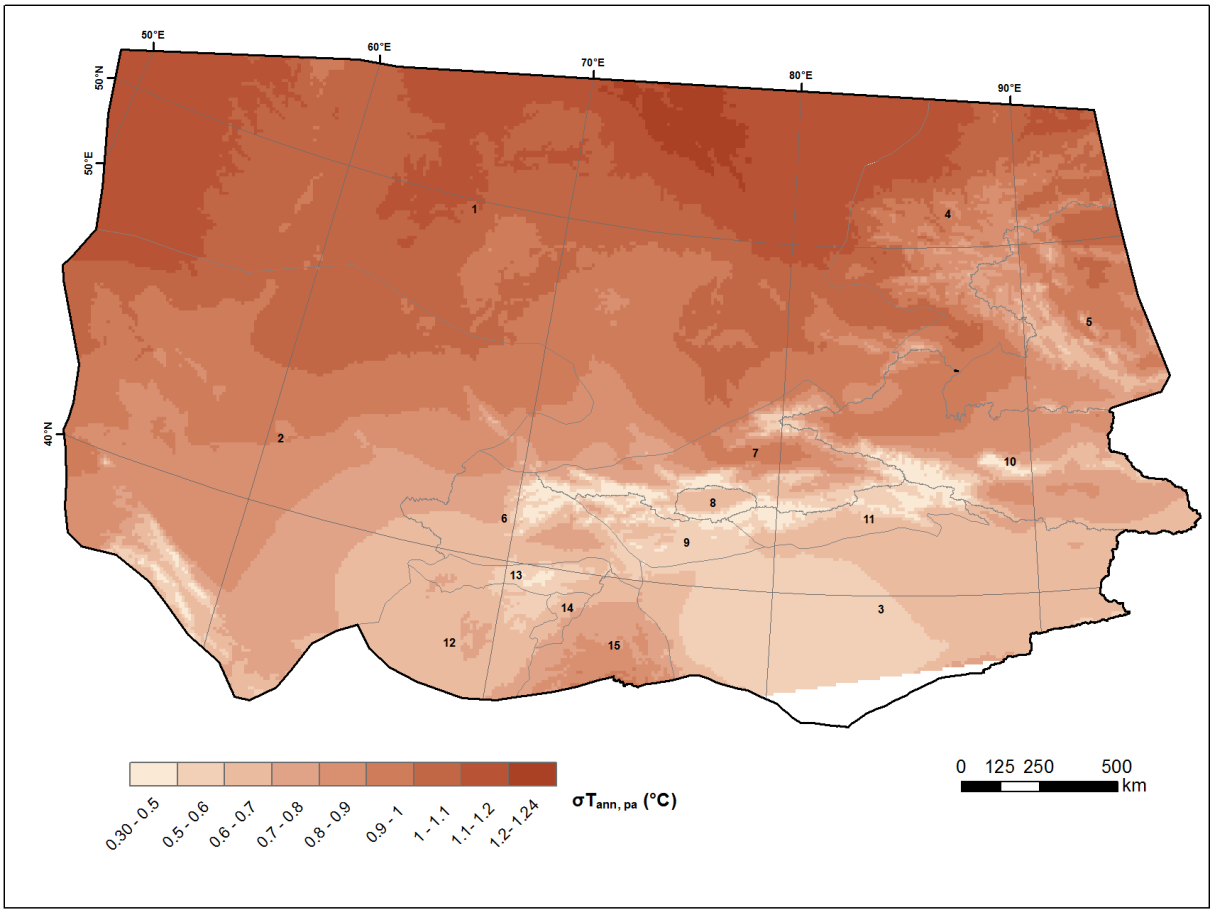

Figure 2.15 Long-term standard deviation of annual air temperature in 1951 – 2010

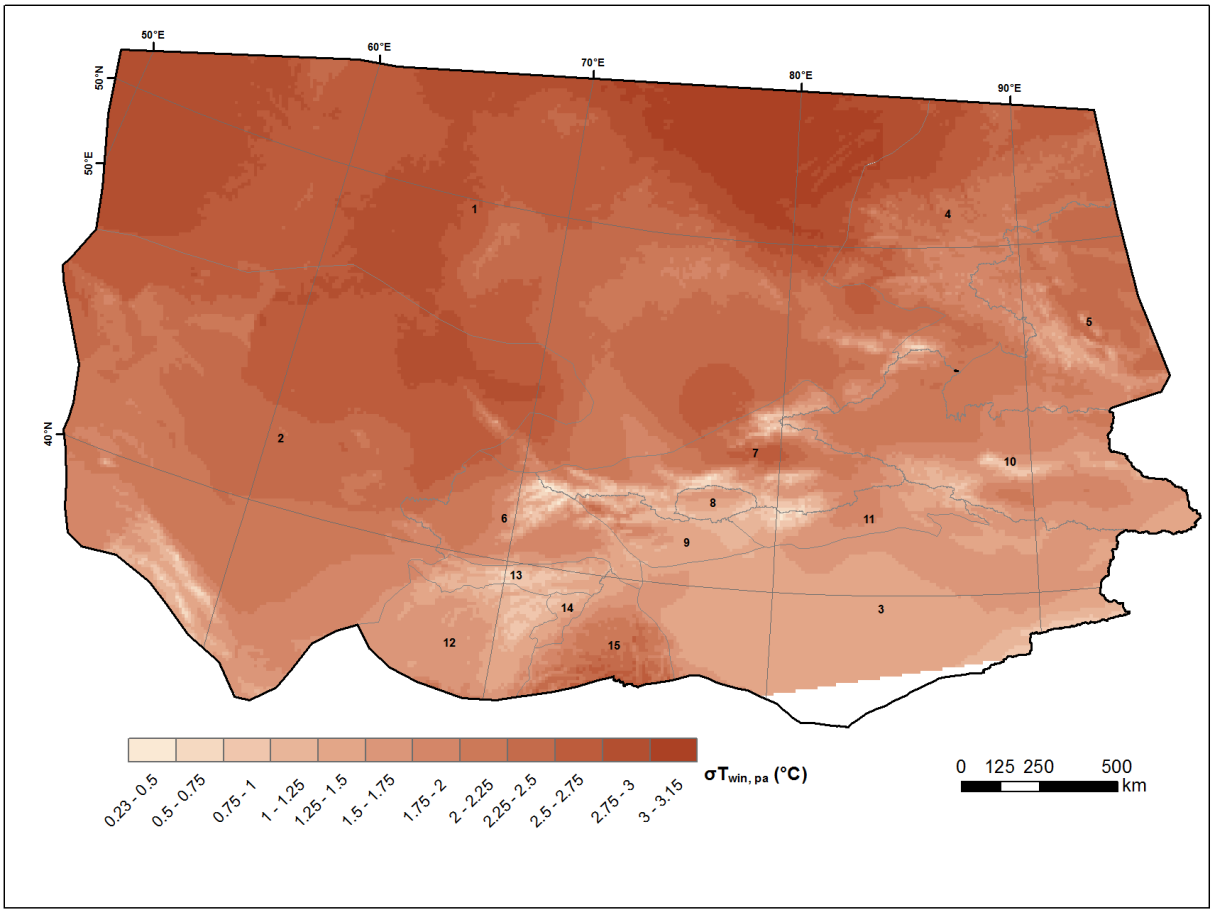

Figure 2.16 Long-term standard deviation of winter air temperature in 1951 – 2010

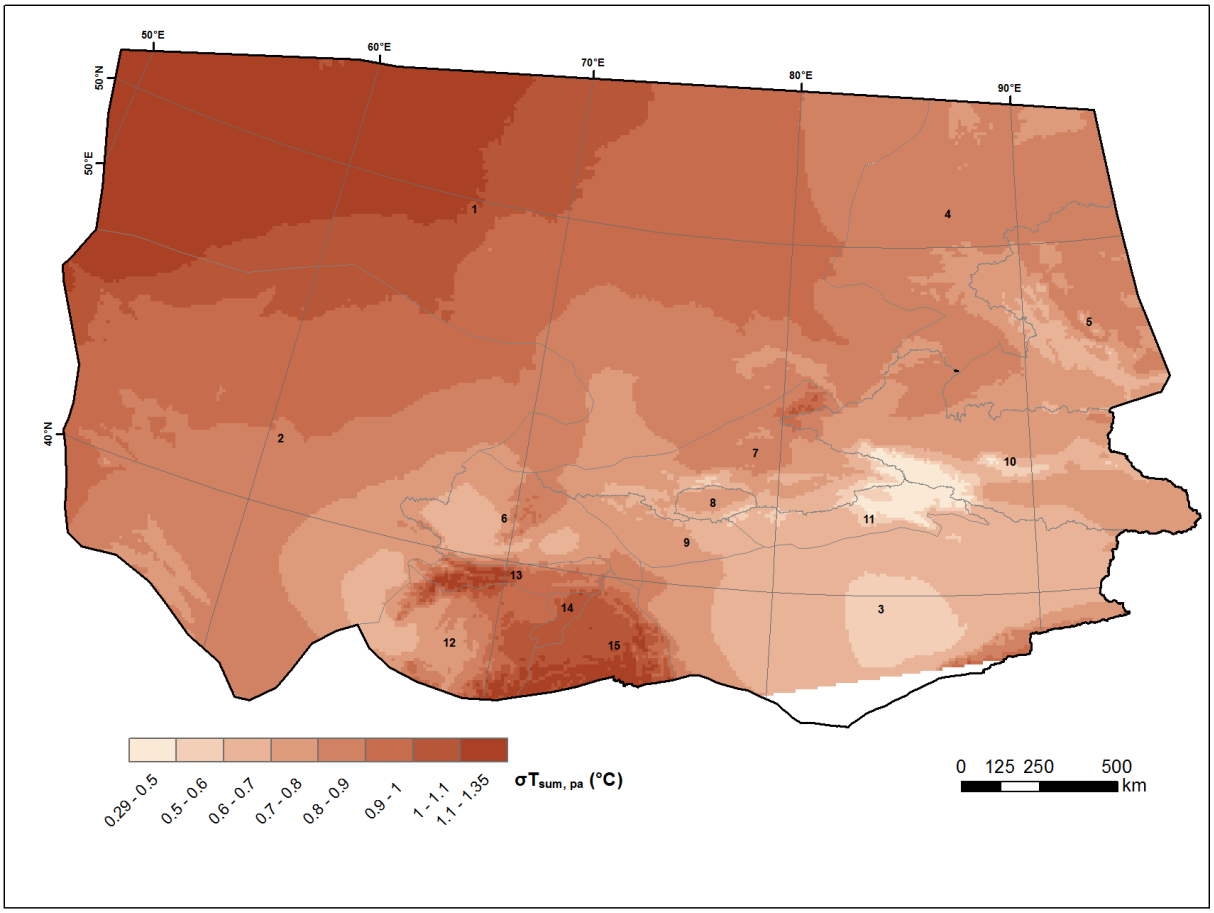

Figure 2.17 Long-term standard deviation of summer air temperature in 1951 – 2010

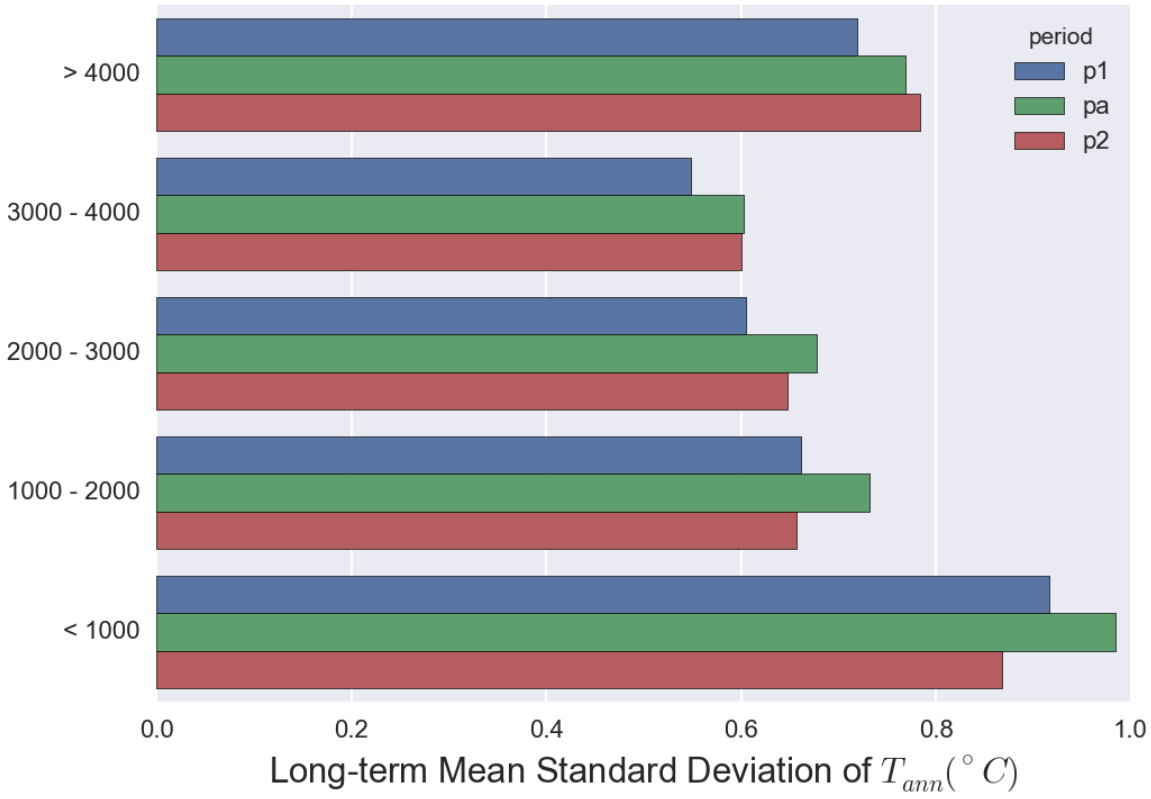

Figure 2.18 Long-term standard deviation of annual air temperature in different elevation ranges

P1: 1951 – 1976, P2: 1977 – 2010, Pa: 1951 - 2010

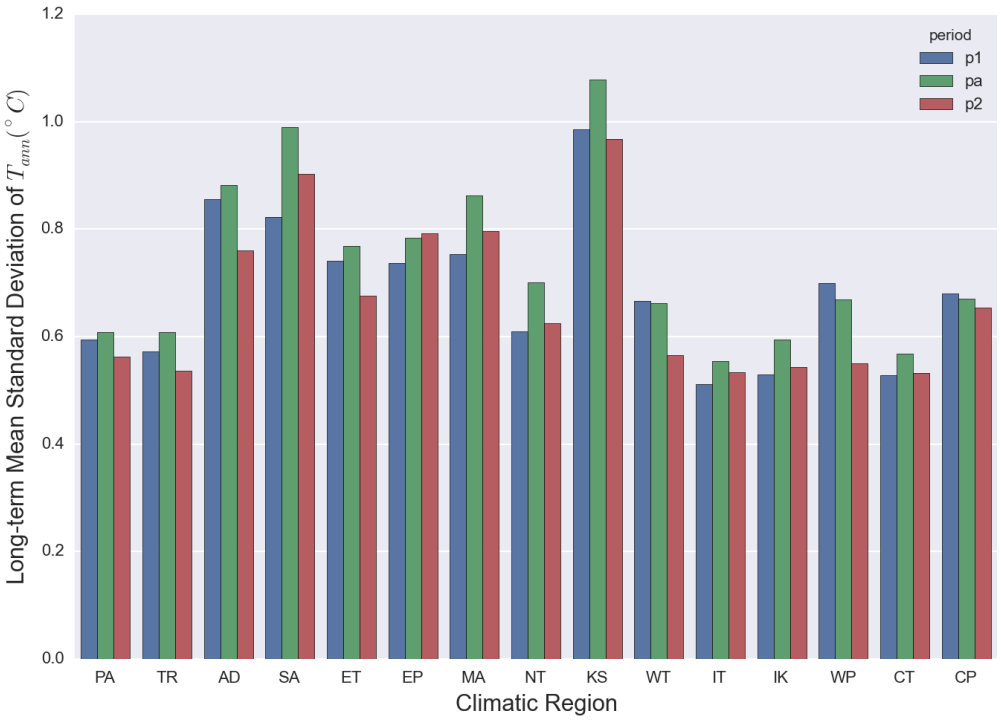

Figure 2.19 Long-term standard deviation of annual air temperature in different climatic regions

P1: 1951 – 1976, P2: 1977 – 2010, Pa: 1951 - 2010

Figure 2.20 Long-term standard deviation of annual air temperature in different elevation ranges within climatic regions

P1: 1951 – 1976, P2: 1977 – 2010, Pa: 1951 – 2010

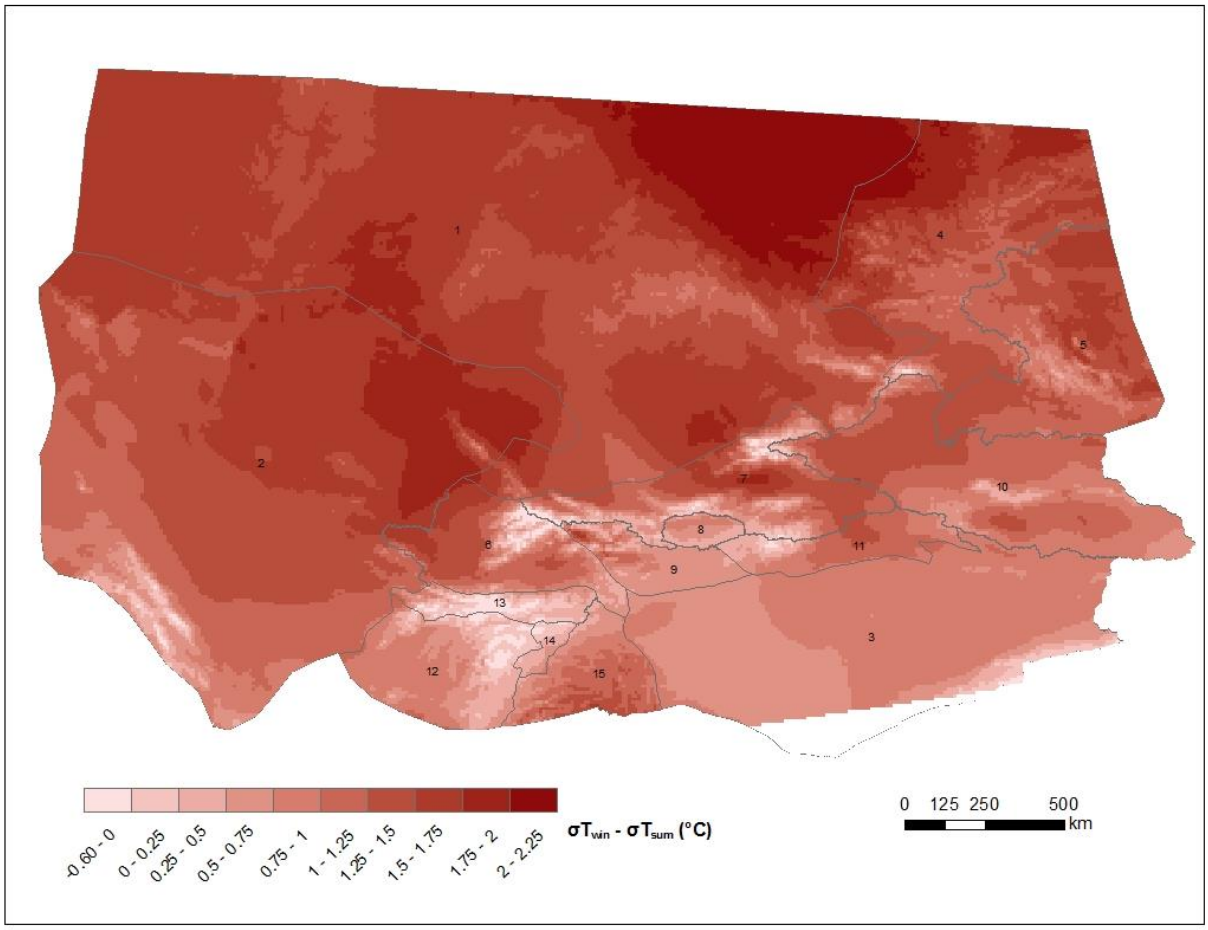

Figure 2.21 Differences between long-term standard deviation of air temperatures in winter and summer air temperature during 1951 – 2010

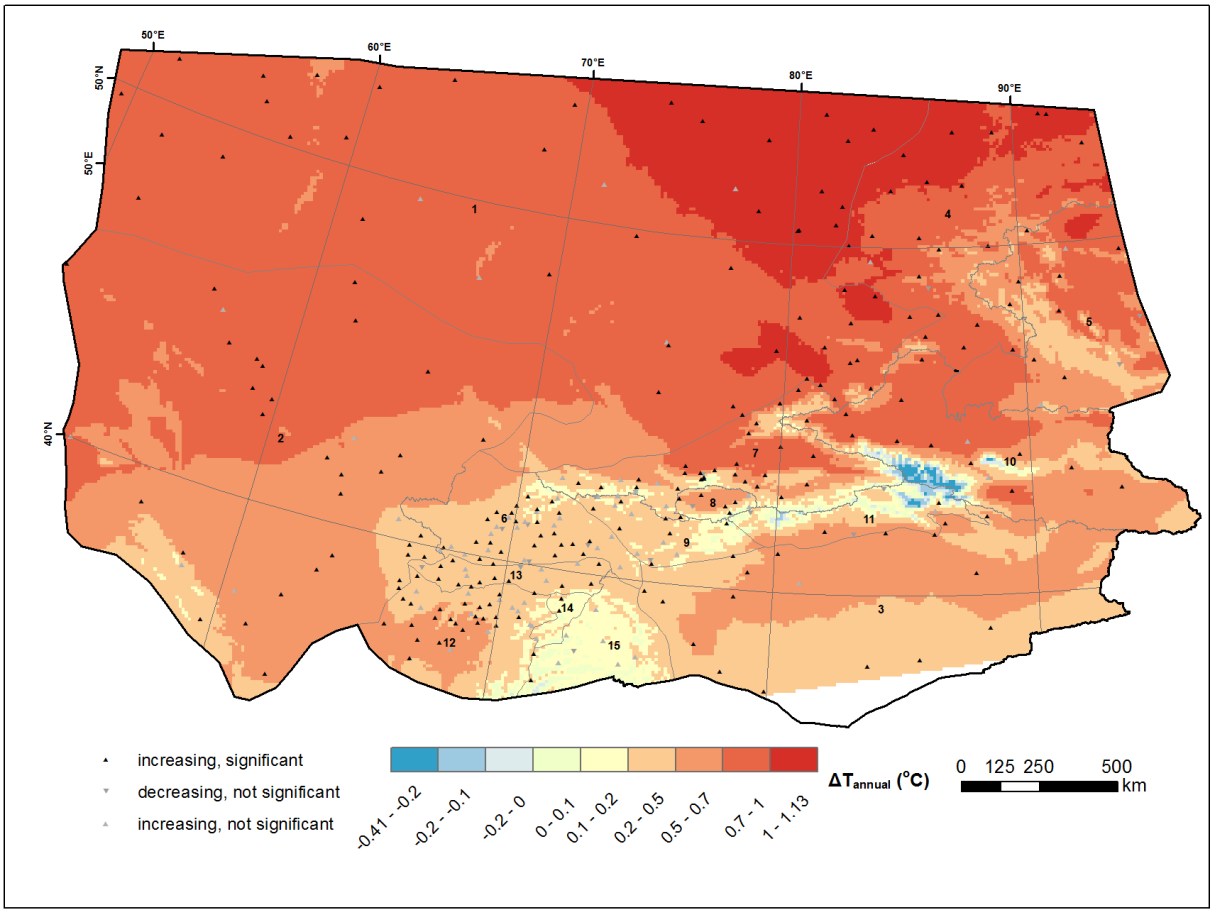

Figure 2.22 Difference of long-term normal annual air temperature between 1951 – 1976 and 1977 – 2010

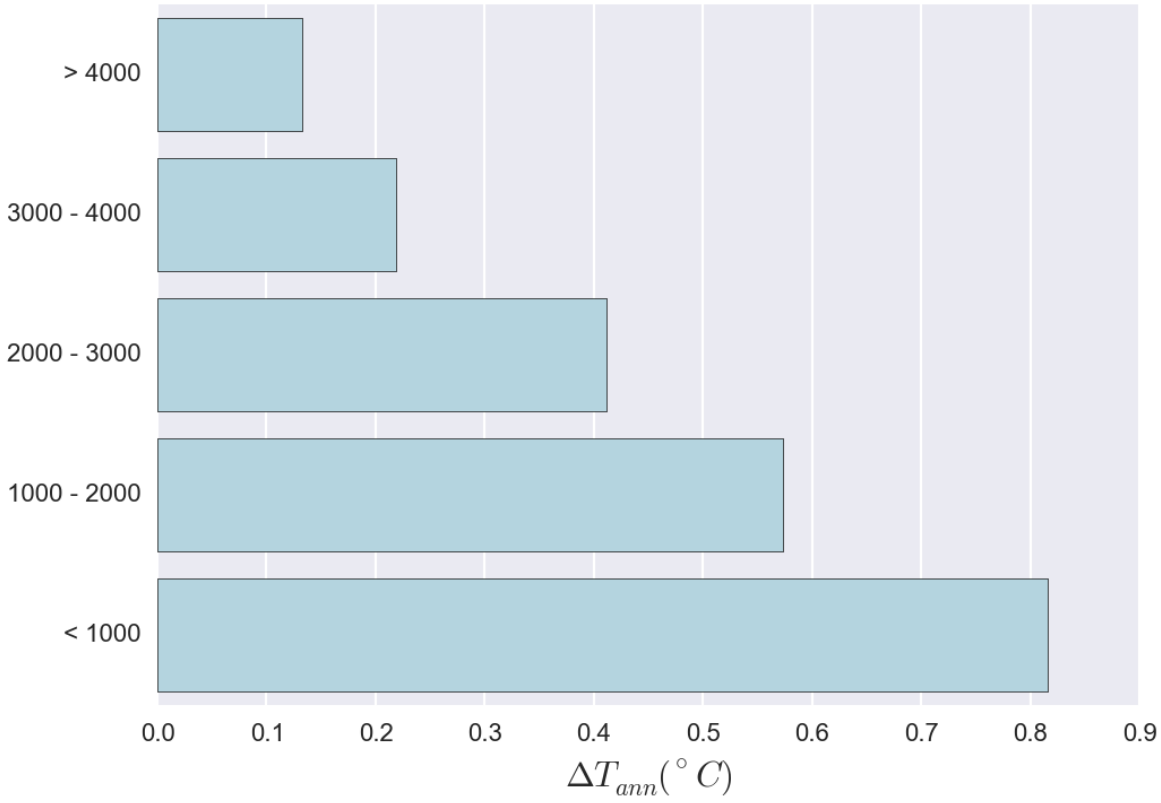

Figure 2.23 Difference of long-term normal annual air temperature between 1951 – 1976 and 1977 – 2010 in different elevation ranges

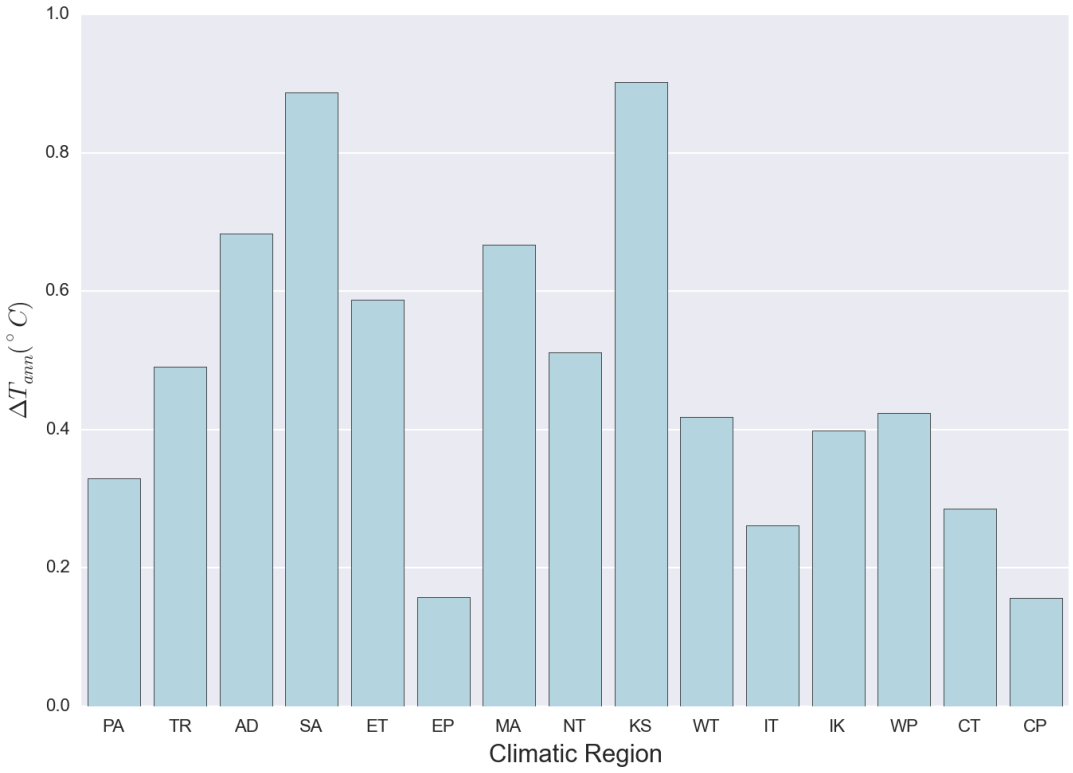

Figure 2.24 Difference of long-term normal annual air temperature between 1951 – 1976 and 1977 – 2010 in different climatic regions

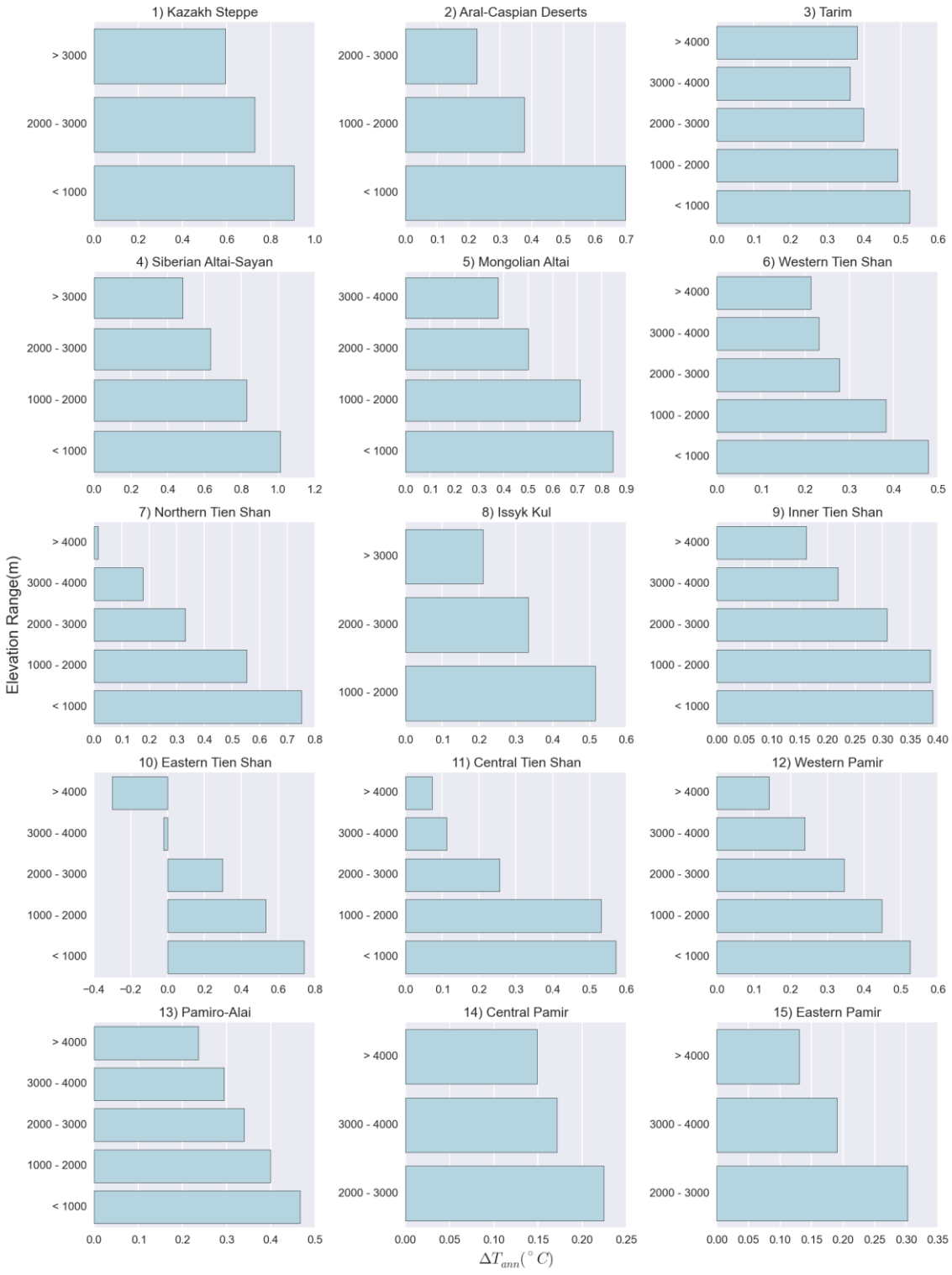

Figure 2.25 Difference of long-term normal annual air temperature between 1951 - 1976 and 1977 - 2010 in different elevation ranges within climatic regions

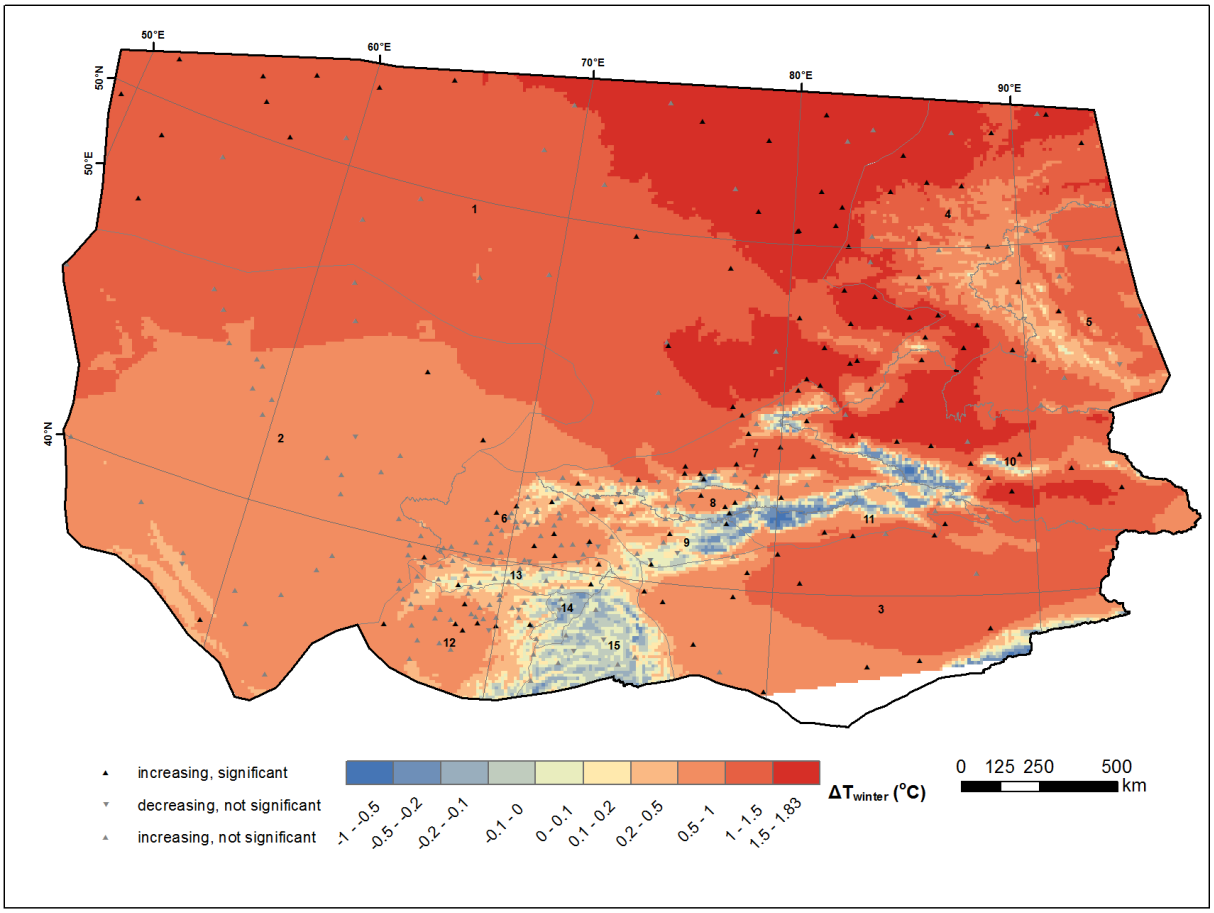

Figure 2.26 Difference of long-term normal winter air temperature between 1951 - 1976 and 1977 – 2010

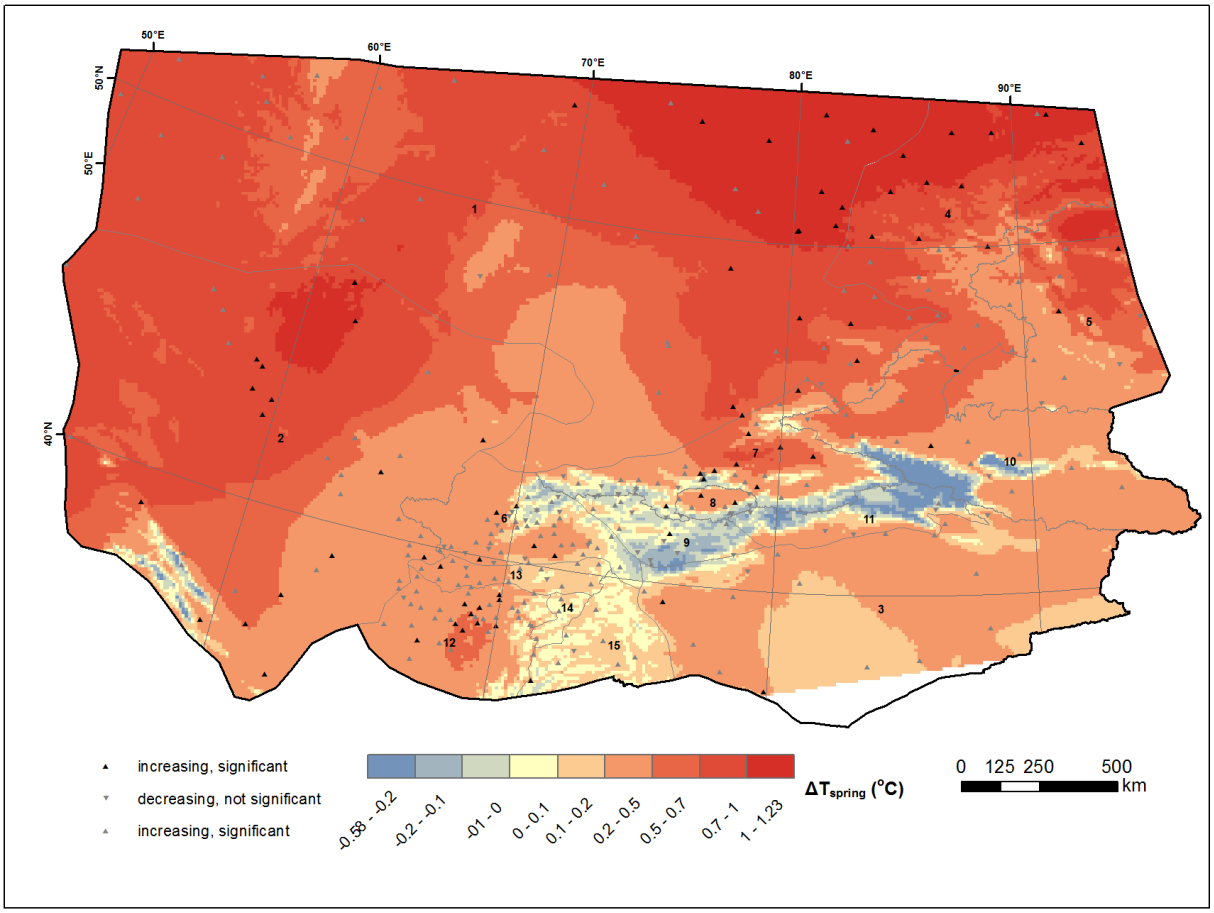

Figure 2.27 Difference of long-term normal spring air temperature between 1951 - 1976 and 1977 – 2010

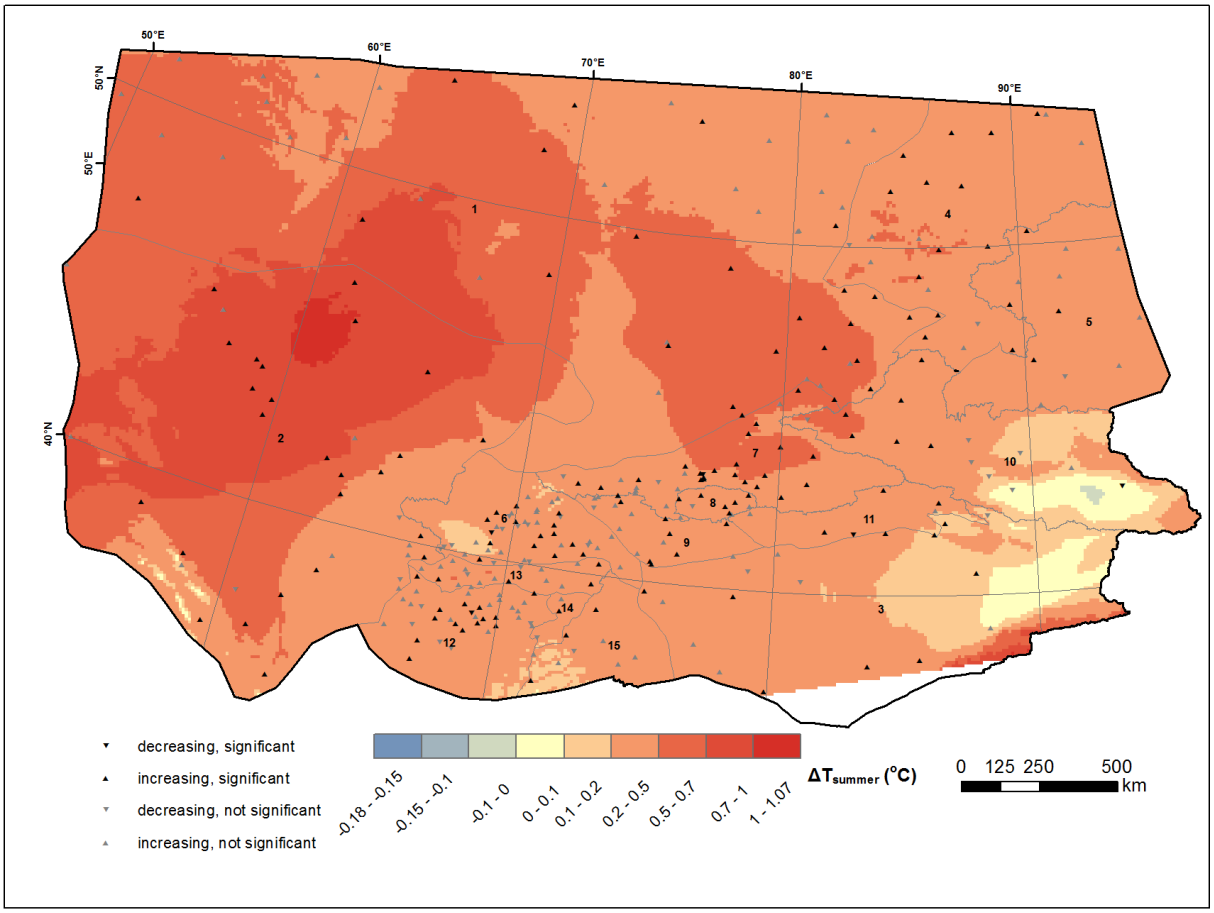

Figure 2.28 Difference of long-term normal summer air temperature between 1951 - 1976 and 1977 – 2010

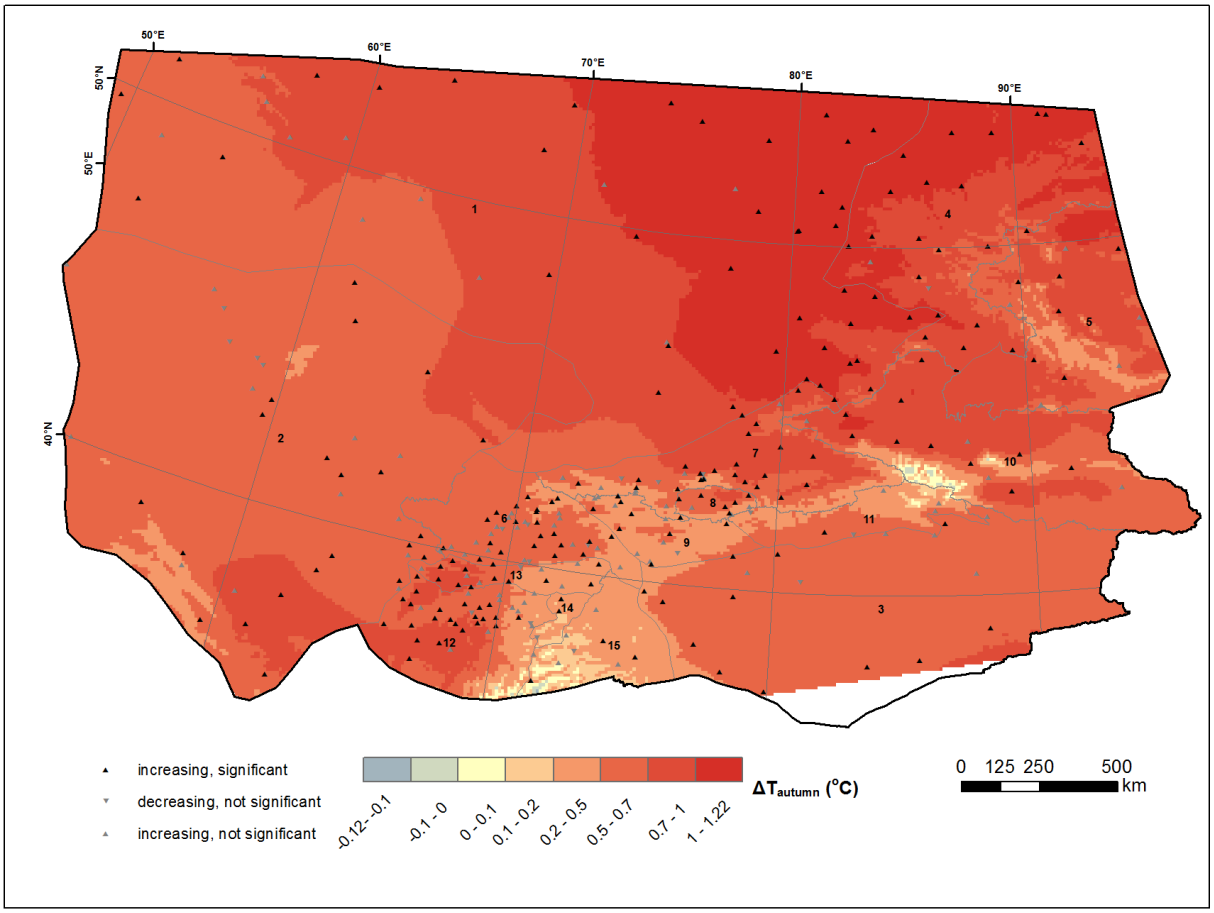

Figure 2.29 Difference of long-term normal autumn air temperature between 1951 - 1976 and 1977 – 2010

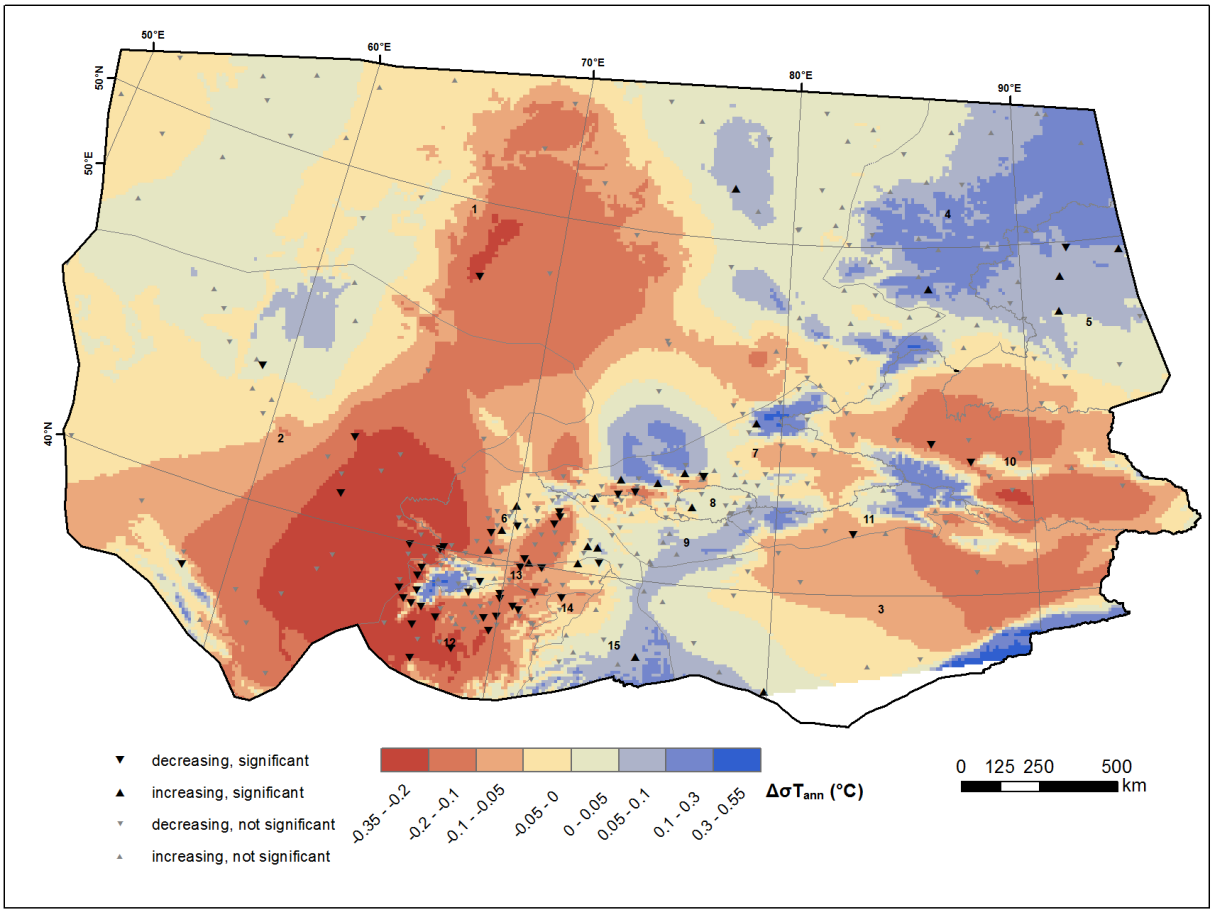

Figure 2.30 Difference of long-term standard deviation of annual air temperature between 1951 - 1976 and 1977 – 2010

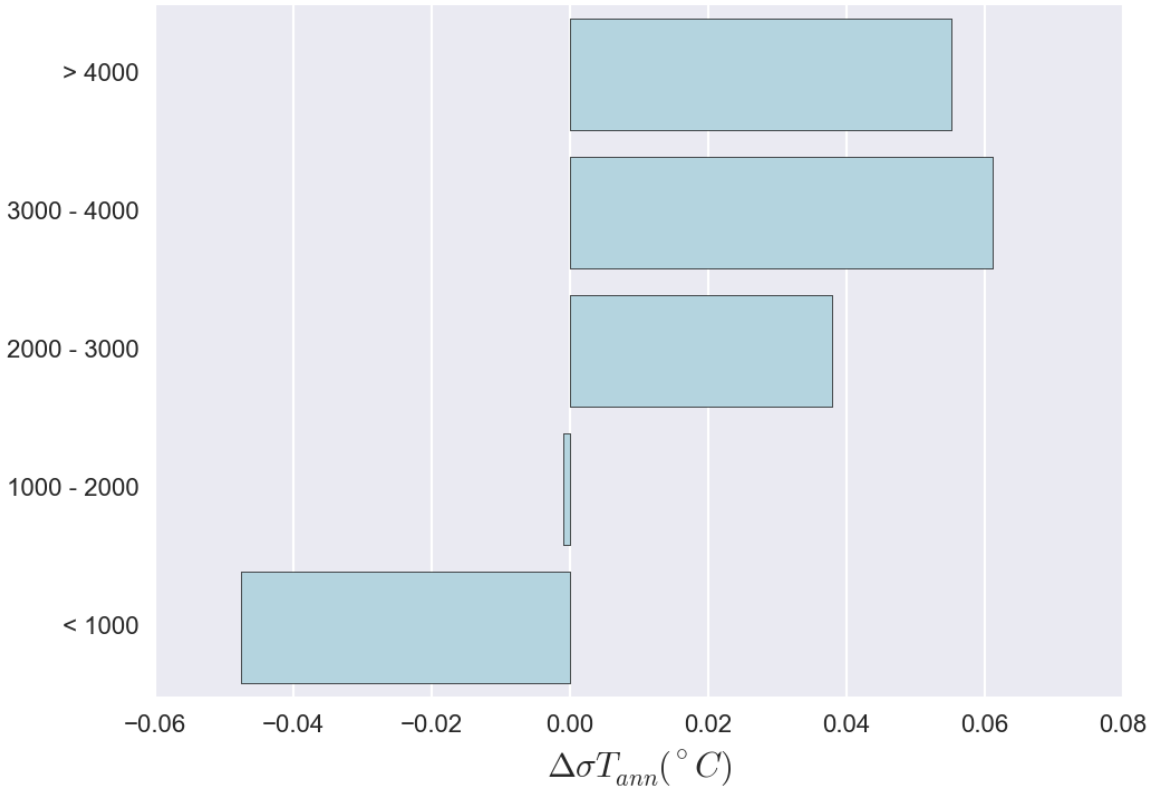

Figure 2.31 Difference of long-term standard deviation of annual air temperature between 1951 - 1976 and 1977 – 2010 in different elevation rangs

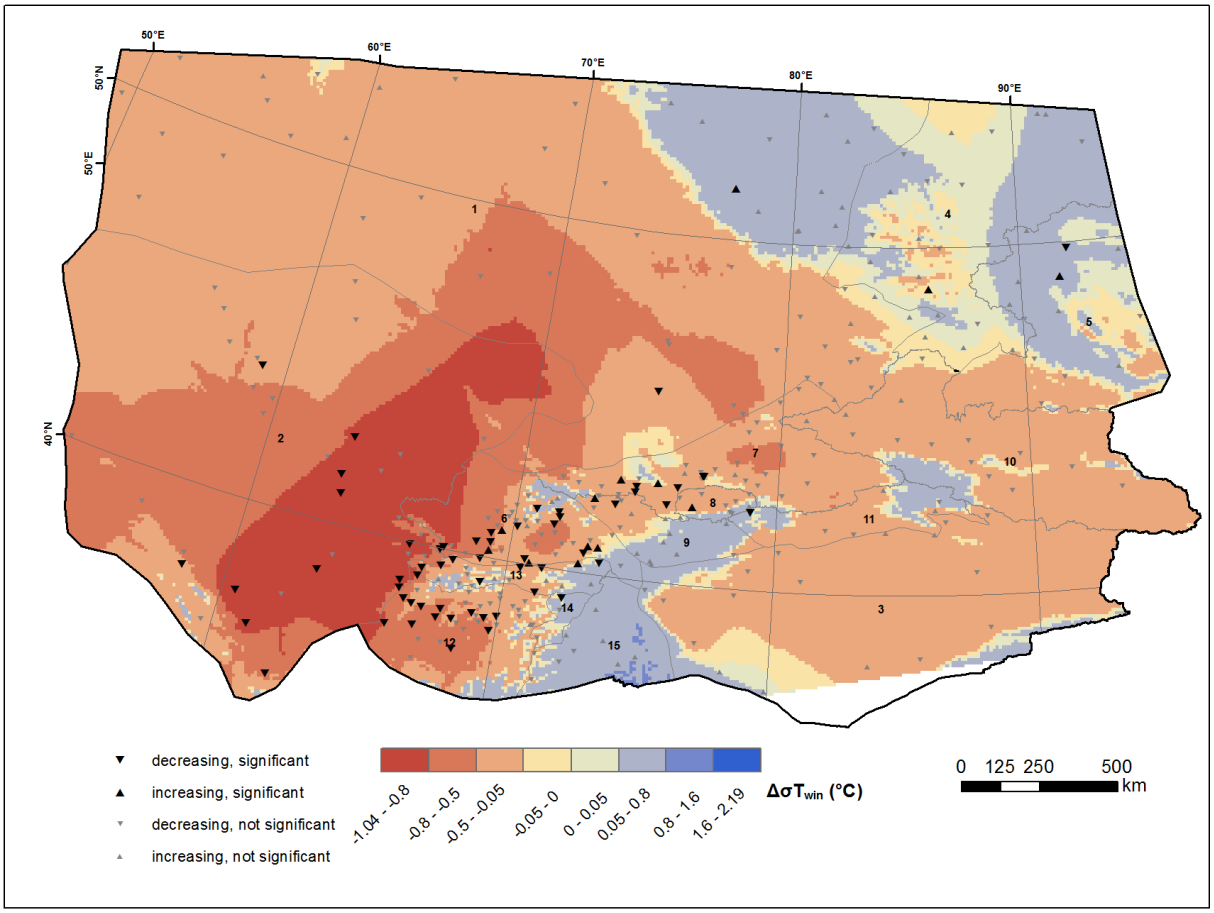

Figure 2.32 Difference of long-term standard deviation of winter air temperature between 1951 - 1976 and 1977 – 2010

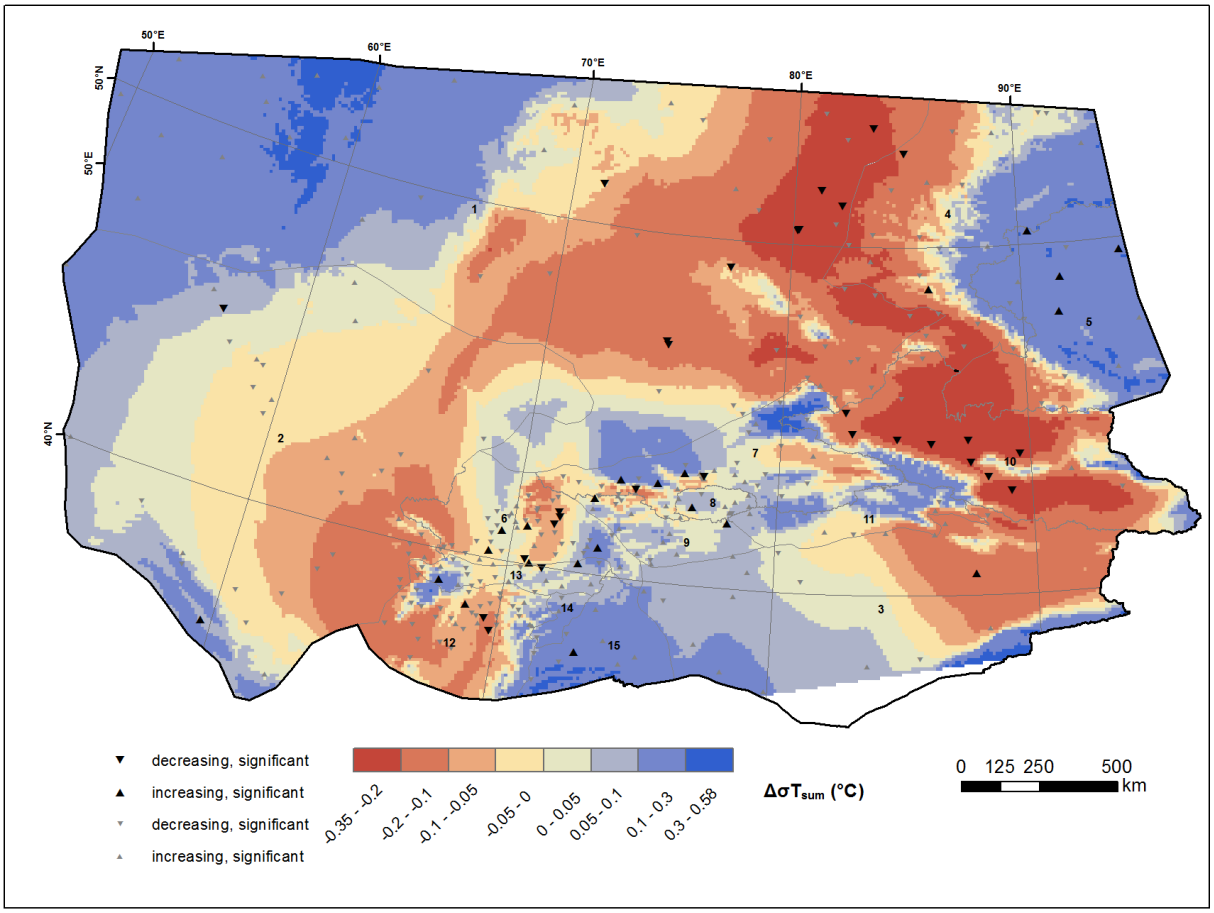

Figure 2.33 Difference of long-term standard deviation of summer air temperature between 1951 - 1976 and 1977 – 2010

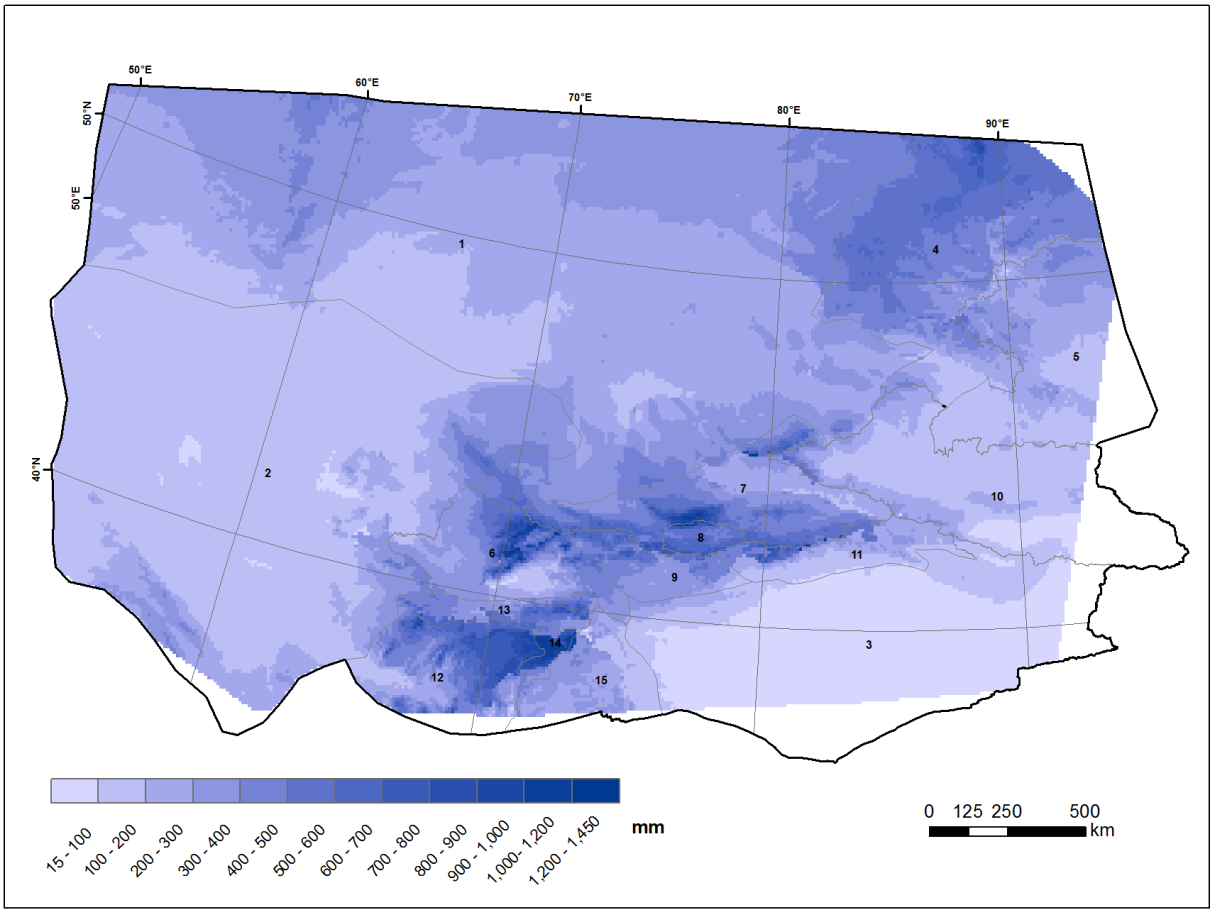

Figure 2.34 Long-tern normal annual precipitation in CA from 1951 to 2010

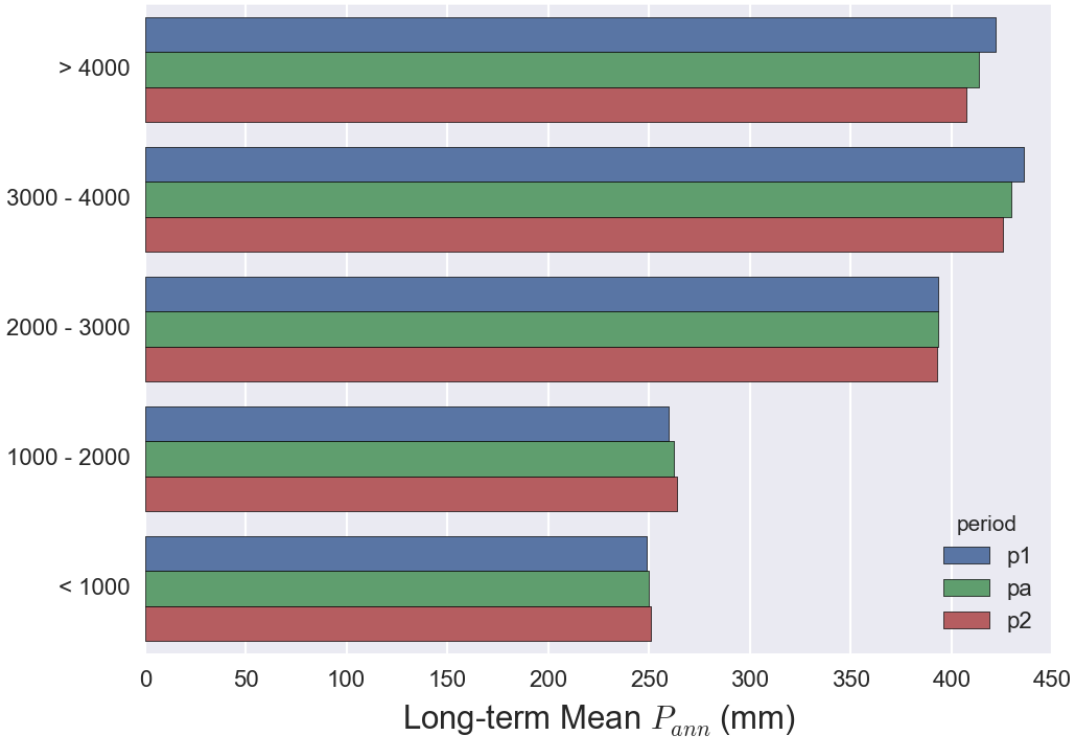

Figure 2.35 Long-term normal annual precipitation in different elevation ranges

P1: 1951 – 1976, P2: 1977 – 2010, Pa: 1951 - 2010

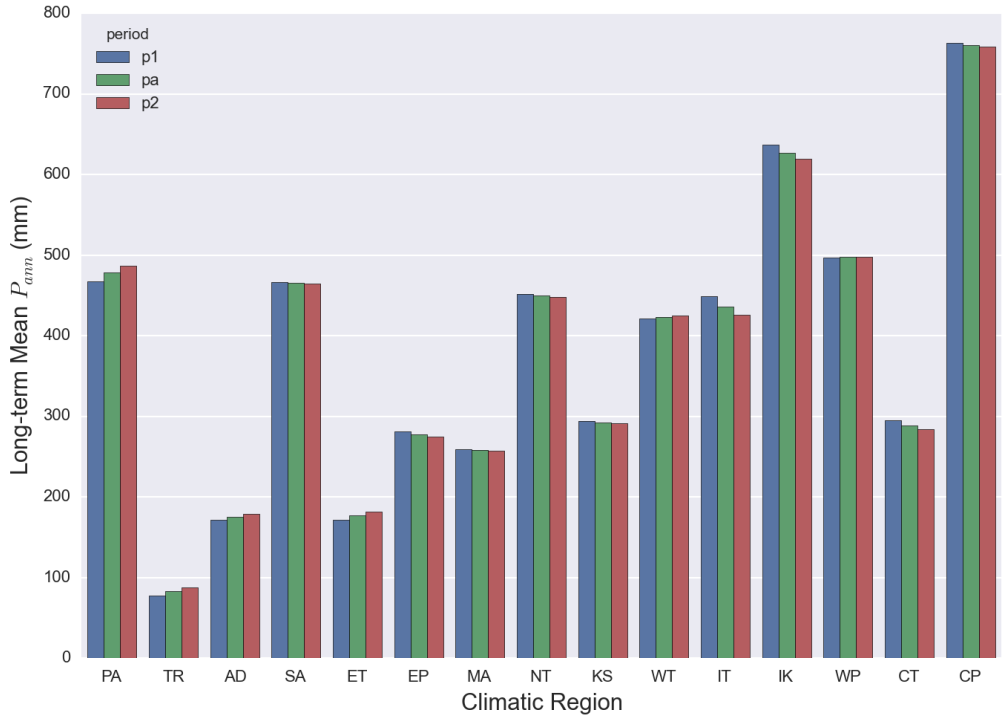

Figure 2.36 Long-term normal annual precipitation in different climatic regions

P1: 1951 – 1976, P2: 1977 – 2010, Pa: 1951 - 2010

Figure 2.37 Regional mean of long-term normal seasonal share of precipitation during 1951 to 2010 in central Asia and different climatic regions

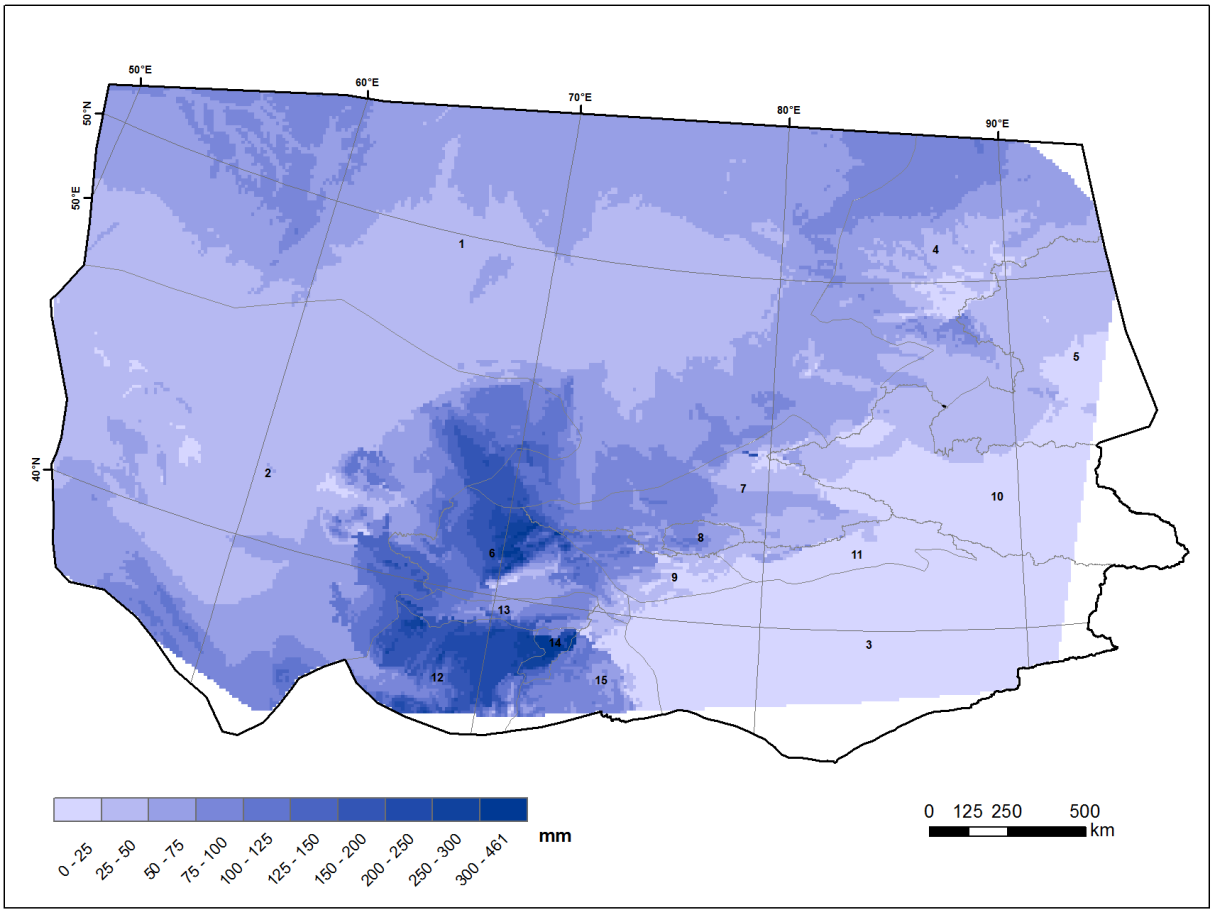

Figure 2.38 Long-tern normal winter precipitation in CA from 1951 to 2010

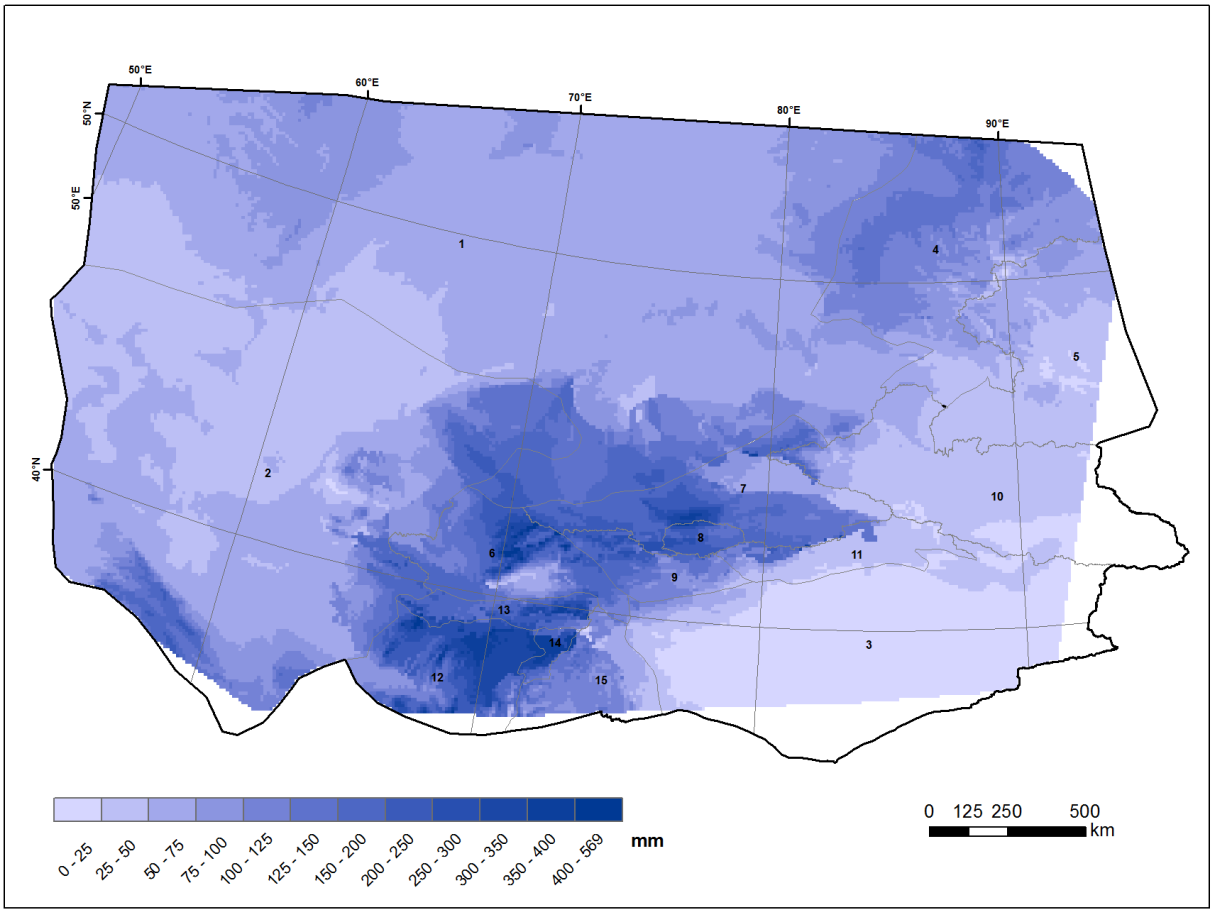

Figure 2.39 Long-tern normal spring precipitation in CA from 1951 to 2010

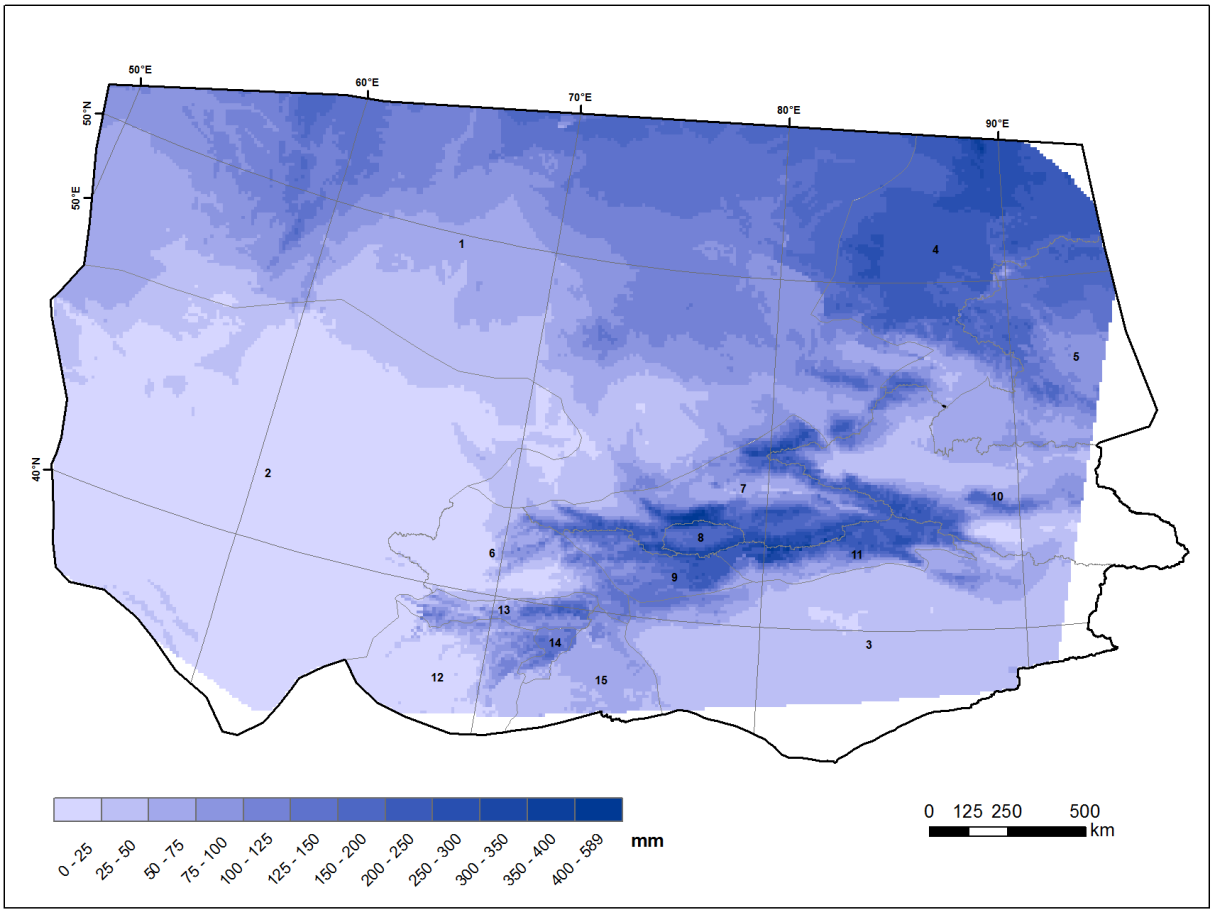

Figure 2.40 Long-tern normal summer precipitation in CA from 1951 to 2010

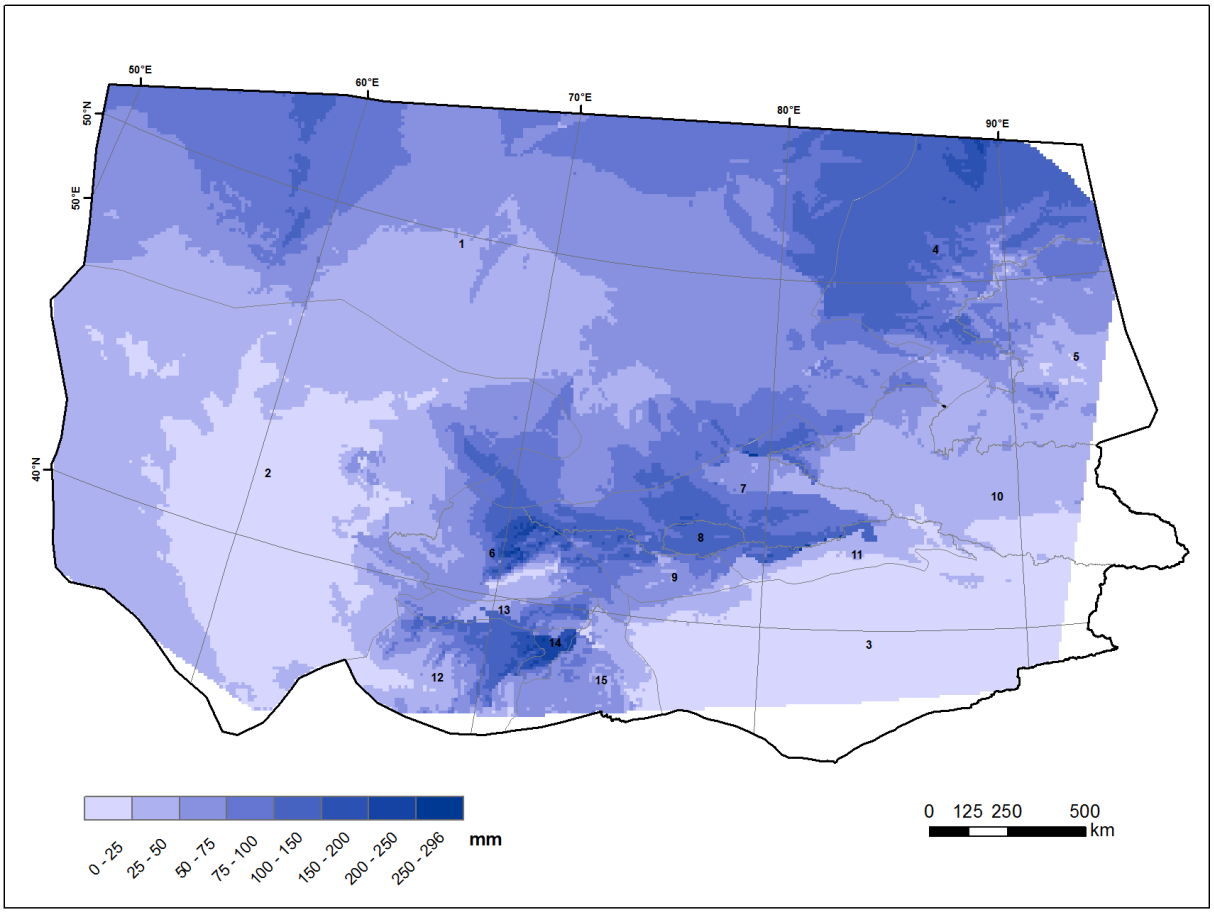

Figure 2.41 Long-tern normal autumn precipitation in CA from 1951 to 2010

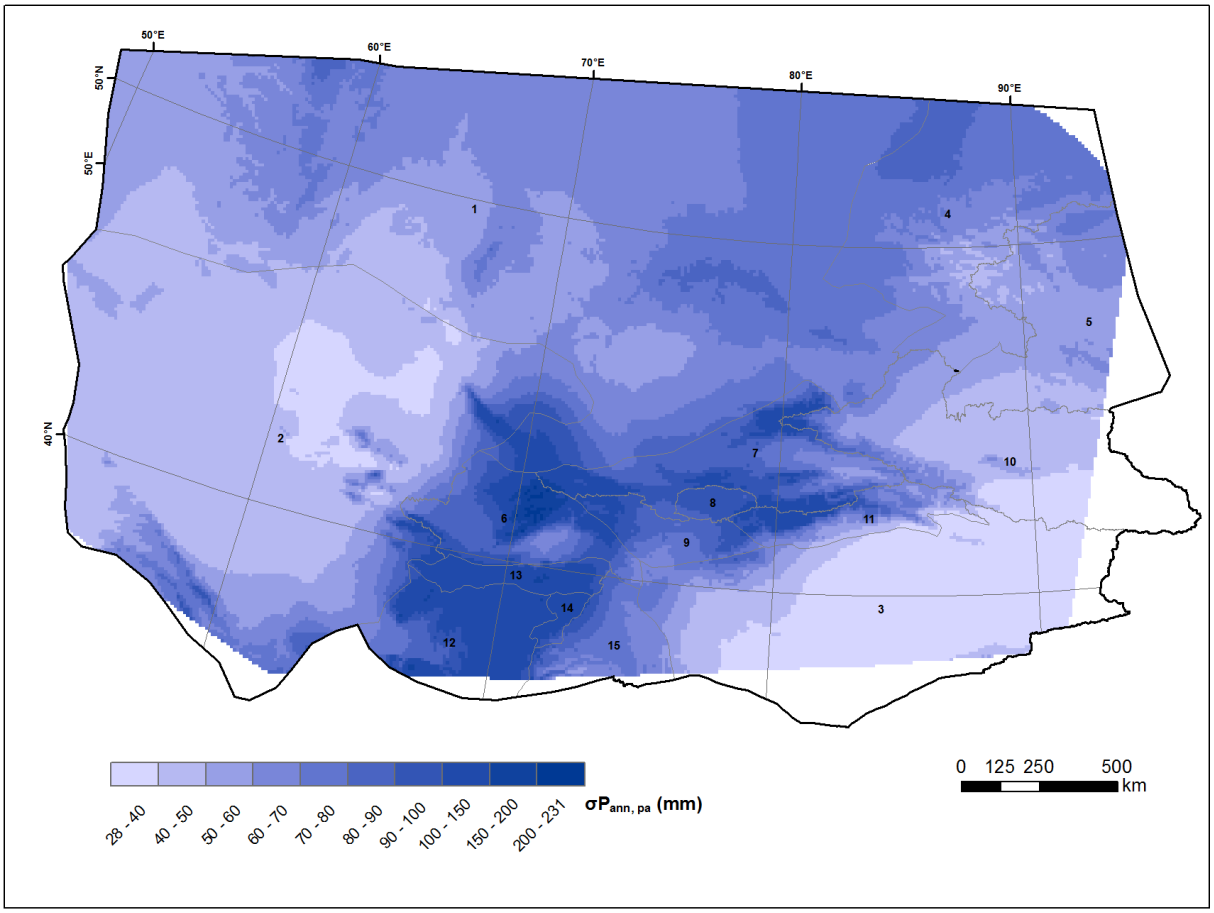

Figure 2.42 Long-tern standard deviation of annual precipitation in CA from 1951 to 2010

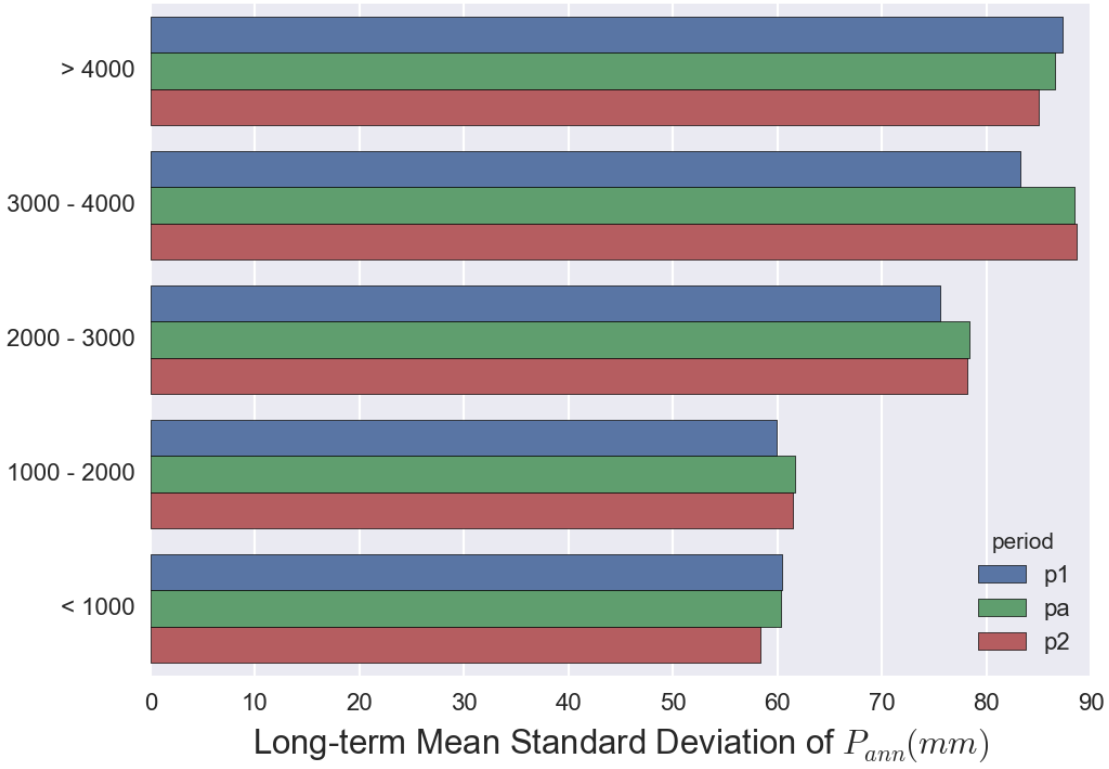

Figure 2.43 Long-term standard deviation of annual precipitation in different elevation ranges

P1: 1951 – 1976, P2: 1977 – 2010, Pa: 1951 - 2010

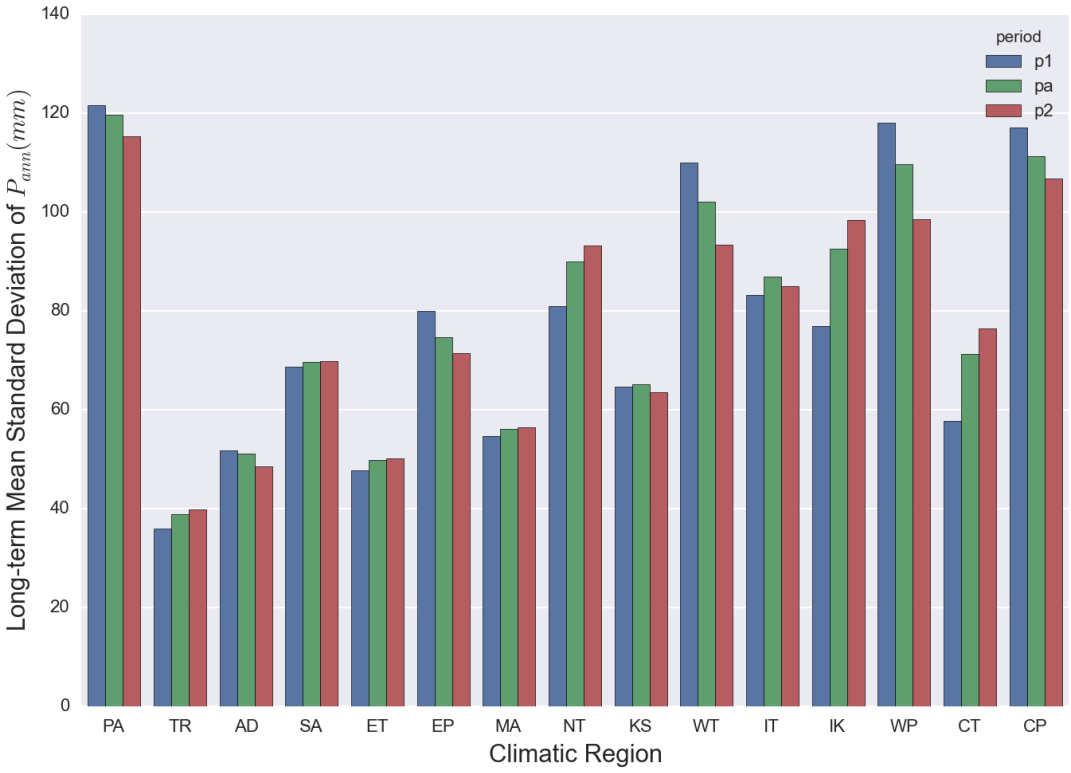

Figure 2.44 Long-term standard deviation of annual precipitation in different elevation ranges

P1: 1951 – 1976, P2: 1977 – 2010, Pa: 1951 – 2010

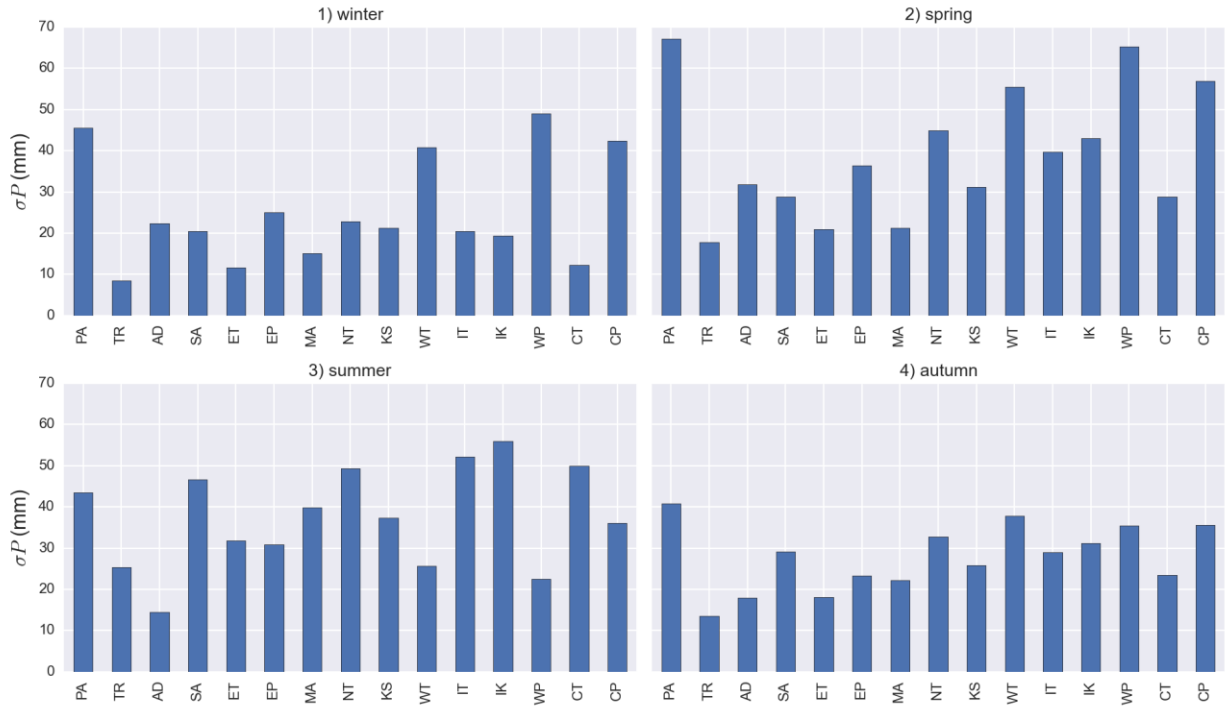

Figure 2.45 Long-term standard deviation of seasonal precipitation during 1951 to 2010 in different climatic regions

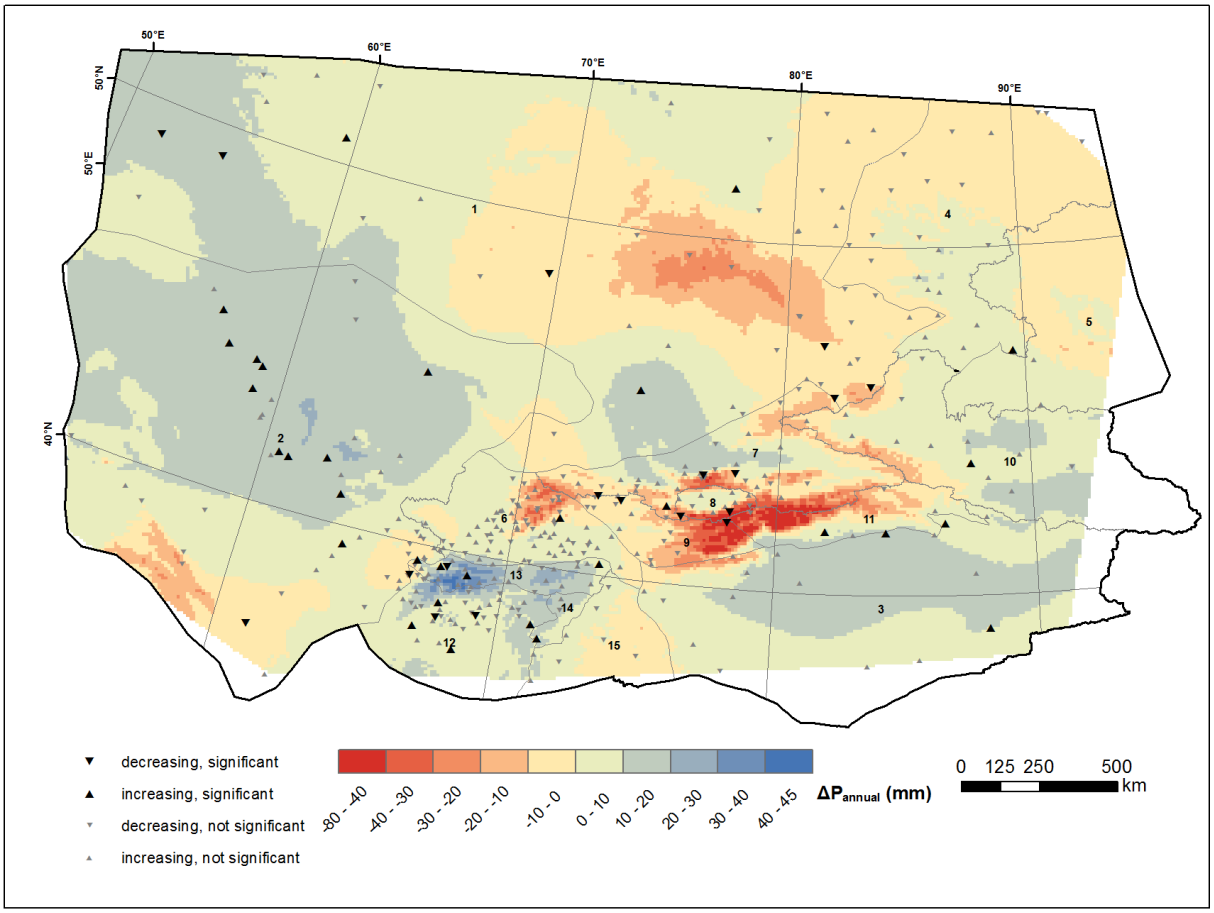

Figure 2.46 Difference of long-term normal annual precipitation between 1951 - 1976 and 1977 – 2010

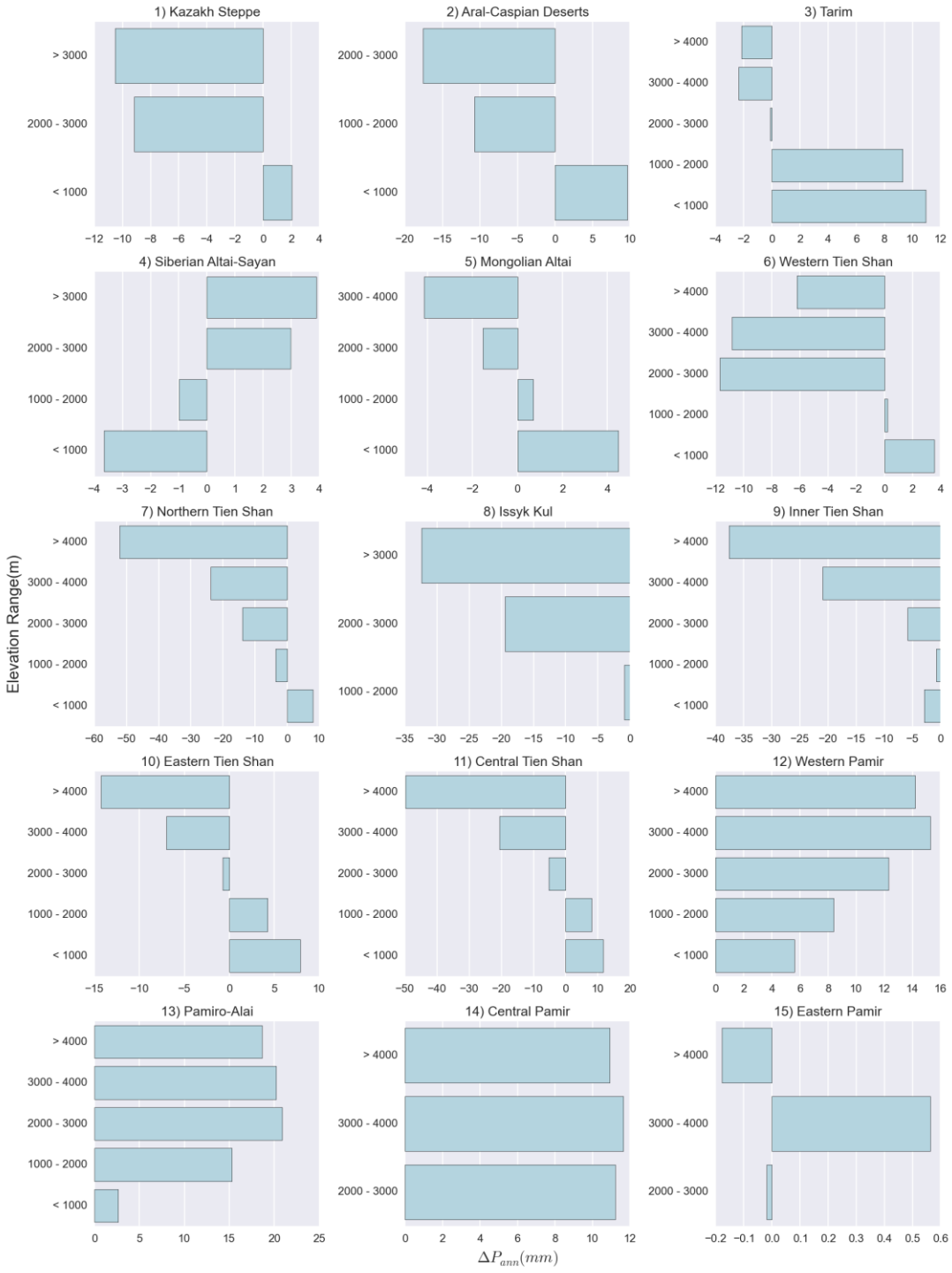

Figure 2.47 Difference of long-term normal annual precipitation between 1951 - 1976 and 1977 - 2010 in different elevation ranges within climatic regions

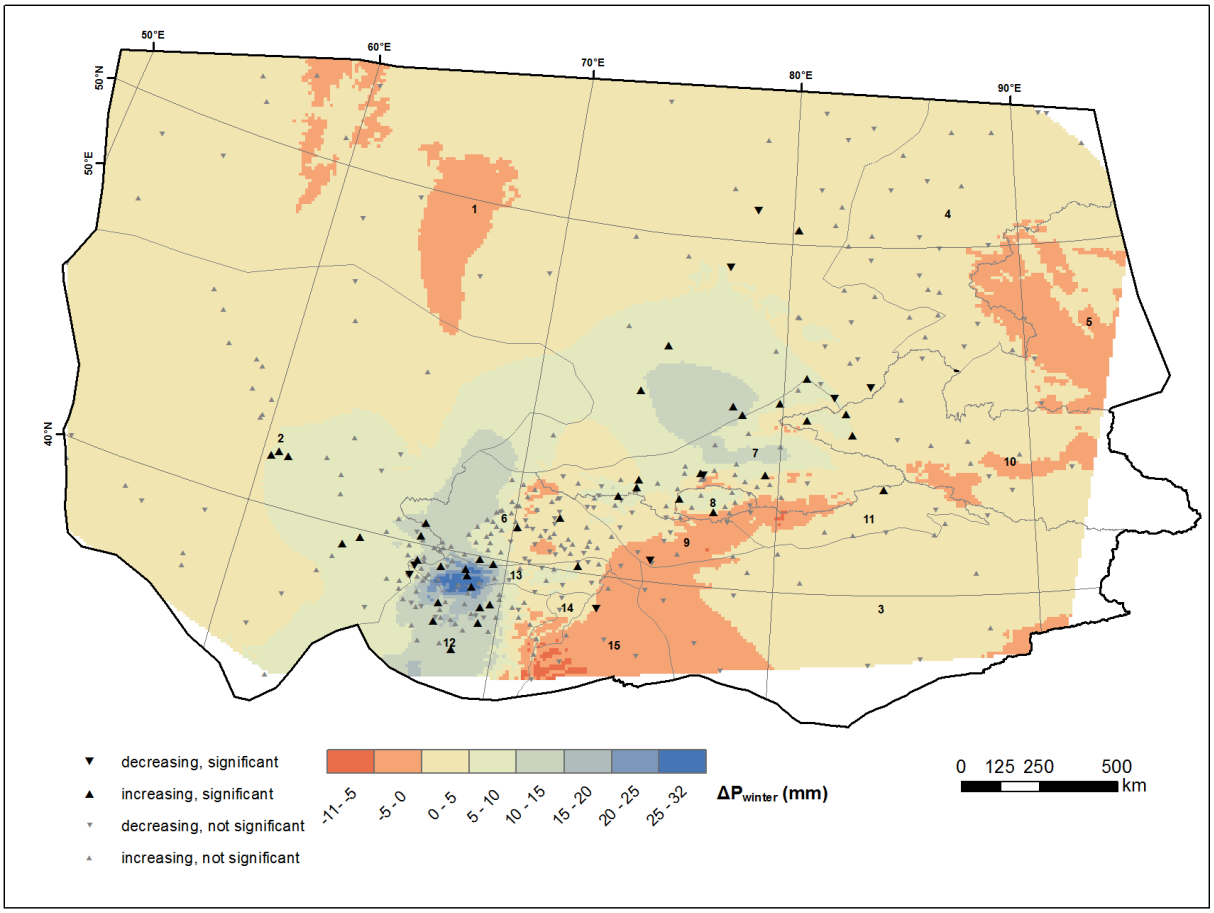

Figure 2.48 Difference of long-term normal winter precipitation between 1951 - 1976 and 1977 – 2010

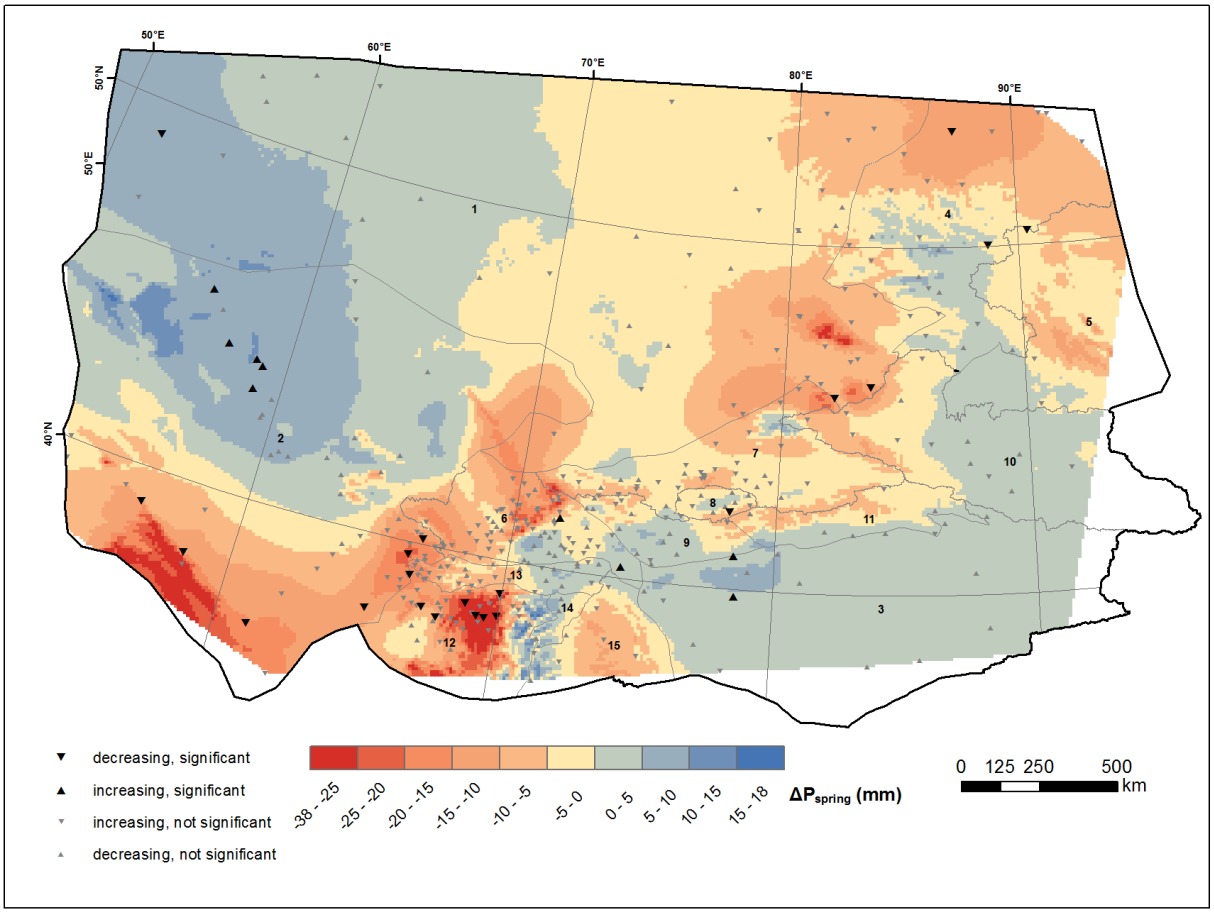

Figure 2.49 Difference of long-term normal spring precipitation between 1951 - 1976 and 1977 – 2010

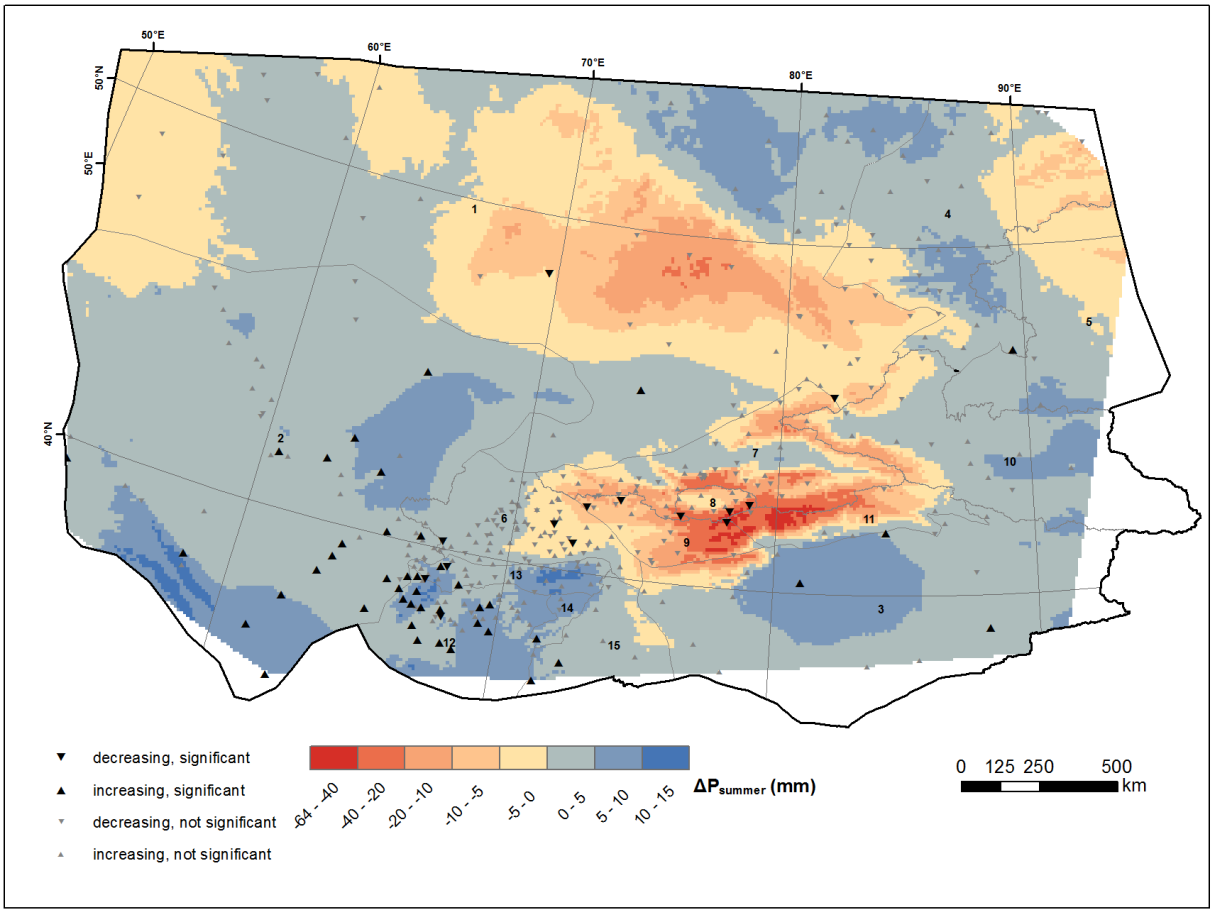

Figure 2.50 Difference of long-term normal summer precipitation between 1951 - 1976 and 1977 – 2010

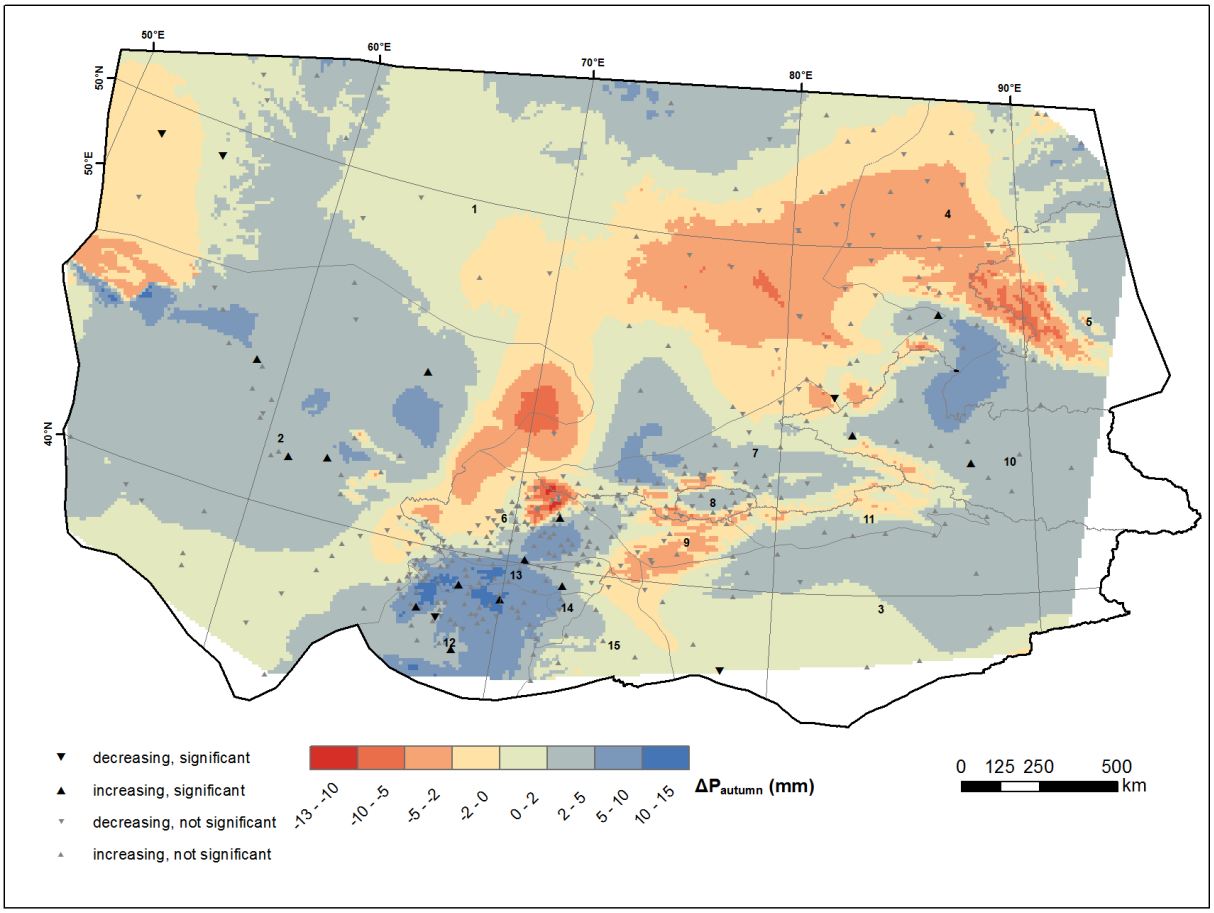

Figure 2.51 Difference of long-term normal autumn precipitation between 1951 - 1976 and 1977 – 2010

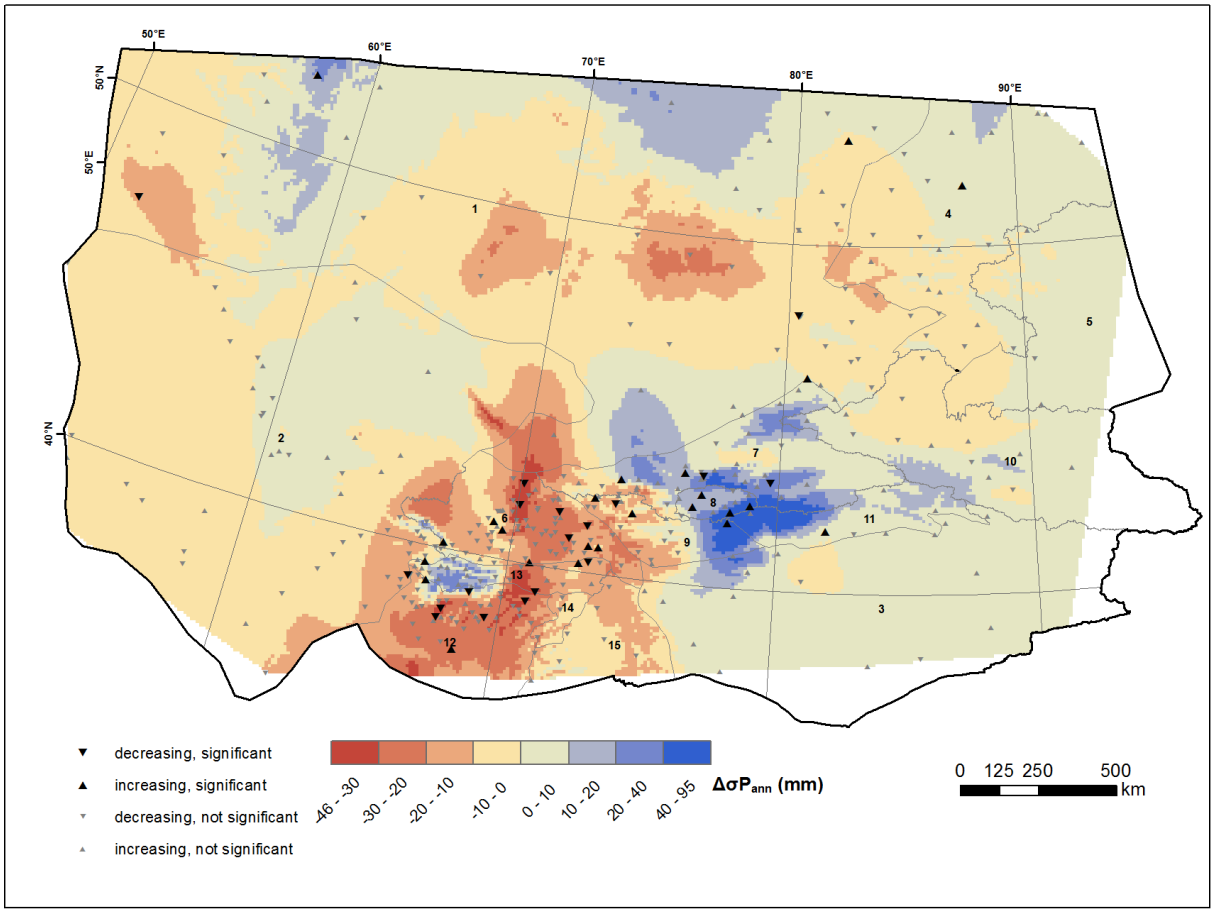

Figure 2.52 Difference of long-term standard deviation of annual precipitation between 1951 - 1976 and 1977 – 2010

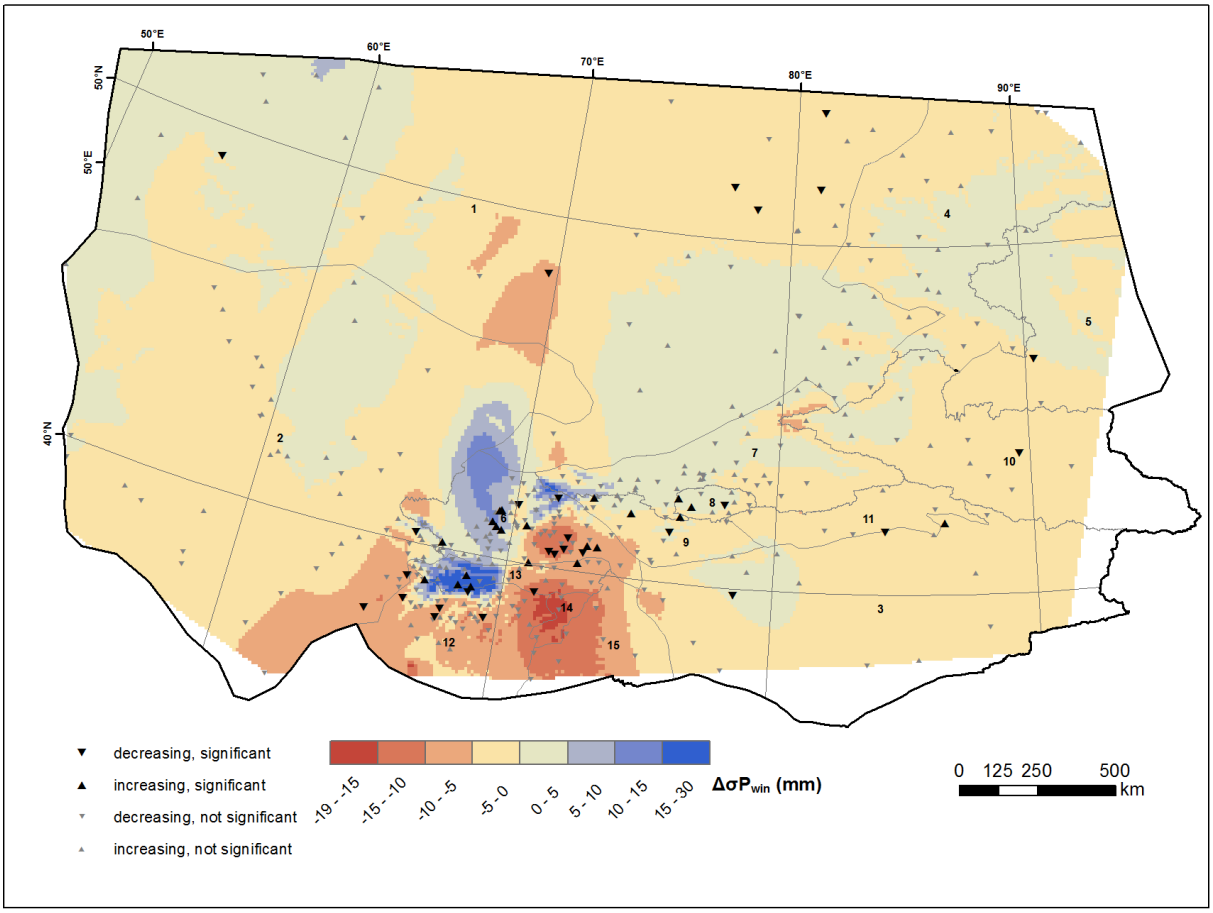

Figure 2.53 Difference of long-term standard deviation of winter precipitation between 1951 - 1976 and 1977 – 2010

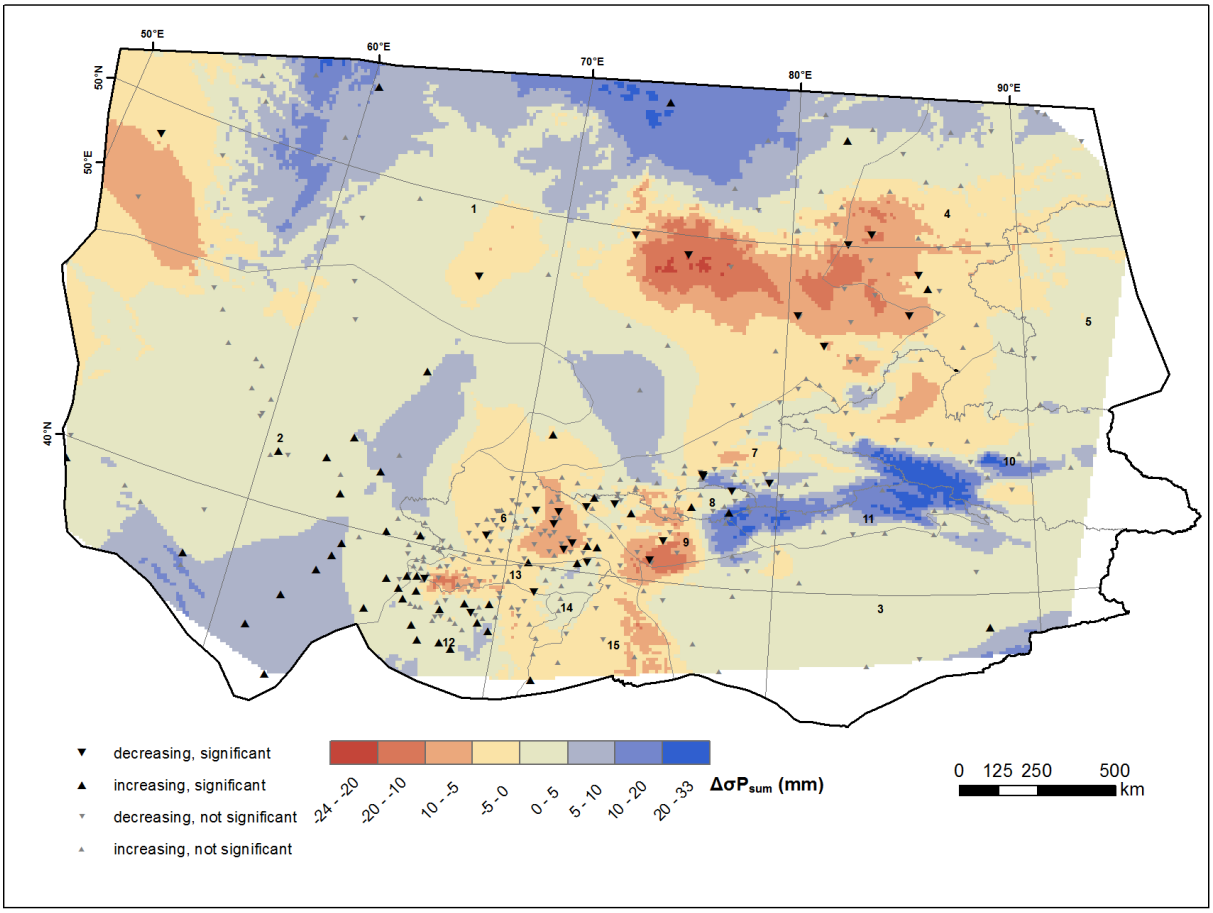

Figure 2.54 Difference of long-term standard deviation of summer precipitation between 1951 - 1976 and 1977 – 2010

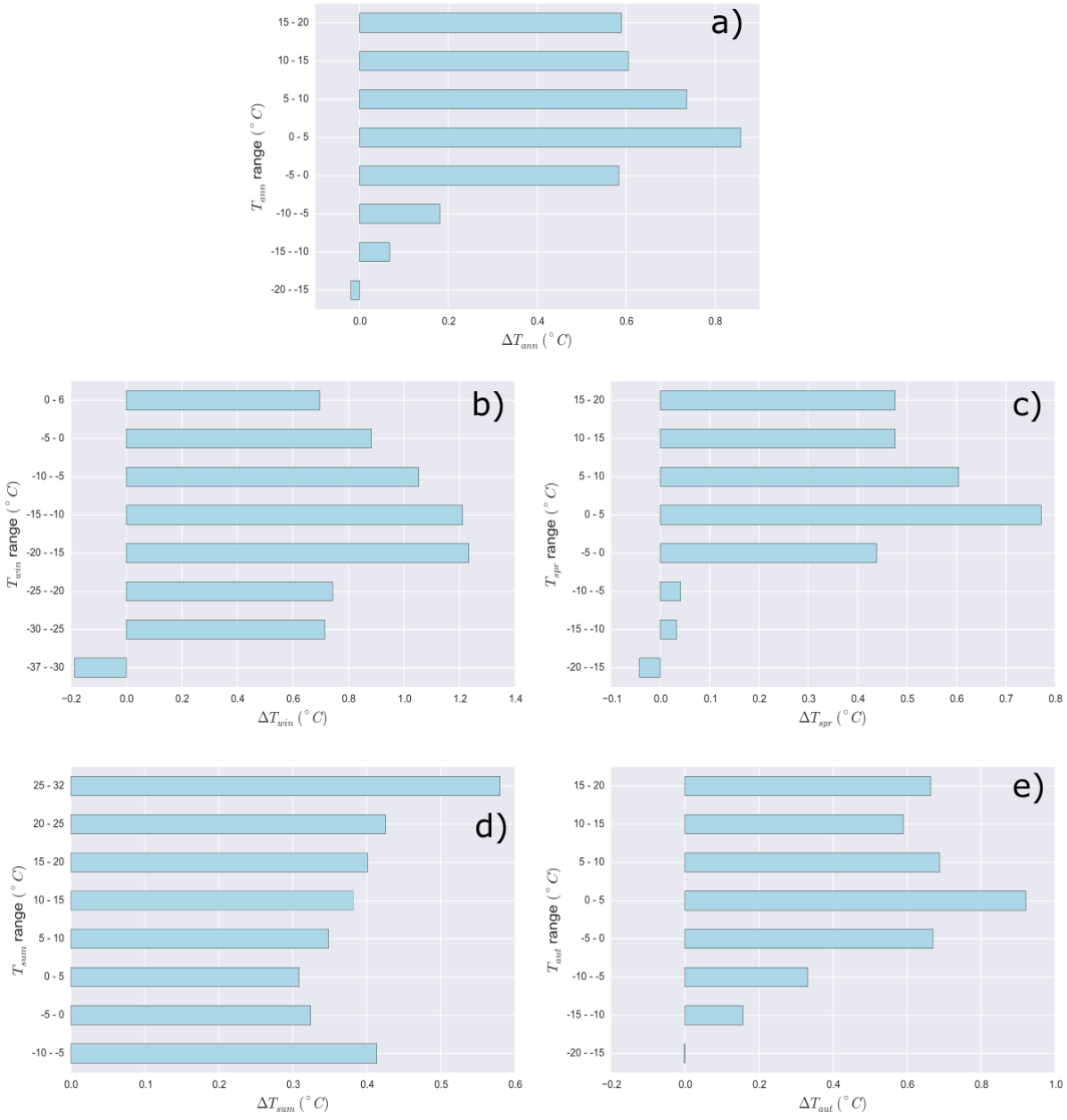

Figure 2.55 Differences between long-term normal air temperature between 1951 -1976 and 1977 – 2010 against long-term normal air temperature in 1951 – 2010

References

Agrawala, S., M. Barlow, H. Cullen, and B. Lyons. 2001. The Drought and Humanitarian Crisis in Central and Southwest Asia: A Perspective of Climate, IRI Report.

Aizen, V. B., Aizen, E. M., & Melack, J. M. (1996). Precipitation, melt and runoff in the northern Tien Shan. Journal of Hydrology, 186(1-4), 229–251.

Aizen V. B., E. M. Aizen, J. Melack and J. Dozier, 1997. Climate and Hydrologic Changes in the Tien Shan, Central Asia. J. Climate, 10, 6, 1393-1404

Aizen, V.B., E.M. Aizen, V. A. Kuzmichenok. 2007a: Glaciers and Hydrological Changes in the Tien Shan: Simulation and Prediction, Environmental Research Letters, http://dx.doi.org/10.1088/1748-9326/2/4/045019

Aizen, V. B., Kuzmichenok, V. a., Surazakov, A. B., & Aizen, E. M. (2007b). Glacier changes in the Tien Shan as determined from topographic and remotely sensed data. Global and Planetary Change, 56(3-4), 328–340. http://doi.org/10.1016/j.gloplacha.2006.07.016

Aizen, V. B., Aizen, E. M., & Kuzmichenok, V. a. (2007c). Geo-informational simulation of possible changes in Central Asian water resources. Global and Planetary Change, 56(3-4), 341–358. http://doi.org/10.1016/j.gloplacha.2006.07.020

Aizen, V. B., Mayewski, P. a., Aizen, E. M., Joswiak, D. R., Surazakov, A. B., Kaspari, S., … Finaev, A. (2009). Stable-isotope and trace element time series from Fedchenko glacier (Pamirs) snow/firn cores. Journal of Glaciology, 55(190), 275–291. http://doi.org/10.3189/002214309788608787

Aizen, V. B., Aizen, E., ZHOU, H., in preparation. Climate changes in CA during the 20th century

Beckers, J. M., & Rixen, M. (2003). EOF calculations and data filling from incomplete oceanographic datasets. Journal of Atmospheric and Oceanic Technology, 20(12), 1839–1856. http://doi.org/10.1175/1520-0426(2003)020<1839:ECADFF>2.0.CO;2

Bernaola-Galvan, P., Ivanov, P. Ch., Amaral, L.N., and Stanley, H.E.: *Phys. Rev. Lett.* **87** (2001), 168105

Boroffka, N.G. O., 2010. Archaeology and Its Relevance to Climate and Water Level Changes: A Review. In The Aral Sea Environment With contributions by numerous experts. Series: The Handbook of Environmental Chemistry, Vol. 7 , XIV, Eds.: Kostianoy, Andrey G.; Kosarev, Aleksey N. , 332p.

Bryson, R. (1986). Airstream Climatology of Asia. In Y. Xu (Ed.), Proceedings of International Symposium on the Qinghai-Xizang Plateau and Mountain Meteorology SE - 36 (pp. 604–619). American Meteorological Society. http://doi.org/10.1007/978-1-935704-19-5_36

Cohen, J. L., Furtado, J. C., Barlow, M. a, Alexeev, V. a, & Cherry, J. E. (2012). Arctic warming, increasing snow cover and widespread boreal winter cooling. Environmental Research Letters, 7(1), 014007. http://doi.org/10.1088/1748-9326/7/1/014007

Daly, C., Neilson, R., & Phillips, D. (1994). A statistical-topographic model for mapping climatological precipitation over mountainous terrain. Journal of Applied Meteorology 33, 140 – 158. Retrieved from http://journals.ametsoc.org/doi/abs/10.1175/1520-0450(1994)033<0140:ASTMFM>2.0.CO;2

Farinotti, D., Longuevergne, L., Moholdt, G., Duethmann, D., Mölg, T., Bolch, T., … Güntner, A. (2015). Substantial glacier mass loss in the Tien Shan over the past 50 years. Nature Geoscience, 8(9), 716–722. http://doi.org/10.1038/ngeo2513

Feng, G.-L., Gong, Z.-Q., Zhi, R., & Zhang, D.-Q. (2008). Analysis of precipitation characteristics of South and North China based on the power-law tail exponents. Chinese Physics B, 17(7), 2745. Retrieved from http://stacks.iop.org/1674-1056/17/i=7/a=065

Feng, S., Hu, Q., & Qian, W. (2004). Quality control of daily meteorological data in China, 1951–2000: a new dataset. International Journal of Climatology, 24(7), 853–870. http://doi.org/10.1002/joc.1047

Finaev A.F. 2005. On research of glaciation in the Central Asia. Water resources of the Central Asia. Dushanbe: Institute of Water Issues, Hydropower Engineering and Ecology, Academy of Sciences, N2. pp. 70-80. (rus)

Fotheringham, S. A., Brunsdon, C., & Charlton, M. (2002). Geographically weighted regression - the analysis of spatially varying relationships. John Wiley & Sons.

Fukuda, K., Eugene Stanley, H., & Nunes Amaral, L. A. (2004). Heuristic segmentation of a nonstationary time series. Phys. Rev. E, 69(2), 21108. http://doi.org/10.1103/PhysRevE.69.021108

Giese E et al 2007 Long term analysis of air temperature trends in central Asia Erdkunde 186–202

Menne, M. J., Williams, C. N., & Vose, R. S. (2009). The U.S. Historical Climatology Network Monthly Temperature Data, Version 2. Bulletin of the American Meteorological Society, 90(7), 993–1007. http://doi.org/10.1175/2008BAMS2613.1

Micklin, P. (2007). The Aral Sea Disaster. Annual Review of Earth and Planetary Sciences, 35(1), 47–72. http://doi.org/10.1146/annurev.earth.35.031306.140120

Mokhov, I., and V.K, Petukhov,(1999), Atmospheric of action and tendencies of their change. Izv, Acad, Sci, USSR, Atmos.Oceanic Phys.,36,292-299.

Mountain Research Initiative (MRI) EDW Working Group. (2015). Elevation-dependent warming in mountain regions of the world. Nature Clim. Change, 5(5), 424–430. http://doi.org/10.1038/nclimate2563\rhttp://www.nature.com/nclimate/journal/v5/n5/abs/nclimate2563.html#supplementary-information

Hengl, T. (2009). A practical guide to geostatistical mapping, University of Amsterdam.

Jeong, J.-H., Ou, T., Linderholm, H. W., Kim, B.-M., Kim, S.-J., Kug, J.-S., & Chen, D. (2011). Recent recovery of the Siberian High intensity. Journal of Geophysical Research: Atmospheres, 116(D23), n/a–n/a. http://doi.org/10.1029/2011JD015904

Lawrimore, J. H., Menne, M. J. , Gleason, B. E., Williams, C. N., Wuertz, D. B., Vose, R. S., and Rennie, J. (2011), An overview of the Global Historical Climatology Network monthly mean temperature data set, version 3, J. Geophys. Res., 116, D19121, doi:10.1029/2011JD016187.

Levene, Howard (1960). "Robust tests for equality of variances". In Ingram Olkin, Harold Hotelling, et alia. Contributions to Probability and Statistics: Essays in Honor of Harold Hotelling. Stanford University Press. pp. 278–292.

Lioubimtseva, E., 2002. Arid Environments. In: M. Shahgedanova (editor) Physical Geography of Northern Eurasia, Oxford University Press, Oxford, pp.267-283

Lydolph, P. E. (1977). Climates of the Soviet Union. Amsterdam [etc.]: Elsevier.

Kadukin, A. I. and R. K. Klige, 1991. The water balance of the Caspian Sea and Aral Sea. In Proc: "Hydrology of Natural and Manmade Lakes", Eds: G. Schiller, R. Lemmelà, and M. Spreafico; Vienna, 11-24 August, 1991; IAHS Publication, No. 206, pp 55-61

Kondrashov, D., Denton, R., Shprits, Y. Y., & Singer, H. J. (2014). Reconstruction of gaps in the past history of solar wind parameters. Geophysical Research Letters, 41(8), 2702–2707. http://doi.org/10.1002/2014GL059741

Konovalov, 2003: Prostranstvennaya ekstrapolyaciya i izmenchivost' characteristic klimata na territorii Central'noi Azii. [Spatial extrapolation and variability of climatic characteristics on the territory of Central Asia]. Izvestiya Akademii Nauk, Seriya Geographicheskaya. [News of Russian Academy of Science; Ser. Geography], N5, pp. 97-106 (Russ)

Kotlyakov, V. M. (Ed.). (1997). World Atlas of Snow and Ice Resources. Moscow.

Narama, C., Kääb, A., Duishonakunov, M., & Abdrakhmatov, K. (2010). Spatial variability of recent glacier area changes in the Tien Shan Mountains, Central Asia, using Corona

(~1970), Landsat (~2000), and ALOS (~2007) satellite data. Global and Planetary Change, 71(1-2), 42–54. http://doi.org/10.1016/j.gloplacha.2009.08.002

Panagiotopoulos, F., Shahgedanova, M., Hannachi, A., Stephenson, D.B., 2005. Observed trends and teleconnections of the Siberian High: a recently declining center of action. Journal of climate 18, 1411–1422.

Pepin, N. C., & Lundquist, J. D. (2008). Temperature trends at high elevations: Patterns across the globe. Geophysical Research Letters, 35(14), L14701. http://doi.org/10.1029/2008GL034026

Peterson, T.C., and R.S. Vose, 1997: An overview of the Global Historical Climatology Network temperature database. Bull. Amer. Meteor. Soc., 78 (12), 2837-2849

Qian, W., Tang, X. & Quan, L. (2004). Regional characteristics of dust storms in China. Atmospheric Environment, 38(29), 4895–4907. http://doi.org/10.1016/j.atmosenv.2004.05.038

Rangwala, I., & Miller, J. R. (2012). Climate change in mountains: A review of elevation-dependent warming and its possible causes. Climatic Change, 114(3-4), 527–547. http://doi.org/10.1007/s10584-012-0419-3

Shibuo, Y., Jarsjö, J., & Destouni, G. (2007). Hydrological responses to climate change and irrigation in the Aral Sea drainage basin. Geophysical Research Letters, 34(21), 1–5. http://doi.org/10.1029/2007GL031465

Siegfried, T., Bernauer, T., Guiennet, R., Sellars, S., Robertson, A. W., Mankin, J., … Yakovlev, A. (2012). Will climate change exacerbate water stress in Central Asia? Climatic Change, 112, 881–899. http://doi.org/10.1007/s10584-011-0253-z

Storch, H. von, & Zwiers, F. W. (2002). Statistical Analysis in Climate Research. Cambridge University Press. Retrieved from http://www.amazon.com/Statistical-Analysis-Climate-Research-Storch/dp/0521012309

Sun, J., Zhang, M., & Liu, T. (2001). Spatial and temporal characteristics of dust storms in China and its surrounding regions, 1960–1999: Relations to source area and climate. Journal of Geophysical Research, 106(D10), 10325. http://doi.org/10.1029/2000JD900665

Taft, R. L. (1970), "Name Search Techniques", Albany, New York: New York State Identification and Intelligence System

Trenberth, K. E., & Josey, S. A. (2007). Observations: surface and atmospheric climate change. In: Climate Change 2007: The Physical Science Basis. Contribution of Working Group I to the Fourth Assessment Report of the Intergovernmental Panel on Climate Change, 164(236 - 336), 235–336. http://doi.org/10.5194/cp-6-379-2010

Tóth, B., Lillo, F., & Farmer, J. D. (2010). Segmentation algorithm for non-stationary compound Poisson processes. The European Physical Journal B, 78(2), 235–243. http://doi.org/10.1140/epjb/e2010-10046-8

Unger-Shayesteh, K., Vorogushyn, S., Farinotti, D., Gafurov, A., Duethmann, D., Mandychev, A., & Merz, B. (2013). What do we know about past changes in the water cycle of Central Asian headwaters? A review. Global and Planetary Change, 110, 4–25. http://doi.org/10.1016/j.gloplacha.2013.02.004

Williams, M.W. and V.G. Konovalov. 2008. *Central Asia Temperature and Precipitation Data, 1879-2003,* Boulder, Colorado: USA National Snow and Ice Data Center. http://dx.doi.org/10.7265/N5NK3BZ8

WMO. (2003). Global Cryosphere Warch (GCW) Implementation Plan. World Meteorological Organization Report (Vol. 6). Retrieved from http://scholar.google.com/scholar?hl=en&btnG=Search&q=intitle:World+meteorological+organization+global+atmosphere+watch#4

Xu, Q., 2001: Abrupt change of the mid-summer climate in central East China by the influence of atmospheric pollution. Atmos Environ 35:5029–5040

Yatagai, A., and T. Yasunari, 1994: Trends and decadal-scale fluctuations of surface air temperature and precipitation over China and Mongolia during the recent 40 year period (1951–1990). J. Meteor. Soc. Japan, 72, 937–957

Zhang, X., Lu, C., & Guan, Z. (2012). Weakened cyclones, intensified anticyclones and recent extreme cold winter weather events in Eurasia. Environmental Research Letters, 7(4), 44044. http://doi.org/10.1088/1748-9326/7/4/044044

Chapter 3 Constructing a long-term snow cover extent dataset from AVHRR and MODIS data for central Asia from 1986 to 2008

1 Introduction

Seasonal snow cover is one of the most important land surface components which influence surface energy balance (**Walsh et al., 1985; Kumar, 1988; Barnett et al., 1989; Marks and Dozier, 1992; Groisman et al., 1994; Aizen et al., 2000, 2002; Bednorz, 2004; Gong, 2004; Armstrong and Brun, 2010**) and hydrological budget (**Willmott et al., 1985; Dozier, 1987; Soulsby et al., 1997; Lettenmaier et al., 1999; Verbunt et al., 2003; Bales et al., 2006**). The varying extent and amount of seasonal snow cover modify the surface energy balance mainly via its high albedo (**Kukla and Kukla, 1974; Robinson and Kukla, 1985; Robinson et al., 1986**). Furthermore, the snow melting process consumes a large amount of energy and is known to be a factor delaying atmosphere heating (**Aizen et al., 2000**). Seasonal snow cover is also a major water resource in arid/semi-arid regions. More than one-sixth of world population relies on seasonal snow and glacier melt water for water supply (**Barnett et al., 2005**). Snow melt contributes up to 60% of river runoff in central Asia (CA) river basins **(Aizen and Aizen, 1995; Aizen et al., 1996**). Decrease in seasonal snow cover area is one of the major consequences of CA climate change, which may contribute negatively to the developing economies of new central Asian countries (**Lioubimtseva and Henebry, 2009**). Because of its complex effect on land surface energy and water balance, seasonal snow cover is one of the most important components in various climatological **(Brown, 2000; Dye, 2002; Bamzai, 2003; Wang et al., 2005; Armstrong and Brun, 2010**) and hydrological applications (**Tekeli et al., 2005; Parajka and Bloschl, 2008; Seidel and Martinec, 2010; Bavera et al., 2011**).

The traditional way to quantify seasonal snow is to monitor snow characteristics manually in a network (i.e. snow surveys along of snow courses) of ground based meteorological stations. Snow survey can provide accurate information about seasonal snow cover, but the spatial scale of this information is constrained. In many parts of the world, the sparse network of meteorological stations cannot provide enough data to generate long-term snow datasets over large areas. Optical remote sensing is one of the alternatives for extracting snow cover information. Since ice is highly reflective in visible band and moderately absorptive in the near-infrared band **(Warren, 1982; Crane & Anderson, 1984; Dozier, 1989**), pixels with pure snow tend to have high reflectance in the visible band; low reflectance in the near-infrared band; low brightness temperature in the far-infrared band. For pixels with partial snow, the spectral characteristics also depend on the properties of other objects within the pixel (**Painter et al., 2009**). Compared with traditional ground snow survey, areal observation of snow cover extent over a large area can be easily obtained from optical remote sensing data. Currently a variety of optical satellite sensors are available for regional to continental scale snow monitoring, which includes the Advanced Very High Resolution Radiometer (AVHRR) (**Ramsay, 1998**), Moderate Resolution Imaging Spectroradiometer (MODIS) **(Hall et al., 2001; Hall et al., 2002**), Geostationary Operational Environmental Satellites (GEOS) (Romanov et al., 2000; Romanov, 2003), SPOT VEGETATION (**Xiao et al., 2002**) and Medium Resolution Imaging Spectrometer (MERIS) (**Malcher et al., 2003**).

Until now there has been no long term high resolution areal snow cover data available in CA, despite the large archive of historical AVHRR data over this region since the 1980s. Snow cover data derived from historical satellite images might not be comparable with the snow product derived from the relatively new MODIS sensors. The aim of this study is to

produce an accurate long-term continuous (or near continuous) snow cover dataset with high spatial resolution (1 km) in the form of daily snow cover and 8-day maximum snow cover from historical AVHRR and MODIS satellite images for central Asia. Such a dataset with its long temporal coverage, large spatial coverage, and internal comparability, will accurately demonstrate the variability of seasonal snow cover in central Asia, and contribute to the climatological study and hydrological modeling work.

2 Research Area

In this study Amu Dar'ya River basin (**Figure 3.01**) within central Asia (CA) was selected as the place for validating snow cover product, and evaluating the ability of the snow product to provide information about spatial and temporal variation of snow cover extent. The total length of Amu Dar'ya River is about 2400 km, and the drainage basin totals about 950, 000 km^2. The Amu Dar'ya River and its major tributaries originate in the Pamir Mountains and flow through Tajikistan valleys, and Turkmenistan and Uzbekistan deserts to meet the Aral Sea. The Amu Dar'ya River Basin's main terrain type is plains (60% area of the basin) with elevation lower than 1000 m. The high mountainous regions with elevation greater than 3000m cover about 15% of the area. Major land cover types within the Amu Dar'ya River Basin are shrubland (48.48%), bare ground (23.26%), and grassland (18.52%); while cropland is 6.89%, urban built 0.25%, and forest only 0.003% (**Table 3.1**), based on University of Maryland (UMD) Land Cover Classification data (**Hansen et al., 1998, 2000**).

3 Data Sources

In this study, all 1 km AVHRR Local Area Coverage (LAC) and High Resolution Picture Transmission (HRPT) data have been collected in the raw Level1b format (**NOAA, 1998, 2007**) over central Asia via NOAA Comprehensive Large Array-data Stewardship System (CLASS) (http://www.class.ncdc.noaa.gov/) from the 1980s to 2008 (**Figure 3.02**). MODIS Terra daily and 8-day snow cover product (MOD10A1v5 and MOD10A2v5 respectively) over central Asia between 2000 and 2009 has been obtained from the National Snow and Ice Data Center (NSIDC) (http://nsidc.org/data/modis/). MODIS tiles used in this study include h21v3 to h24v3, h21v4 to h25v4, h22v5 to h25v5 (**Figure 3.01**).

Auxiliary data utilized by this study include Digital Elevation Model (DEM), reanalysis climate data, snow survey data, and land cover information. Topography in this research region was described by DEM downloaded from the Consultative Group on International Agricultural Research (CGIAR) (http://srtm.csi.cgiar.org/). The DEM has been resampled to 500 m and 1 km resolution, to be used in the processing of AVHRR and MODIS images. Monthly surface temperatures from NCEP reanalysis data have been collected from NOAA Earth System Research Laboratory (ESRL) (http://www.esrl.noaa.gov/), and employed as auxiliary data in the snow identification process of AVHRR images.

Snow survey data in the Former Soviet Union were obtained from the NSIDC **(Krenke, 1998**) and used to assess the accuracy of snow identification results in daily composite AVHRR data. The University of Maryland (UMD) Land Cover Classification data at 1 km resolution (**Hansen et al., 1998, 2000**), derived from AVHRR satellite images between 1981 and 1994, was also obtained for analyzing the effect of land cover type on the accuracy of snow detection.

4 Methodology

In processing AVHRR and MODIS data, all images were projected into the Albers central Asia coordinate system, of which the parameters are shown in **Table 3.2**. The general steps are illustrated in **Figure 3.03**.

4.1 AVHRR Data Processing

4.1.1 Data Preprocessing

The Specialized AVHRR Processing System (SAPS), which is a generalized version of the Canadian AVHRR Processing System (CAPS) (**Khlopenkov et al., 2010**) was used to import AVHRR Level1b images, conduct data calibration, perform georeferencing and generate daily composites. The SAPS software builds scan line specific calibration parameters based on quality control flags and internal calibration data in the file head, and performs calibration over the visible, near-infrared and shortwave infrared bands using a time dependent piecewise linear calibration method, and over the thermal bands with nonlinear corrections, which ensures long term radiometric consistency of the AVHRR image series. The SAPS software employs a two-step process of image georeferencing to achieve high geometric accuracy **(Khlopenkov and Trishchenko, 2010**). The first step is the basic geometric correction using an orbit model initialized with the most appropriate ephemeris data. The second step is a digital image matching procedure to account for systematic shifts and errors. A correlation surface was calculated between AVHRR imagery and reference image chips, from which GCPs were found and used to build a second order polynomial to adjust the image. Such a procedure ensures a high success rate of geometrically well corrected scenes.

After calibration and geometric correction, AVHRR images were made into daily composites following the criteria of maximum NDVI, minimum value at visible band, least cloudiness condition and limited view zenith. To assess the cloudiness in each pixel, SAPS applied the SPARC pixel-scene identification algorithm (**Khlopenkov and Trishchenko, 2007**) on each AVHRR image, providing mask files of cloudiness, snow and water. The final baseline products came from AVHRR preprocessing include daily composite top-of-atmosphere (TOA) visible and near infrared reflectance, TOA band 4 and 5 temperature brightness, cloudiness rating and binary mask files of snow and water.

4.1.2 Snow Cover Identification

A new aggregated membership rating scheme has been designed for accurately detecting snow from AVHRR images. The general framework of the snow identification scheme is depicted in **Figure 3.04**. In the beginning, all pixels are initialized as undecided. Then a series of membership tests are performed on each pixel for the three possible pixel types (snow, nonsnow and cloud). Each test is implemented as a membership function, which gives a membership rating for the specific pixel type being tested based on AVHRR spectral bands and auxiliary data. The membership rating ranges from 0 to 1, indicating the likeliness of a pixel belonging to one specific pixel type. Details for each membership function are described later in this section. For each possible pixel type, ratings from different tests are combined using a geometric average to create an aggregated membership rating. After the calculation of aggregated membership ratings for snow/nonsnow/cloud, those aggregated ratings are compared and the pixel type of the maximum rating is chosen as the type for that pixel. Pixels having same rating values for snow/nonsnow/cloud remained as undecided. In the last step, the intermediary result is combined with the water mask and nodata mask files

provided by SAPS to generate the final result. The coding scheme (**Table 3.3**) used for the result images is same as the one used by MODIS snow cover product.

The parameters used in the snow/nonsnow/cloud membership tests were tuned manually against visually interpreted snow cover from AVHRR data in 1996, as it is a year with abundant data generated by different types of AVHRR sensors (**Figure 3.02**). All the values of those parameters are reported in **Table 3.4**.

Snow membership tests module

The snow membership tests module consists of five membership tests, as shown in Figure 3.5. Each membership test provides a membership rating based on a designated function with specific spectral band information and auxiliary data as input. The sinusoidal function **(Burrough and McDonell, 1998**) has been utilized as the basic functional form for constructing membership tests. The shape of the sinusoidal function (**Figure 3.06**) is adjusted by changing the controlling parameters to fit the shape of snow probability function (snow probability vs. spectral band or function of spectral bands).

The first membership test in the snow module is built on AVHRR Band1 reflectance. It makes use of the snow's property of high reflectivity in visible band. The sinusoidal function used in this test is defined as:

$$R(z) = \begin{cases} \frac{1}{1+\left(\frac{z-b_1-d_1}{d_1}\right)^2}, & z < b_1 + d_1 \\ 1, & z \geq b_1 + d_1 \end{cases}, \qquad \textbf{Equation 3.1}$$

where R(z) is the result rating, z is the input data, b_1 and d_1 are the parameters controlling shape of the sinusoidal function. The left side of the curve of the function is an upward slope

where the rating goes up to 1 with increasing z, while the right side is a constant line of rating at 1 (**Figure 3.06-a**). The parameter b_1 is the z value of middle point of the slope, while d_1 is the half of the width of the left side slope. Such kind of sinusoidal function can be referred to as left-side-sinusoidal, and a similar function form is also used in some other membership tests which will be described later.

The second membership test is based on the AVHRR NDSI, which is defined as:

$$\mathrm{NDSI_{AVHRR}} = \frac{\mathrm{Band1-Band3a}}{\mathrm{Band1+Band3a}}. \qquad \textbf{Equation 3.2}$$

The left-side-sinusoidal function is employed in the test (**Figure 3.06-b**).

The third membership test examines the AVHRR Band3b and Band1 reflectance ratio. The sinusoidal function is defined as:

$$R(z) = \begin{cases} 1, \ z \leq \ b_2 - d_2 \\ \frac{1}{1+\left(\frac{z-b_2+d_2}{d_2}\right)^2}, \ z > b_2 - d_2 \end{cases}, \qquad \textbf{Equation 3.3}$$

where R(z) is the result rating, z is the input data, b_2 and d_2 are the parameters controlling shape of the sinusoidal function. The left side of the function curve is a constant line at 1, while the right side is a downward slope where the rating goes down from 1 with increasing z (**Figure 3.06-c**). The parameter b_2 is the z value of middle point of the slope, while d_2 is the half of the width of the right side slope. Such kind of functions was referred to as right-side-sinusoidal, and a similar function form is also used in some other membership tests.

In the third test, the parameters (b_2, d_2) are calculated as the result of two sine functions to allow parameter fluctuations in different months. The sine functions take the form:

$$p(m) = A\sin\left(\frac{\pi\, m}{13}\right) + B, \qquad \textbf{Equation 3.4}$$

where p(m) is the value of parameter (b_2 or d_2), m is the month (1 to 12), and A and B are parameters for controlling the sine function. Notice that each AVHRR image can only have either Band3a or Band3b, so for a single image only one of the test2 and test3 is performed.

The fourth membership test examines the AVHRR Band4 Brightness Temperature, with information from monthly surface temperature from the NCEP reanalysis dataset. The sinusoidal function used in this test is defined as:

$$R(z) = \begin{cases} \frac{1}{1+(\frac{z-b_1-d_1}{d_1})^2}, z < b_1 + d_1 \\ 1, b_1 + d_1 \le z \le b_2 - d_2 \\ \frac{1}{1+\left(\frac{z-b_2+d_2}{d_2}\right)^2}, z > b_2 - d_2 \end{cases}, \qquad \textbf{Equation 3.5}$$

where R(z) is the result rating, z is the input data, b_1, b_2, d_1, and d_2 are the parameters controlling shape of the sinusoidal function. The curve of the sinusoidal function has an upward slope on the left, a constant line in the middle and a downward slope on the right side (**Figure 3.06-d**). The parameters b_1 and d_1 control the shape of the upward slope, while b_2 and d_2 determine the shape of the downward slope. In this test, the parameter b_1 is the corresponding monthly surface temperature in Kelvin minus 20K, and b_2 is calculated as a sine function, which has the same form as **Equation 3.4**.

Besides these four tests, the snow mask provided by SAPS using SPARC algorithm has also been incorporated in the fifth test. The function form used to transform the binary snow mask file to a rating is defined as:

$$R(z) = (r_1 - r_2)z + r_2 \qquad \textbf{Equation 3.6}$$

where R(z) is the result rating, z is the snow mask file in which 1 stands for snow and 0 stands for nonsnow, r_1 and r_2 are parameters used, which are precision and commission error rate of the snow mask provided by SAPS, respectively.

Nonsnow membership tests module

There are also five membership tests in the nonsnow membership tests module, each corresponding to one membership tests in the snow membership tests module with same input data, to give ratings of likeliness to nonsnow for each pixel. The first one is the membership test based on AVHRR Band1 reflectance, which makes use of a right-side-sinusoidal function (**Figure 3.06-a**). The second test employed a left-side-sinusoidal function to give a rating based on AVHRR NDSI (**Figure 3.06-b**). The third test, which examines the AVHRR Band3b and Band1 reflectance ratio, is relied on a left-side-sinusoidal function (**Figure 3.06-c**), with its parameters b_1 and d_1 determined from sine functions in the same form as **Equation 3.4**. In the fourth test, the AVHRR Band4 Brightness Temperature data is examined by a left-side-sinusoidal function (**Figure 3.06-d**). The last test, which incorporates the snow mask file into the scheme, uses the same function form as **Equation 3.6**, but with different parameters r_1 and r_2 as the commission error rate and precision of the nonsnow class determined by SAPS snow mask, respectively.

Cloud membership tests module

Currently, the cloud test module is solely based on the cloudiness file generated by SAPS scene identification procedure, which is already a membership rating for cloud. A simple linear function is used to transform the cloudiness from its original value range (0 - 255) to the new value range (0 - 1), thus incorporating the existing knowledge of cloud into the snow identification scheme.

Visual comparisons between snow cover generated by the membership rating scheme and the SPARC algorithm (**Figure 3.07**) showed that the membership rating scheme fixed several problems exists in the SPARC algorithm when used in CA, including false cloud or snow detection at high reflective desert area (ellipse 1 and 3 in **Figure 3.07-a**) and misclassification of desiccated salt lake bottom as snow (ellipse 2 in **Figure 3.07-a**). The snow cover from membership rating scheme also has less omission error compared with SPARC snow in mountainous regions in summer time (**Figure 3.07-b**). More details about the accuracy of snow identification are discussed in Sections 5.1 to 5.3.

4.1.3 Maximum Snow Cover Composition and Cloud / Gap Removal

Daily AVHRR snow cover was composited into 8-day maximum-snow-extent data, and then further processed by a four step cloud removal algorithm to create cloud / gap free snow cover product. Details of the algorithm will be described in the next section. The end products of AVHRR processing include daily AVHRR snow cover, and 8-day AVHRR cloud / gap free snow cover.

4.2 MODIS Data Processing

All daily (MOD10A1) and 8-day (MOD10A2) MODIS snow cover data were first imported from original HDF format to TIFF format, reprojected to the Albers central Asia coordinate system and then mosaiced and clipped to the extent of the research area using MRT Toolkit (**Land Processes DAAC and USGS EROS Center, 2002**).

The 8-day MODIS maximum-snow-extent data was further processed into a cloud / gap free snow cover using a four step cloud removal algorithm modified from the methodology proposed by (**Gafurov and Bárdossy, 2009**).

(1) The first step is a spatial filter based on regional snow transition elevation. The basic idea is to find the regional minimum snow elevation, which is the lowest elevation where snow pixel exists; and the regional maximum snow elevation, which is the highest elevation above which all pixels are snow covered, or cloud obscured / data gap. Then cloud / gap pixels above the maximum snow elevation are marked as snow, and those pixels below the minimum snow elevation as non-snow.

(2) The cloud / gap pixels survived the first step will go through another spatial filter step, which is based on snow cover information in neighboring pixels. Each cloud or gap pixel will be examined and if any one of its four direct neighbors were covered by snow, it would be set as snow pixel.

(3) The third step makes use of elevation and snow cover information in eight neighboring pixels. Each cloud or gap pixel will be tested and assigned as snow covered, if any of its eight neighboring pixels were covered by snow with an elevation lower than the central cloud / gap pixel.

(4) The last step is a temporal filter based on time series analysis of snow cover series in each pixel. The start day of snow accumulation and the end day of snow melt are found for each pixel in each year from the time series analysis. The time period between these two days in the same year is defined as the snow season for the pixel, while the time period between the end of snow melt and the start of snow accumulation in the next year is defined as the nonsnow season. Then cloud obscured or data gap pixels were marked as snow or non-snow depend on whether it falls in the snow season or nonsnow season.

4.3 Correction of 8-day Cloud / Gap Free AVHRR Snow

The 8-day AVHRR cloud/gap free snow cover data were further processed to generate a corrected 8-day AVHRR snow cover which can be used to calculate snow cover statistics that are comparable to those calculated from MODIS data. In this study, we conduct the correction procedure over Amu Dar'ya Basin. 8-day AVHRR and MODIS cloud/gap free snow in the year 2003 to 2007 were used as training data set for building correction functions and providing auxiliary data for the correction procedure.

There are two basic assumptions for designing the correction method. The first one is that the relationship between Snow Cover Area Percentage (SCAP) calculated from AVHRR and MODIS data can be well described by a linear function. Thus, a corrected AVHRR SCAP, which is comparable to the MODIS SCAP can be calculated from the linear function. The second one is that the relative spatial structure of snow distribution within one specific small region is determined by the interaction between synoptic systems, topography effects and underlying vegetation, and such relative spatial snow distribution pattern is stable and can be described by a probability of snow map. With the knowledge of corrected SCAP in each

small region, a critical value that can be used to distinguish snow and nonsnow can be found in the long term probability of snow map.

The segmentation of research region into small sub-regions is the very basis for the correction. The Amu Dar'ya Basin was first divided into 6 climatic regions, which are southern Pamir, eastern Pamir, central Pamir, western Pamir, Pamiro-Alai and Plain (**Figure 3.08-a**), based on our understanding of climatic regimes and synoptic systems in this region (**Chapter 1**). Then each climatic region was segmented into Elementary Hillslope Areas (EHA) **(Francke et al., 2008**) using GRASS 'r.watershed' tool as a series of half watershed **(GRASS Development Team, 2009**). The main parameter used in the process of creating EHAs is the minimal size of EHA. After several tests, different values have been chosen for different climatic regions. In eastern Pamir and western Pamir, the minimal EHA size was set to be 3000 km^2, while in southern Pamir, central Pamir and Pamiro-Alai it was set to be 2000 km^2, and in the climatic region of Plains, the value was 10, 000 km^2.

(1) Segmentation of the research region into EHAs.

(2) Calculate SCAP from both MODIS and AVHRR 8-day cloud/gap free snow data for each EHA.

(3) Build regression functions for each EHA as specified by the following formula:

$$SCAP_{MODIS} = a * SCAP_{AVHRR} + b * SCAP_{longterm} + c * SCAP_{AVHRR} * SCAP_{longterm} + d$$

Equation 3.7

where a, b, c and d are the parameters to be estimated; $SCAP_{longterm}$ is the long term average AVHRR SCAP for this 8-day period.

(4) Calculate a corrected SCAP, and then a corrected snow cover area (SCA) by using the regression function constructed in step 3 in each EHA

(5) For each 8-day period, calculate the long term probability of snow for each pixel using all available AVHRR data in this 8-day period

(6) For each EHA, find the critical value of long term probability of snow which meets the following requirement that the area of pixels with probability of snow greater than the critical value equals the corrected SCA.

$$\mathrm{Area}_{P_{snow}>P_{critical}} = \mathrm{SCA}_{corrected} \qquad \textbf{Equation 3.8}$$

(7) In each EHA, mark all pixels with snow probability greater than the $P_{critical}$ as snow, while others as nonsnow.

In order to assess the validity of the linear models, F-tests have been done for each linear model, and t-tests have been conducted for parameters in each model. The results suggested that in the test site of Amu Dar'ya Basin, all of them are significant. Further analysis of performances of the linear models at each EHA (**Figure 3.08-b**) shows that large portion of the models have an adjusted R-square greater than 0.90, especially for models in Western Pamir and Pamiro-Alai, with adjusted R-squares greater than 0.95. In very steep EHAs in Eastern Pamir, or very flat EHAs in Plains, the adjusted R-squares are relatively low, but still higher than 0.8. There is only one model with adjusted R-square lower than 0.8, which located in the middle of the climatic region of Plains.

5 Validation

In this section, confusion matrix and related performance measures (**Table 3.5**) were used to evaluate the accuracy of the AHVRR snow data.

5.1 Comparison of daily AVHRR snow cover with ground snow measurement

The daily AVHRR snow cover were compared with ground snow measurement data in the Former Soviet Union (FSU) and Russian Federation obtained from NSIDC (**Krenke, 1998**). The measurements were conducted by personnel in more than 1345 stations, with 361 stations within the extent of the CA as we defined. Variables in this dataset include the longitude and latitude for each station, snow cover type, degree of snow coverage, snow depth, snow density, and snow cover features. The snow depth measurements were carried out at the station with a fixed snow measuring rod, or in snow survey routes which is less than 5 km away from the station using a portable snow measuring rod. All data records for these 361 stations in the time period between 1987 and 1996 have been extracted for the comparison. One problem exists in using the data is that the snow measurements were only conducted in the snow season, or in another word, there is no 'nonsnow' record in the dataset. So only a result of the Probability of Detection (POD) of snow identification can be derived here.

To relate the point snow measurement data conducted at station or snow route with daily AVHRR snow cover, a 5 by 5 rectangle centered at the point where the measurement was carried out was made for each ground snow record. If all AVHRR snow cover pixels are 'nodata', then the record was marked as 'nodata by AVHRR' and excluded from the comparison; if any of the 25 AVHRR pixels are 'snow', then we marked the record as 'snow by AVHRR'; if the majority of the 25 pixels are 'cloud', then the record was marked as 'cloud by AVHRR'; under all other situations, the record was noted as 'nonsnow by AVHRR'. The

result of the comparison is presented in **Table 3.6**. The POD for snow of the daily AVHRR snow cover is 88.18%. It is understandable that with decreasing snow depth, the accuracy of snow mapping using optical remote sensing data goes down (**Wang et al., 2009**). The POD when snow depth is less than 3cm is 65.31%, while the value is 91.13% when the depth is greater than 3cm. Most of the missed snow cases happened in the low snow depth situation.

5.2 Comparison of snow cover from different AVHRR sensors in the same date

The daily AVHRR snow cover provide information in a long time period from 1986 to 2008 making use of AVHRR images acquired by different sensors from the NOAA6 in 1986 to NOAA18 in 2008. Comparisons of snow cover from different AVHRR sensors were conducted to make sure that the snow identification scheme works consistently for data from different AVHRR sensors

To conduct such comparison, AVHRR swaths acquired in the same date but from different sensors were matched into images pairs if they are overlapped geographically. Then pairs, which meet the following criterion, were extracted for the comparison:

1. There are more than 500, 000 overlapped pixels with view zenith less than 55° between the two swaths.
2. The percentages of snow from both swaths are greater than 10%.
3. The percentages of land from both swaths are greater than 10%.

Such criteria were designed to reduce the need for computational resources, and avoid the imbalance problems in calculating confusion matrix (**Cohen, 1960**). The results of general accuracy, omission rate, commission rate for snow and kappa coefficient were reported in Table 3.7. Notice that there are no pairs for the comparison between NOAA6 and NOAA9.

And for the cases of NOAA9 vs NOAA11 and NOAA14 vs NOAA15, there are no pairs meet the above requirements.

The general accuracy for the comparisons of different sensor pairs are always greater than 90.29%, with the highest value of 95.66% in the sensor pair of NOAA12 vs NOAA14. The kappa coefficients are all greater than 0.80, with the highest one 0.91 also for the sensor pair of NOAA12 vs NOAA14. The empirical explanation of Kappa coefficient suggest that a kappa value greater than 0.8 can be interpreted as 'almost perfect agreement (**Cohen, 1960**).This suggests that the snow identification scheme performs similar with data came from different AVHRR sensors, but the consistency is in a slightly higher level for the sensor pair NOAA12 and NOAA14. This is understandable since the parameters used in the snow identification scheme were manually tuned against visually interpreted snow cover in 1996 from AVHRR images acquired by NOAA12 or NOAA14.

5.3 Comparison between daily AVHRR and MODIS snow cover

The Amu Dar'ya Basin within the CA region was selected as the validation site for conducting the relative validation of daily AVHRR snow cover against daily MODIS snow cover. Daily MODIS and AVHRR snow cover data in 2003 were used in the validation.

In order to link MODIS snow cover with AVHRR snow cover, the daily MODIS and AVHRR snow cover were aligned to make 4 MODIS pixels corresponding to 1 AVHRR pixel exactly, since the pixel resolution for MODIS snow cover is 500 m, while that for AVHRR is 1000 m. Then the MODIS snow cover data were aggregated into 1000 m resolution by the following method.

1. Calculate the area percentage of each pixel type within the new 1km pixel using the information from the four 500 m pixels
2. Sort the pixel types by the area percentages from low to high
3. Remove 'nodata' and 'not decided' from the sorted list of pixel types
4. If the new list of pixel types is empty, then set the new 1 km pixel as 'nodata'.
5. Remove 'cloud' from the sorted list of pixel type
6. If the new list of pixel types is empty, then set the new 1km pixel as 'cloud'.
7. If there is only one pixel type in the remaining list with the largest area percentage then set the new 1 km pixel to that type.
8. Extract the pixel types that have the largest value of area percentage, set the new pixel by the priority rule: snow > land > snow covered lake ice > lake.

The confusion matrix for the comparison in the Amu Dar'ya Basin has been calculated. The confusion matrices and related accuracy statistics were also calculated to analyze the effects of climatic regions, altitudinal belts, aspect class, slope class, and land cover on the accuracy of the daily AVHRR snow cover (**Figure 3.09**).

The general accuracy for the comparison in the Amu Dar'ya Basin is 98.51%, with a kappa coefficient of 0.89, which suggests a nearly perfect agreement between daily MODIS and AVHRR snow cover. The omission rate for snow is 16.38%, while the commission rate for snow is 3.88%. This means that the daily AVHRR snow cover might systematically underestimate the snow cover, compared with snow data from MODIS.

In the Plain areas within the Amu Dar'ya Basin, the daily AVHRR snow cover performs very well, with a general accuracy at 99.60%, and a kappa coefficient of 0.92. In

other climatic regions, such as southern Pamir, eastern Pamir, western Pamir and Pamiro-Alai, the general accuracies are at about 92% and the kappa coefficients are about 0.80. The central Pamir has the lowest values for the general accuracy and kappa coefficient, which are 86.38% and 0.71 respectively.

From the accuracy statistics calculated for different altitudinal belts, the accuracy decreases with increasing elevation. The highest values for the general accuracy and kappa coefficient are 99.88% and 0.91, in areas with elevation less than 1000 m, while the lowest values are 89.15% and 0.78 in areas with elevation higher than 4000 m.

The Amu Dar’ya Basin was divided into 8 aspect classes and 10 slope classes. For all aspect classes, the general accuracies are all at about 98% and the kappa coefficients are at about 0.88, which indicates that the aspect has no significant effect on the accuracy of the snow detection scheme. From the result calculated for different slope classes, both of the general accuracy and the kappa coefficient goes down with the slope increases. The general accuracy falls down from 99.87% in the slope class of 0° to 1.21° to 87.85% for the steep slope class 30.12° to 52°, while the kappa coefficient decreases from more than 0.92 to 0.71. Most of the error comes from failing detection of snow. The omission rates for regions with slope steeper than 13.75° are much higher than the omission rate for the Amu Dar’ya Basin.

The accuracy of the daily AVHRR snow cover in different land cover type zones was analyzed using the land cover type information obtained from UMD Land Cover Classification data at 1km resolution. The 'Evergreen Needleleaf Forest', 'Evergreen Broadleaf Forest', 'Deciduous Needleleaf Forest' and 'Mixed Forest' in the original UMD land cover data have been grouped into a common 'Forest' type. And similarly, the 'Woodland' and 'Wooded

Grassland' have been transformed into 'Woodland', while 'Shrubland' and 'Closed Shrubland' were marked as 'Shrubland'. Other land cover types addressed in the comparison are 'Grassland', 'Cropland', 'Bare ground' and 'Urban and Built'. In the major land cover type zones (Shrubland, Grassland, Cropland and Bare ground), of which the total area is more than 99% of the area in the Amu Dar'ya Basin, the daily AVHRR snow cover provided nearly same snow information as the daily MODIS snow. The general accuracies are all above 97% and the kappa coefficients are all higher than 0.88. For other land cover types, the daily AVHRR snow data did not perform so well. In the land cover types 'Woodland' and 'Urban and Built', the kappa coefficients are 0.73 and 0.78, respectively. The omission rates for these two land cover types, which are 34.83% and 35.37 respectively, are much higher than the value for the whole Amu Dar'ya Basin. The worst case happened in the land cover type zone of 'Forest'. The general accuracy for this zone is 86.50%, and the kappa coefficient is 0.60, due to a high omission rate at 48.47%.

Thus, in the validation site of Amu Dar'ya Basin, the daily AVHRR snow cover provided very high agreement with daily MODIS snow cover, with a slightly underestimation of snow. Part of the underestimation might come from the way the MODIS and AVHRR data were linked. For places covered by forest, the daily AVHRR snow cover significantly underestimated the snow occurrence. Fortunately, forest is not a major land cover type in the Amu Dar'ya Basin (less than 0.004% in area) and central Asia, this problem does not damage the credibility of this data.

5.4 Comparison of Corrected AVHRR Snow vs. 8-day Cloud/Gap Filled MODIS Snow

The comparison between corrected 8-day AVHRR Snow against 8-day MODIS cloud/gap free snow cover was conducted in the Amu Dar'ya Basin, using data in 2002 and 2003. Two different types of comparison have been done. The first one is a pixel-to-pixel comparison, which has been done in a similar way as the comparison between daily AVHRR and MODIS snow cover. Statistics like general accuracy, omission / commission rate for snow and kappa coefficient were calculated in this kind of comparison. Another one is the comparison between AVHRR and MODIS Snow Cover Area Percentage (SCAP) time series. The Pearson's R between the AVHRR and MODIS SCAP time series were calculated to assess the comparability of the two dataset. These two types of comparisons have been conducted for the Amu Dar'ya Basin, climatic regions and altitudinal belts within the basin, different aspect classes and slope classes, and land cover type zones (**Figure 3.10**).

The general accuracy, calculated for the Amu Dar'ya Basin, is 95.61%, with an omission rate of 11.09% and commission rate of 16.07%. The kappa coefficient is 0.84, while the Pearson's R between the two SCAP time series is 0.99, which suggest good overall performance of the corrected 8-day AVHRR snow cover in the validation site. The SCAP time series calculated from corrected 8-day AVHRR snow cover can provide nearly same information about the evolution of snow cover as the MODIS data.

The examinations of the accuracy of corrected 8-day AVHRR snow cover in different climatic regions, altitudinal belts slope classes and aspect classes suggest that under most circumstances the accuracies are in a similar level as the accuracy statistics calculated for the whole Amu Dar'ya Basin. In very high and steep regions or low and flat zones, the accuracy

represented by general accuracy and kappa coefficient is relatively lower. For example, in the climatic region of Plains (low and flat), the kappa coefficient is 0.76; and the kappa coefficients for eastern and central Pamir (high and steep) are 0.75 and 0.78 respectively; while the kappa coefficients for southern Pamir, western Pamir and Pamiro-Alai are always greater than 0.82. The aspect class has no significant effect on the accuracy of the corrected 8-day AVHRR snow cover. The values of Pearson's R calculated for different comparison regions are all greater than 0.96, with most cases larger than 0.99.

The accuracy of the corrected 8-day AVHRR snow cover in different land cover type zones has also been analyzed. The results suggest that the performance is sufficient for most land cover types. For the land cover type Woodland, Shrubland, Grassland, Cropland and Bare Ground, the values of general accuracy are greater than 93%, and the values of kappa coefficient are greater than 0.79. In the Forest land cove zone where the daily AVHRR snow cover does not perform well (kappa coefficient equals to 0.60), the 8-day corrected AVHRR snow cover show a significant improvement with a kappa coefficient of 0.89. Problems exist for the land cover type Urban and Built, with kappa coefficient at 0.63, and a high commission rate of 46.05%. That is caused by the fact that most Urban and Built areas are located in low elevation flat zones with sporadic snow, which does not fit in the assumption of the correction method quite well. Since only 0.255% of the Amu Dar’ya Basin in area is Urban and Built, this problem will not affect the ability of the data set. Thus, the 8-day corrected AVHRR snow cover provided quite accurate snow information, compared with 8-day MODIS cloud/gap free snow cover. Time series of SCAP calculated from the 8-day corrected AVHRR snow cover are with very high correlation with the SCAP time series calculated from 8-day MODIS cloud/gap free snow cover.

6 Snow Cover in Amu Dar'ya Basin

6.1 Spatial and Seasonal Distribution

The 8-day corrected AVHRR snow cover was used to analyze the snow cover change in the Amu Dar'ya R. Basin in the period between 1986 and 2008. Long term monthly mean SCAP plots (**Figure 3.11**) for the Amu Dar'ya R. Basin, climatic regions and altitudinal belts have been produced from the 8-day corrected AVHRR snow cover following the mapping rule described in Table 3.8. Long term monthly snow probability maps (**Figure 3.12**) have also been generated to visualize the general spatial snow distribution within the Amu Dar'ya R. Basin.

The snow distribution in the Amu Dar'ya R. Basin, and each climatic region and altitudinal belt within the basin, shared a similar temporal pattern. December to February is the period of highest snow cover, with maximum snow cover in January. The July to September period has the least snow, with minimum snow cover in August.

Comparison of long term monthly mean SCAP calculated for each altitudinal belts suggests the spatial distribution of snow is positively related with elevation. Comparison between the long term snow probability map (**Figure 3.12**) and the DEM (**Figure 3.8-a**) also confirms our finding. For example, the Plains at the western part of the basin with an average elevation of 654 m, have a maximum long term SCAP of about 32% in January, while other climatic regions at the eastern mountainous part of the basin with average elevations higher than 2800 m, have maximum long term SCAP greater than 80%. Within Plains, most of the snow occurs at the southern mountainous part, while other places in the Plains only have sporadic snow, therefore much smaller snow probability (**Figure 3.12**). The long term SCAP

in January and August for each climatic region against its mean elevation (**Figure 3.13**) also shows the positive relationship between snow cover and elevation more clearly with the only exception in eastern Pamir. It has an average elevation of 4361 m asl, which is higher than the average elevation of southern Pamir (4321 m). However, the eastern Pamir receives less snow than southern Pamir because of its orographic location in a precipitation shade of the central Pamir, which limits atmospheric moisture penetration from the westerlies.

6.2 Trend of Annual Snow Cover Cycle Change

Snow cover statistics describing the timing of snow season, including Snow Covering Days (SCD), Snow Cover Onset Date (SCOD) and Snow Cover Melting Date (SCMD), were derived from the corrected AVHRR snow data for the Amu Dar'ya Basin, six climatic regions, five altitudinal belts by 1000 m elevation within each climatic region.

The SCD is defined as a sum of days with snow cover in a hydrological year for each pixel. Based on analysis of long term meteorological data in the research region, the hydrological year is defined as from the 31st 8-day period to 30th 8-day period in the next year. SCOD and SCMD are defined as the start and end 8-day period of snow duration within a hydrological year for each pixel. An approximate algorithm (**Wang and Xie, 2009**) to calculate SCOD and SCMD has been used.

$$SCOD=D'-SCD', \qquad \textbf{Equation 3.9}$$

where SCD' is the snow covering days within the period of snow starting season, which was determined by the climate regime of our research region. In Amu Dar'ya Basin, the start was defined at the 241st date in a year (August 29th as the start of the 31st 8-day period) and the end at the 361th date in a year (November 27th as the start of the 46th 8-day period). D' is the

Julian day of the end of the defined snow starting season. Similarly, the SCMD is calculated by:

$$SCMD=D"+SCD" , \quad \textbf{Equation 3.10}$$

where SCD" is the snow covering days within the periods of snow melting season, which is defined as the period from the 17th date in a year (January 17th as the start of the 3rd 8-day period) to the 177th date in a year (June 26th as start of the 23rd 8-day period) for our study region based on the analysis of long term meteorological data.

Mann-Kendall tests were conducted on each series of snow statistics (SCD, SCOD and SCMD) to detect possible trend of snow cover change. Results with p-values less than 0.1 were reported in (**Table 3.9**). Slopes calculated from linear regression were also reported in the table as an indicator of the general direction of the change.

The results of the trend detection tests suggest:

1. There are significant decreasing trends of SCD in mountainous regions with high elevation in the Amu Dar'ya Basin (-1.00 day/year in the altitudinal zone > 4000 m) and the climatic regions of southern Pamir (-0.80 day/year), eastern Pamir (-1.01 day/year), western Pamir (-0.77 day/year in the altitudinal zone 3000 – 4000 m, and -1.20 day/year in the altitudinal zone > 4000 m) and Pamiro-Alai (-0.43 day/year in the altitudinal zone 3000 m – 4000 m). Such trends were accompanied by earlier SCMD.

2. In the altitudinal belt of elevation greater than 3000 m within the Plains, both of the SCOD (-0.16 day/year) and SCMD (-0.74 day/year) shifts earlier, which results in an earlier snow season.

3. In central Pamir, especially in the altitudinal belts higher than 4000 m, the SCOD delays slightly (0.03 day/year), while the SCMD does not have significant trend of change.

7 Discussion

There are several limitations in the snow identification scheme and the method to correct AVHRR 8-day data. The validation result of daily AVHRR against daily MODIS snow cover in different land cover type zones suggest that the snow identifications scheme does not perform well in forested area, with a very high omission rate. This might be caused by the fact that forest canopy can obscure the surface from visible sensors (**Hall et al., 1998; Salminen et al., 2009**). Further enhancement of the snow identification scheme should take the NDVI as an indicator of forested area into consideration. The validation result of the corrected 8-day AVHRR snow against 8-day MODIS cloud/gap free snow points out that the correction method works quite well in Elementary Hillslope Areas (EHAs) that have typical hillslope topography, but not so well for low elevation plains or very high and steep mountainous areas. One of the basic assumptions in designing the correction method is that the relative spatial structure of snow distribution within each EHA is stable. Thus the long term snow probability map can be used in combination with a linearly corrected AVHRR SCAP value within the EHA to generate the corrected AVHRR snow data. In regions with typical hillslope topography, the topography has a very strong effect on the snow distribution so such assumption proved quite well. But at the low elevation Plains and very high steep mountainous areas this assumption might be violated, which leads to a not very good performance of the correction method. Further development of the correction method might introduce more flexible snow probability maps, with adjusted snow probability for different

elevation, slope or land cover types. In the snow timing analysis as a show case of the ability of the result dataset, the approximation method for calculating SCMD and SCOD might limit our ability for detecting possible timing trend in lower plains with little snow and high mountains. In future studies, other more exact method might be considered (**Gafurov, 2009**).

8 Conclusion

An aggregated rating based snow identification scheme was designed to generate accurate AVHRR snow cover from all available AVHR level1b raw data over central Asia. A correction method, based on known long term snow probability in small sub regions has been developed for generating corrected 8-day AVHRR snow cover which is comparable to 8-day MODIS snow. Validation results of daily AVHRR snow cover against ground based snow survey data, and the daily MODIS snow cover show-high accuracy of the snow identification scheme. The comparison of the corrected 8-day AVHRR snow cover with 8-day MODIS cloud / gap free snow indicates high comparability between snow data from corrected AVHRR and MODIS. Results of snow cover distribution and historical changes analysis in Amu Dar'ya Basin, which utilized the newly developed snow dataset provide information about the spatial and temporal patterns of snow distribution in this basin, as well as the variable snow cover change over this region. This accurate long term snow dataset derived AVHRR and MODIS data is suitable for the study of seasonal snow cover in mountainous regions and might be a unique opportunity for the climatological and hydrological study of seasonal snow cover and water resources change in central Asia over the past twenty years.

Tables

Table 3.1 Area percentage of climatic regions, altitudinal zones, aspect classes, slope classes and land cover type zones in Amu Dar'ya Basin

Climatic Region	Area Percentage (%)	**Altitudinal Zone**	Area Percentage (%)	**Aspect Class**	Area Percentage (%)
Southern Pamir	3.38	<1000	64.6	0-45	16.52
Eastern Pamir	3.03	1000-2000	11.33	45-90	13.45
Central Pamir	0.99	2000-3000	9.17	90-135	9.22
Western Pamir	8.61	3000-4000	7.37	135-180	8.42
Pamiro-Alai	2.3	>4000	7.53	180-225	9.67
Plain	81.68			225-270	11.81
				270-315	14.61
				315-360	16.29
Total Area for Amu Dar'ya Basin	959036 km^2				

Slope Class	Area Percentage (%)	**Land Cover Type**	Area Percentage (%)
0-1.21	57.64	Forest	0.004
1.21-3.84	15.28	Woodland	0.721
3.84-7.07	8.94	Shrubland	48.476
7.07-10.31	6.01	Grassland	18.518
10.31-13.75	4.53	Cropland	6.891
13.75-17.18	3.18	Bare Ground	23.258
17.18-20.82	2.23	Urban and Built	0.255
20.82-24.87	1.4		
24.87-30.12	0.66		
30.12-52	0.13		

Table 3.2 Parameters of the Albers central Asia coordinate system

Datum	
Name	WGS84
Major semiaxis, a(m)	6378137
Ellipsoid flattening	0.00335281068118
Projection	
Type	Albers Conical Equal Area
First parallel (degree)	47
Second parallel (degree)	38
Central meridian (degree)	85
Latitude of origin (degree)	0
False easting (m)	3000000
False northing (m)	0
Extent	
Top (m)	6000000
Left (m)	300000
Right (m)	5300000
Bottom (m)	3300000
Pixel Size	
AVHRR, x and y (m)	1000
MODIS, x and y (m)	500

Table 3.3 Coding scheme used in snow identification result

Value	Pixel Type
1	No Decision
25	Snow free land
37	lake or inland water
50	cloud obscured
100	snow covered lake ice
200	snow
255	No Data

Table 3.4 Parameters used in membership tests in snow and nonsnow modules

Membership Test	Parameters				
Snow B1	b1 = 0.18	d1 = 0.07			
Nonsnow B1	b2 = 0.27	d2 = 0.16			
Snow NDSI	b1 = 0.4	d1 = 0.2			
Nonsnow NDSI	b2 = 0.2	d2 = 0.2			
Snow Ratio31	A_{b1} = 0.18	B_{b1} = 0.42	A_{d1} = 0.12	B_{d1} = 0.13	
Nonsnow Ratio31	A_{b2} = 0.75	B_{b2} = 0.45	A_{d2} = 0.6	B_{d2} = 0.1	
Snow BT4	b1 = $T_{surface}$ - 20K	d1 = 7.5K	A_{b2} = 12K	B_{b2} = 266K	d2 = 7.5K
Nonsnow BT4	A_{b1} = 12K	A_{d1} = 266K	d1 = 7.5K		
Snow snow_mask	r_1=0.7	r_2=0.3			
Nonsnow snow_mask	r_1=0.15	r_2=0.85			

Table 3.5 Confusion matrix and definition of performance measures

		Predicted by AVHRR data	
		Snow	Non-snow
Actual	Snow	True Positive (TP)	False Negative (FN)
	Non-snow	False Positive (FP)	True Negative (TN)

Performance measures	Definition
General accuracy	$\frac{\mathrm{TP}+\mathrm{TN}}{\mathrm{TP}+\mathrm{TN}+\mathrm{FP}+\mathrm{FN}}$
Kappa coefficient	$\frac{\text{general accuracy}-\Pr(\mathrm{e})}{1-\Pr(e)}$, $while\ \Pr(e)=\left(\frac{TP+FP}{Total}*\frac{TP+FN}{Total}\right)+\left(\frac{TN+FP}{Total}*\frac{TN+FN}{Total}\right)$, $\mathrm{T}otal=TP+TN+FP+FN$
omission	$\frac{\mathrm{FN}}{\mathrm{TP}+\mathrm{FN}}$
commission	$\frac{\mathrm{FP}}{\mathrm{TP}+\mathrm{FP}}$
Probability of detection (POD)	$\frac{\mathrm{TP}}{\mathrm{TP}+\mathrm{FN}}=1-\text{omission}$

Table 3.6 Comparison result between Daily AVHRR Snow with Ground Snow Survey

Year	Depth >3			Depth<=3			All		
	Snow	Total	POD (%)	Snow	Total	POD (%)	Snow	Total	POD (%)
1987	416	433	96.07	42	73	57.53	458	506	90.51
1988	155	171	90.64	36	54	66.67	191	225	84.89
1989	174	196	88.78	47	74	63.51	221	270	81.85
1990	157	193	81.35	34	48	70.83	191	241	79.25
1991	40	49	81.63	4	6	66.67	44	55	80.00
1992	211	233	90.56	8	10	80.00	219	243	90.12
1993	398	433	91.92	5	9	55.56	403	442	91.18
1994	240	257	93.39	10	12	83.33	250	269	92.94
1995	202	220	91.82	11	20	55.00	213	240	88.75
1996	432	476	90.76	27	37	72.97	459	513	89.47
All	2425	2661	91.13	224	343	65.31	2649	3004	88.18

Table 3.7 Comparison result of AVHRR snow from different sensors

Sensor Pair	Year	General Accuracy (%)	Omission (%)	Commission (%)	Kappa Coefficient
NOAA6 vs NOAA9	no pairs				
NOAA9 vs NOAA10	no pairs meet the requirements				
NOAA10 vs NOAA 11	199 1	93.34	10.75	16.82	0.82
NOAA11 vs NOAA12	199 2	93.91	21.64	6.10	0.82
NOAA-12 vs NOAA14	199 6	95.66	6.15	0.40	0.91
NOAA14 vs NOAA 15	no pairs meet the requirements				
NOAA14 vs NOAA 16	200 1	91.91	17.84	5.81	0.82
NOAA16 vs NOAA17	200 1	93.18	4.16	20.97	0.82
NOAA17 vs NOAA 18	200 8	90.29	7.18	17.09	0.80

Table 3.8 Mapping Rules to aggregate 8-day data to monthly data[12]

Month	Approximate 8-day periods	Time period (non-leap year)
Jan	1, 2, 3, 4	01/Jan to 01/Feb
Feb	5, 6, 7, 8	02/Feb to 05/Mar
Mar	8, 9, 10, 11	26/Feb to 29/Mar
Apr	12, 13, 14, 15	30/Mar to 30/Apr
May	16, 17, 18, 19	01/May to 01/Jun
Jun	20, 21, 22, 23	02/Jun to 03/Jul
Jul	24, 25, 26, 27	04/Jul to 04/Aug
Aug	27, 28, 29, 30	28/Jul to 28/Aug
Sep	31, 32, 33, 34	29/Aug to 29/Sep
Oct	35, 36, 37, 38	30/Sep to 31/Oct
Nov	39, 40, 41, 42	01/Nov to 02/Dec
Dec	43, 44, 45, 46	03/Dec to 03/Jan

Table 3.9 Trend of Snow Covering Days (SCD), Snow Cover Onset Date (SCOD) and Snow Cover Melt Date (SCMD)

Statistics Type	Region	Altitudinal Range (m)	Slope (day/year)	Mann-Kendall Test's P
SCD	Amu Dar'ya	3000 - 4000	-0.4912	0.07
SCD	Amu Dar'ya	>= 4000	-1.0082	0.02 *
SCD	Southern Pamir	All	-0.8012	0.04 *
SCD	Southern Pamir	>= 4000	-1.0447	0.02 *
SCD	Eastern Pamir	All	-1.0118	0.03 *
SCD	Eastern Pamir	< 4000	-0.2752	0.02 *
SCD	Eastern Pamir	>= 4000	-1.2089	0.03 *
SCD	Western Pamir	3000 - 4000	-0.7651	0.04 *
SCD	Western Pamir	>= 4000	-1.2033	0.01 *
SCD	Pamiro-Alai	3000 - 4000	-0.4330	0.05 *
SCD	Pamiro-Alai	>= 4000	-0.6756	0.07
SCOD	Amu Darya	2000 -3000	-0.2623	0.01 *
SCOD	Central Pamir	All	0.0063	0.05 *
SCOD	Central Pamir	>= 4000	0.0252	0.03 *
SCOD	Western Pamir	All	-0.0226	0.09
SCOD	Western Pamir	2000 - 3000	-0.3002	0.02 *
SCOD	Pamiro-Alai	>= 4000	0.1339	0.07
SCOD	Plain	>= 3000	-0.1592	0.08
SCMD	Amu Dar'ya	3000 - 4000	-0.4192	0.02 *
SCMD	Amu Dar'ya	>= 4000	-0.2340	0.02 *
SCMD	Southern Pamir	All	-0.1374	0.05
SCMD	Southern Pamir	>= 4000	-0.1848	0.02 *
SCMD	Eastern Pamir	All	-0.3290	0.02 *
SCMD	Eastern Pamir	< 4000	-0.0851	0.06
SCMD	Eastern Pamir	>= 4000	-0.3943	0.02 *
SCMD	Western Pamir	3000 - 4000	-0.4443	0.02 *
SCMD	Western Pamir	>= 4000	-0.2162	0.02 *
SCMD	Pamiro-Alai	3000 - 4000	-0.2522	0.09
SCMD	Pamiro-Alai	>= 4000	-0.1583	0.05 *
SCMD	Plain	>= 3000	-0.7386	0.01 *

** indicates trend detected under a significant level of 0.05*

'All' indicates that the test is conducted over the whole climatic region

Figures

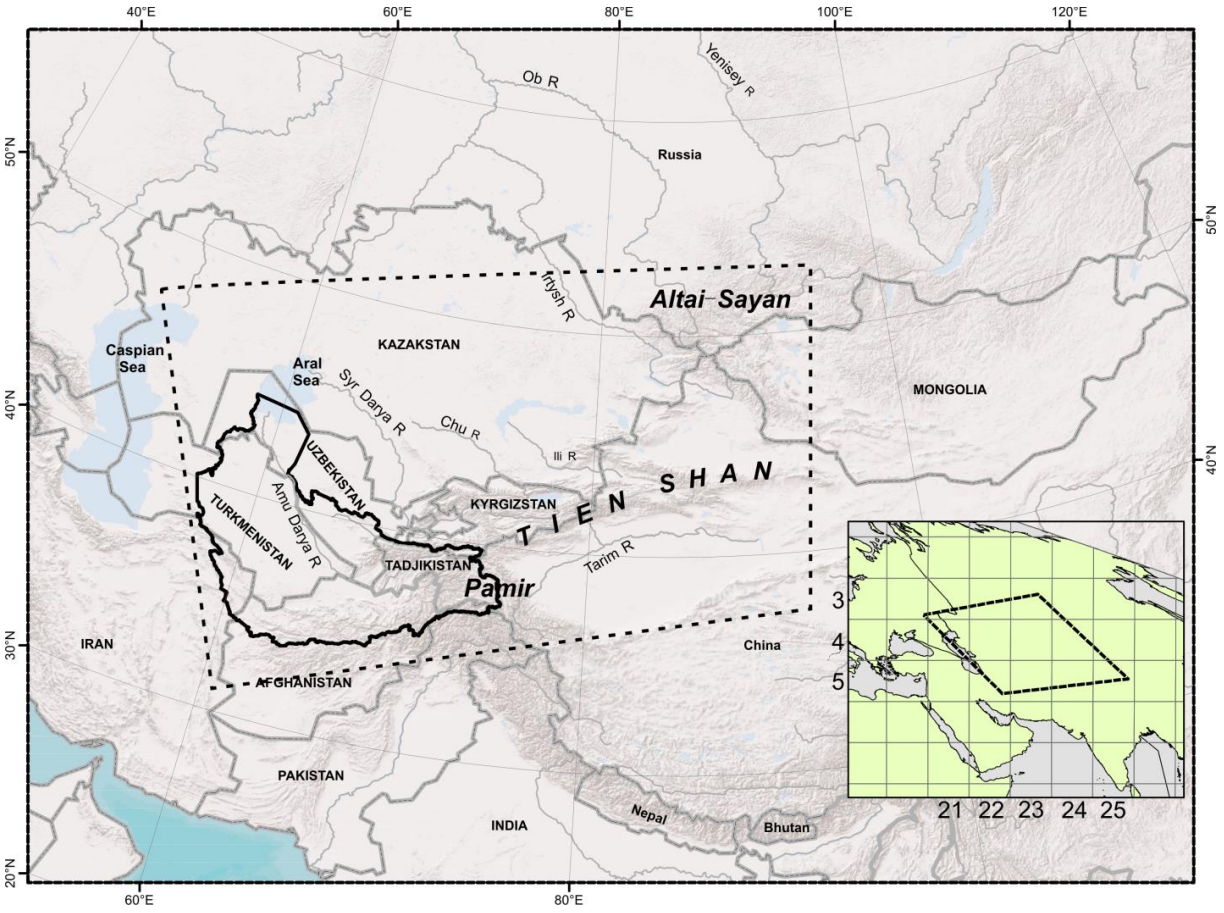

Figure 3.01 Location of central Asia (CA) and the Amu Dar'ya Basin (ADB)1

CA is delineated by the dashed.

The Amu Dar'ya River Basin is delineated by the bold polygon.

The inset map shows the location of CA within the Eurasia continent,

and the MODIS tiles utilized in this research.

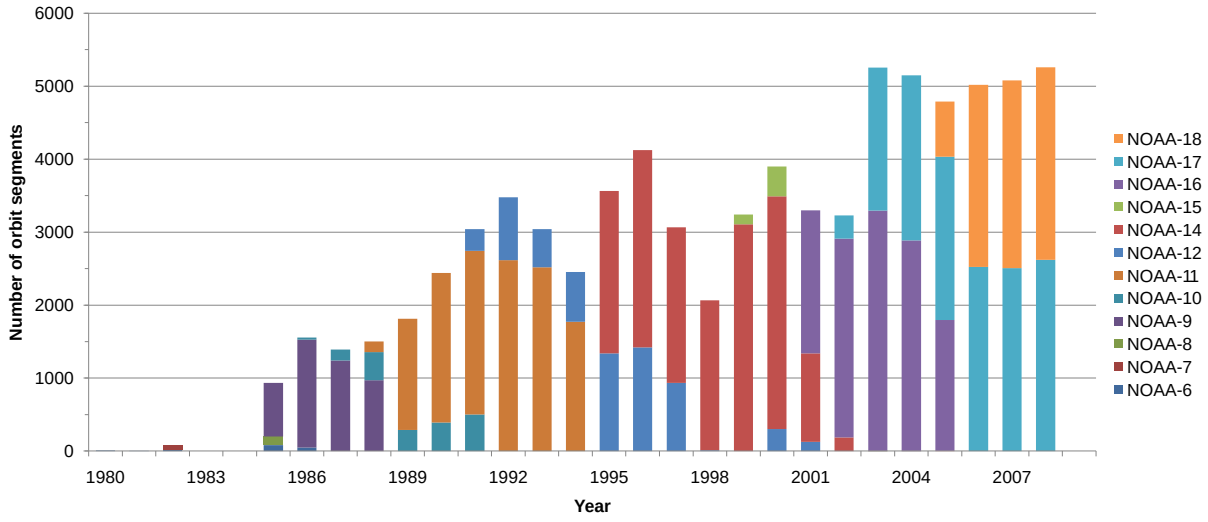

Figure 3.02 Contents of AVHRR Level1b data archive by acquisition year and satellite mission2

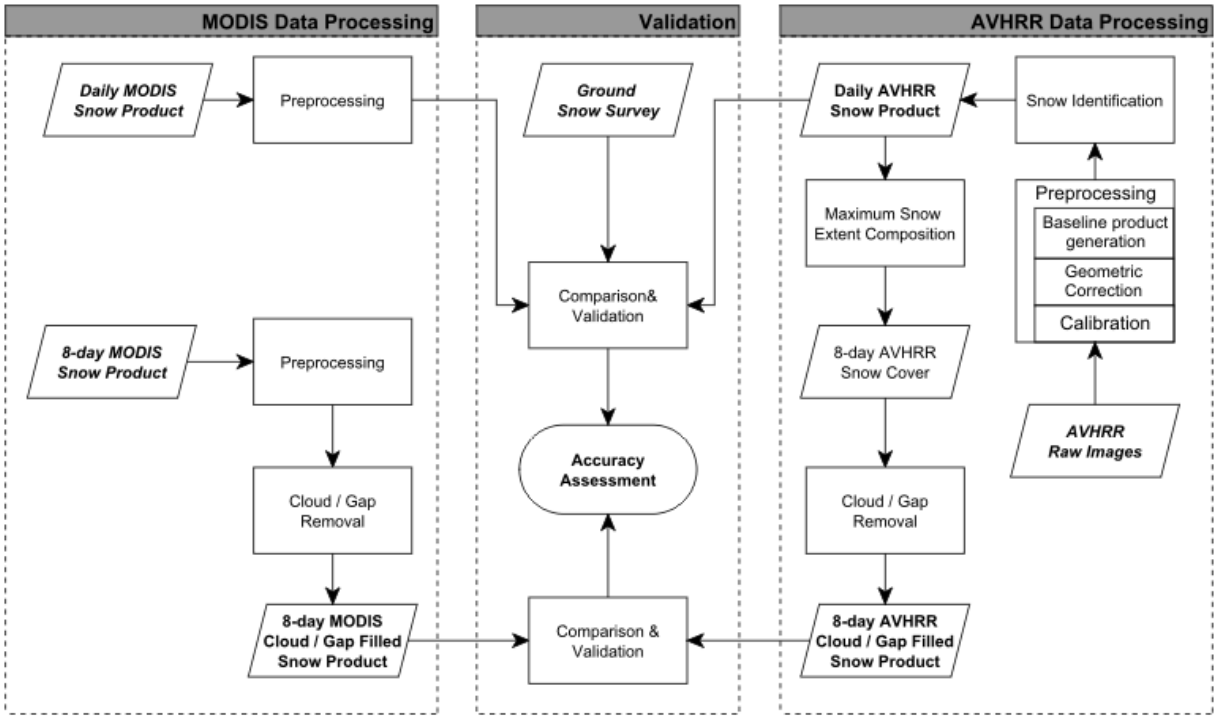

Figure 3.03 Flow chart of AVHRR and MODIS data processing3

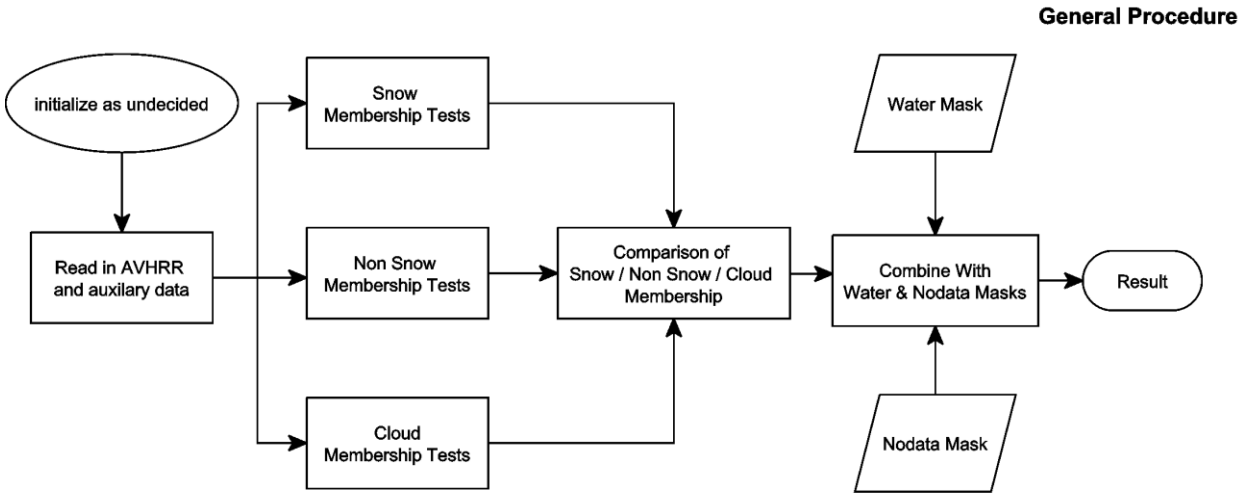

Figure 3.04 Flow chart of the general procedure in snow identification scheme4

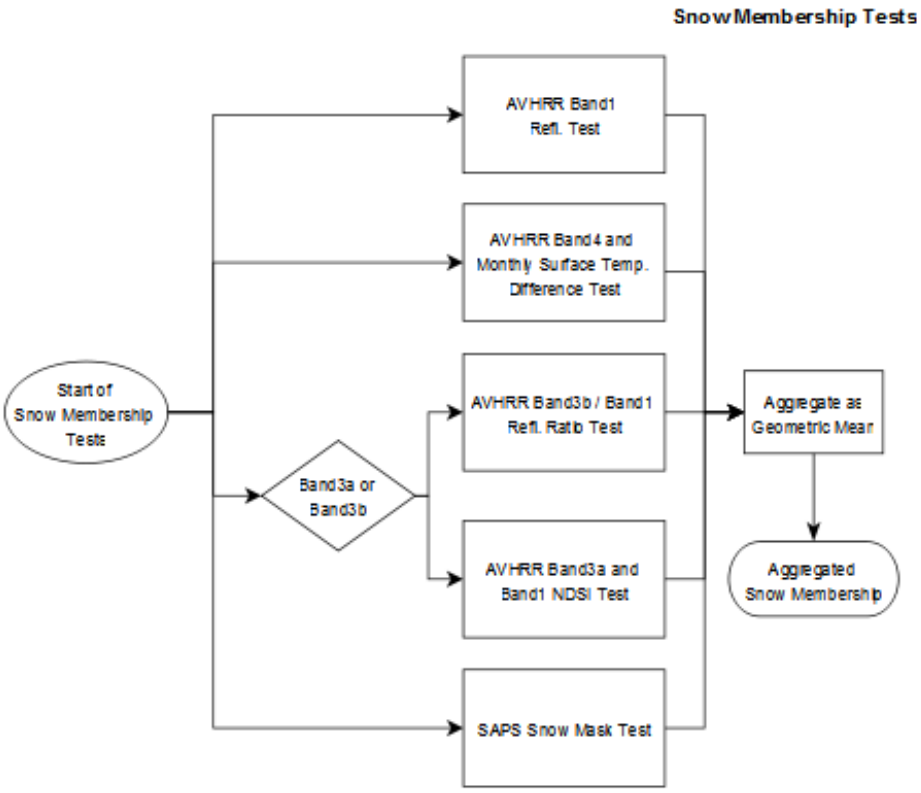

Figure 3.05 Flow chart of the Snow Membership Tests Module5

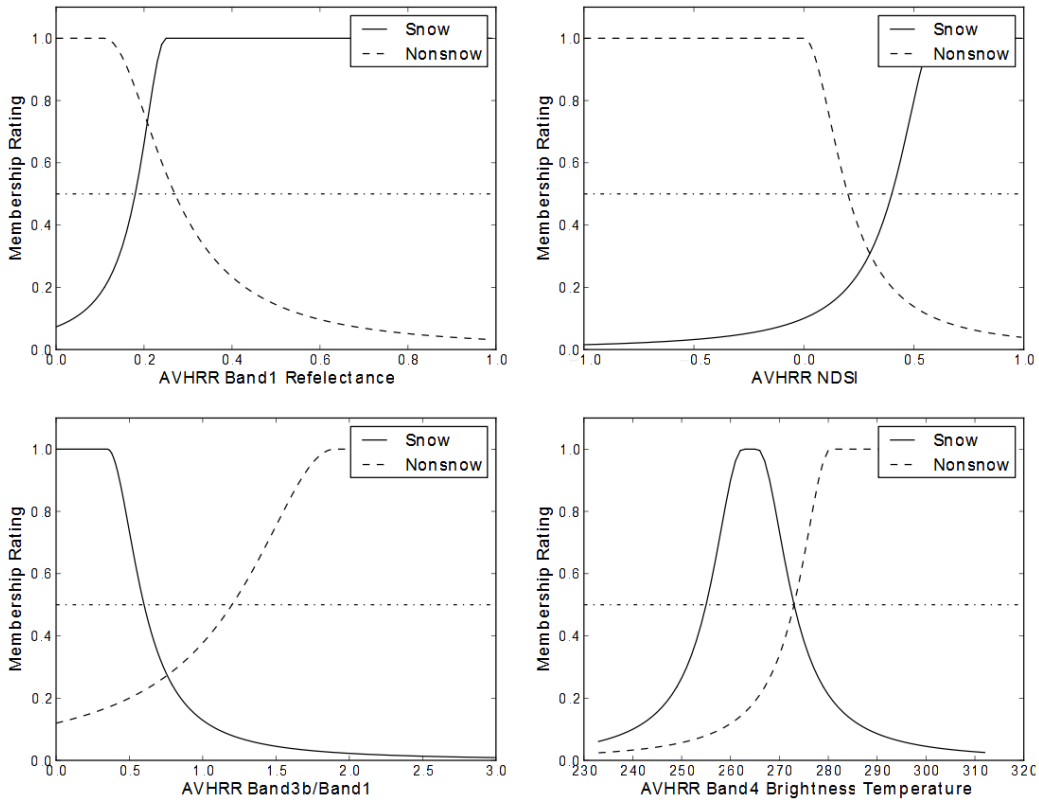

Figure 3.06 Membership functions used in the snow and nonsnow modules6

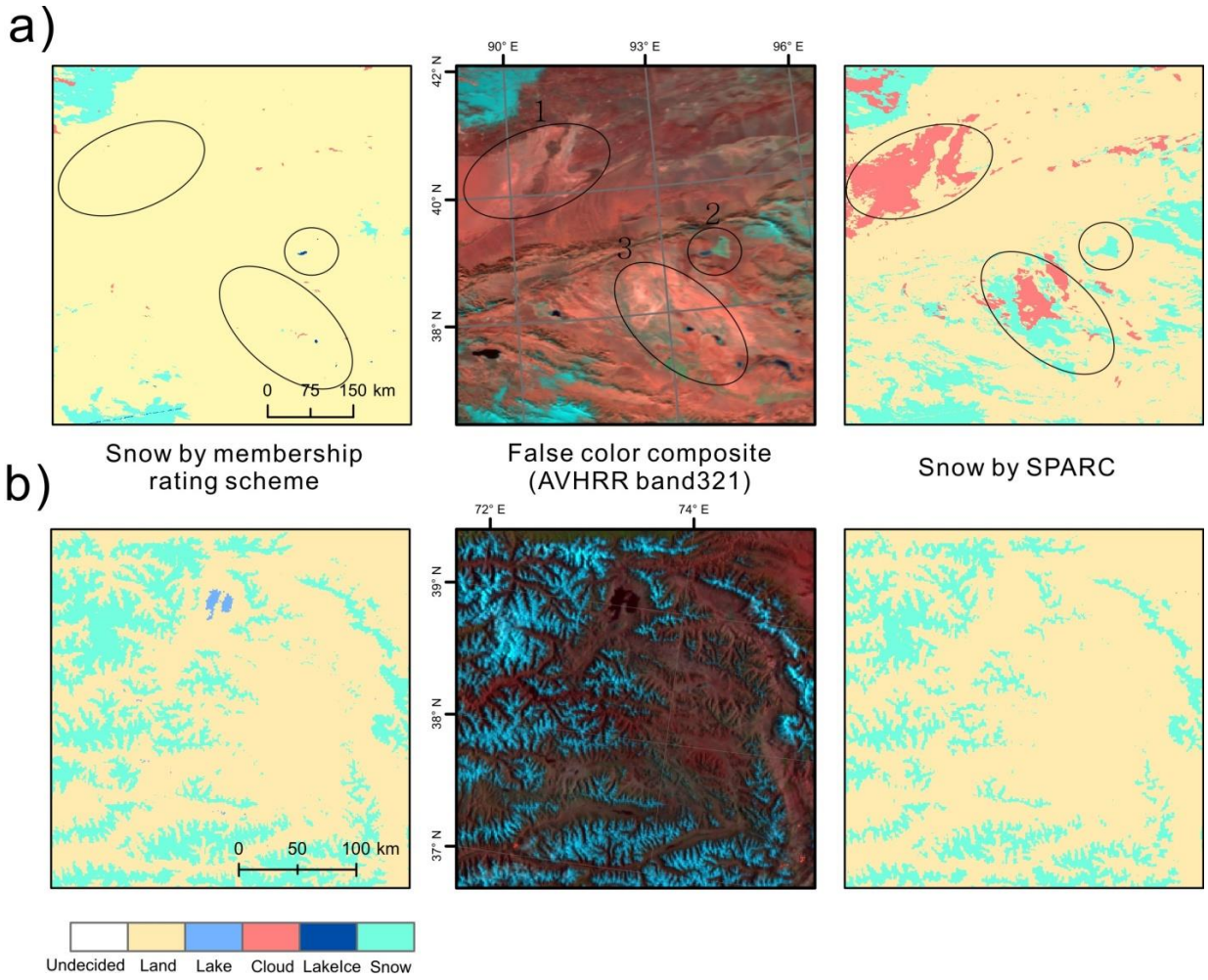

Figure 3.07 Comparison between snow identification results generated by SPARC and the membership rating scheme7

a) 1995-12-27, Eastern Xinjiang and Qinghai; b) 1996-07-10, Central and Eastern Pamir

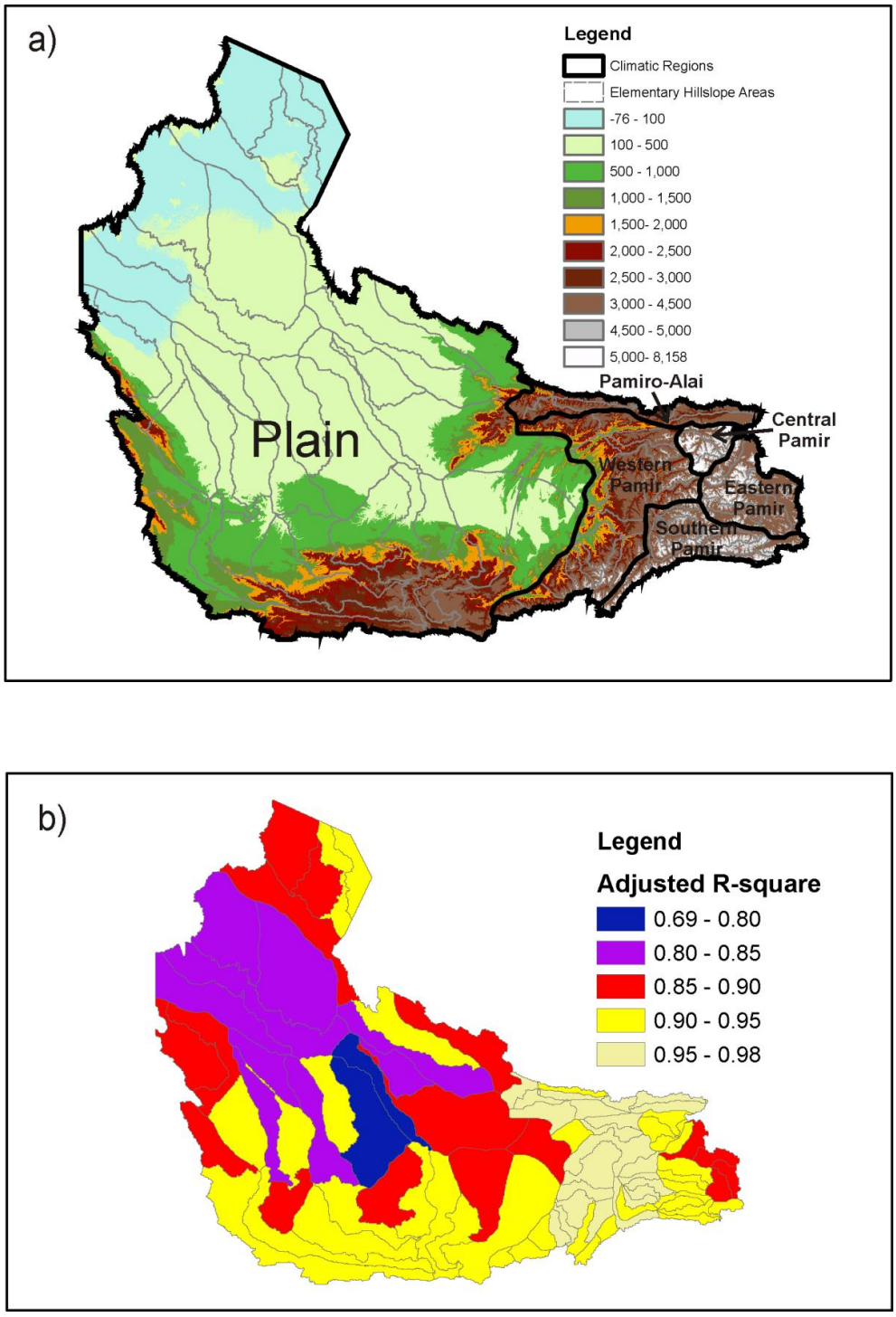

Figure 3.08 Model performance assessment in the Amu Dar'ya Basin (ADB)8

a) Climatic Regions and Elementary Hillslope Areas (EHA) in the ADB

b) Adjusted R^2 in different EHAs in the ADB

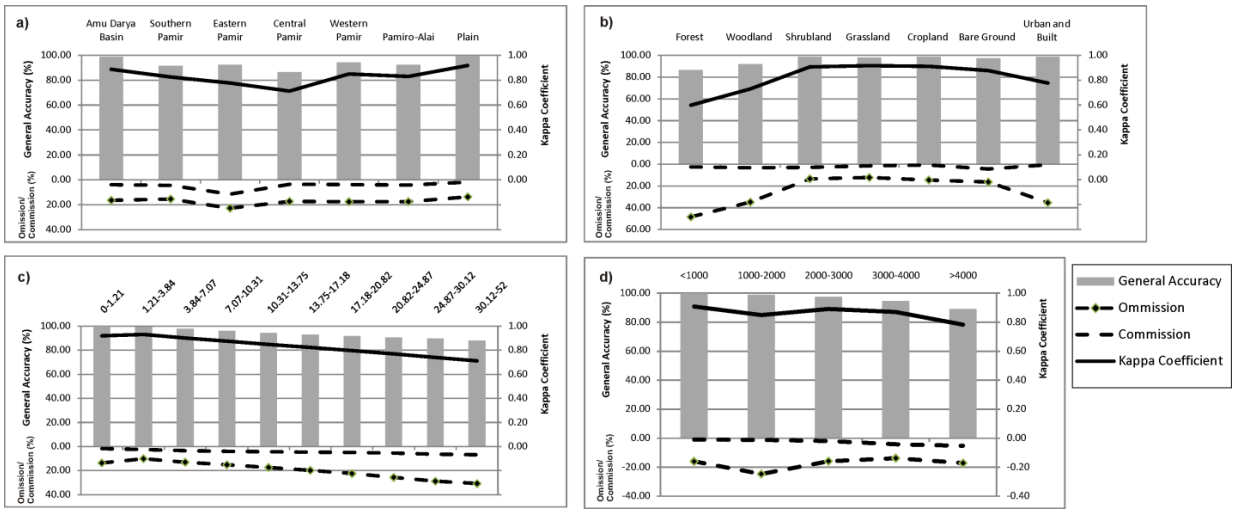

Figure 3.09 Comparison between Daily AVHRR and MODIS snow data9

a) by climatic region; b) by land cover type; c) by slope class; d) by altitudinal zone

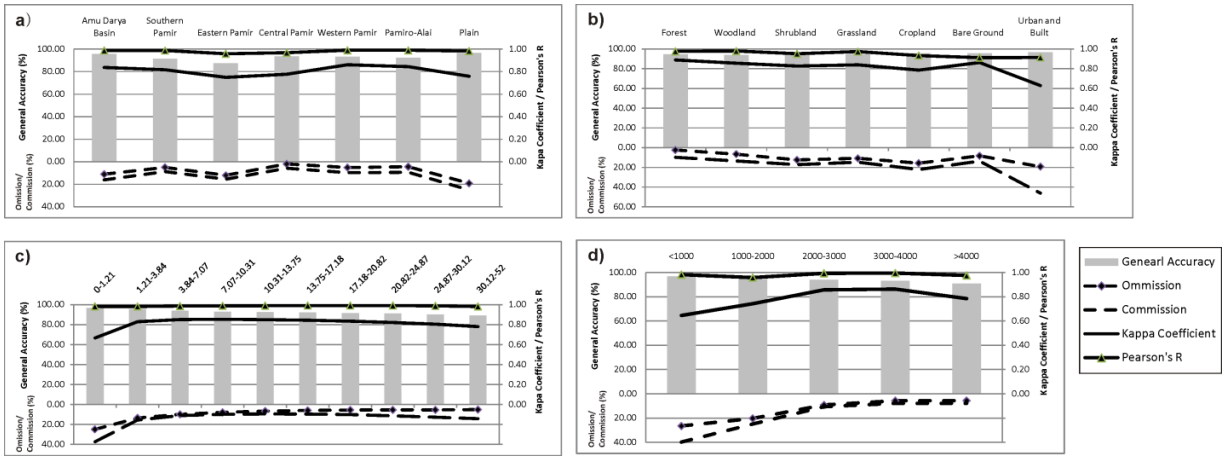

Figure 3.10 Comparison between Corrected AVHRR and 8-day Cloud /Gap filled MODIS snow10

a) by climatic region; b) by land cover type; c) by slope class; d) by altitudinal zone

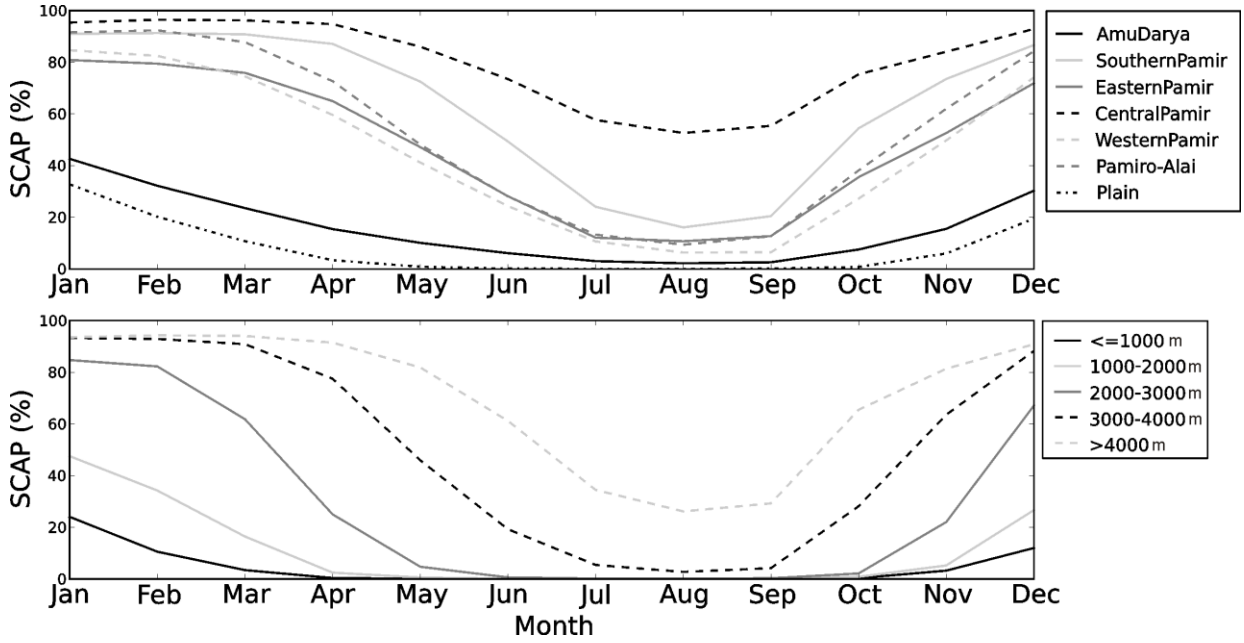

Figure 3.11 Long-term monthly mean Snow Cover Area Percentage (SCAP) in different climatic regions and altitudinal zones11

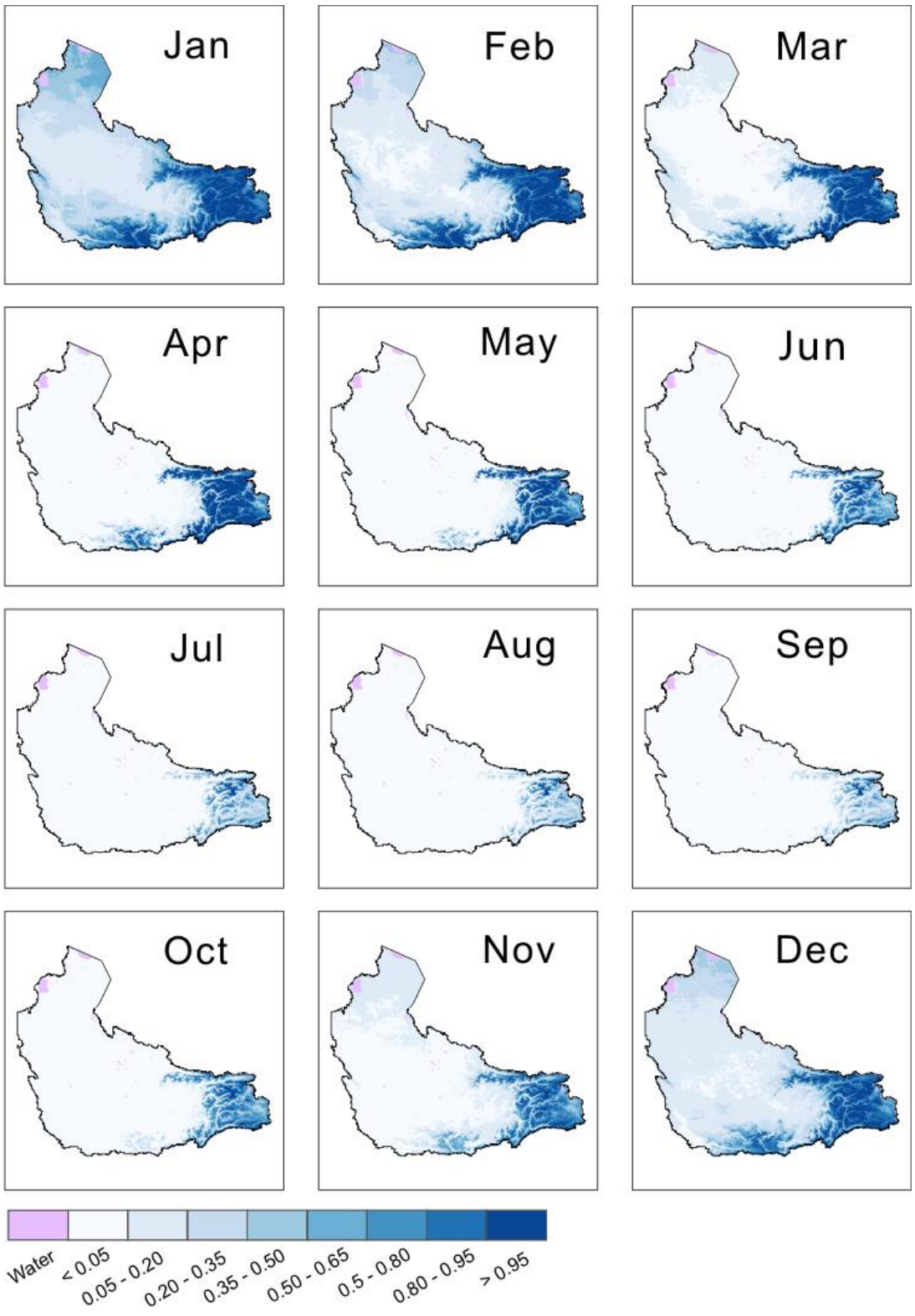

Figure 3.12 Long-term monthly snow probability maps12

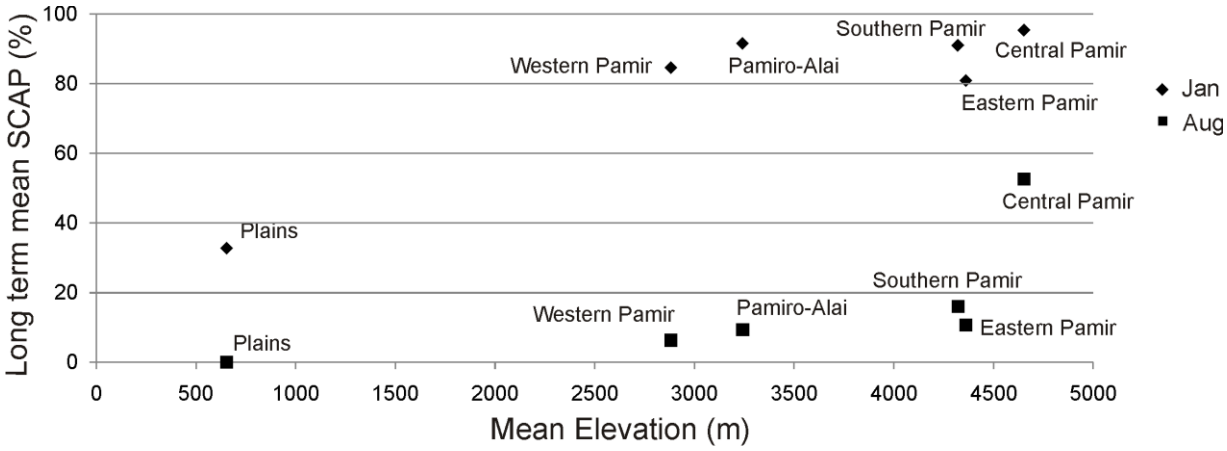

Figure 3.13 Long-term mean SCAP in January and August in relation with mean elevation for different climatic regions13

References

Aizen, V.B., Aizen, E.M., 1995. Characteristics of runoff formation at the Kirgizskiy Alatoo, Tien Shan, in: Proceedings of a Boulder Symposium, IAHS Publ. No.228. pp. 413-430.

Aizen, V.B., Aizen, E.M., Melack, J.M., 1996. Precipitation, melt and runoff in the northern Tien Shan. Journal of Hydrology 186, 229-251.

Aizen, E.M., Aizen, V.B., Melack, J.M., Krenke, A.N., 2000. Heat exchange during snow ablation in plains and mountains of Eurasia. Journal of Geophysical Research 105, 013-27.

Aizen, V.B., Aizen, E.M., Melack, J., Nakamura, T., Kobayashi, S., 2002. Estimation of the energy used to melt snow in the Tien Shan mountains and Japanese Islands. Global and Planetary Change 32, 349-359.

Aizen, V.B., Aizen, E.M., Zhou, H., Surazakov A.B., Nikitin, S.A.. 2012. Climate, Snow, Glaciers and River runoff changes in Pamir in the last 80 years. Journal of Climate (submitted).

Armstrong, R.L., Brun, E., 2010. Snow and Climate: Physical Processes, Surface Energy Exchange and Modeling [Paperback]. Cambridge University Press; 1 edition.

Bales, R.C., Molotch, N.P., Painter, T.H., Dettinger, M.D., Rice, R., Dozier, J., 2006. Mountain hydrology of the western United States. Water Resources Research 42, 1-13.

Bamzai, A. S., 2003. Relationship between snow cover variability and Arctic oscillation index on a hierarchy of time scales. International Journal of Climatology, 23(2), 131–142.

Barnett, T.P., Dümenil, L., Schlese, U., Roeckner, E., Latif, M., 1989. The Effect of Eurasian Snow Cover on Regional and Global Climate Variations. Journal of the Atmospheric Sciences 46, 661-686.

Barnett, T.P., Adam, J.C., Lettenmaier, D.P., 2005. Potential impacts of a warming climate on water availability in snow-dominated regions. Nature 438, 303-9.

Bavera, D., De Michele, C., Pepe, M., Rampini, A., 2011. Melted snow volume control in the Snowmelt Runoff Model using a snow water equivalent statistically-based model. Hydrological Processes c, n/a-n/a.

Bednorz, E., 2004. Snow cover in eastern Europe in relation to temperature, precipitation and circulation. International Journal of Climatology 24, 591-601.

Brown, R.D., 2000. Northern Hemisphere Snow Cover Variability and Change, 1915–97. Journal of Climate 13, 2339-2355.

Burrough, P.A., McDonell, R.A., 1998. Principles of Geographical Information Systems. Oxford University Press, USA; 2 edition.

Cohen, J., 1960. A coefficient of agreement for nominal scales. Educational and psychological measurement 20, 37–46.

Crane, R. G., & Anderson, M. R. 1984. Satellite discrimination of snow/cloud surfaces. International Journal of Remote Sensing, 5(1), 213–223.

Dozier, J., 1987. Recent research in snow hydrology. Review of Geophysics 25, 153-161.

Dozier, J., 1989. Spectral signature of alpine snow cover from the landsat thematic mapper. Remote Sensing of Environment 28, 9-22.

Dye, D.G., 2002. Variability and trends in the annual snow-cover cycle in Northern Hemisphere land areas, 1972-2000. Hydrological Processes 16, 3065-3077.

Francke, T., Güntner, A., Mamede, G., Müller, E.N., Bronstert, A., 2008. Automated catena-based discretization of landscapes for the derivation of hydrological modelling units. International Journal of Geographical Information Science 22, 111-132.

GRASS Development Team, 2009. GRASS GIS 6.4.2svn Reference Manual.

Gafurov, a., Bárdossy, A., 2009. Cloud removal methodology from MODIS snow cover product. Hydrology and Earth System Sciences 13, 1361-1373.

Gong, G., 2004. Sensitivity of atmospheric response to modeled snow anomaly characteristics. Journal of Geophysical Research 109, D06107.

Groisman, P.Y., Karl, T.R., Knight, R.W., Stenchikov, G.L., 1994. Changes of Snow Cover, Temperature, and Radiative Heat Balance over the Northern Hemisphere. Journal of Climate 7, 1633-1656.

Hall, D.K., Foster, J.L., Verbyla, D.L., Klein, A.G., Benson, C.S., 1998. Assessment of Snow-Cover Mapping Accuracy in a Variety of Vegetation-Cover Densities in Central Alaska. Remote Sensing of Environment 66, 129-137.

Hall, D.K., Riggs, G.A., Salomonson, V.V., 2001. Algorithm theoretical basis document (ATBD) for the MODIS snow and sea ice-mapping algorithms. Science Branch NASA.

Hall, D.K., Riggs, G.A., Salomonson, V.V., DiGirolamo, N.E., Bayr, K.J., 2002. MODIS snow-cover products. Remote Sensing of Environment 83, 181-194.

Hansen, M., DeFries, R., Townshend, J.R.G., Sohlberg, R., 1998. UMD Global Land Cover Classification, 1 Kilometer, 1.0 [WWW Document]. URL http://glcf.umiacs.umd.edu/data/landcover/

Hansen, M.C., Defries, R.S., Townshend, J.R.G., Sohlberg, R., 2000. Global land cover classification at 1 km spatial resolution using a classification tree approach. International Journal of Remote Sensing 21, 1331-1364.

Khlopenkov, K.V., Trishchenko, A.P., 2007. SPARC: New Cloud, Snow, and Cloud Shadow Detection Scheme for Historical 1-km AVHHR Data over Canada. Journal of Atmospheric and Oceanic Technology 24, 322-343.

Khlopenkov, K.V., Trishchenko, A.P., Luo Y., 2010. Achieving Subpixel Georeferencing Accuracy in the Canadian AVHRR Processing System. IEEE Transactions on Geoscience and Remote Sensing 48, 2150-2161.

Krenke, A., 1998. Former Soviet Union hydrological snow surveys, 1966-1996, Edited by NSIDC [WWW Document]. URL http://nsidc.org/data/g01170.html

Kukla, G.J., Kukla, H.J., 1974. Increased Surface Albedo in the Northern Hemisphere: Did satellites warn of the weather troubles of 1972 and 1973? Science 183, 709-14.

Kumar, O.B., 1988. Eurasian snow cover and seasonal forecast of Indian summer monsoon rainfall. Hydrological sciences journal 33, 515-525.

Land Processes DAAC, USGS EROS Center, 2002. MODIS Reprojection Tool User's Manual.

Latifovic, R., Trishchenko, A.P., Chen, J., Park, W.B., Khlopenkov, K.V., Fernandes, R., Pouliot, D., Ungureanu, C., Luo, Y., Wang, S., others, 2005. Generating historical AVHRR 1 km baseline satellite data records over Canada suitable for climate change studies. Canadian Journal of Remote Sensing 31, 324–346.

Lettenmaier, D.P., Wood, A.W., Palmer, R.N., Wood, E.F., Stakhiv, E.Z., 1999. Water resources implications of global warming: A US regional perspective. CLIMATIC CHANGE 43, 537-579.

Lioubimtseva, E., Henebry, G.M., 2009. Climate and environmental change in arid Central Asia: Impacts, vulnerability, and adaptations. Journal of Arid Environments 73, 963-977.

Malcher, P., Floricioiu, D., Rott, H., 2003. Snow mapping in Alpine areas using medium resolution spectrometric sensors. IGARSS 2003. 2003 IEEE International Geoscience and Remote Sensing Symposium. Proceedings (IEEE Cat. No.03CH37477) 00, 2835-2837.

Marks, D., Dozier, J., 1992. Climate and energy exchange at the snow surcace in the alpine region of the Sierra-Nevada .2. snow cover energy-balance. Water Resources Research 28, 3043-3054.

NOAA, 1998. NOAA Polar Orbiter Data User's Guide [WWW Document]. URL http://www2.ncdc.noaa.gov/docs/podug/index.htm

NOAA, 2007. NOAA KLM USER'S GUIDE [WWW Document]. URL http://www.ncdc.noaa.gov/oa/pod-guide/ncdc/docs/klm/index.htm

T.H. Painter, et al., 2009. Retrieval of subpixel snow covered area, grain size and albedo from MODIS, Remote Sensing of Environment 113, 868-879

Ramsay, B.H., 1998. The interactive multisensor snow and ice mapping system. Hydrological Processes 12, 1537–1546.

Robinson, D.A., Kukla, G., 1985. Maximum surface albedo of seasonally snow-covered lands in the Northern Hemisphere. Journal of Climate and Applied Meteorology 24, 402-411.

Robinson, D.A., Scharfen, G., Serreze, M.C.M., Kukla, G., Barry, R.G., 1986. Snow melt and surface albedo in the arctic basin. Geophysical Research Letters 13, 945-948.

Romanov, P., Gutman, G., Csiszar, I., 2000. Automated Monitoring of Snow Cover over North America with Multispectral Satellite Data. Journal of Applied Meteorology 39, 1866-1880.

Romanov, P., 2003. Mapping and monitoring of the snow cover fraction over North America. Journal of Geophysical Research 108, 1-15.

Salminen, M., Pulliainen, J., Metsämäki, S., Kontu, A., Suokanerva, H., 2009. The behaviour of snow and snow-free surface reflectance in boreal forests: Implications to the performance of snow covered area monitoring. Remote Sensing of Environment 113, 907-918.

Seidel, K., Martinec, J., 2010. Remote Sensing in Snow Hydrology: Runoff Modelling, Effect of Climate Change. Springer; Softcover reprint of hardcover 1st ed. 2004 edition.

Soulsby, C., Helliwell, R.C., Ferrier, R.C., Jenkins, A., Harriman, R., 1997. Seasonal snowpack influence on the hydrology of a sub-arctic catchment in Scotland. JOURNAL OF HYDROLOGY 192, 17-32.

Verbunt, M., Gurtz, J., Jasper, K., Lang, H., Warmerdam, P., Zappa, M., 2003. The hydrological role of snow and glaciers in alpine river basins and their distributed modeling. JOURNAL OF HYDROLOGY 282, 36-55.

Walsh, J.E., Jasperson, W.H., Ross, B., 1985. Influences of snow cover and soil moisture on monthly air temperature. Monthly weather review 113, 756-768.

Wang, L., Sharp, M., Brown, R., Derksen, C., Rivard, B., 2005. Evaluation of spring snow covered area depletion in the Canadian Arctic from NOAA snow charts. Remote Sensing of Environment 95, 453-463.

Wang, X., Xie, H., 2009. New methods for studying the spatiotemporal variation of snow cover based on combination products of MODIS Terra and Aqua. Journal of Hydrology 371, 192-200.

Wang, X., Xie, H., Liang, T., 2009. Comparison and validation of MODIS standard and new combination of Terra and Aqua snow cover products in northern Xinjiang, China. Hydrological Processes 429, 419- 429.

Warren, S. G. (1982). Optical properties of snow. Reviews of Geophysics and Space Physics, 20(1), 67–89.

Willmott, C.J.C.J., Rowe, C.M.C.M., Mintz, Y., 1985. Climatology of the terrestrial seasonal water cycle. Journal of Climatology 5, 589–606.

Xiao, X., Moore, B., Qin, X., Shen, Z., Boles, S., 2002. Large-scale observations of alpine snow and ice cover in Asia: Using multi-temporal VEGETATION sensor data. International Journal of Remote Sensing 23, 2213-2228.

Chapter 4 Change of seasonal snow cover in central Asia from 1986 to 2008

1 Introduction

Seasonal snow cover is an important part of the hydrological cycle, affecting glacier mass balance (**Jansson et al., 2003**), soil moisture content (**Edwards et al., 2007**) and river runoff (**Doizer, 1987; Singh, 2010**). In many arid or semi-arid regions, seasonal snow cover is the major water resources for both natural ecosystems and human society, storing solid precipitation in the cold season and releasing them in the warm season as melt water when there is high water requirement. It is estimated that more than one-sixth of the world's population relies on melt water from seasonal snow and glaciers (**Barnett et al., 2005**). In central Asia (CA), melt water from seasonal snow cover is the dominant component of river runoff, as pointed out by various researches of selected river basins (**Aizen et al., 1995; 1996; Chevallier et al., 2014; Pohl et al., 2014**) or general estimation for large regions (**Barnett et al., 2005**).

Seasonal snow cover is sensitive to the changing climate, as numerous studies report a decrease of seasonal snow cover since the 1970s in the northern hemisphere which is mainly associated with increasing temperature (**Groisman et al., 1994; Dye, 2002; Choi et al., 2010; Peng et al., 2013**). Studies based on in-situ meteorological observations since the end of the 19th century (**Aizen et al., 1997; Lioubimtseva et al., 2005; Aizen et al., in preparation**) and climate model simulations (**Mannig et al., 2013; IPCC, 2014**) have shown a general increase of temperature in CA and a further warming up to 7 °C until the end of the 21st century. Possible decrease of seasonal snow cover extent and the associated decrease of river runoff are the major consequences of climate change in CA, in contrast with an increasing

population and growing demands of water resources for irrigation and industrial development. Such a contradiction of decreasing water supply and increasing water demand might contribute negatively to the developing economies of central Asian countries (**Ososkova et al., 2010; Bernauer et al., 2012; Siegfried et al., 2012**).

Various efforts have been spent on studying seasonal snow cover in CA, dating back to the time of the former Soviet Union (FSU). From a current perspective, those studies are outdated by using only data before the 1990s (**Kotlyakov et al., 1997**), or working on the whole northern hemisphere using coarse resolution satellite images (**Brown et al., 2000; Dye and Tucker, 2003**), or focusing on small sub-regions within CA using recent satellite images or station observations (**Liang et al. 2008; Wang et al., 2008; Zhou et al., 2013; Wang et al., 2013; Dietz et al., 2014**). Our group's previous work (**Zhou et al., 2013**) constructed a long term historical archive of snow cover extent data using AVHRR satellite images from 1986 to 2008 for the whole CA, and analyzed the patterns of snow cover change in the Amu Dar'ya Basin. The results showed a significant decrease of Snow Covering Days (SCD) in mountainous regions with elevation greater than 3000 m in the basin, accompanied by both earlier Snow Cover Melting Date (SCMD) and Snow Cover Onset Date (SCOD). Dietz et al. (**2014**) also analyzed the snow cover distribution and its changes from 1986 to 2014 using AVHRR data within the boundaries of Kazakhstan, Kyrgyzstan, Tajikistan, Turkmenistan and Uzbekistan, showing that both SCOD and SCMD shifted earlier in elevation zone between 2100 m and 3500 m, while no significant change of SCD was detected in any elevation zone.

In this study a series of snow cover statistics derived from the AVHRR snow cover extent data archive for the whole central Asia geographical region were analyzed to quantify 1) the spatial distribution and timing characteristics of snow cover duration, 2) effect of the

determining factors for seasonal snow cover distribution, including elevation, relative location to major mountain systems and latitude, and 3) the changing patterns of seasonal snow cover for the research period from 1986 to 2008.

2 Research Area

In this study central Asia (CA) is defined as the geographical region spanning from 51 °E to 113 °E, and from 32 °N to 56 °N, located in the center of the Eurasian continent (**Figure 4.01**). The Mongolian Steppe and the Gobbi Desert sit in its east, while the Caspian Sea is located in the west. Western Siberia and the Altai-Sayan Mountains sit in the north, while the Taklamakan and the Karakum deserts are located in the south. The CA region covers an area of ~ 6.3×10^6 km^2, including the entire territory of Kazakhstan, Kyrgyzstan, Tajikistan, Turkmenistan and Uzbekistan, as well as Xinjiang Autonomous Region in northwestern China and southwestern Siberia in Russia.

Though the major terrain type within CA is plains (**Figure 4.01**), CA is also home to major mountain systems extending for more than 5000 km in length, from the Altai Mountains in the north (**Figure 4.01-A**), the Tien Shan Mountains in the middle (**Figure 4.01-B**), to the Pamir Plateau in the south (**Figure 4.01-C**). High mountains in CA modulate the air mass movement and control moisture distribution and atmospheric pressure in low to mid latitude of Asia. Various studies have pointed out that the westerlies is the dominant wind in CA, bringing moisture to this region from as far as the Atlantic Ocean (**Aizen et al. 2004; Aizen et al., 2005; Aizen et al., 2009; Mölg et al., 2013**). The high mountains also serve as 'water towers' (**Barnet et al., 2005; Immerzeel et al., 2010**), capturing and storing solid

precipitation in winter as seasonal snow cover, and releasing melt water to rivers in spring and early summer.

CA is also home to several large endorheic basins. The Caspian Sea in the west of CA is the largest saline inland sea in the world. The Aral Sea, with water contributed mainly from the Amu Dar'ya River and the Syr Dar'ya River, has been suffering from desiccation problem since the 1960s due to water diversion for irrigated agriculture (**Micklin, 2007**). Another major inland river in CA is the Tarim River, which is the largest and longest inland river in China, flowing through the Taklamakan desert. The Lake Balkhash-Ili River Basin and the Lake Issyk Kul Basin are also large endorheic basins in CA. As the major rivers in these basins originate in high mountains, melt water from seasonal snow in high elevation provides vital water resources to arid or semi-arid plains in the lower reaches.

To better understand the spatial variability of seasonal snow cover and its changing patterns, CA is subdivided into 15 climatic regions (**Figure 4.01**), according to certain climatic considerations and topographical features (**Aizen et al., in preparation; Chapter 1**).

3 Data and methods

3.1 Snow cover statistics

Snow cover extent data derived from Advanced Very High Resolution Radiometer (AVHRR) were used as the basis for calculating snow cover statistics in this research. All AVHRR level1b data available for CA (**NOAA, 1998; NOAA, 2007**) were collected and processed with Special AVHRR Processing Software (SAPS) (**Khlopenkov et al., 2007**) for calibration and georectification. An aggregated rating based snow identification scheme was

used to generate daily AVHRR snow cover extent, which was further composited into 8-day maximum-snow-extent data. The 8-day maximum-snow-extent data went through a set of spatial and temporal filters for filling cloudy pixels or gaps (**Zhou, et al., 2013**). A series of snow cover statistics were calculated from the 1km resolution 8-day AVHRR Cloud/Gap Free Maximum Snow Extent data.

3.1.1 Snow Cover Area Percentage (SCAP) and Perennial Snow Cover Area Percentage (PSCAP)

The 8-day Cloud/Gap Free Maximum Snow Extent data at 1km resolution was synthesized into 5 km SCAP data by calculating the percentage of snow covered area within the 5 km grid, for representing the variation of snow cover in CA. Then PSCAP was computed as the minimum value of SCAP at each 5 km grid point in all 8-day periods from 1986 to 2008 to represent the spatial distribution of perennial snow and glaciers.

3.1.2 Snow Covering Days (SCD)

SCD is defined as the number of days covered by snow in a hydrological year for a grid point. The start of a hydrological year in CA is defined as August 29th, which is the start of 31st 8-day period, based on analysis of long term meteorological and hydrological data in the research region. SCD was first calculated at 1 km resolution then synthesized to 5 km resolution with the mean function.

3.1.3 Snow Cover Onset Date (SCOD) and Snow Cover Melt Date (SCMD)

SCOD and SCMD were calculated as the start and end of stable snow duration in a hydrological year at each 1 km grid point for describing the timing of seasonal snow cover using an approximation algorithm (**Wang et al., 2009; Zhou et al., 2013**). Both SCOD and

SCMD for each hydrological year calculated at 1 km resolution were then synthesized to 5 km resolution by the mean function.

SCOD is calculated by the following equation:

$$SCOD=D'-SCD', \quad \textbf{Equation 4.1}$$

where SCD' is the number of days with snow cover within the period of snow starting season, which was determined by the climate regime of the research region, while D' is the Julian day of the end of the defined snow starting season.

Similarly, SCMD is calculated as:

$$SCMD= D'' +SCD'', \quad \textbf{Equation 4.2}$$

where SCD'' is the number of days covered by snow within the period of snow melting season, and D'' is the Julian day of the start of the defined snow melting season.

Based on analysis of long term meteorological and hydrological data in the research region, the snow starting season is defined as from the start of a hydrological year, which is August 29th (the start of the 31st 8-day period in a year) to December 27th (the start of the 46th 8-day period in a year). The snow melting season is defined as the period from January 17th (the start of the 3rd 8-day period in a year) to the May 1st (the start of the 16th 8-day period in a year) for CA.

3.1.4 Maximum Snow Cover (SCmax) and Day of Maximum Snow Cover (DSCmax)

SCmax and DSCmax were derived from SCAP data at 5 km resolution, with SCmax defined as the maximum SCAP at each grid point in a hydrological year, and DSCmax as the corresponding date when SCmax was observed.

3.1.5 Long term mean snow cover statistics

Long term mean values, as well as standard deviations of SCAP, SCD, SCOD, SCMD, SCmax and DSCmax were calculated to represent the general distribution of seasonal snow cover in CA from 1986 to 2008.

Simple linear regression and segmented regression (**Muggeo et al., 2008**) with five different types of model formulations (**Table 4.2**) were conducted in R (*https://www.r-project.org/*) to analyze the dependence of long-term mean SCD ($\overline{SCD}$) on elevation and latitude in different climatic regions. Comparisons of the performance of these models for each climatic region were conducted based on adjusted R^2, AIC and ANOVA test with significance level at 0.05. Comparisons among the 'Only latitude', 'Only elevation' and 'Elevation and latitude' models show relative importance of elevation and latitude on $\overline{SCD}$ in different climatic regions. Comparison between 'Only elevation' and 'Breaking elevation', and comparison between 'Elevation and latitude' and 'Breaking elevation and latitude' examine and analyze the existence of segmented linear relationship between $\overline{SCD}$ and elevation.

3.2 Trend of change analysis

Both linear trend test and Mann-Kendall test (**Mann, 1945; Kendal, 1975**) were performed on time series of SCD, SCOD, SCMD, SCmax and DSCmax for detecting possible trend of change of snow cover statistics. The slopes calculated by Theil-Sen regression (**Theil, 1950; Sen, 1968; Fernandes et al., 2005**) were reported as indicators of the general direction and magnitude of change, for grid points where both tests show a same sign of change and have p-values less than 0.05.

Hierarchical Clustering (**Lattin et al., 2003**) analysis was applied at each climatic region for each trend slope calculated to group clustering points with same direction and similar magnitude of change together. Location (standardized projected x and y coordinates in meters) and magnitudes of significant trend of change were used as input variables. For each cluster, the mean and standard deviation of magnitudes of change were reported.

3.3 Auxiliary data

The Digital Elevation Model (DEM) obtained from the Consultative Group on International Agricultural Research (CGIAR) (*http://srtm.csi.cgiar.org/*) was used to describe topography in CA. The DEM at 90 m resolution has been reprojected to the same coordinate system (**Zhou, et al., 2013**) as the snow cover statistics data, and resampled to 5 km resolution.

Gridded monthly air temperature and precipitation dataset derived from an archive of 457 stations in CA was used in this study to provide a general overview of climate change during the research period in CA (**Chapter 2**). Regional averaged values of air temperature and precipitation were calculated in defined latitudinal and longitudinal ranges, corresponding to groups of regions (**Table 4.1**) in Aral Sea, Altai, northeastern Kazakh Steppe, Pamir and different parts of Tien Shan.

4 Results

4.1 Spatial distribution of seasonal snow cover

Long-term mean snow covering days ($\overline{SCD}$) (**Figure 4.03**) was used as the main seasonal snow cover characteristic in following analysis, since the long-term mean snow

cover onset date ($\overline{SCOD}$) (**Figure 4.04**) and the long-term mean snow cover melt date ($\overline{SCMD}$) (**Figure 4.05**) have very similar spatial distribution patterns as $\overline{SCD}$. The whole CA has an area weighted mean of 95.2 days for $\overline{SCD}$ with a standard deviation of 65.7 days. Comparison among these snow cover characteristics (**Figure 4.01, Figure 4.03, Figure 4.04, and Figure 4.05**) shows that the mountainous areas of Altai, Tien Shan and Pamir with elevation greater than 3000 m, accounting for 2.8% of total area in CA, are the places experiencing the highest $\overline{SCD}$, most of the time greater than 240 days. Those mountainous areas are also the places with the highest perennial snow cover area percentage (PSCAP) (**Figure 4.02**). Vast areas in northern CA, spanning from the Kazakh Steppe to the low elevation areas (< 3000 m) in Siberian Altai, have $\overline{SCD}$ in the range of 90 – 240 days; while southern CA with elevation lower than 3000 m, spanning from Aral-Caspian to Tarim, have $\overline{SCD}$ in the range of 0 – 90 days. Places with low values of $\overline{SCD}$ (0 - 30 days) account for 27.0% of total area in CA, which mainly distributed in deserts, including the Karakorum Desert spanning from Aral-Caspian to southeastern part of Western Pamir, the Taklamakan Desert in Tarim, and the Kumtag Desert at the southeastern part of Eastern Tien Shan. Low values of $\overline{SCD}$ below 30 days can also be observed in rain shadows of great mountains, such as the western coast of Lake Issyk Kul and the southeastern part of Inner Tien Shan (**Figure 4.03**).

Most places in CA have long-term mean maximum snow cover ($\overline{SCmax}$) higher than 95%. Two main places with $\overline{SCmax}$ less than 95% are the Karakorum Desert and the Taklamakan-Kumtag deserts spanning from Tarim to southeastern part of Eastern Tien Shan (**Figure 4.06**). The long-term mean day of maximum snow cover ($\overline{DSCmax}$) is later than Jan 1st for most places in CA. High mountains in Pamir, Tien Shan and Altai have earlier

$\overline{DSCmax}$ before Jan 5th, compared with vast areas with lower elevation (< 3000 m) which have $\overline{DSCmax}$ between Jan 5th and Jan 26th (**Figure 4.07**).

4.2.1 Plains

Aral-Caspian Desert (AD) has a short area weighted mean of $\overline{SCD}$ (36.2 $\pm$ 27.5 days). The shortest $\overline{SCD}$ (0 - 5 days) can be observed in its southwestern part along the seashore of the Caspian Sea, and in its southeastern part in the Karakum Desert. Longer $\overline{SCD}$ (108.1 $\pm$ 29.7 days) are observed along the Kopet Dag Mountains at the southern border of AD with the Iranian Plateau. Except for those local cases, the $\overline{SCD}$ shows an increasing trend along latitude, from about 10.6 $\pm$ 7.0 days at its southern part to about 54.0 $\pm$ 18.4 days in its northern part. The maximum snow coverage of 45.3% is observed at the 1st day of year (**Figure 4.08-2**). The snow cover shrinks quickly to below 0.01% on the 100th day of year (Apr 10), leaving only the Kopet Dag Mountains hosting remaining snow cover. After about the 300th day of year (Oct 27), snow cover starts building up.

Kazakh Steppe (KS) has a moderate value of average $\overline{SCD}$ (124.5 $\pm$ 32.6 days). The $\overline{SCD}$ increases with latitude, from about 91.6 $\pm$ 24.9 days in the south to 139.8 $\pm$16.1 days in the north. At maximum, 83.6% of KS area is covered by snow at the 1st day of year (**Figure 4.08-1**) and stays above 80% until approximately the 50th day of year (Feb 19), then drops down quickly to below 1% on the 110th day of year (Apr 20). The snow cover starts building up on approximately the 270th day of year (Sept 27).

4.2.2 Altai and surrounding areas

Siberian Altai-Sayan (SA) has a longer area weighted mean of $\overline{SCD}$ (172.1 $\pm$ 47.5 days) than its southeastern neighbor Mongolian Altai (MA) (101.3 $\pm$ 53.2 days),

because SA receives more moisture from the westerlies due to its northwest location to the Altai Mountains. High mountains (> 3000 m) facing north or west in SA have long $\overline{SCD}$ (294.0 $\pm$ 31.8 days). At lower elevation, when surrounded by high mountains the mean $\overline{SCD}$ is 123.1 $\pm$ 24.8 days, while in open environment, the mean $\overline{SCD}$ is longer at 166.3 $\pm$ 19.0 days. The maximum snow cover is observed at the end of a calendar year at about 75.0% (**Figure 4.08-4**). The snow coverage stays above 60% to around the 100th day of year (Apr 10), then goes down to below 1% on about the 170th day of year (Jun 19), while the snow cover expansion starts on around the 220th day of year (Aug 8).

MA also has long $\overline{SCD}$ in mountains with a mean value of 225.6 $\pm$ 45.7 days, though shorter than in the mountains of SA. The western Mongolia part of this climatic region experiences even shorter $\overline{SCD}$ (63.6 $\pm$ 21.8 days) compared with the southern part of this climatic region (103 $\pm$ 18.7 days), since it is surrounded by the Eastern Sayan Mountains in the north, the Mongolian Altai Mountains in the south, the Siberian Altai Mountains in the west and the Mongolian Plateau in the east. The snow coverage in MA reaches its maximum of 69.9% at the beginning of a calendar year (**Figure 4.08-5**), shrinks down to around 2% on the 160th day of year (Jun 9), and then starts expanding on around the 250th day of year (Sep 7).

4.2.3 Tien Shan and surrounding areas

Western Tien Shan (WT) has a short mean $\overline{SCD}$ (80.2 $\pm$ 67.8 days) mainly because of the existence of a large area of warm and dry plains in its western part with low values of $\overline{SCD}$ (37.6 $\pm$ 18.1 days), including the Fergana valley. The mountainous areas in the northeastern part of WT have longer $\overline{SCD}$ (227.6 $\pm$ 63.8 days). In WT, the maximum snow

cover of 58.8% of the total area happens on the 9th day of year (Jan 9), and decreases to the minimum of 2.2% on the 209th day of year (Jul 28) (**Figure 4.08-6**).

The mean $\overline{SCD}$ in Inner Tien Shan (IT) is 162.5 ± 79.5 days, while vast areas of high mountains greater than 3000 m in IT, including the At-Bashi and the Kokshal mountains, experience $\overline{SCD}$ around 204.1 ± 71.0 days. The lower plains to the western slope of those mountains have relative low $\overline{SCD}$, with a mean of 91.7 ± 2.1 days; while places located in rain shadow of those mountains at the eastern slope have mean $\overline{SCD}$ of 11.8 ± 3.9 days. The maximum snow cover of 86.1% happens on the 41st day of year (Fed 10) and goes down to the minimum of 16.5% on the 209th day of year (Jul 28) (**Figure 4.08-9**).

Northern Tien Shan (NT) has a mean $\overline{SCD}$ of 136.3 ± 70.3 days, and the high mountains in its northern and southern part have mean $\overline{SCD}$ of 259.5 ± 45.0 days, while its lower elevation plains experience a mean $\overline{SCD}$ of 81.4 ± 25.6 days. The valley in the southwestern part of NT between the Kirgizskiy and the Moldo Too Mountains, as well as the valley in the southeastern part of NT between the Ketman and the Kokshal Mountains, have $\overline{SCD}$ of 23.7 ± 13.7 days, which are the lowest in NT, due to their location in the rain shadow of mountains surrounding them. In general, the snow cover in NT shrinks from the peak of 80.7% on the 25th day of year (Jan 25) to the minimum of 5.0% on the 209th day of year (Jul 28) (**Figure 4.08-7**).

The climatic region of Issyk Kul (IK) has a mean $\overline{SCD}$ of 108.6 ± 97.2 days. The high elevation mountains in the northern and southern part of IK have long $\overline{SCD}$ (207.4 ± 78.6 days), while the lower plains surrounding the warm Lake Issyk Kul experience much shorter $\overline{SCD}$, from 3.0 ± 9.8 days at the western lake shore to 81.0 ± 23.4 days at the eastern

lake shore. The snow cover in IK reaches its maximum of 51.3% on the 41st day of year (Feb 10) and goes down to the minimum value of 9.0% on the 209th day of year (Jul 28) (**Figure 4.08-8**).

Central Tien Shan (CT) has a mean $\overline{SCD}$ of 111.5 ± 95.4 days, where the high mountains have high values of 206.4 ± 83.2 days, while the low elevation areas along foot of mountain ranges having low values of 32.8 ± 13.8 day. The lowest $\overline{SCD}$ (0 - 5 days) can be observed at the southeastern part of CT bordering TR, as this part of CT is sitting in the rain shadow of the Samin Ula Mountain. Its maximum snow cover of 60.2% happens on the 9th day of year (Jan 9) while the minimum coverage of 9.6% occurs on the 209th day of year (Jul 28) (**Figure 4.08-11**).

Eastern Tien Shan (ET) has a shorter mean $\overline{SCD}$ (75.8 ± 59.7 days) than other climatic regions in Tien Shan. Similar to other climatic regions, its high elevation mountain ranges experience long time of snow cover (212.6 ± 72.6 days). The ET can be further separated into a northern and a southern part by the mountain ranges extending from west to east in the middle of the region. The southern part (Turfan basin) has much shorter $\overline{SCD}$ (13.8 ± 8.2 days) compared with the northern (Jungar basin) one (90.6 ± 24.0 days). The snow cover in ET reaches its maximum status of 59.4% at the beginning of a year, and then shrinks down to about 2% on the 110th day of year (Apr 20). The snow cover starts accumulating on about the 270th day of year (Sept 27) (**Figure 4.08-10**).

Tarim (TR) is the climatic region with the shortest area weighted mean $\overline{SCD}$ (20.2 ± 27.2 days). It also has the highest coefficient of variation (1.35) of $\overline{SCD}$ among all climatic regions in CA, which suggests that snow only appears occasionally in most places in Tarim.

The minimum value of $\overline{SCD}$ of 0.0 shows that there are places in TR where snow had not been observed by AVHRR sensors during the 23-years research period. Areas with the shortest $\overline{SCD}$ (0 - 5 days) are mostly located at the eastern part of TR in the Kumtag Desert, while relatively longer $\overline{SCD}$ (104.7 $\pm$ 65.5 days) can be observed at high mountain ranges, e.g., the Kunlun Mountains in the southern part of TR bordering the Tibetan Plateau. The TR has much lower maximum snow coverage at about 27.9% compared with other climatic regions, happening on around the 9th day of year (Jan 9) (**Figure 4.08-3**). The snow cover goes down quickly to below 1% of the total area of TR on about the 50th day of year (Fed 19) and stay at similar values until about the 300th day of year (Oct 27), with snow cover only exists in high mountains during this time.

4.2.4 Pamir and surrounding areas

Western Pamir (WP) has an area weighted mean $\overline{SCD}$ of 83.7 $\pm$ 87.5 days, with large variation within the region. The high mountains in the eastern part of WP have a mean $\overline{SCD}$ of 238.0 $\pm$ 47.4 days, while the plains along the Amu Dar'ya River and its tributaries have a mean $\overline{SCD}$ of 10.9 $\pm$ 7.9 days. Valleys surrounded by mountains in WP also experience low $\overline{SCD}$ at a similar level. Its snow cover reaches the peak value of 56.4% on the 9th day of year (Jan 9), and shrinks down to the minimum of 3.1% on the 249th day of year (Sept 6) (**Figure 4.08-12**).

Pamiro-Alai (PA) has a mean $\overline{SCD}$ of 162.6 $\pm$ 86.0 days, with 47.8% of its area higher than 3000 m have a mean $\overline{SCD}$ of 237.5 $\pm$ 52.6 days. The relatively lower mountain valleys in PA, for example, the Zaravshan Valley in the west, have lower $\overline{SCD}$ at 53.6 $\pm$ 22.9 days. Similar to WP, it also sees the maximum snow coverage on the 9th day of year (Jan 9)

with a value of 80.6%, and the minimum snow coverage on the 249th day of year (Sept 6) with a value of 13.5% (**Figure 4.08-13**).

Central Pamir (CP), with most of its areas higher than 3000 m, has the longest mean $\overline{SCD}$ (256.7 $\pm$ 78.3 days) in all climatic regions. At maximum, 97.9% of CP is covered by snow on the 49th day of year (Feb 18), while the lowest amount of snow cover (40.4%) happens on the 257th day of year (Sept 14) (**Figure 4.08-14**).

Eastern Pamir (EP) has a shorter mean $\overline{SCD}$ (171.0 $\pm$ 94.9 days) compared with CP although it sits in the similar elevation range. Obstruction of moisture bearing westerly to EP by the high mountains in nearby WP and CP causes the lower $\overline{SCD}$ in EP. In EP, though high values of $\overline{SCD}$ (228.3 $\pm$ 80.5 days) can still be observed at high mountain regions (> 3500 m), the lower elevation valleys (1800 m – 3500 m) surrounded by mountains usually see quite short $\overline{SCD}$ (38.5 $\pm$ 42.2 days), with the smallest values (0 – 5 days) found in most of the eastern part, between the Sarikol and Taxkorgan ranges, or to the east of the Taxkorgan range. It has the maximum snow coverage of 83.5% on the 57th day of year (Feb 26) and shrinks down to the minimum of 32.2% on the 257th day of year (Sept 14) (**Figure 4.08-15**).

4.2 Factors affecting seasonal snow cover duration

It is well known that elevation, relative location to major mountains and latitude are the main factors determining the spatial distribution of seasonal snow cover (**Kotlyakov, 1997; Severskiy & Severskiy, 2003; Parajka et al., 2010; Dietz et al., 2014**). This section revisit this topic with more comprehensive and advanced data for CA, using $\overline{SCD}$ as the representative of snow cover duration.

4.2.1 Snow cover duration with elevation

Examination of the relationship between $\overline{SCD}$ with elevation (**Figure 4.09 and Figure 4.10**) for the whole CA shows the positive correlation between them with a mean increasing rate of 2.3 days / 100 m (Pearson's r = 0.34, p-value = 0.0). The magnitude of the correlation varies across different elevation zones and climatic regions.

Below ~2000 m, $\overline{SCD}$ is not strictly increasing with elevation, especially for the elevation zone below 1000 m (**Figure 4.09**). Climatic regions with substantial portions of flat areas below 1000 m, including KS, AD, SA and ET, all show weakened positive or even negative relationship between $\overline{SCD}$ and elevation for places under 1000 m. Tarim and Mongolian Altai, as climatic regions with large portion of flat areas, also have similar weakened positive relationship between $\overline{SCD}$ and elevation, for places below 3000 m and below 2000 m, respectively (**Figure 4.10**). This indicates that other variables, e.g. latitude, might also have a strong influence on $\overline{SCD}$ distribution for flat areas, which will be discussed in following part of this section.

Between 2000 m and 5000 m, the positive relationship between $\overline{SCD}$ and elevation is relatively stable compared with places under 2000 m. And the mean increasing rate for this elevation range is 5.8 days / 100 m, which is much higher than the mean increasing rate for the whole CA.

For places with elevation higher than 5000 m, the values of $\overline{SCD}$ in mountainous regions tend to stabilize at about 320 days (e.g., Eastern Pamir and Pamiro-Alai) (**Figure 4.10-15 and Figure 4.10-13**) to 350 days (e.g., Central Tien Shan and Central Pamir) (**Figure 10-11 and Figure 10-14**) without any increase with elevation. The stabilizing phenomenon is

related to the fact that under 5 km spatial resolution, most of the high elevation grid points with elevation greater than 5000 m are mainly filled with perennial snow or glaciers (**Figure 4.02**).

4.2.2 Snow cover duration and latitude

Examination of the relationship between $\overline{SCD}$ with latitude in condition of elevation (**Figure 4.11-a**) shows a positive relationship between $\overline{SCD}$ and latitude. Increasing rates of $\overline{SCD}$ by latitude for each 1000 m elevation zone were calculated, showing increasing rates of about 9 days / degree for elevation zones below 3000 m. In higher elevation the increasing rates tend to be higher, with the strongest increasing rate of 15.3 days / degree exists in the elevation zone above 4000 m (**Figure 4.11-b**).

4.2.3 Classification of climatic regions

Five different types of linear statistical models (**Table 4.2**) were fitted to the $\overline{SCD}$, elevation and latitude data in each climatic region. Climatic regions were classified into three groups based on comparisons of the performance of those models.

4.2.3.1 Plain climatic regions

Kazakh Steppe (KS, **Figure 4.10-1**) and Aral-Caspian Deserts (AD, **Figure 4.10-2**) are the only two climatic regions with the 'Only latitude' model performing significantly better than the 'Only elevation' model. The adjusted R^2 values for the 'Only latitude' model are 0.52 and 0.49 for KS and AD, respectively, while the adjusted R^2 values for the 'Only elevation' model are 0.02 and 0.01. This shows that for climatic regions with mainly flat plains, latitude might have a stronger influence on $\overline{SCD}$ than elevation.

Segmented regression with the 'Breaking elevation' model shows a critical elevation at ~1750 m for both KS and AD, separating the relationship between $\overline{SCD}$ and elevation to two parts. In the lower elevation part, $\overline{SCD}$ has large variations at the same elevation and smaller increasing rate of $\overline{SCD}$ by elevation, while in the higher elevation part $\overline{SCD}$ increases with elevation consistently and more quickly. Both climatic regions have similar increasing rates at the higher elevation zone, which are 12.1 days / 100 m and 11.3 days / 100 m, respectively. Comparisons among the 'Elevation and latitude', 'Breaking elevation' and 'Breaking elevation and latitude' models for these two climatic regions show that the performance of the first one is at a similar level as the latter two, despite the latter two's more complex structure. Such a lack of improvement of performance for complex models indicates that most of the variation of $\overline{SCD}$ in the lower elevation part in these two climatic regions can be accounted for by the effect of latitude.

4.2.3.2 Windward climatic regions

Climatic regions other than KS and AD can be classified to two groups based on the criteria whether a significant break of the relationship between $\overline{SCD}$ and elevation exists in the elevation range from 1000 m to 3000 m. For Siberian Altai-Sayan (SA, **Figure 4.10-4**), Western Tien Shan (WT, **Figure 4.10-6**), Northern Tien Shan (NT, **Figure 4.10-7**), Western Pamir (WP, **Figure 4.10-12**), Pamiro-Alai (PA, **Figure 4.10-13**) and Central Pamir (CP, **Figure 4.10-14**), the segmented regression with 'Breaking elevation' and 'Breaking elevation and latitude' either cannot find a significant breaking point, or the resulting linear model does not perform better than the corresponding simple linear model. This group was named as windward group since climatic regions in this group are in general located to the windward side of nearby major mountain systems. In this group, there are positive relationships between

$\overline{SCD}$ and elevation. The increasing rates are not constant but increase with elevation until elevation reaches ~5000 m, and the changes in these rates occur slowly and continuously.

4.2.3.3 Leeward climatic regions

For Mongolian Altai (MA, **Figure 4.10-5**), Issyk Kul (IK, **Figure 4.10-8**), Inner Tien Shan (IT, **Figure 4.3-9**), Central Tien Shan (CT, **Figure 4.10-11**), Eastern Tien Shan (ET, **Figure 4.10-10**), and Eastern Pamir (EP, **Figure 4.10-15**), segmented linear models perform better than corresponding simple linear models. This group was named as leeward group since these climatic regions are in general located to the leeward side of nearby major mountain systems. In this group, the increasing rates of SCD with elevation are insignificant at low elevation zone, speed up at a certain critical elevation, and then stabilize when the elevation reaches approximately 5000 m.

The increasing rates of $\overline{SCD}$ with elevation for MA are 1.2 days / 100 m and 15.9 days / 100 m, for places below and above 2215 m, respectively. In areas surrounding the Tien Shan Mountains, the critical elevation separating the relationship between SCD and elevation can be observed in the range from 2700 – 2900 m for different climatic regions. The increasing rates for the lower part are 5.5 days / 100 m, 5.2 days / 100 m, 1.7 days / 100 m and 1.6 days / 100 m, for IK, IT, ET and CT respectively; while for higher part the increasing rates are 16.3 days / 100 m, 11.5 days / 100 m, 16.2 days / 100 m and 15.7 days / 100m, respectively. The EP, sitting at the leeward side of Pamir Plateau, has the smallest increasing rate of $\overline{SCD}$ for low elevation (< 2750 m) at 0.4 days / 100 m, while the increasing rate for high elevation part is 13.2 days / 100 m, only 2 – 3 days smaller than in MA, ET and CT.

Tarim (TR) has shorter $\overline{SCD}$ at all elevation zones compared with any other climatic region in CA (**Figure 4.10-3**). The increasing rate of $\overline{SCD}$ is also smaller than in other climatic regions, and shows a break at around 3000 m. The increasing rates are 1.4 days / 100 m and 8.8 days / 100 m for places below and above 3000 m, respectively. Since several nearby mountains of the head water for Tarim River are also included, the elevation range for TR goes up to higher than 5000 m. TR has an exceptional low $\overline{SCD}$ (< 250 days) for the places above 5000 m because most of such high elevation areas are located at its far southeastern border with Tibetan Plateau with relatively low amount of precipitation (**Kotlyakov, 1997; Aizen et al., in preparation**).

4.2.4 Linear modeling of snow covering days

To synthesize the relationship between $\overline{SCD}$ with elevation and latitude, linear regression models for $\overline{SCD}$ using elevation and latitude as independent variables were fitted separately for plains, windward and leeward climatic regions (**Table 4.3**). For plains and windward climatic regions, the 'Elevation and latitude' model was used, while for leeward climatic regions the 'Breaking elevation and latitude' model was used. Latitude has a similar effect on $\overline{SCD}$ for all three types of regions. Elevation has similar effect for plains and windward climatic regions. In leeward climatic regions, the general critical elevation separating zones with different types of relationships is 2335 m detected by segmented regression. At lower elevation, the increasing rate for $\overline{SCD}$ with elevation is much smaller (0.7 days / 100 m) compared with the other two types of regions, though in higher elevation the $\overline{SCD}$ increases at a much faster rate (10.7 days / 100 m).

4.3 Trend of seasonal snow cover change

The evolution of area weighted mean monthly SCAP for the whole CA (**Figure 4.12**) during the past 23 years shows no significant trend of change. The annual area weighted mean SCAP for the whole CA dropped down to its minimum in 1988, increased to its maximum in 1993, then stayed relatively stable around the long term mean value of 25 days. Theil-Sen regression and Mann-Kendal test analysis of gridded SCD, SCOD, SCMD, SCmax and DSCmax were conducted, showing no significant trend of change for SCmax and DScmax for most places during the period from 1986 to 2008, while SCD, SCOD and SCMD exhibit spatial heterogeneous changes across CA (**Figure 4.13, Figure 4.14, and Figure 4.15**).

In places below 2000 m, the mean trend of change ($\overline{\alpha_{SCD}}$) for places with significant ($\alpha = 0.05$) change is slightly less than 0 days / year. The $\overline{\alpha_{SCD}}$ decreases with increasing elevation, with the lowest value of -1.57 days / year observed in the elevation range above 4000 m (**Figure 4.16-a**). The values of $\overline{\alpha_{SCD}}$ for most climatic regions are either around or below 0 days / year, except KS, ET and CT, which have $\overline{\alpha_{SCD}}$ at 0.13, 0.13 and 0.85 days / year, respectively (**Figure 4.16-b**).

4.3.1 Areas with decreasing seasonal snow

Vast areas of southern KS, northern AD, SA and MA experienced decreases of SCD. There are two main clusters with significant decreasing SCD: 1) places surrounding Aral Sea, where SCD decreased at a rate of -1.43 days / year while SCMD shifted earlier in the similar place with greater geographical extent to the east and southwest, at a rate of -1.00 days / year; 2) southern part of SA centered in the Altai-Sayan Mountains, where SCD decreased at a mean rate of -1.56 days / year, in companion with later SCOD (0.99 days / year) and earlier SCMD (-0.89 days / year).

Mountains in Tien Shan also experienced significant decreasing SCD. From ET and CT in the eastern branch of Tien Shan, to IT, IK, NT and WT in the western branch of Tien Shan, SCD decreased in places above 2000 m (**Figure 4.16-c-6 to Figure 4.16-c-11**). A cluster of significant decreasing SCD can be observed in the mountains between ET and CT, with a mean rate of decreasing SCD at -1.16 days / year, associated with later SCOD (0.68 days / year) and earlier SCMD (-0.73 days / year). In contrast, SCD increased in the lower elevation areas (< 3000 m) in ET and CT (**Figure 4.16-c-10 and Figure 4.16-c-11**). Another cluster of significant decreasing SCD is located in the mountains among southwestern NT, eastern WT and IT, with a mean rate of -1.18 days / year. In eastern WT mountains (> 3000 m), significant decreasing SCD occurred with an average rate of -1.22 days / year, associated with postponed SCOD (0.60 days / year) and earlier SCMD (-0.94 days / year). In southwestern NT mountains (2000 – 4000 m)**,** SCD decreased with a rate of -1.05 days / year, in companion with both later SCOD (0.63 days / year) and earlier SCMD (-0.75 days / year). SCD decreased nearly everywhere in IT, especially at its western and southern high mountains at elevation range from 2500 m to 4500 m, with an average rate of -1.28 days / year. Those places also witnessed earlier SCMD with a mean rate of -0.92 days / year. SCOD also turned later, but in a smaller area mainly at its southern high mountains with elevation greater than 3000 m, and with a smaller magnitude of 0.72 days / year.

Mountainous areas with elevation above 3000 m in Pamir, as well as in PA which is the transition zone between Pamir and Tien Shan, witnessed significant decreasing SCD (**Figure 4.16-c-12 to Figure 4.16-c-15**) with a mean rate of -1.59 days / year. In PA, SCD decreased significantly with an average rate of -1.28 days / year associated with earlier SCMD (-0.77 days / year) in the eastern end of the valley with high elevation (> 2500 m). In WP, the

eastern high mountains bordering CP and EP at elevation higher than 3000 m experienced decreasing SCD with a mean speed of -1.78 days / year. Those places also witnessed SCOD shifted later while SCMD moved earlier with rates of 0.75 days / year and -0.80 days / year, respectively. Most of the places in CP, especially its southern part with elevation higher than 4000 m, saw significant decrease of SCD at a mean rate of -0.80 days / year. The dominating feature of snow cover change in EP is the wide spread significant trend of decreasing SCD at a mean rate of -1.46 days / year, associated with delayed SCOD across different elevation zone from 2000 m to higher than 5000 m. The mean magnitude of change for the trend of SCOD is 0.84 days / year, with stronger magnitude at higher elevation, especially at the elevation range 4000 - 5000 m. There is less number of grid points with significant trend of change for SCMD, which mostly clustered in the center of EP with a mean change rate of -0.85 days / year.

4.3.2 Areas with increasing seasonal snow

Increasing SCD can be observed in the northeastern part of KS and the northwestern part of SA. Those places, as part of the center of Siberian High (north of 48 °N, east of 65 °E) in winter (**Jeong et al., 2011; Hasanean et al., 2013**), experienced an increase of SCD at a rate of 0.96 days / year, associated mainly with later SCMD (0.71 days / year).

Lower elevation areas below 2000 m in CT and ET also witnessed increasing SCD, in contrast with the decrease of SCD in their high mountain areas (> 2000 m) (**Figure 4.16-c-10 and Figure 4.16-c-11**). In CT, places along its southeastern border with Tarim at the elevation zone of 1000 - 2000 m saw increasing SCD with a mean rate of 1.52 days / year, as well as earlier SCOD (-0.64 days / year) and later SCMD (0.85 days / year). In the northern and northeastern part of ET, significant increase of SCD spread widely across different

elevations with an average rate of 1.58 days / year. The increasing trend of SCD was associated with earlier SCOD (-1.01 days / year) and later SCMD (0.92 days / year).

Mid-elevation areas in the western part of the climatic regions WT, PA and WP also experienced significant increasing of SCD. In WT, places in the elevation range of 1000 – 2000 m (**Figure 4.16-c-6**) to the west of the Ugamskiy Range and the Chatkalskiy Range have increasing SCD with an average rate of 1.15 days / year, associated with earlier SCOD at an average rate of -0.82 days / year; while SCMD did not have significant trend. In PA, there exist patches of places with increasing SCD (1.24 days / year) associated with earlier SCOD (-0.72 days / year) in the western opening of the valley at the elevation range 1000 m – 2000 m (**Figure 4.16-c-13**). In the northwestern part of WP bordering PA, places to the west of mountain ranges at elevation range 1000 m - 3000 m (**Figure 4.16-c-12**) experienced an increase of SCD at an average rate of 0.83 days / year, as well as SCOD shifting earlier with a mean rate of -0.72 days / year.

5 Discussion

5.1 Spatial distribution of snow cover

As presented in section 4.2, elevation is the determining factor for the distribution of long-term mean snow covering days, though the relationship varies across different climatic regions, while latitude also has a strong influence in KS and AD. Differentiation of the relationship between snow covering days and elevation is mainly related to the climatic region’s relative location to nearby major mountains and plateaus (Altai, Tien Shan, and Pamir).

Leeward climatic regions tend to have shorter $\overline{SCD}$ at the same elevation compared with corresponding windward climatic regions. MA has shorter mean values of $\overline{SCD}$ at all elevation zones than SA (**Figure 4.17-a**), and the differences are most distinct (up to 100 days) in elevation zones 1000 m - 2000 m and 2000 m - 3000 m. EP also has shorter $\overline{SCD}$ than other climatic regions in Pamir, with the highest difference of about 145 days happens in the elevation belt from 3000 m – 4000 m (**Figure 4.17-c**). Comparison of the $\overline{SCD}$ distribution in windward and leeward side in Tien Shan (**Figure 4.17-b**) shows that values of mean $\overline{SCD}$ in windward climatic regions are about 70 days longer than leeward climatic regions in the elevation zones 1000 m - 2000 m and 2000 m - 3000 m, and about 20 days longer in the elevation zone 3000 m - 4000m. For places above 4000 m or lower than 1000 m, the leeward side has slightly longer mean $\overline{SCD}$, with differences less than 20 days.

The distribution of $\frac{SCD}{Elev}$ is not homogeneous within each climatic region. For example, the mid-elevation (2000 m – 3000 m) zones in WT and WP with orthogonal direction to the westerlies tend to have both higher SCD and stronger $\frac{SCD}{Elev}$ than other places in these two climatic regions. In CT and EP, areas landlocked by nearby mountains tend to have longer SCD and smaller $\frac{SCD}{Elev}$ than other places in the same climatic region. The effects of relative location to major nearby mountains have been accounted for at a regional scale by classification of climatic regions as windward or leeward, while the local scale effect has not been fully accounted for. To further analyze the influence of the relative location the formulation of appropriate indices for the local scale effect might be required. A combination of elevation, latitude and relative location might be the basis for a geographical distributed statistical model for long term snow cover distribution. Such a model will be useful for

providing simple but realistic schemes for parameterization in hydrological / climate / land surface modeling, as well as a useful tool for water sources management.

5.2 Change of snow cover

Places surrounding Aral Sea have experienced significant decrease of SCD, mainly associated with earlier SCMD. The spring temperature in this region increased with a rate of 0.09 °C / year, while the winter precipitation decreased with a rate of -0.55 mm / year (**Figure 4.18**). The Altai climatic regions, especially SA also witnessed significant decreasing SCD. The annual temperature increased significantly at a rate of 0.03 °C / year, while annual precipitation decreased at a rate of -2.39 mm / year. The change of spring temperature accounts for most of the annual temperature change, with an increasing trend of 0.07 °C / year (**Figure 4.19**).

In high mountains of Tien Shan and Pamir, SCD decreased significantly mainly associated with earlier SCMD, though Central Pamir was also affected by widespread delayed SCOD. Linear trend analysis suggests that both Pamir and Tien Shan have experienced significant increases of spring temperature at rates of 0.06 and 0.05 days / year, respectively (**Figure 4.20 and Figure 4.21**), while the annual and winter air temperature and annual and seasonal precipitation do not have significant changes.

Comparisons of the annual and seasonal temperature and precipitation trends for places with significant decreasing SCD suggests that the increasing spring air temperature is a main driving factor for the decreasing SCD. This also explains the more widespread and stronger trend of decreasing SCMD (earlier snow melt) compared with the trend of increasing SCOD (later snow accumulation) (**Figure 4.15 and Figure 4.16**).

Significant increase of SCD can be observed in the northeastern Kazakh Steppe. Several studies have reported increasing Eurasian snow cover after the mid-1990s (**Jeong et al., 2011**), especially in Siberia which is close to the northeastern KS. The Siberian High (SH) has seen a resurgence in recent years since the mid-1990s after a long term decline from the late 1960s to the early 1990s (**Jeong et al., 2011**). Cohen et al., (**2010**) and Jeong et al. (**2011**) suggest the increasing snow cover in southern Siberia lead to the bouncing back of SH. The spring precipitation increased with a rate of 0.78 mm / year, though not significantly, which might help explain the increase of SCD. SCD also increased significantly in the low elevation areas between Tarim and Central Tien Shan and in low elevation places in Eastern Tien Shan. The winter temperature at this region decreased at a rate of -0.06 °C / year, while winter precipitation increased at a rate of 0.17 mm / year (**Figure 4.23**), which is in favor of increasing SCD.

Compared with our previous study about snow cover changes in the Amu Dary'a Basin (**Zhou et al., 2013**), the results reported in this chapter confirmed the previous findings of decreasing SCD and SCMD shifting later in most places in the Amu Dary'a basin, while SCOD has shifted earlier in Western Pamir and delayed in Central Pamir. This study provides much more spatial details about the heterogeneous snow cover changes for CA, as the trend detection have been conducted at the level of grids with 5 km resolution, instead of the level of elevation zones. An independently conducted analysis of snow cover change in the Central Asian republics from 1986 to 2014 (**Dietz et al., 2014**) has drawn conclusions which are slightly different compared with what has been found in this chapter. The authors reported that a general negative trend of SCD cannot be found, which might be a result of different research period. It is also possible that the different spatial scale of the trend statistic

calculation might lead to the different conclusions about SCD changes, as the authors are conducting trend statistics calculation at each 100 m elevation zones across the Central Asia Republics. Both studies are in agreement that SCMD shifted earlier, especially in the elevation from 2000 – 3500 m.

The decreasing SCD in high mountains in Altai, Tien Shan and Pamir in the research period from 1986 to 2008, as presented in section 4.3.1, can result in a decrease of water resource in CA, as less water is available stored in seasonal snow cover in the cold season. The earlier SCMD, associated with a significant increase of spring air temperature in those mountain regions might lead to a change of the timing and seasonal distribution of streamflow.

6 Conclusion

Analysis of the long term mean snow cover statistics shows that the whole CA has an area weighted mean of $\overline{SCD}$ of 95.2 $\pm$ 65.7 days, with most places have $\overline{SCmax}$ greater than 95% before Jan 26th. High mountainous regions of Altai, Tien Shan and Pamir, accounting for ~2.8% of total area in CA, have $\overline{SCD}$ longer than 240 days and $\overline{DSCmax}$ before Jan 5th. The northern part of CA, from Kazakh Steppe to Siberian Altai and Mongolian Altai, have SCD in the range of 90 - 240 days, while the southern part of CA have SCD in the range of 0 – 90 days. Deserts and rain shadows of major mountains, which also accounts for about 27.0% of total area in CA, have $\overline{SCD}$ in the range of 0 - 30 days.

Simple linear regression and segmented linear regression analysis show that elevation is the most important factor determining the distribution of $\overline{SCD}$ among elevation, latitude and relative location to major mountains. The relationship between $\overline{SCD}$ and elevation varies

according to the relative location to nearby major mountain systems. Latitude also has a strong influence in plain climatic regions (Kazakh Steppe and Aral-Caspian Desert). Climatic regions other than KS and AD were classified as windward and leeward regions, based on the different types of relationship between SCD and elevation. A positive relationship with a magnitude of 5.9 days / 100 m can be found for plains and windward side mountainous regions, while the magnitude changes from 0.7 days / 100 m to 10.0 days / 100 m at ~2335 m for leeward side mountainous regions. Latitude affects the distribution of $\overline{SCD}$ with a magnitude of 9 – 10 days / degree.

Analysis of the snow cover change reveals several areas with different types of snow cover change. Increasing SCD can be observed in the northeastern Kazakh Steppe with a rate of 0.96 days / year, lower elevation area below 2000 m in Central Tien Shan and Eastern Tien Shan with a rate of about 1.5 days / year, as well as mid-elevation areas (1000 m – 3000 m) in Western Tien Shan, Pamiro-Alai and Western Pamir with rates of 1.15 days / year, 1.24 days / year and 0.83 days / year, respectively. Decreased SCD can be observed at places surrounding Aral Sea with a rate of -1.43 days / year while SCMD shifted earlier in the same place though with greater geographical extent. Mountains in Altai, Tien Shan and Pamir also witnessed significant decreases of SCD, with rates of -1.56 days / year, -1.16 days / year and -1.59 days / year. Such decreases of SCD mainly associated with earlier SCMD, with rates of -0.89 days / year, -0.73 days / year and -0.81 days / year for mountainous areas in Altai, Tien Shan and Pamir, respectively. The decreases of SCD and the SCMD shifting earlier can be attributed mainly to the significant strong increase of spring air temperatures.

Tables

Table 4.1 Region definitions as longitudinal and latitudinal ranges

Region	description	latitudinal range	longitudinal range
Aral Sea	Places surrounding Aral Sea	52.5°N – 67.5 °N	42.5°E – 47.5 °E
Northeastern KS	Northeastern part of Kazakh Steppe	50 °N – 55 °N	70 °E – 82.5 °E
Altai	Siberian Altai-Sayan and Mongolian Altai	47.5 °N - 52.5 °N	80 °E - 95 °E
Pamir	Central Pamir and Eastern Pamir	37.5 °N - 40 °N	72.5 °E - 75 °E
Western mountains of Tien Shan	junction of major mountains among Tien Shan climatic regions	40 °N – 42.5 °N	70 °E - 80 °E
Boundary zone among Central Tien Shan, Tarim and Eastern Tien Shan	Lower plains spanning from Central Tien Shan to Tarim and Eastern Tien Shan	40 °N – 42.5 °N	80 °E - 90 °E

Table 4.2 Linear models for $\overline{SCD}$ with elevation and latitude

ID	short name	formula in R style	description
1	Only latitude (OL)	SCD ~ Lat	$\overline{SCD}$ depends on latitude only
2	Only elevation (OE)	SCD ~ Elev	$\overline{SCD}$ depends on elevation only
3	Elevation and latitude (EL)	SCD ~ Elev + Lat	$\overline{SCD}$ depends on both elevation and latitude
4	Breaking elevation (BE)	SCD ~ Elev : I(Elev > critical_elevation)	$\overline{SCD}$ depends on elevation only, with the relationship breaks at a certain critical elevation
5	Breaking elevation and latitude (BEL)	SCD ~ Elev : I(Elev > critical_elevation) + Lat	$\overline{SCD}$ depends on elevation and latitude, with the relationship breaks at a certain critical elevation

Table 4.3 Regression result for $\overline{SCD}$ with elevation and latitude for different types of climatic regions[16]

Region name	Regression model	R^2
Plains	SCD = 0.0585 elev + 9.6778 lat – 380.0674	0.8927
Leeward side mountainous regions	SCD = 0.0068 elev + 10.0256 lat - 388.9821 (elev < 2335) SCD = 0.1004 elev + 10.0256 lat - 388.9821 (elev >= 2335)	0.7181
Windward side mountainous regions	SCD = 0.0611 elev + 9.1655 lat – 366.9686	0.8234

Figures

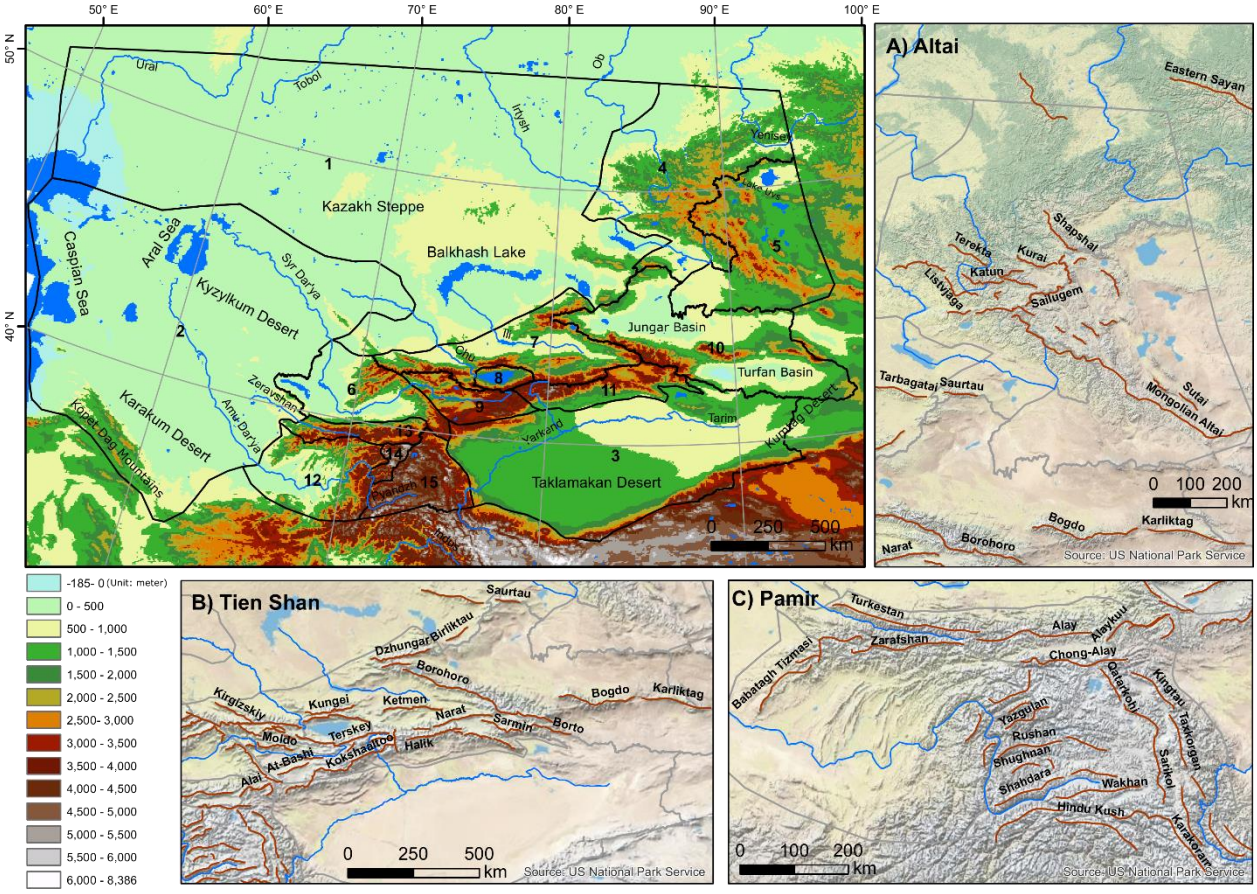

Figure 4.01 Topography and climatic regions in central Asia (CA)

Main map shows the digital elevation model derived from GGIAR SRTM data and division of climatic regions in CA:

1: Kazakh Steppe (KS), 2: Aral-Caspian Desert (AD), 3: Tarim (TR); 4: Siberian Altai-Sayan (SA), 5: Mongolian Altai (MA); 6. Western Tien Shan (WT), 7: Northern Tien Shan (NT), 8: Issyk Kul (IK), 9: Inner Tien Shan (IT), 10: Eastern Tien Shan (ET), 11: Central Tien Shan (CT); 12: Western Pamir (WP), 13: Pamiro-Alai (PA), 14: Central Pamir (CP), 15: Eastern Pamir (EP)

Inset maps A), B) and C) show major mountain systems in Altai, Tien Shan and Pamir.

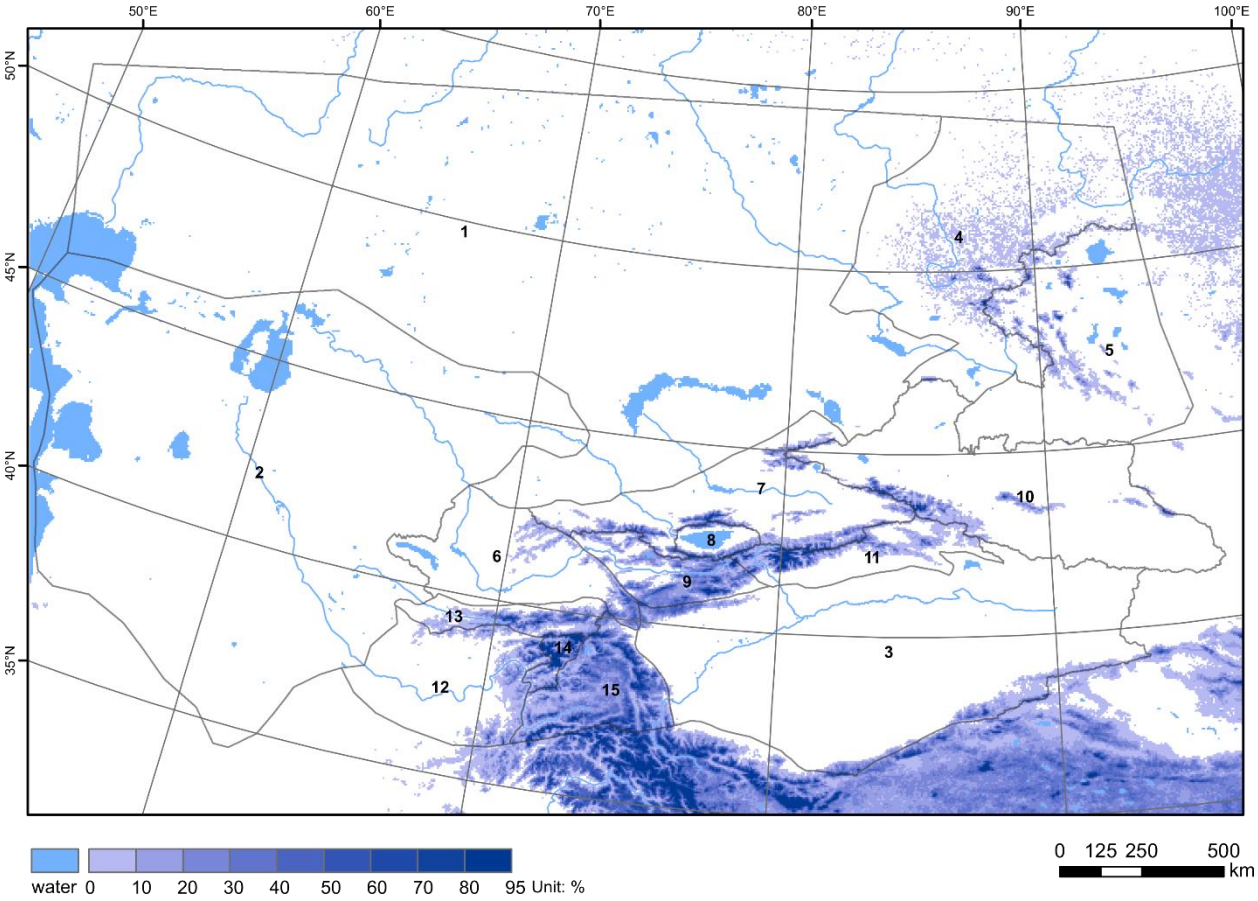

Figure 4.02 Perennial Snow Cover Area Percentage (PSCAP) from 1986 to 2008 in CA

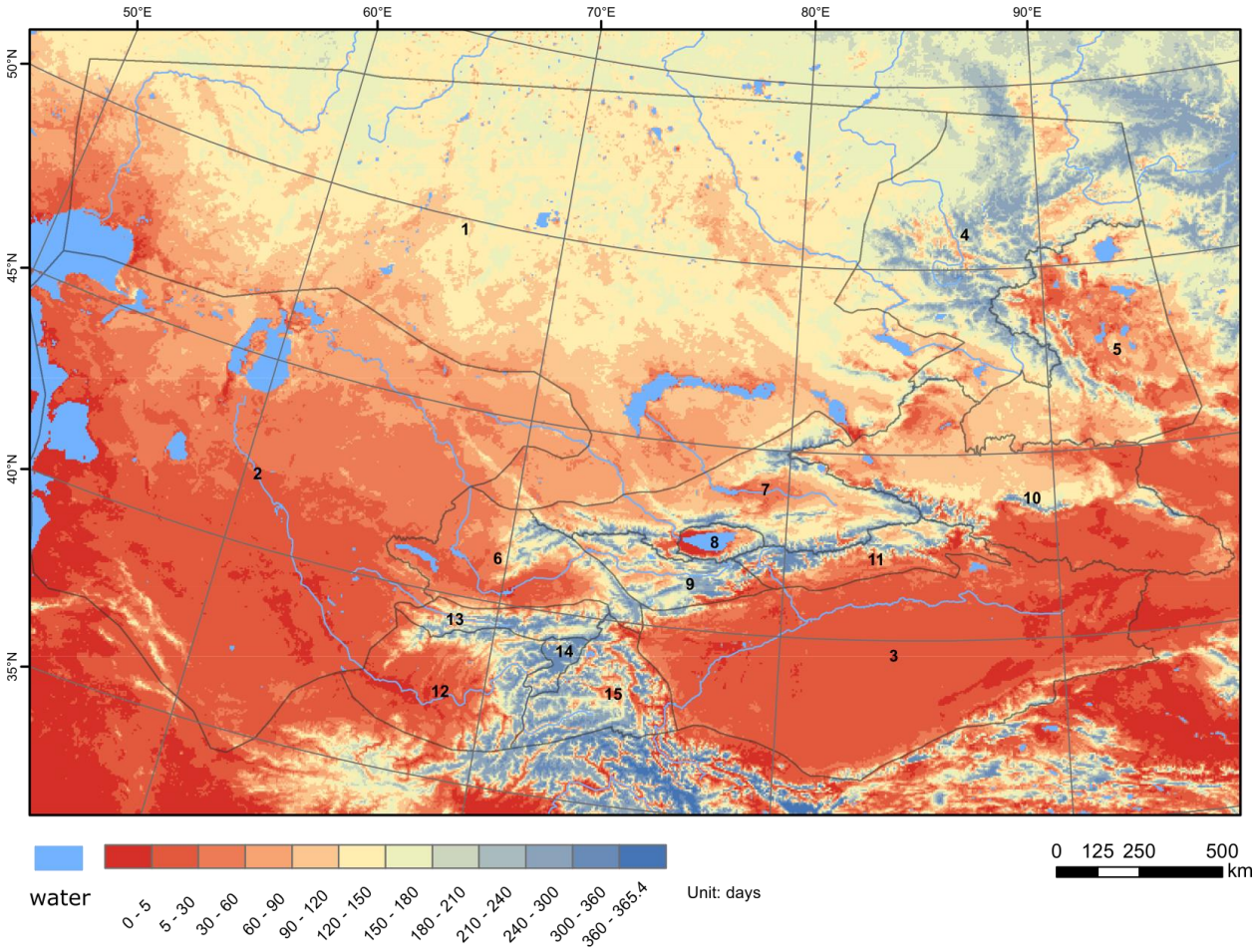

Figure 4.03 Long-term mean Snow Covering Days (SCD) from 1986 to 2008 in CA

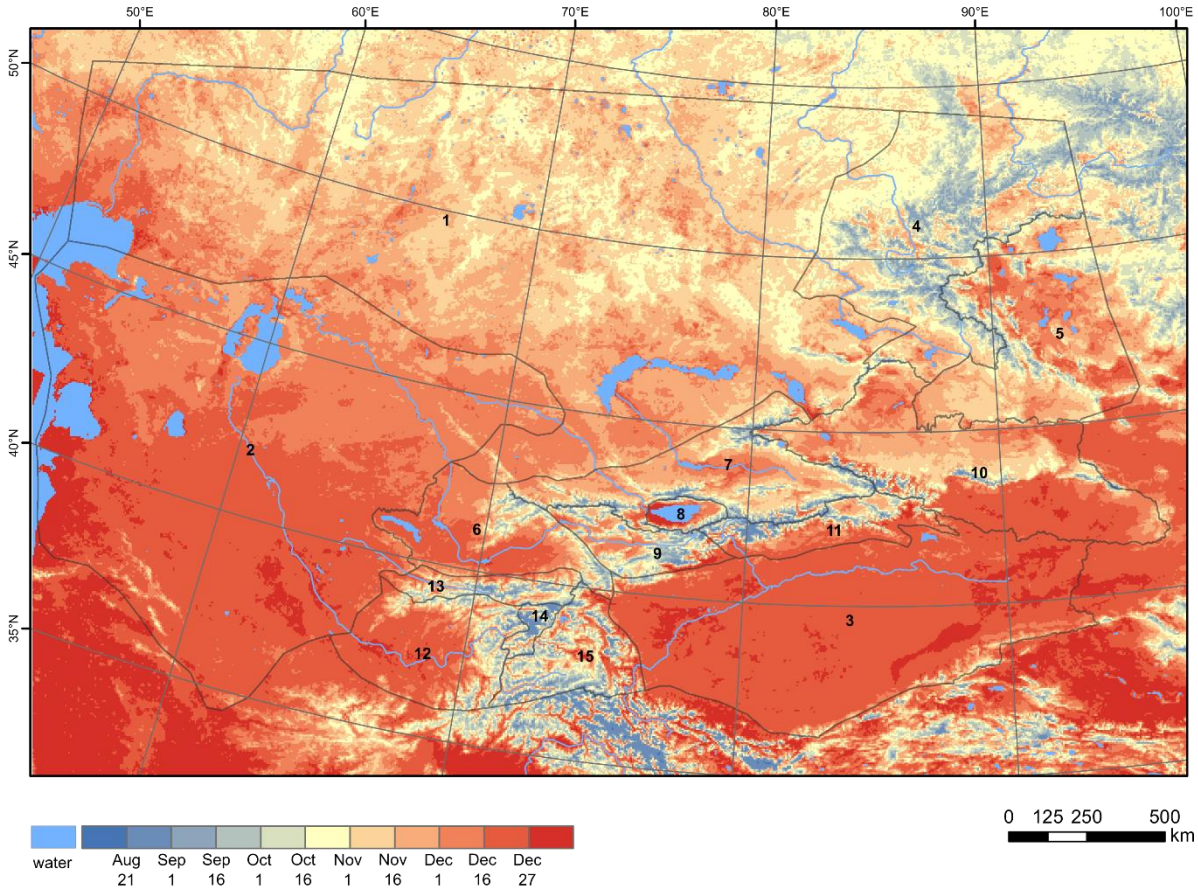

Figure 4.04 Long-term mean Snow Cover Onset Date (SCOD) from 1986 to 2008 in CA

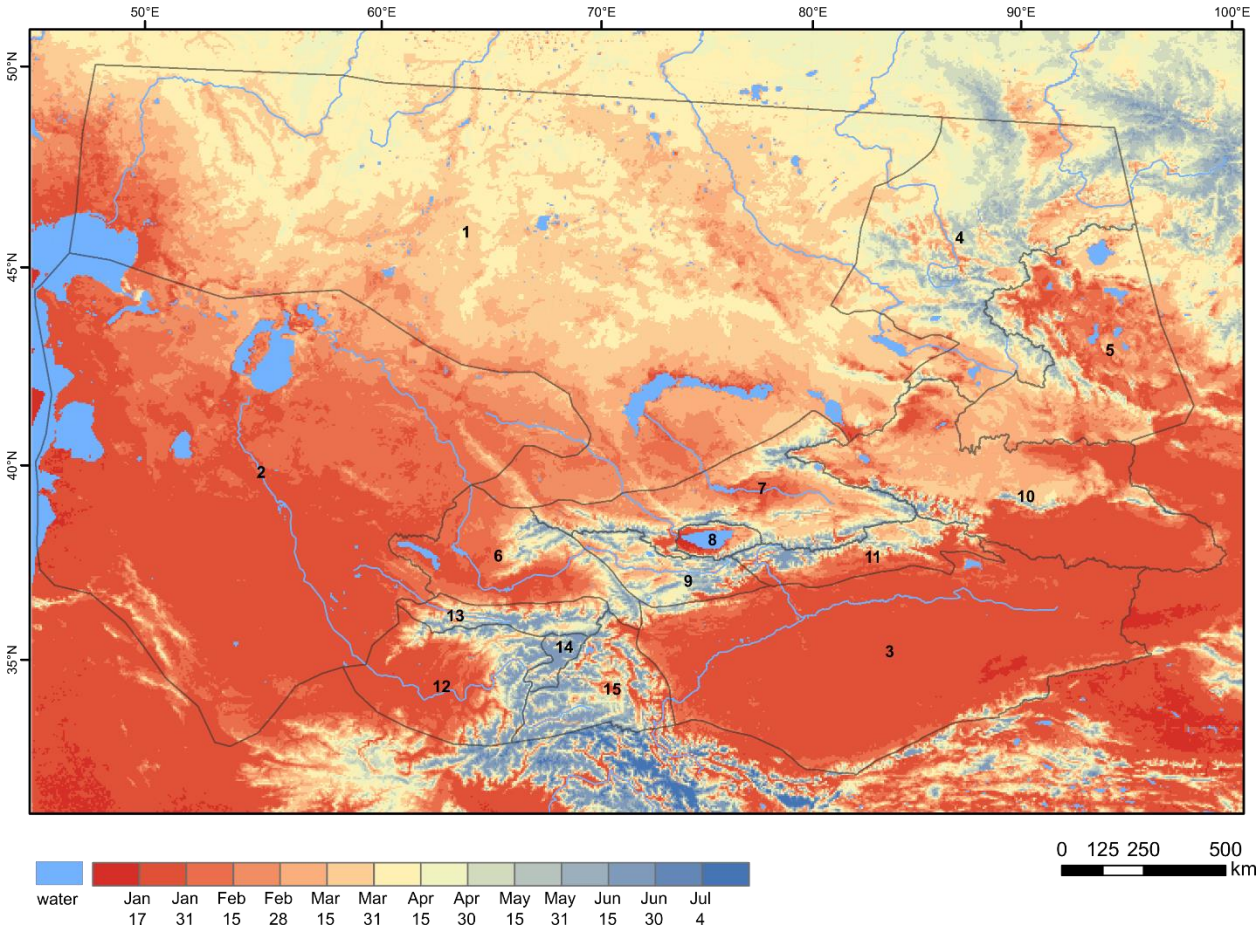

Figure 4.05 Long-term mean Snow Cover Melt Date (SCMD) from 1986 to 2008 in CA

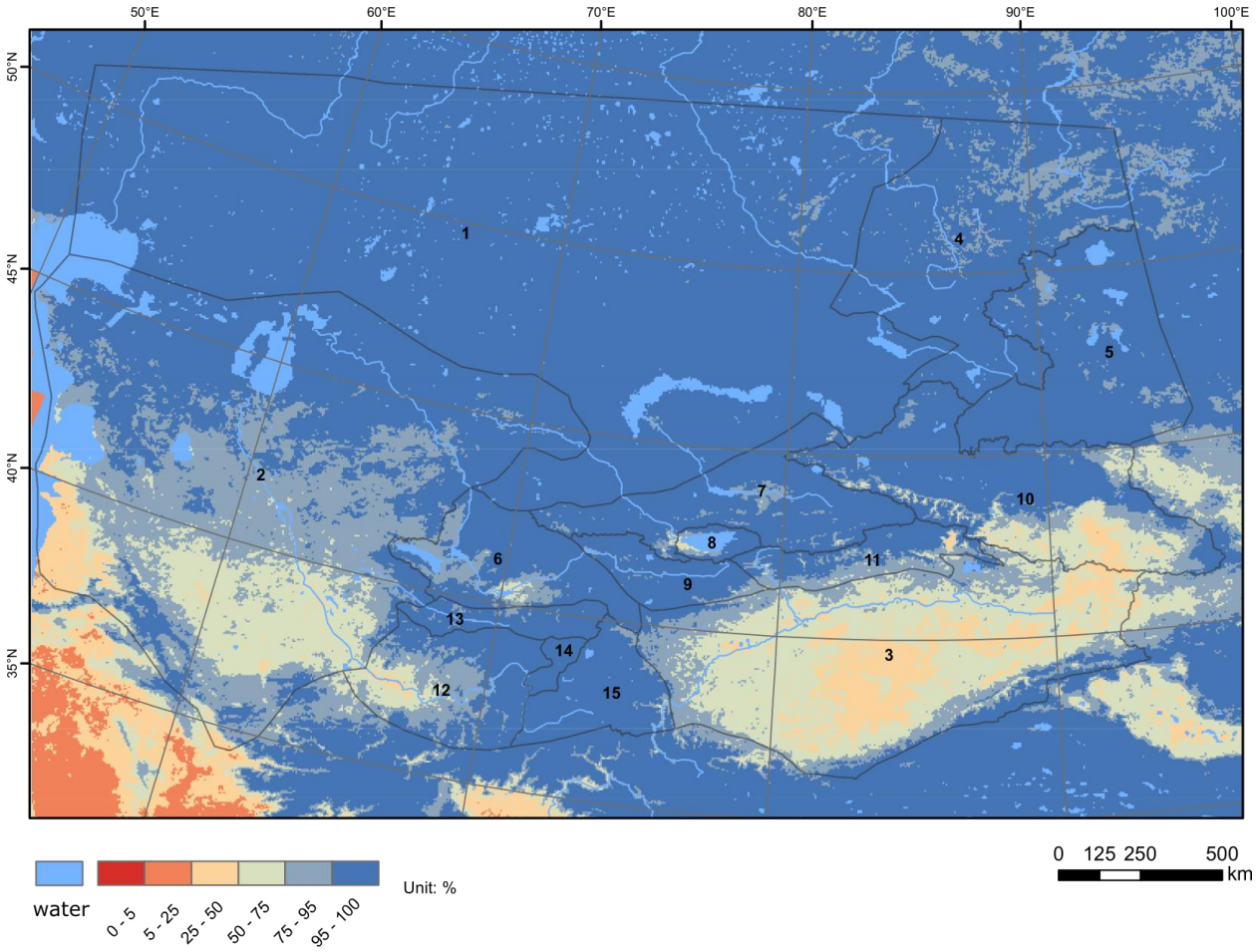

Figure 4.06 Long-term mean Maximum Snow Cover Area Percentage (SCmax) from 1986 to 2008 in CA

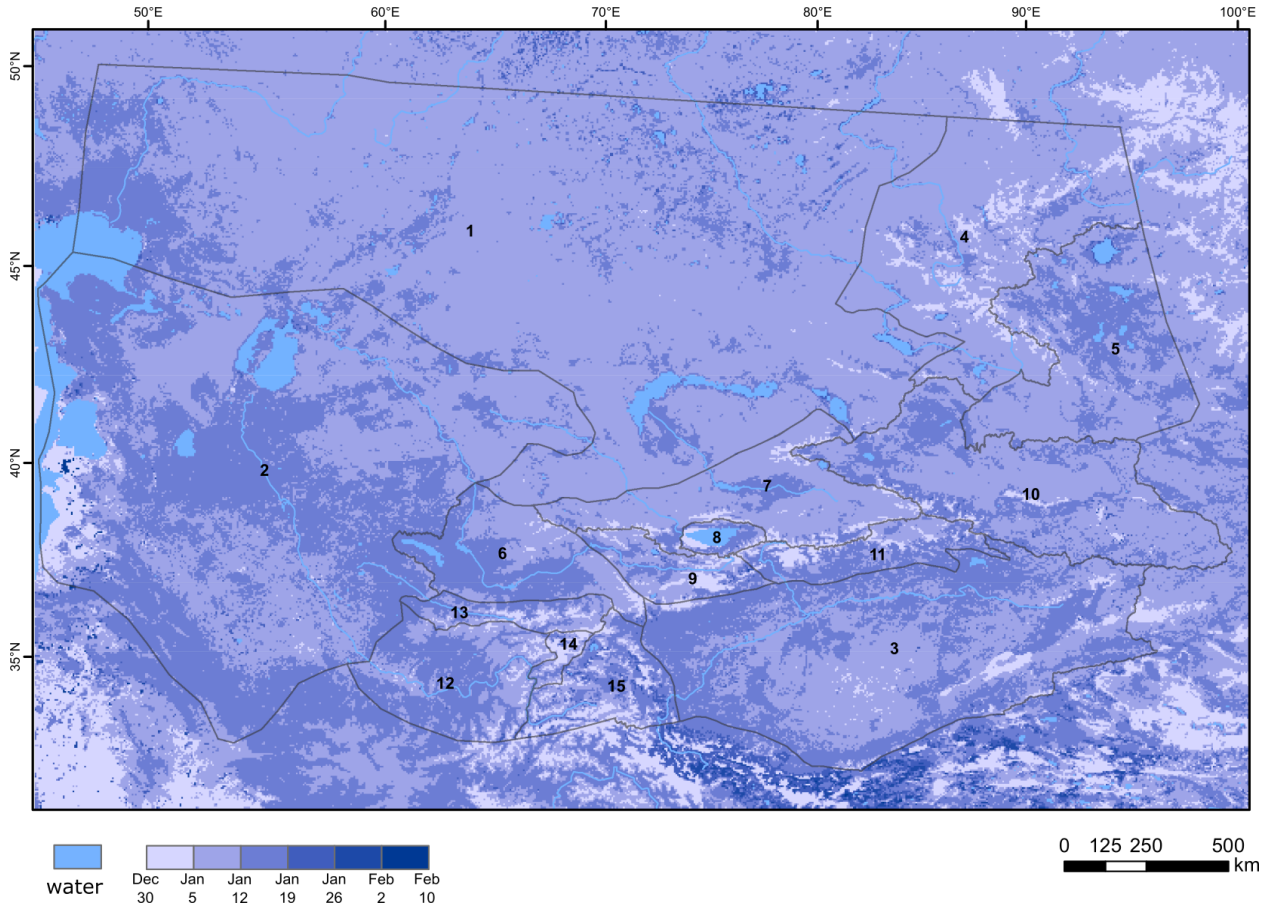

Figure 4.07 Long-term mean Day of Maximum Snow Cover (DSCmax) from 1986 to 2008 in CA

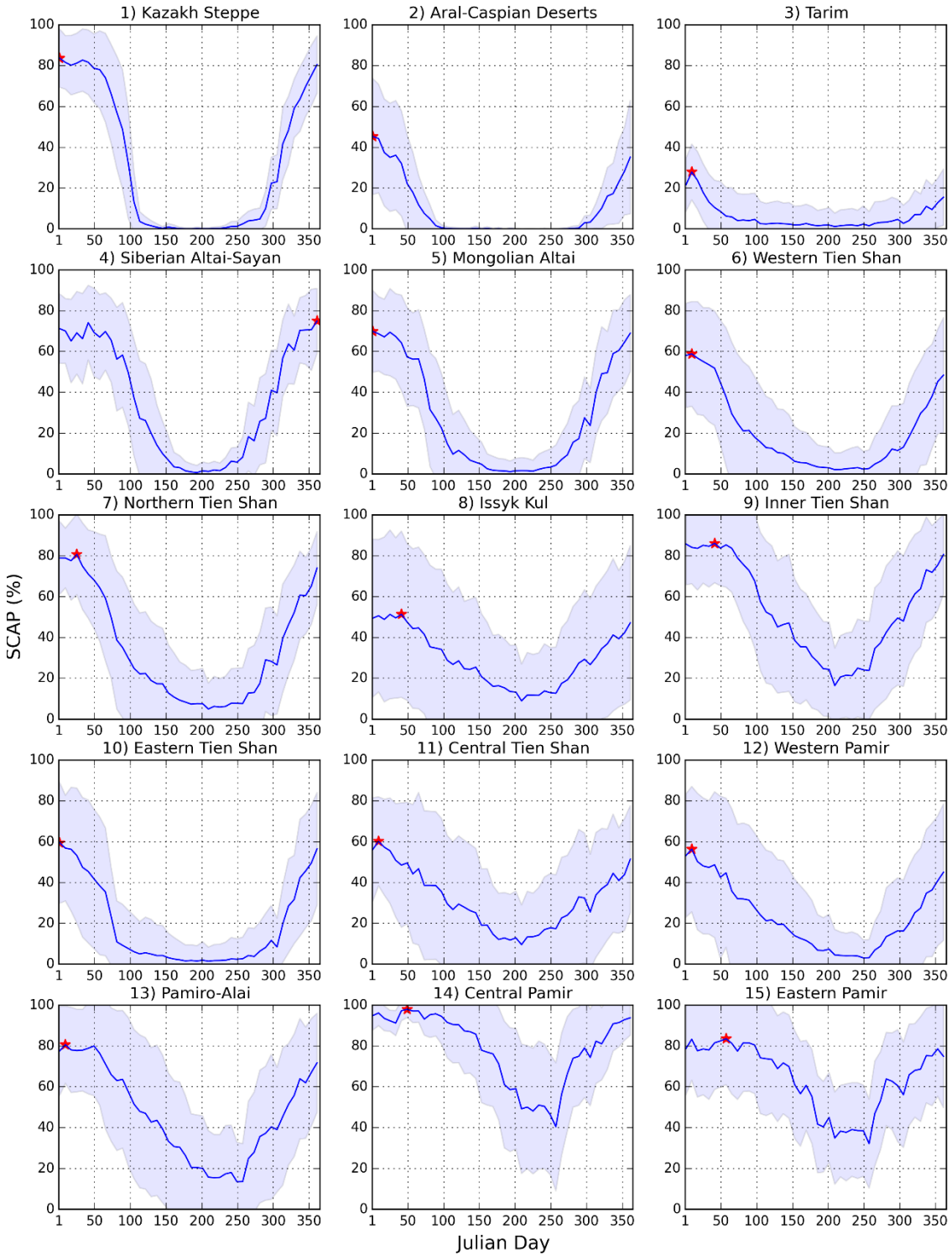

Figure 4.08 Long-term mean 8-day SCAP and maximum SCAP for each climatic region

The star shows the date for maximum SCAP, while light blue span indicates 2 std of SCAP

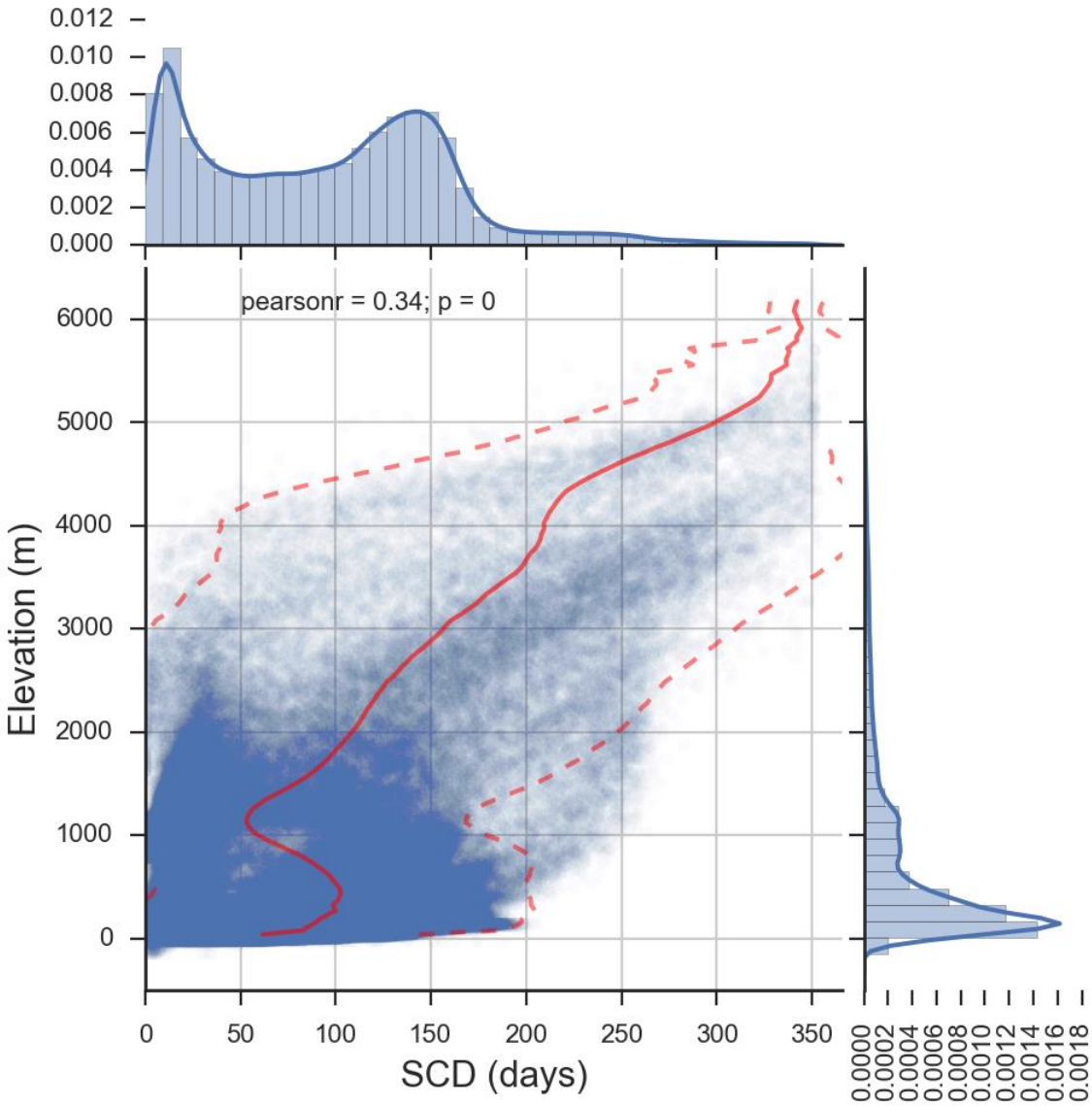

Figure 4.09 Scatterplots of long-term mean SCD against elevation in CA

red solid line showing the moving mean, dash lines showing the extent of 2 moving std

upper panel depicting the histogram and density of SCD distribution

right panel depicting the histogram and density of elevation distribution

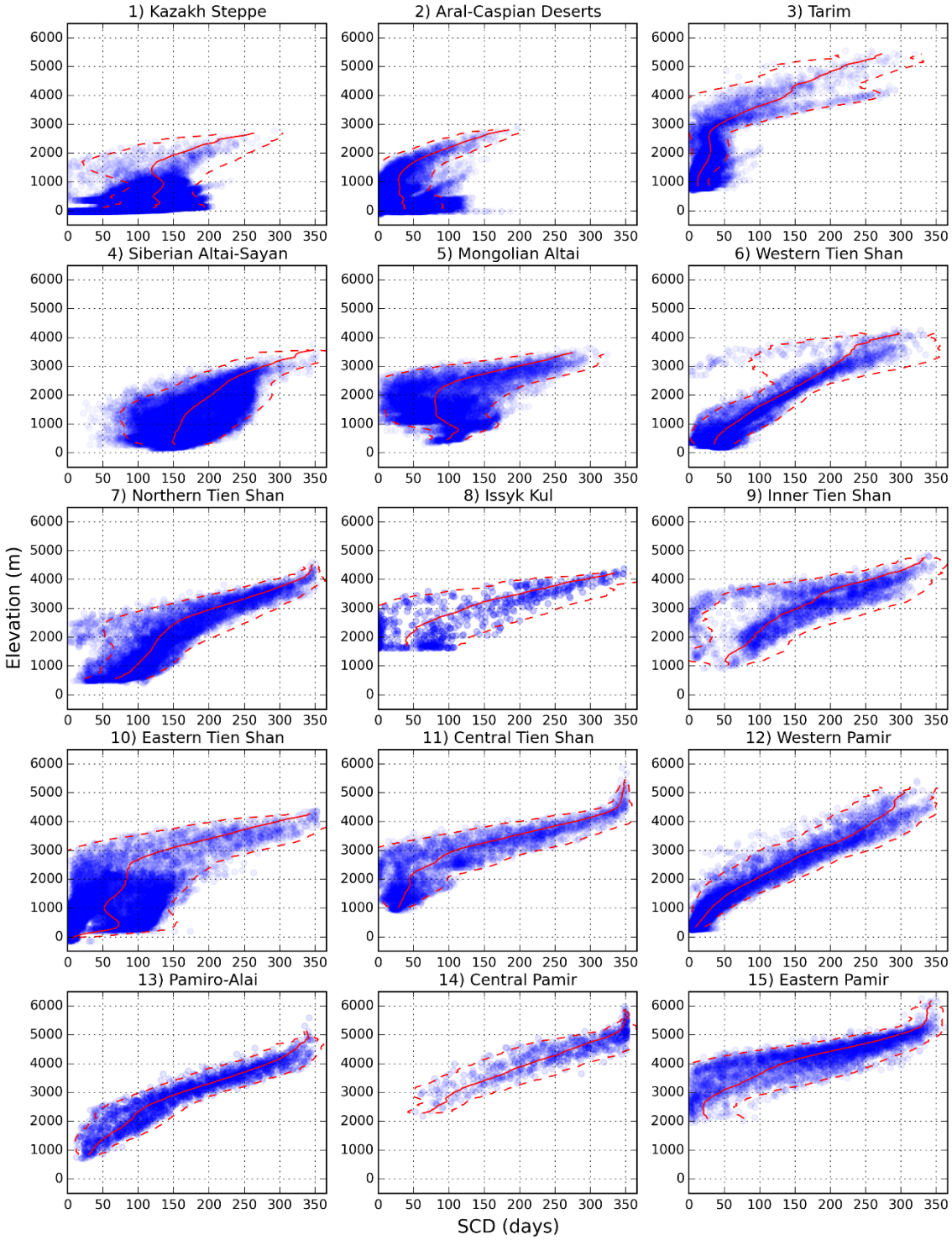

Figure 4.10 Scatterplots of long-term mean SCD against elevation in each climatic region

red solid line showing the moving mean, dash lines showing the extent of 2 moving std

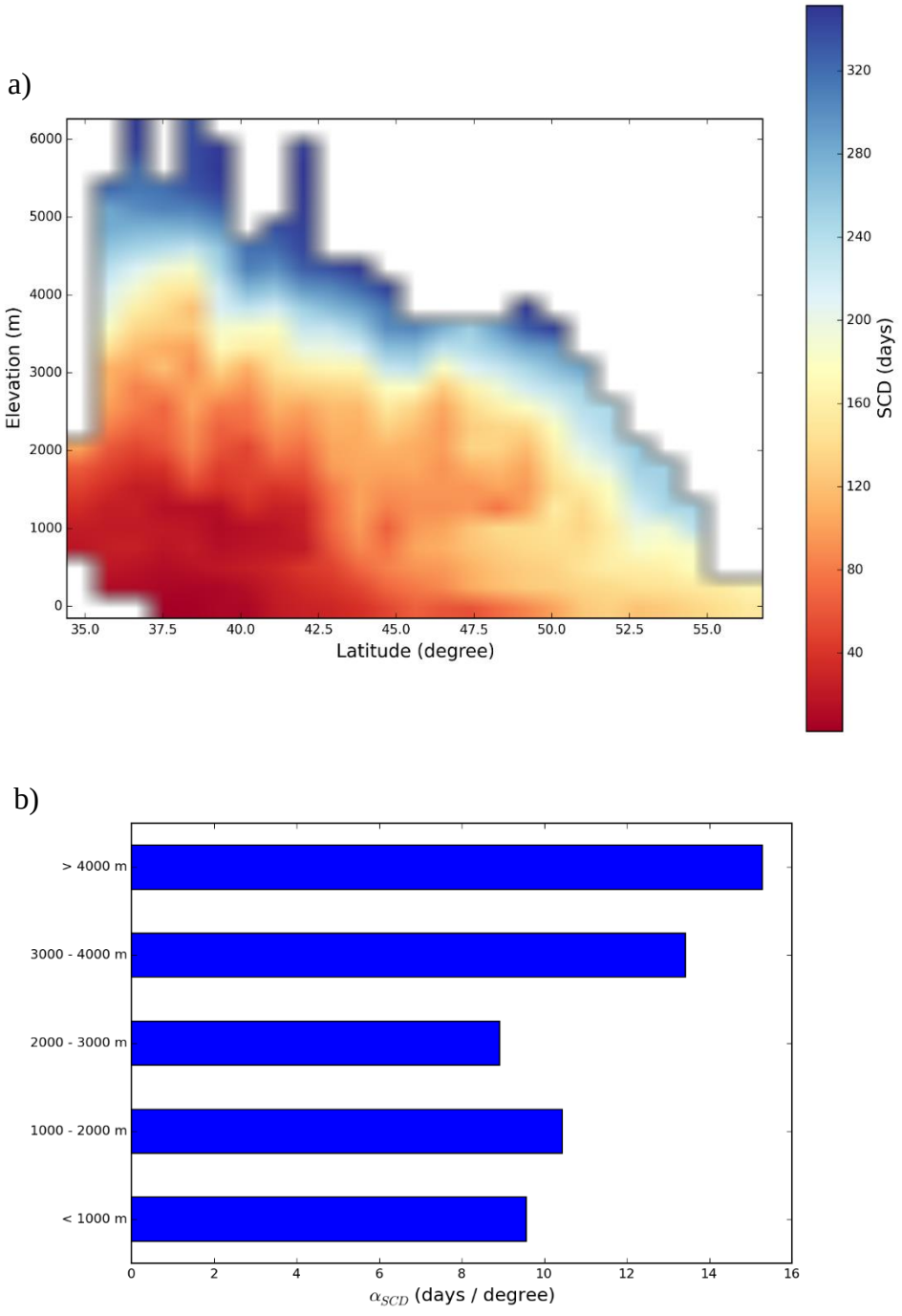

Figure 4.11 Relationship between long-term mean SCD, latitude and elevation

a) Relationship between long-term mean SCD and latitude in condition of elevation

b) Increasing rates of $\overline{SCD}$ by latitude in different elevation zones

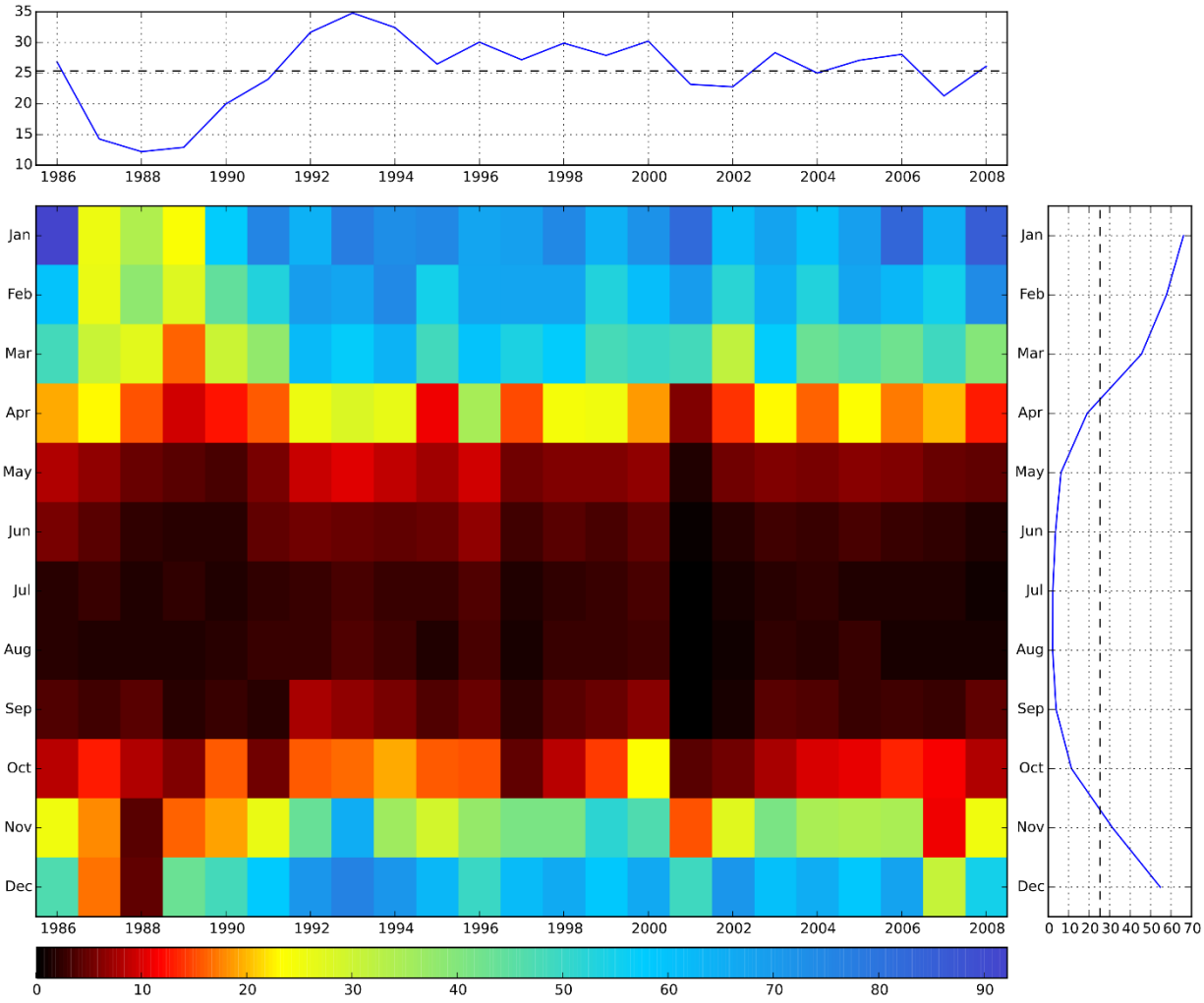

Figure 4.12 Monthly SCAP in CA from 1986 to 2008

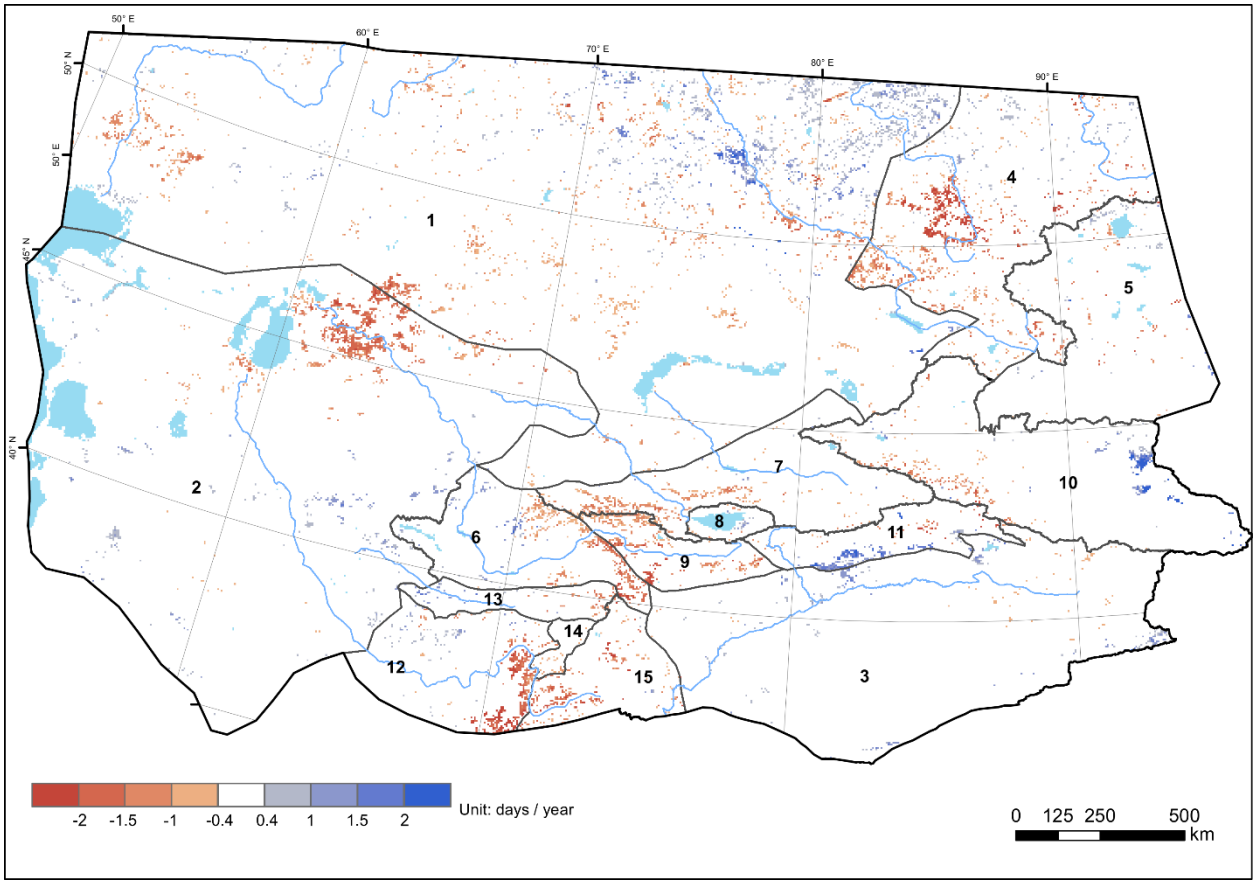

Figure 4.13 Trend of SCD change detected by Theil-Sen regression

Only places showing significant changes under Mann-Kendal test with significant level of 0.05 were shown.

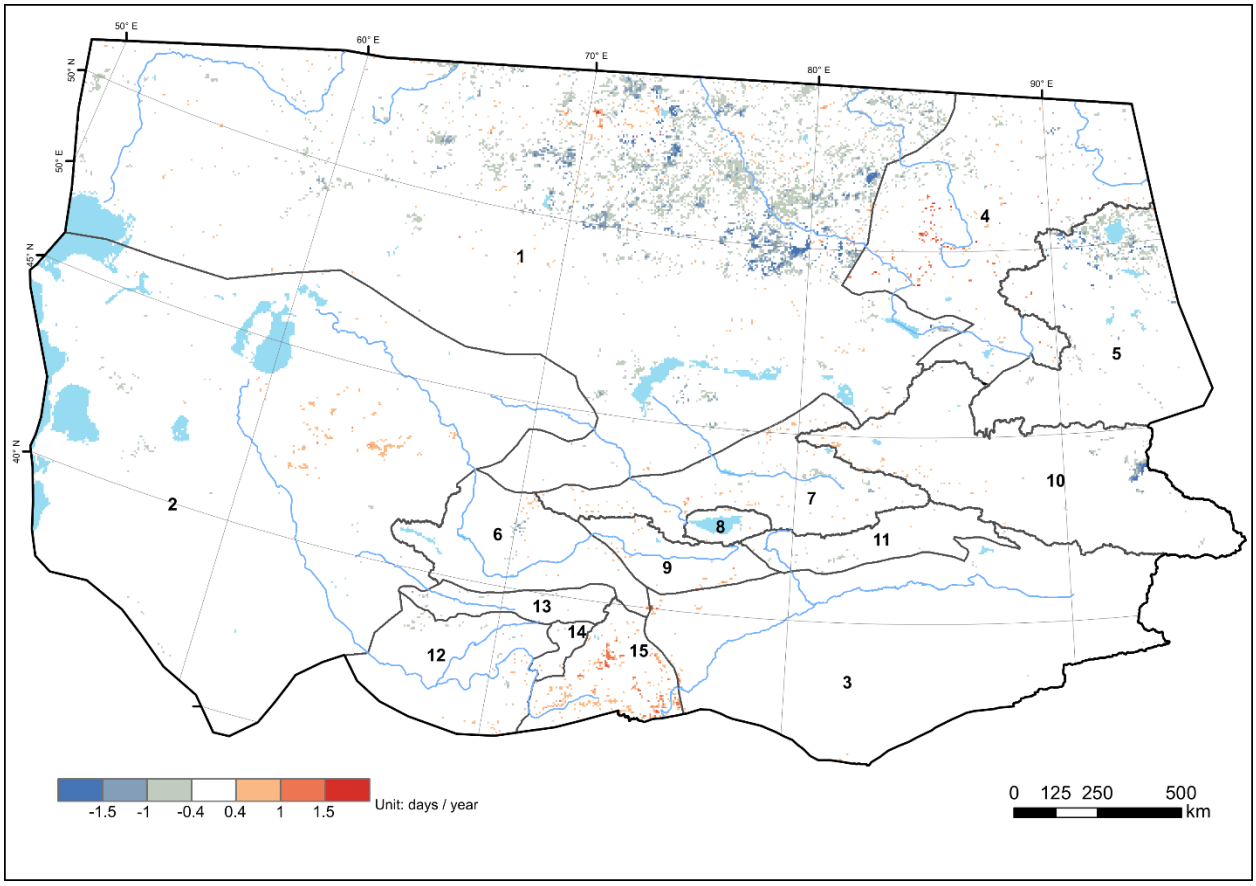

Figure 4.14 Trend of SCOD change detected by Theil-Sen regression

Only places showing significant changes under Mann-Kendal test with significant level of 0.05 were shown.

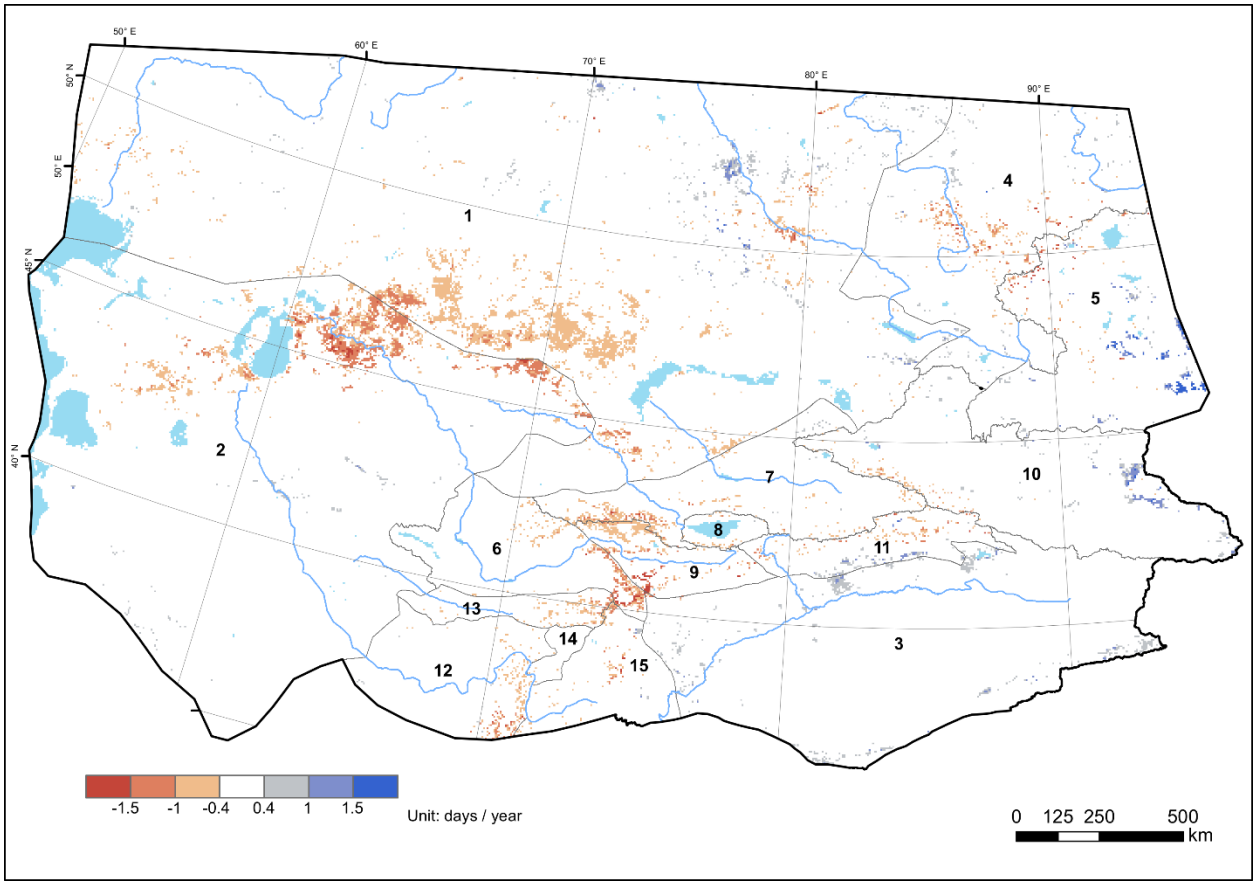

Figure 4.15 Trend of SCMD change detected by Theil-Sen regression

Only places showing significant changes under Mann-Kendal test with significant level of 0.05 were shown.

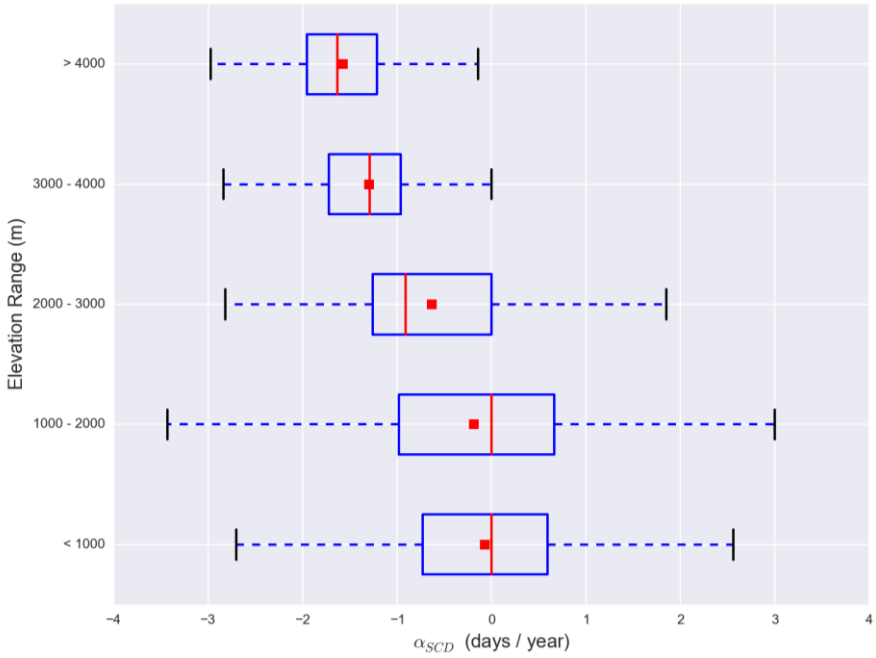

Figure 4.16 a) Box plots of trend of SCD in different elevation ranges

Only places showing significant changes under Mann-Kendal test with significant level of 0.05 were included. Red dots indicate mean values while red lines indicate median values, same for Figure 4.16 b) and c)

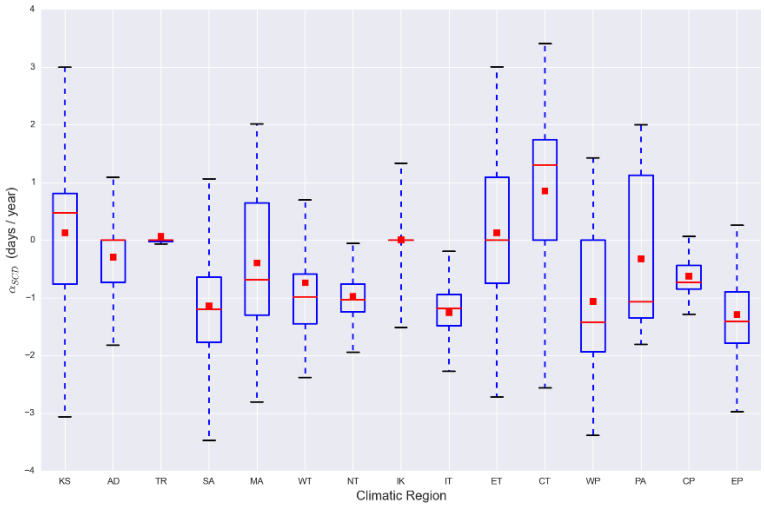

Figure 4.16 b) Box plots of trend of SCD in different climatic regions

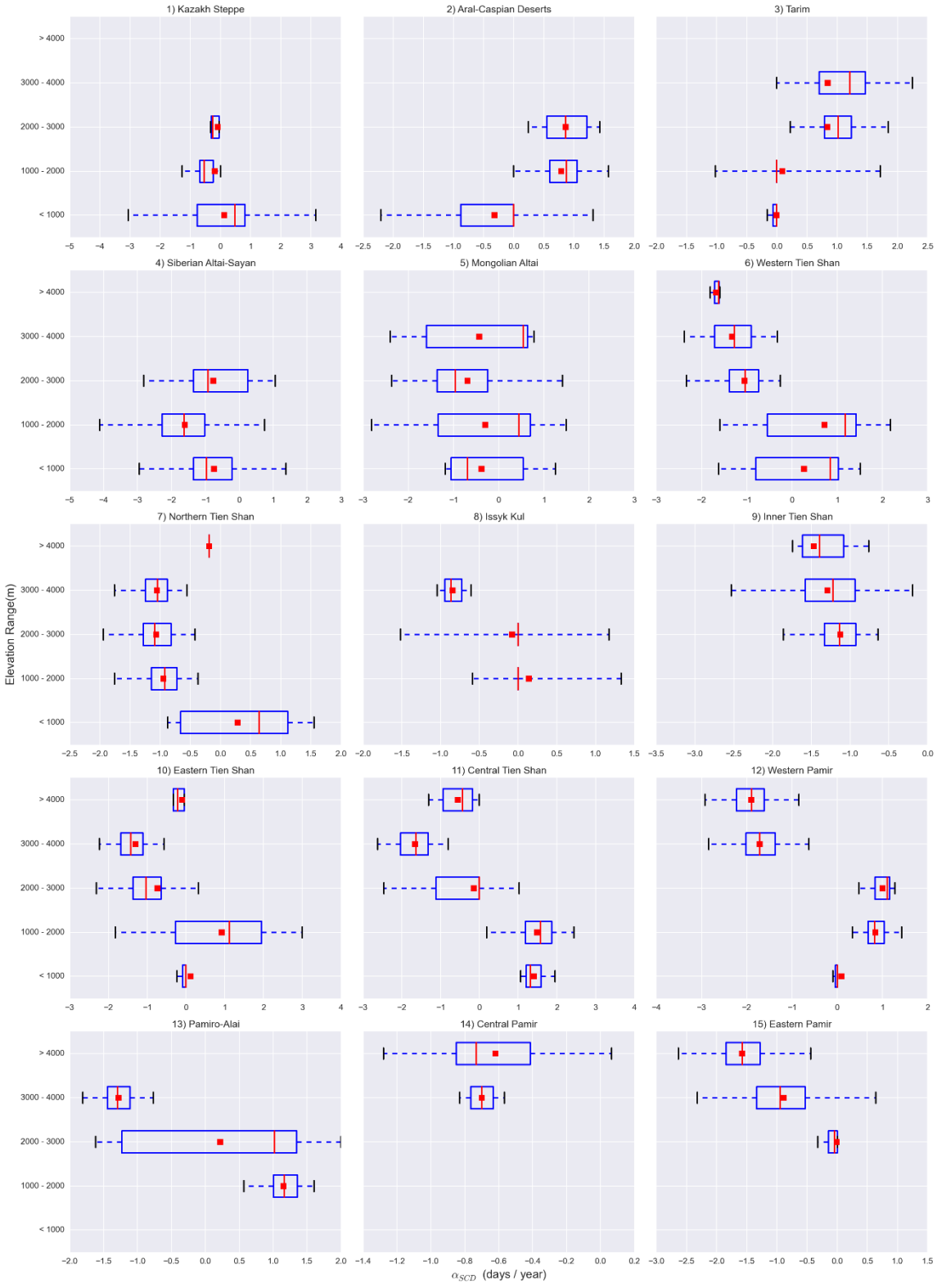

Figure 4.16 c) Box plots of trend of SCD in different elevation ranges within each climatic region

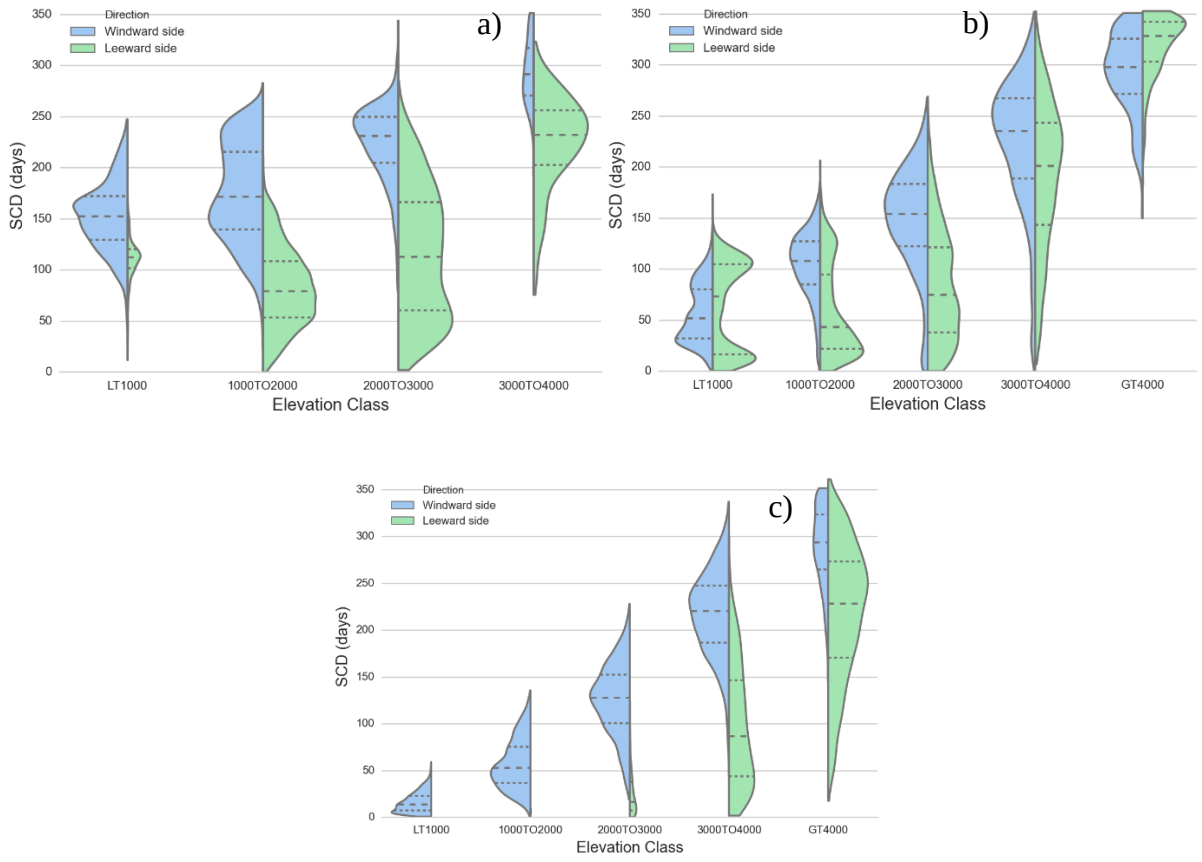

Figure 4.17 SCD distribution between windward and leeward climatic regions

a) in Altai, Windward side: Siberian Altai-Sayan (SA); Leeward side: Mongolian Altai (MA)

b) in Tien Shan, Windward side: Western Tien Shan (WT), Northern Tien Shan (NT); Leeward side: Issyk Kul (IK), Central Tien Shan (CT), Eastern Tien Shan (ET) Inner Tien Shan (IT)

c) in Pamir, Windward side: Western Pamir (WP), Pamiro-Alai (PA), Central Pamir (CP); Leeward side: Eastern Pamir (EP)

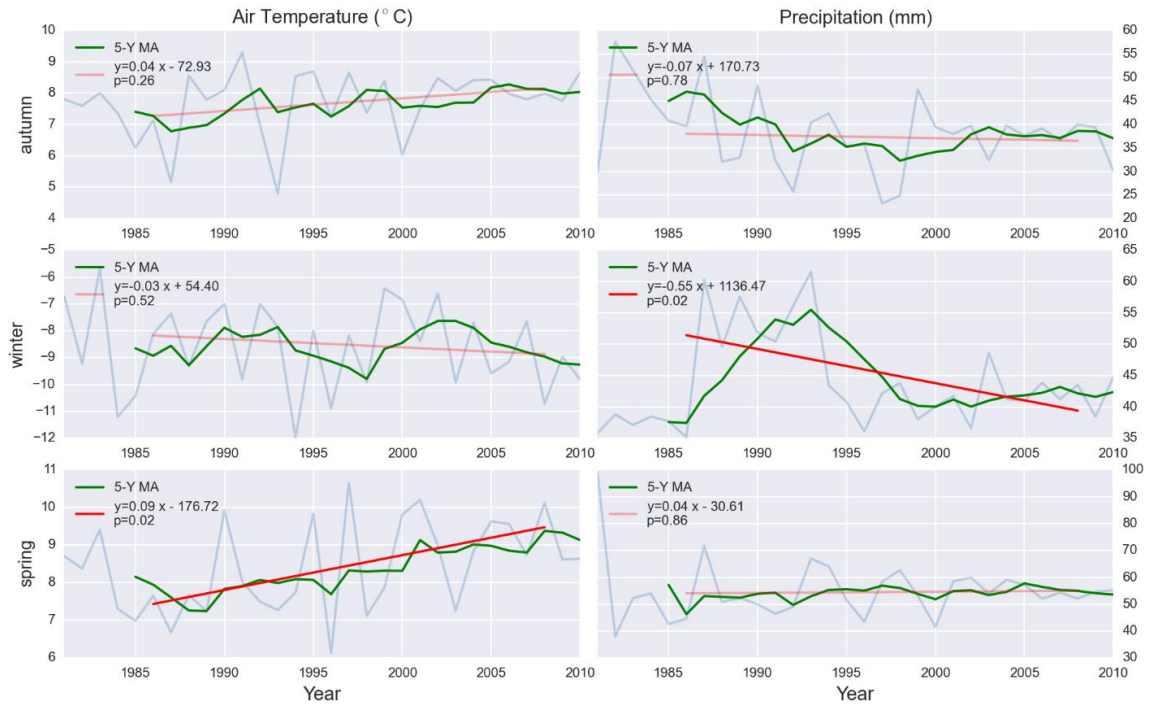

Figure 4.18 Air temperature and precipitation change in areas surrounding Aral Sea

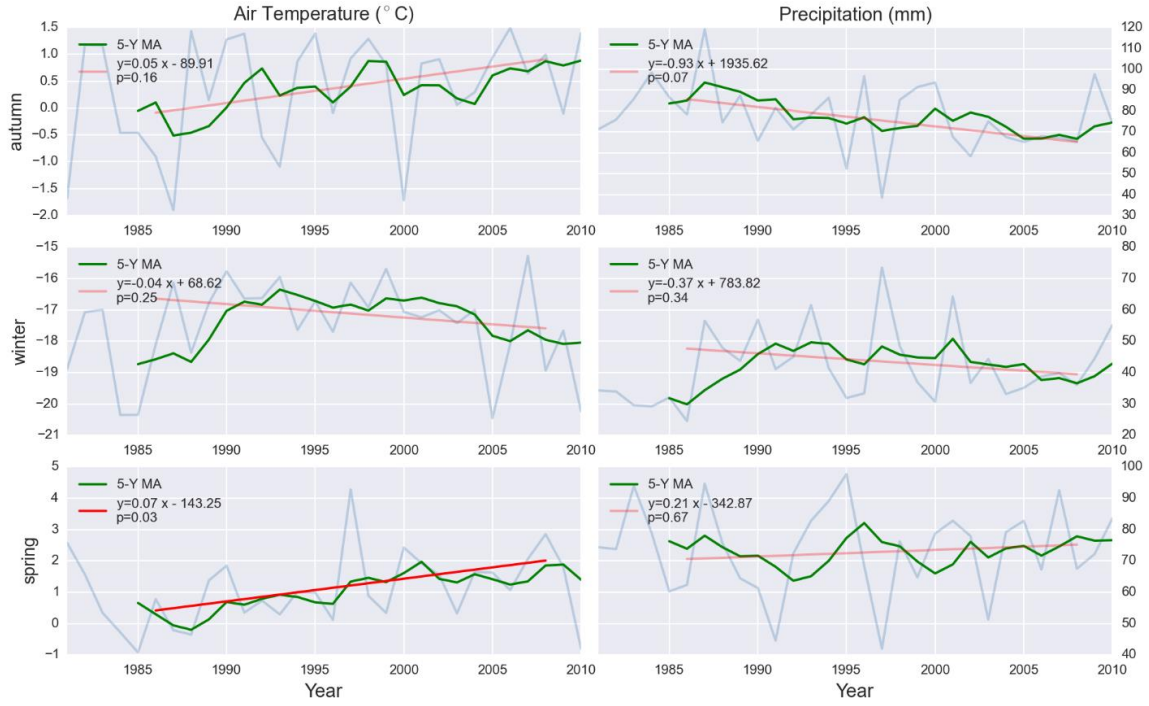

Figure 4.19 Air temperature and precipitation change in Altai

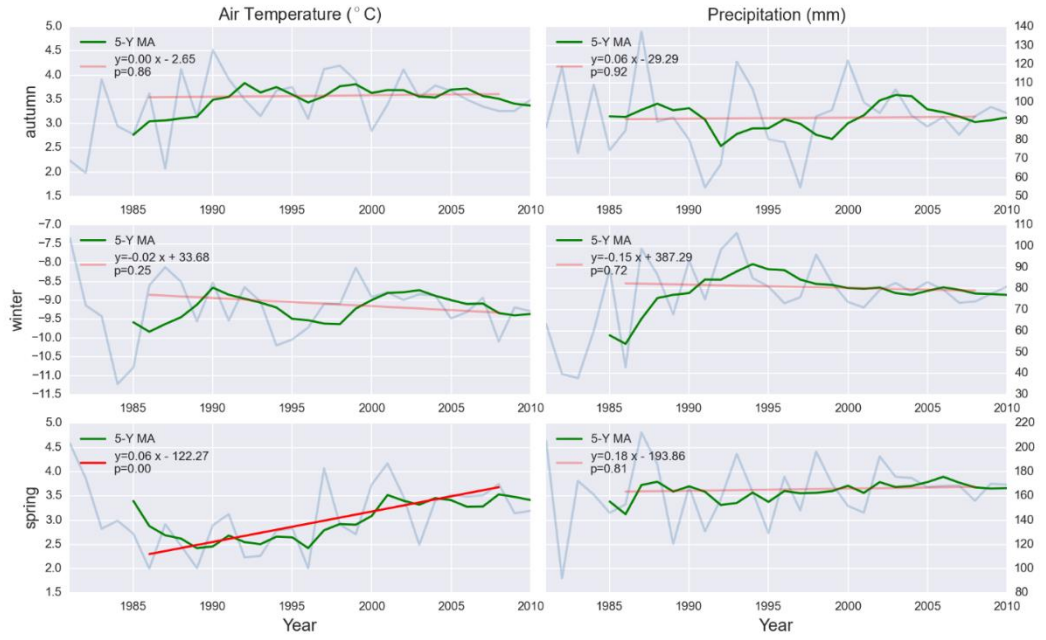

Figure 4.20 Air temperature and precipitation change in western mountains of Tien Shan

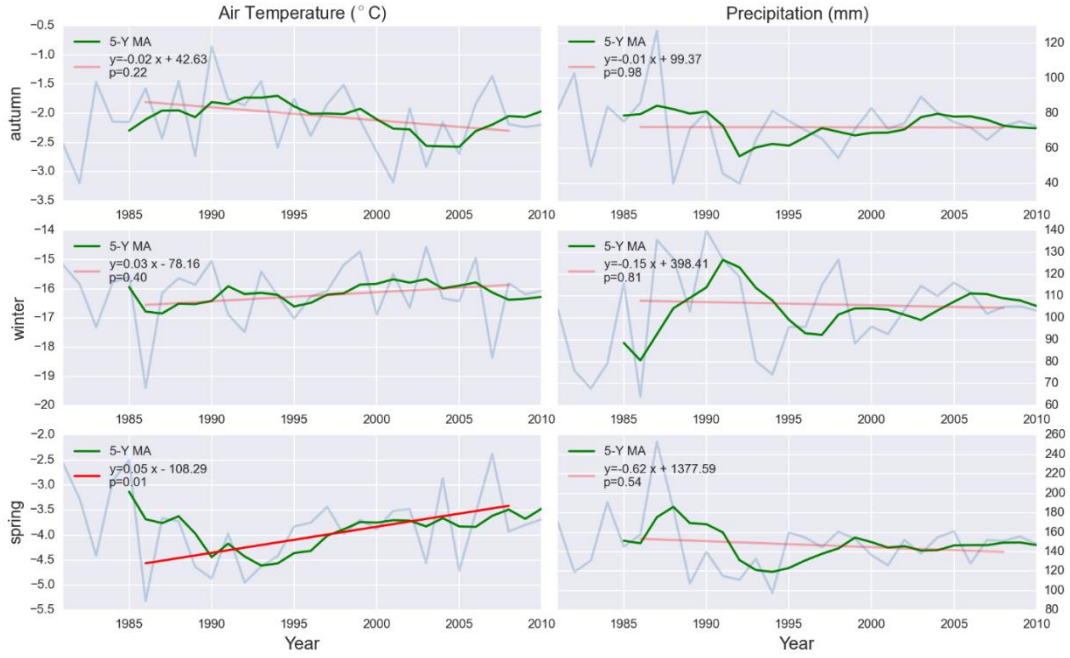

Figure 4.21 Air temperature and precipitation change in Pamir

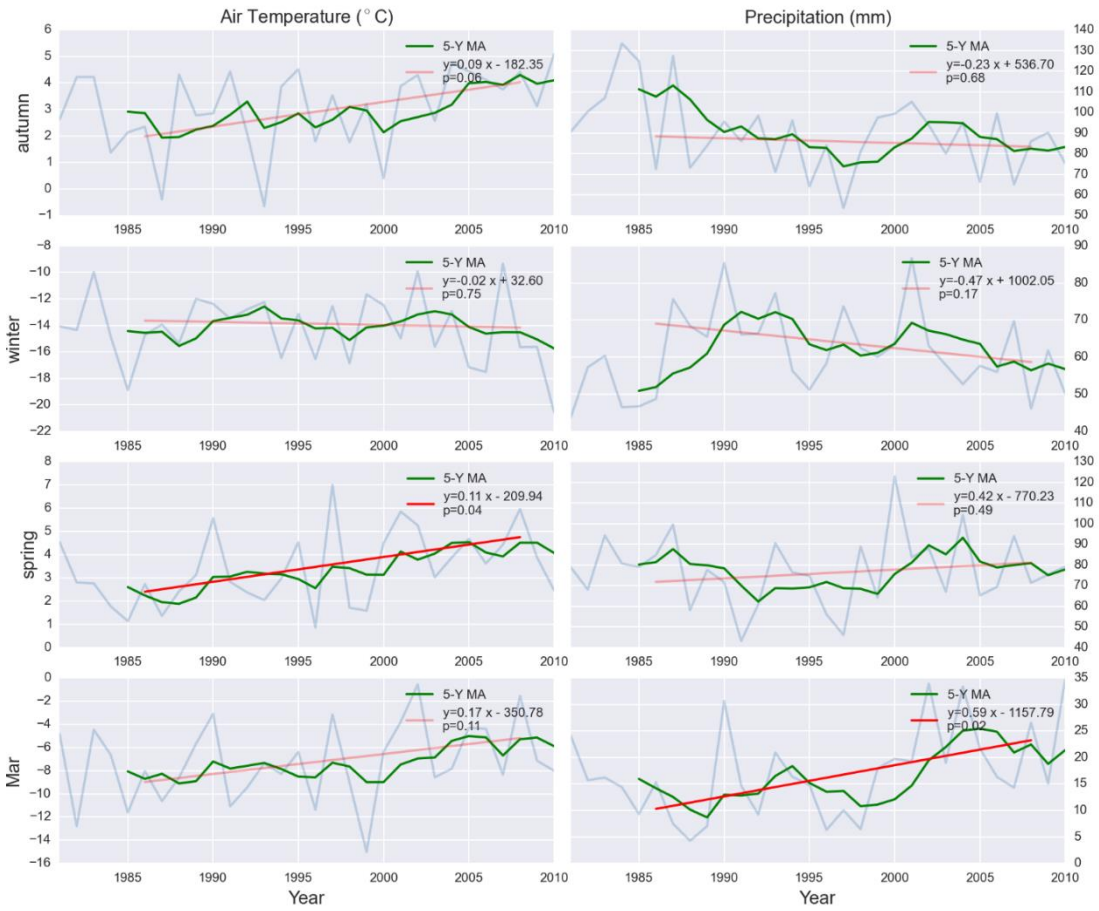

Figure 4.22 Air temperature and precipitation change in Northeastern Kazak Steppe

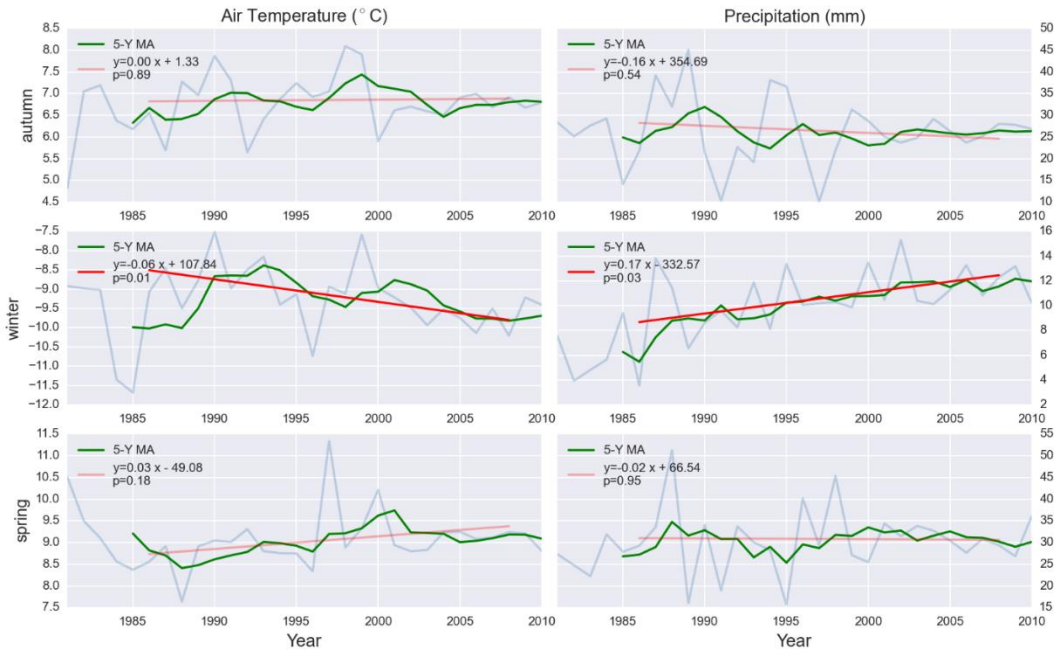

Figure 4.23 Air temperature and precipitation change in in boundary zone among Central Tien Shan, Tarim and Eastern Tien Shan

References

Aizen, V. B., Aizen, E. M., & Melack, J. M. (1995). Climate, snow cover, glaciers, and runoff in the Tien Shan, Central Asia. Water Resources Bulletin, 31(6), 1113–1129.

Aizen, V. B., Aizen, E. M., & Melack, J. M. (1996). Precipitation, melt and runoff in the northern Tien Shan. Journal of Hydrology, 186(1-4), 229–251.

Aizen, V. B. (2004). Association between atmospheric circulation patterns and firn-ice core records from the Inilchek glacierized area, central Tien Shan, Asia. Journal of Geophysical Research, 109(D8). http://doi.org/10.1029/2003JD003894

Aizen, V. B., Aizen, E., Fujita, K., Nikitin, S. A., Kreutz, K. J., & Takeuchi, L. N. (2005). Stable-isotope time series and precipitation origin from firn-core and snow samples, Altai glaciers, Siberia. Journal of Glaciology, 51(175), 637–654. http://doi.org/doi:10.3189/172756505781829034

Aizen, V. B., Mayewski, P. a., Aizen, E. M., Joswiak, D. R., Surazakov, A. B., Kaspari, S., … Finaev, A. (2009). Stable-isotope and trace element time series from Fedchenko glacier (Pamirs) snow/firn cores. Journal of Glaciology, 55(190), 275–291. http://doi.org/10.3189/002214309788608787

Aizen, V. B., Aizen, E. M., ZHOU, H., in preparation, Climate changes in central Asia in the 20th century

Barnett, T. P., Adam, J. C., & Lettenmaier, D. P. (2005). Potential impacts of a warming climate on water availability in snow-dominated regions. Nature, 438(7066), 303–9. doi:10.1038/nature04141

Bernauer, T., & Siegfried, T. (2012). Climate change and international water conflict in Central Asia. Journal of Peace Research, 49, 227–239. doi:10.1177/0022343311425843

Böhner, J., & Bohner, J. (2006). General climatic controls and topoclimatic variations in Central and High Asia. Boreas., 35(2), 279–295. http://doi.org/10.1080/03009480500456073

Brown, R. D. (2000). Northern Hemisphere Snow Cover Variability and Change, 1915–97. Journal of Climate, 13(13), 2339–2355. doi:10.1175/1520-0442(2000)013<2339:NHSCVA>2.0.CO;2

Bryson, R. (1986). Airstream Climatology of Asia. In Y. Xu (Ed.), Proceedings of International Symposium on the Qinghai-Xizang Plateau and Mountain Meteorology SE - 36 (pp. 604–619). American Meteorological Society. http://doi.org/10.1007/978-1-935704-19-5_36

Chevallier, P., Pouyaud, B., Mojaïsky, M., Bolgov, M., Olsson, O., Bauer, M., & Froebrich, J. (2014). River flow regime and snow cover of the Pamir Alay (Central Asia) in a changing climate. Hydrological Sciences Journal, (July), 1–16. http://doi.org/10.1080/02626667.2013.838004

Choi, G., Robinson, D. a., & Kang, S. (2010). Changing Northern Hemisphere Snow Seasons. Journal of Climate, 23(19), 5305–5310. doi:10.1175/2010JCLI3644.1

Cohen, J., Foster, J., Barlow, M., Saito, K., & Jones, J. (2010). Winter 2009-2010: A case study of an extreme Arctic Oscillation event. Geophysical Research Letters, 37(July), 1–6. doi:10.1029/2010GL044256

Dietz, A., Conrad, C., Kuenzer, C., Gesell, G., & Dech, S. (2014). Identifying Changing Snow Cover Characteristics in Central Asia between 1986 and 2014 from Remote Sensing Data. Remote Sensing, 12752–12775. doi:10.3390/rs61212752

Dozier, J. (1987). Recent research in snow hydrology. Review of Geophysics, 25(2), 153–161. doi:10.1029/RG025i002p00153

Dye, D. G. (2002). Variability and trends in the annual snow-cover cycle in Northern Hemisphere land areas, 1972-2000. Hydrological Processes, 16(15), 3065–3077. http://doi.org/10.1002/hyp.1089

Dye, D. G. and Tucker, C. J. (2003). Seasonality and trends of snow-cover, vegetation index, and temperature in northern Eurasia. Geophysical Research Letters, 30(7), 3–6. doi:10.1029/2002GL016384

Edwards, A. C., Scalenghe, R., & Freppaz, M. (2007). Changes in the seasonal snow cover of alpine regions and its effect on soil processes: A review. Quaternary International, 162-163, 172–181. doi:10.1016/j.quaint.2006.10.027

Fernandes, R., & G. Leblanc, S. (2005). Parametric (modified least squares) and non-parametric (Theil–Sen) linear regressions for predicting biophysical parameters in the presence of measurement errors. Remote Sensing of Environment, 95(3), 303–316. doi:10.1016/j.rse.2005.01.005

Groisman, P. Y., Karl, T. R., Knight, R. W., & Stenchikov, G. L. (1994). Changes of Snow Cover, Temperature, and Radiative Heat Balance over the Northern Hemisphere. Journal of Climate, 7(11), 1633–1656. doi:10.1175/1520-0442(1994)007<1633:COSCTA>2.0.CO;2

Hasanean, H. M., Almazroui, M., Jones, P. D., & Alamoudi, a. a. (2013). Siberian high variability and its teleconnections with tropical circulations and surface air temperature over Saudi Arabia. Climate Dynamics, 41, 2003–2018. doi:10.1007/s00382-012-1657-9

Immerzeel, W. W., van Beek, L. P. H., & Bierkens, M. F. P. (2010). Climate change will affect the Asian water towers. Science (New York, N.Y.), 328(5984), 1382–5. http://doi.org/10.1126/science.1183188

IPCC. (2014). Climate Change 2014: Impacts, Adaptation, and Vulnerability. Part B: Regional Aspects. Contribution of Working Group II to the Fifth Assessment Report of the Intergovernmental Panel on Climate Change [Barros, V.R., C.B. Field, D.J. Dokken, M.D. Mastrandrea, K.J. Mach, T.E. Bilir, M. Chatterjee, K.L. Ebi, Y.O. Estrada, R.C. Genova, B. Girma, E.S. Kissel, A.N. Levy, S. MacCracken, P.R. Mastrandrea, and L.L. White (eds.)]. Cambridge, United Kingdom and New York, NY, USA: Cambridge University Press.

Jansson, P., Hock, R., & Schneider, T. (2003). The concept of glacier storage: a review. Journal of Hydrology, 282(1-4), 116–129. doi:10.1016/S0022-1694(03)00258-0

Jeong, J.-H., Ou, T., Linderholm, H. W., Kim, B.-M., Kim, S.-J., Kug, J.-S., & Chen, D. (2011). Recent recovery of the Siberian High intensity. Journal of Geophysical Research: Atmospheres, 116(D23), n/a–n/a. doi:10.1029/2011JD015904

Khlopenkov, K. V., & Trishchenko, A. P. (2007). SPARC: New Cloud, Snow, and Cloud Shadow Detection Scheme for Historical 1-km AVHHR Data over Canada. Journal of Atmospheric and Oceanic Technology, 24(3), 322–343. doi:10.1175/JTECH1987.1

Kotlyakov, V. M. (Ed.). (1997). World Atlas of Snow and Ice Resources. Moscow.

Lattin, J., Carroll, D., & Green, P. (2002). Analyzing Multivariate Data. Duxbury Press; 1 edition. Retrieved from http://www.amazon.com/Analyzing-Multivariate-CD-ROM-Duxbury-Applied/dp/0534349749/ref=sr_1_1?s=books&ie=UTF8&qid=1323192580&sr=1-1

Liang, T., Huang, X., Wu, C., Liu, X., Li, W., Guo, Z., & Ren, J. (2008). An application of MODIS data to snow cover monitoring in a pastoral area: A case study in Northern Xinjiang, China. Remote Sensing of Environment, 112(4), 1514–1526. doi:10.1016/j.rse.2007.06.001

Lioubimtseva, E., & Henebry, G. M. (2009). Climate and environmental change in arid Central Asia: Impacts, vulnerability, and adaptations. Journal of Arid Environments, 73(11), 963–977. doi:10.1016/j.jaridenv.2009.04.022

Lydolph, P. E. (1977). Climates of the Soviet Union. Amsterdam [etc.]: Elsevier.

Mannig, B., Müller, M., Starke, E., Merkenschlager, C., Mao, W., Zhi, X., … Paeth, H. (2013). Dynamical downscaling of climate change in Central Asia. Global and Planetary Change, 110, 26–39. doi:10.1016/j.gloplacha.2013.05.008

Micklin, P. (2007). The Aral Sea Disaster. Annual Review of Earth and Planetary Sciences, 35, 47–72. http://doi.org/10.1146/annurev.earth.35.031306.140120

Mölg, T., Maussion, F., & Scherer, D. (2013). Mid-latitude westerlies as a driver of glacier variability in monsoonal High Asia. Nature Climate Change, 4(1), 68–73. doi:10.1038/nclimate2055

Muggeo, V. M. R. (2008). segmented: An R package to Fit Regression Models with Broken-Line Relationships. R News, 8(May), 20–25. doi:10.1159/000323281

NOAA. (1998). NOAA Polar Orbiter Data User's Guide. Retrieved September 1, 2009, from http://www2.ncdc.noaa.gov/docs/podug/index.htm

NOAA. (2007). NOAA KLM USER'S GUIDE. Retrieved September 1, 2009, from http://www.ncdc.noaa.gov/oa/pod-guide/ncdc/docs/klm/index.htm

Ososkova, T., Gorelkin, N., & Chub, V. (2000). Water resources of central Asia and adaptation measures for climate change. Environmental Monitoring and Assessment, Retrieved from http://link.springer.com/article/10.1023/A:1006394808699

Parajka, J., Pepe, M., Rampini, A., Rossi, S., & Blöschl, G. (2010). A regional snow-line method for estimating snow cover from MODIS during cloud cover. Journal of Hydrology, 381(3-4), 203–212. http://doi.org/10.1016/j.jhydrol.2009.11.042

Peng, S., Piao, S., Ciais, P., Friedlingstein, P., Zhou, L., & Wang, T. (2013). Change in snow phenology and its potential feedback to temperature in the Northern Hemisphere over the last three decades. Environmental Research Letters, 8(1), 014008. doi:10.1088/1748-9326/8/1/014008

Pohl, E., Knoche, M., Gloaguen, R., Andermann, C., & Krause, P. (2014). The hydrological cycle in the high Pamir Mountains: how temperature and seasonal precipitation distribution influence stream flow in the Gunt catchment, Tajikistan. Earth Surface Dynamics Discussions, 2(2), 1155–1215. http://doi.org/10.5194/esurfd-2-1155-2014

Rototaeva, O.V. 1983. Glaciologicheskoe raionirovanie Pamira (The Pamir glaciological zoning). Data of Glaciological Studies, V. 46, M., pp. 39-51(in Russ.)

Schiemann, R., Glazirina, M. G., & Schär, C. (2007). On the relationship between the Indian summer monsoon and river flow in the Aral Sea basin. Geophysical Research Letters, 34(5), L05706. http://doi.org/10.1029/2006GL028926

Sen, P. K. (1968). Estimates of the regression coefficient based on Kendall's tau. Journal of the American Statistical Association, 63, 1379 – 1389.

Severskiy, I. V., & Severskiy, E. V. (2003). The influence of local factors on snow cover and seasonal ground freezing in the Tien Shan. In Phillips, Springman, & Arenson (Eds.), Permafrost (pp. 1023 – 1028).

Siegfried, T., Bernauer, T., Guiennet, R., Sellars, S., Robertson, A. W., Mankin, J., … Yakovlev, A. (2012). Will climate change exacerbate water stress in Central Asia? Climatic Change, 112, 881–899. doi:10.1007/s10584-011-0253-z

Singh, V. P. (2010). Snow and Glacier Hydrology (p. 756). Springer; Softcover reprint of hardcover 1st ed. 2001 edition. Retrieved from http://www.amazon.com/Glacier-Hydrology-Science-Technology-Library/dp/9048156351/ref=sr_1_1?s=books&ie=UTF8&qid=1323193452&sr=1-1

Sorg, A., Bolch, T., Stoffel, M., Solomina, O., & Beniston, M. (2012). Climate change impacts on glaciers and runoff in Tien Shan (Central Asia). Nature Climate Change, 2(10), 725–731. http://doi.org/10.1038/nclimate1592

Surazakov, a B., Aizen, V. B., Aizen, E. M., & Nikitin, S. a. (2007). Glacier changes in the Siberian Altai Mountains, Ob river basin, (1952–2006) estimated with high resolution imagery. Environmental Research Letters, 2(4), 045017. http://doi.org/10.1088/1748-9326/2/4/045017

Theil, H. (1950). A rank-invariant method of linear and polynomial regression analysis, I. Nederlands Akad. Wetensch. Proc., 53, 386 – 392.

Wang, X., & Xie, H. (2009). New methods for studying the spatiotemporal variation of snow cover based on combination products of MODIS Terra and Aqua. Journal of Hydrology, 371(1-4), 192–200. doi:10.1016/j.jhydrol.2009.03.028

Wang, X., Xie, H., & Liang, T. (2009). Comparison and validation of MODIS standard and new combination of Terra and Aqua snow cover products in northern Xinjiang, China. Hydrological Processes, 429(October 2008), 419– 429. doi:10.1002/hyp

You, Q., Fraedrich, K., Ren, G., Ye, B., Meng, X., & Kang, S. (2012). Inconsistencies of precipitation in the eastern and central Tibetan Plateau between surface adjusted data and reanalysis. Theoretical and Applied Climatology, 109(3-4), 485–496. http://doi.org/10.1007/s00704-012-0594-1

Zhou, H., Aizen, E., & Aizen, V. (2013). Deriving long term snow cover extent dataset from AVHRR and MODIS data: Central Asia case study. Remote Sensing of Environment, 136, 146–162. doi:10.1016/j.rse.2013.04.015

Chapter 5 Glacier area and ice volume changes in Central Pamir and Central Tien Shan since the late 20th century

1 Introduction

Glacier meltwater is one of the major water resources for lowland areas in arid / semi-arid central Asia (CA). Glaciers in high mountains accumulate atmospheric moisture as solid precipitation over a long period. Meltwater from glaciers provides reliable water supplies for natural habitat and local communities. It was estimated that meltwater from glaciers contributes 5% to 40% of total annual surface runoff in lowland plains of CA (**Aizen et al., 2007a; Kaser et al., 2010**). In summer, meltwater from CA glaciers can contribute up to 70% of surface runoff in the river basins with large glacierized areas (**Aizen and Aizen, 1993; Aizen et al., 1995; Aizen, et al., 1996**).

Studies of glaciers in Tien Shan and Pamir began in late 19th century. Between the 1880s and the1940s, there are more than 600 scientific papers and books about Tien Shan and Pamir glaciers published, mainly in Russian. Kaulbars (**1875**) presented the first overview of the Tien Shan glaciers while Mushketov (**1896**) provides an overview of the glaciers in Tien Shan and Pamir. The first map of CA glaciers was completed by Russian military topographers in the 1890s. The German explorer Rickmer-Rickmers (1873 – 1965) visited Pamir five times between 1894 and 1906, and published an illustrated book about the glaciers in Turkestan (**Rickmers, 1913**). Glaciers in the Khan-Tengri mountain massif, Central Tien Shan, with the second largest glacier in CA, the Inylchek Glacier, were described by Vorob'ev (**1935**). The importance of glacier meltwater on river discharge and agriculture in CA was analyzed and emphasized by Langwagen (**1908**) in Ili and Chu river basins, which are situated in northern Tien Shan.

The first extensive exploration of the Pamir, the Pamir's High Elevation International Geophysical Expedition, was conducted during 1928 to 1933 by Russian and German scientists to the Fedchenko Glacier in Central Pamir. During the five-year study, the first topographic map of the Fedchenko Glacier was completed based on terrestrial photogrammetry survey. In 1933, the Fedchenko Glacier geophysical observatory was established at 4165 m a.s.l., which was in operation until 1994. The scientific results of this expedition, including data of meteorological, synoptic, geophysical and glaciological observations were published by Gorbunov et al. (**1929**) and Finsterwalder (**1932**). Later, the observatory was named the Gorbunov Station, in memory of the leader of the Russian-German geophysical expedition to Pamir.

After World War II, studies of the alpine areas in Tien Shan and Pamir engaged several scientific research institutes and regional meteorological agencies of the USSR. The main objectives of these studies were to understand the formation of the mountain climate, the impacts of mountain climate on the regime of snow cover, glacier and permafrost, and the roles of different components of the cryosphere in river runoff formation in CA. The first complete book about Pamir glaciers was published by Zabirov (**1955**), providing descriptions of the climatic characteristics, distribution of glaciers in major mountain ranges and river basins, and a preliminary evaluation of the Pamir Holocene-Pleistocene glaciation. The results of his investigations were mainly derived from aerial photographs of the late 1940s and the early 1950s. Glaciers in the Khan-Tengri mountain massif, including the Inylchek Glacier, were further described by Ratcek (**1954**), while the first meteorological observations at the Inylchek Glacier area were conducted during mountaineering expeditions (**Grudzinskiy, 1959**).

A new complex investigation in Central Pamir, particularly on the Fedchenko Glacier, was started in 1958 as the 2nd Pamir's High Elevation International Geophysical Expedition, organized within the framework of International Geophysical Year. The results of this expedition enabled the analysis of changes of the Fedchenko Glacier and Central Pamir glaciers between 1928 and 1958 (**Schulz, 1962; Regensburger, 1963; Dolgushin and Osipova, 1989**). After 1958, the USSR Academy of Sciences and Central Asia Institute of Hydrometeorology continued researches of glaciers in CA until 1991, the collapse of the USSR. The results of these investigations were compiled into the Glacier Inventory of the USSR (**1979**) and numerous papers in the Journal of the Data of Glaciological Studies (Moscow, Russia) and the Proceedings of the Central Asian Hydrometeorological Institute (Tashkent, Uzbekistan).

In the last two decades, several researches reported accelerated retreat of glaciers as a consequence of global and regional warming in Tien Shan (**Narama et al., 2006; Aizen et al., 2007a; Kutuzov and Shahgedanova, 2009; Narama et al., 2010; Osmonov, 2013**) and Pamir (**Khromova, et al., 2006; Zhang et al., 2014; Aizen et al., in preparation**). However, many surging glaciers have also been identified (**Aizen et al., 2007a; Kotlyakov et al., 1997; Glazirin, 2010; Pieczonka and Bolch, 2015**), especially in Central Pamir (**Kotlyakov et al., 2008; Aizen et al., in preparation**). At the same time, studies of glacier mass balance changes in CA were still limited compared with glacier area change studies because of very few in-situ observation of glacier mass balance (**Unger-Shayesteh, et al., 2013**). Evaluation of repeated DEM in different time has been utilized to analyze glacier surface elevation and ice volume changes in Tien Shan (**Surazakov and Aizen, 2006; Aizen et al., 2007a; Pieczonka et al., 2013; Shangguan et al., 2014; Pieczonka and Bolch, 2015**) and Pamir

(**Lambrecht et al., 2014)** with the development of satellite altimetry sensors and products (e.g. SRTM, ICESat).

Most of the recent studies about glacier changes in CA focused on Tien Shan, with only a few studies in Pamir. Moreover, those studies in Pamir are either conducted for a single glacier (**Iawata, et al., 2009; Lambrecht, et al., 2014**), or a small subset of glaciers (**Khromova, et al., 2006; Zhang et al., 2014**). There exists a certain knowledge gap about the glaciers' area and volume changes in Pamir, which is a very important issue in relation with the water resources scarcity in central Asian river basins facing a rapidly growing population (**Bernauer and Siegfried, 2012; Siegfried, et al., 2012**). In addition, the regional geographical differences of glacier distribution and responses of the glaciers to climate changes in Pamir and Tien Shan have not been addressed in previous studies.

In this chapter, the two largest glacierized areas in CA: the Fedchenko Glacier Massif (FGM) in Central Pamir and the Inylchek Glacier Massif (IGM) in Central Tien Shan, were selected as benchmark areas to study glacier changes since the 1970s, when glacier melt in CA increases abruptly due to the regional warming. The changes of glacier area, glacier surface elevation, and ice volume were analyzed based on historical topographical maps, satellite images and altimetry products.

2 Research areas

2.1 Fedchenko Glacier Massif

The Fedchenko Glacier Massif (FGM) (**Figure 5.01-b**) is located in the center of Pamir in Tajikistan. The Ismoily Somony Peak (7495 m) is the highest summit in this area

and in Central Pamir. In this study 1231 glaciers in the FGM were selected, covering an area of 2450 km^2 in 2000. The FGM is the largest glacierized area in Pamir, ~ 1/5 of the total glacierized area of the Pamir (**Dolgushin and Osipova, 1989; Schetinnikov, 1998**). The Fedchenko Glacier is the largest glacier in the FGM, and one of the largest alpine glaciers in the Northern Hemisphere (**Aizen et al., 2009; Lambrecht, et al., 2014**). The length of the Fedchenko Glacier is ~72 km, spreading over an elevation range between 2900 m and 7400 m. The area of the glacier is 687.4 km^2, ~27.5% of the glacier area in the FGM. Meltwater from the Fedchenko Glacier forms the Muksu River, which is the first tributary of the Amu Dar'ya River. A special characteristic of the FGM is the existence of numerous surging and unstable glaciers. The aggressive dynamics of these glaciers create devastating glacier outburst flows for the villages in lower river reaches (**Kotlyakov, et al., 1997**).

In this study, the FGM is further separated into 7 sub-regions (**Figure 5.01-b**) based on the different drainage basins, including: sub-region ① Fedchenko Glacier Basin, sub-region ② Bailyankiyik River Basin, sub-region ③ Upper Tanymas River Basin, sub-region ④ Southern Slope of Bartang River Basin, sub-region ⑤ Upper Vanch and Upper Garmo River Basin, sub-region ⑥ Middle Vanch and Middle Garmo River Basin, and sub-region ⑦ Northern Slope of Muksu River Basin.

The basic climatic characteristics for the FGM, including air temperature and precipitation, are derived from two long-term meteorological stations, the Fedchenko Glacier Station (72.22 °E, 38.84 °N, 4169 m) and the Altyn Mazar Station (72.24 °E, 39.19 °N, 2782 m) (**Figure 5.01-b**). The long-term mean annual temperature is -6.7 °C for the Fedchenko Station and 3.5 °C for the Altyn Mazar Station. January is the coldest month and August is the warmest. Long-term mean annual precipitation in is 175 mm at the Altyn Mazar station and

1129 mm at the Fedchenko Station, over 6 times more than at the Altyn Mazar Station. Precipitation increases with elevation by a rate of almost 14 mm / 100 m. Winter and spring are the seasons with the greatest precipitation for the FGM, with maximum precipitation in March (~13% of annual total). In contrast, summer and autumn are dry seasons, with minimum precipitation in September (less than 2% of annual total) (**Figure 5.02-1**). For analyzing correlation between glacier changes at FGM and local climate changes, the data gaps in monthly air temperature and precipitation data in both stations were reconstructed (**Chapter 2**). Besides, data in the Garm Station (69.95 °E, 39.00 °N, 1316 m) were also included in the analysis, since it is the station with the smallest NoData rate within all nearby stations, and its monthly air temperature and precipitation data have strong positive correlation with the data in the Fedchenko Glacier Station (**Chapter 2**).

2.2 Inylchek Glacier Massif

The Inylchek Glacier Massif (IGM) is located in Central Tien Shan (**Figure 5.01-c**), between the Saridjaz and the Kokshatoo ranges. Peak Pobeda (Russian name) / Tomur Feng (Chinese name) (7439 m) and Peak Khan-Tengri (6995 m) are the highest peaks in the IGM and in Tien Shan. Water discharged from the IGM drains to the Aksu River, which is a major tributary of the Tarim River.

In this study, 236 glaciers were selected in the IGM with a total area of 750 km^2 in the year 2000. The Inylchek Glacier, with an area of 655 km^2, is the largest glacier in Tien Shan, accounting for 87% of total glacier area in the IGM. The Inylchek Glacier consists two major branches: the South Inylchek with an area of 515 km^2 and the North Inylchek with an area of 140 km^2, separated by Lake Merzbacher. Meltwater from the rapidly retreating North Inylchek Glacier was dammed by the South Inylchek Glacier, forming Lake Merzbacher.

Meltwater accumulated in Lake Merzbacher discharged every year in the middle of late summer (**Glazirin, 2010; Xie, et al., 2013**), creating outburst flood that spread approximately 150 km downstream (**Ng et al., 2007**). In this study, the IGM is separated into two sub-regions (**Figure 5.01-c**): the northern region, which contains the North Inylchek Glacier system, and the southern region, which contains the South Inylchek Glacier system.

Since there are no long-term meteorological stations within the IGM, data from the Tien Shan Station (78.11 °E, 41.86 °N, 3611 m) and the Koilu Station (78.97 °E, 42.21 °N, 2800 m) (**Figure 5.01-a and Figure 5.01-c**) were selected for analyzing the local climate at the IGM. These two stations are the nearest stations to the IGM with long-term observations and have shown strong positive correlation with the IGM for both air temperature and precipitation (**Aizen et al, 1997; Aizen &Aizen, 1997; Osmonov, et al., 2013)**. Similar to the FGM, the IGM is also characterized by semi-continental climate but with a lesser amount of precipitation and different timing of the maximum precipitation. The long-term mean annual air temperatures are -7.2 °C and -2.1 °C for the Tien Shan Station and the Koilu Station, respectively. January is the coldest month for both stations while July and August are the warmest months. In contrast to the winter / spring maximum precipitation in the FGM, the IGM has summer maximum precipitation. The long-term mean annual precipitations are 284 mm and 294 mm for the Tien Shan station and the Koilu station, respectively, though precipitation can reach ~900 m at elevations over 6000 m (**Aizen et al., 1997; Aizen & Aizen, 1997**). May-to-August precipitation accounts for ~65% of annual precipitation while November-to-February precipitation only accounts for less than 9% of annual total (**Figure 5.02-2**). In winter, the Asian High atmospheric pressure limited the western atmosphere moisture flows to Central Tien Shan therefore the western moisture penetrates at the end of

spring, when Asian anticyclone weakened and decay. Summer snowfalls play very important role in increasing the glacier surface albedo in IGM protecting the glaciers from intensive melt. However, there is some difference between the climatic conditions and geomorphology of FGM and IGM that determine the regime of the glacier existence in Central Pamir and Central Tien Shan.

3 Data and methods

3.1 Data sources and pre-processing

Various data sources are utilized in this study. In both FGM and IGM, historical satellite images and altimetry products were used, including KH9 images in the 1970s, ETM+ images and SRTM DEM in the early 2000s, and ALOS PRISM images in the late 2000s. In addition, historical military topography maps were also used for analyzing the glacier surface elevation in the 1970s in the IGM (**Table 5.1**).

3.1.1 Satellite images

3.1.1.1 KH9 images

Declassified Hexagon KH9 images were obtained from USGS EarthExplorer (*http://earthexplorer.usgs.gov/*) as digital films scanned in 1800 DPI, with each image covering approximately an area of 161 × 241 km^2 and with spatial resolutions of 6 to 9 m. The distortions of the scanned images were corrected using `Thin Plate Spline` transformation with information provided by the reseau grid marks in the films (**Surazakov and Aizen, 2010**). These images were further orthorectified using the block-triangulation tool provided in the ERDAS Imagine LPS software.

In the FGM, one pair of KH9 images taken in 1975 was used to analyze glacier extent in the 1970s. Orthorectification of these KH9 images was conducted using a 20 m resolution raster DEM derived from the same KH9 stereo-pair as the base DEM. Details about the base DEM will be provided in section 3.1.2.4. The Ground Control Points (GCPs) used in orthorectification include three D-GPS points with centimeter level accuracy surveyed during a field trip to the Fedchenko Glacier in 2009. Another 30 GCPs picked up in Google Earth high resolution imageries (QuickBirds and SPOT5) with accuracies of ~20 m (**Potere, 2008; Surazakov and Aizen, 2010**) were also used. The RMSE values for the resulting block triangulation model are 4.65 m and 4.20 m for the x and the y directions, respectively.

In the IGM, two pairs of KH9 images taken in 1974 and 1976 were used for analyzing the glacier extent in the 1970s. Those images were orthorectified using a 10 m resolution raster DEM generated from ALOS / PRISM stereo-pairs as the base DEM (see section 3.1.2.4 in this chapter for details). The GCPs involved in orthorecitification consist of three D-GPS survey points with an accuracy of 2 m measured during a field trip to the Inylchek Glacier in 2011, and another 12 points from high resolution QuickBird Imageries shared by Google Earth. The positional accuracy of the orthorecitfied images is at a similar level as the KH9 images in the FGM.

3.1.1.2 Landsat ETM+ images

The Landsat ETM+ images have spatial resolutions of 30 m (multispectral bands) and 15 m (panchromatic band) over an area of 180 × 80 km^2. Level 1b Landsat ETM+ images were obtained from USGS EarthExplorer, including two images taken in 2000 for the FGM and one image taken in 2002 for the IGM. Those images were orthorectified using CGIAR SRTM DEM (*http://srtm.csi.cgiar.org*) at 90 m resolution as the base DEM, and GCPs

obtained from Google Earth high resolution images. The resulting images have horizontal accuracies no worse than 15 m.

3.1.1.3 ALOS / PRISM images

The ALOS / PRISM sensor consists of a nadir, a forward and a backward sensor, providing stereoscopic capability by generating image from different point of views simultaneously. Each ALOS / PRISM image covers an area of 35 × 35 km^2 (triplet mode) or 70 × 35 km^2 (nadir only) with a spatial resolution of 2.5 m. Stereo-pairs of level 1b ALOS / PRISM images (nadir and forward) with bundled Rational Polynomial Coefficients (RPCs) were obtained from JAXA (*http://global.jaxa.jp/projects/sat/alos*). There are two pairs in 2006 and 2007 for IGM, and seven pairs in 2006 and 2007 for FGM.

The ALOS / PRISM images were block-triangulated using the ERDAS Imagine LPS software. In the IGM, three D-GPS survey points and 15 points from Google Earth images were used. In the FGM, three D-GPS survey points and 37 Google Earth points were used. The ALOS / PRISM images were orthorectified using DEMs generated from the same triangulated blocks at 10 m resolution as the base DEMs. The block triangulation models for the IGM have RMSE values of 2.22 m and 2.94 m for the x and the y directions, respectively. In the FGM, the RMSE values are 4.04 m for the x direction and 4.91 m for the y direction.

3.1.1.4 DEM derived from satellite images

In the FGM, a 20 m resolution raster DEM was generated from the triangulated block of KH9 images in 1975, and another 10 m resolution DEM was created from the triangulated block of ALOS / PRISM images in 2006 - 2007. In the IGM, the triangulated block of ALOS / PRISM images was used to generate a raster DEM for 2006 - 2007 at 10 m resolution.

All DEM generating procedures were conducted in the eATE program in the ERDAS Imagine LPS software. The program detected matching points in stereo-pairs of images, and calculated the 3D location of those points using the triangulated block model. Blunders in the generated 3D points were manually removed. The remaining points were interpolated to create raster DEMs with voids via TIN interpolation algorithm, which were used for analyzing surface elevation changes between different time periods. Vertical accuracies of generated DEMs were assessed by comparisons with ICESat elevation points in selected ice-free regions. The DEM derived from KH9 images for the FGM has a general accuracy of ~30 m, while a better accuracy of ~6 m can be found in flat areas with slope less than 15°. Moreover, the DEMs derived from ALOS / PRISM images for FGM and IGM have general accuracies of ~ 20 m, while flat regions (slope < 15°) have better accuracies of ~ 5 m.

Mask of voids for each generated DEM was created to clip elevation points converted from raster CGIAR SRTM DEMs. Those clipped points were used with matched 3D points to generate raster DEMs without voids, which were used as base DEMs for orthorectification.

3.1.2 Satellite Altimetry Products

The original SRTM version 1 DEM in 3 arc sec (~ 90 m) spatial resolution with voids was obtained from EarthExplorer as the representation of surface elevation in early 2000s. In addition, the CGIAR SRTM DEM, with voids filled using elevation values from other sources (**Reuter, et al., 2007**), were used as the base DEM for satellite image orthorectification in early 2000s, as well as the general reference DEM for calculating slope and aspect, facilitating further analysis of glacier changes in different topography groups. Comparison of the original SRTM version 1 DEM with ICESat elevation points in selected ice-free regions

suggests that the general accuracy for SRTM DEM is ~16 m, while the accuracy is much better in flat areas with slope less than 15°, with a value of approximately 6 m.

ICESat is another satellite altimetry product used extensively in this study, mainly as a reference elevation data source for analyzing uncertainty of other DEMs, thanks to its very fine vertical accuracy at centimeter level (**Martin, 2005; Schutz, et al., 2005**). The GLA14 Global Altimetry product was obtained from NSIDC (*http://nsidc.org/data/icesat/data.html*) and processed to extract elevation information using the NSIDC GLAS Altimetry elevation extraction Tool (NGAT) (*http://nsidc.org/data/icesat/tools.html*). Since SRTM and other types of DEM used in this study are referenced to the Earth Gravity Model EGM96 ellipsoid for vertical measurements, while ICESat data are referenced to the TOPEX / Poseidon-Jason ellipsoid, the GeoidEval program in GeographicLib software (*http://geographiclib.sourceforge.net/*) was used to calculate the shifts between the two different ellipsoid and transform the elevation data in ICESat to reference the EGM96 ellipsoid.

3.1.3 Topography maps

Eight military topographic maps from Former Soviet Union (FSU) (K44-064 a, b, g, v and K44-065 a, b, g, v) covering the IGM in 1:50,000-scale were used in this study. These maps were derived from aerial photographs acquired within the period from 1976 to 1980. A raster DEM were derived from the topographic maps to represent the surface elevation of the IGM in the 1970s. All maps were scanned in 300 DPI then georectified using the 4 corner points under the Gauss-Kruger projection system with Pulkovo 1942 datum. All contour lines and elevation points were manually delineated, and then transformed to WGS 1984 datum with an accuracy of 3 m, using a 7-parameter Coordinate Frame Rotation transformation

(**Maling, 1992**) with parameters provided by Georepository (*http://georepository.com/transformation_5044/Pulkovo-1942-to-WGS-84-20.html*). The elevation points and contour lines were re-projected to the `CA_Albers` coordinate system (**Table 5.2**), which is a coordinate system defined for all data used in this study. A raster DEM at 100 m spatial resolution was interpolated from the contour lines and elevation points using the ANUDEM algorithm (**Hutchinson, 1989; Hutchinson et al., 2011**), provided by the `Topo2Raster` tool in the ESRI ArcGIS 10.1 software. The nominal horizontal accuracy for the topography maps is 12.5 m, and the nominal vertical accuracy is approximately 6.7 m as 1/3 of the contour line interval (**ASPRS, 1990**). Comparison between the converted raster DEM with ICESat elevation points in selected ice-free regions suggests that the derived raster DEM has a vertical accuracy around 6 m for places with slope less than 15°. For steeper places, the accuracy is about 20 m.

3.2 Glacier delineation and topographic parameter derivation

3.2.1 Glacier delineation

The first step of glacier delineation is to generate the glacier boundaries in early 2000s based on LANDSAT ETM+ imageries using a semi-automatic procedure. Scene-specific critical values were used to separate glacier and permanent snow from other land cover types based on band 4 / band 5 ratio images (**Paul 2003; Raup et al., 2007; Surazakov, 2008**). The automatically generated glacier extents were converted from raster representation to vector polygons. The vector polygons were further manually separated based on topographical features, mainly ridge lines derived from CGIAR SRTM DEM, with each of the resulting polygon representing the boundary of one glacier. Those polygons of glacier boundaries were manually edited based on LANDSAT ETM+ images to correct classification errors. CGIAR

SRTM DEM and ALOS/PRISM DEM were consulted during the manual correction for topography features indicating possible existence of glaciers, especially in the places covered with moraines.

The second step is to produce the glacier boundaries for 1970s and late 2000s by manually editing the glacier boundaries in earlier 2000s based on KH9 or ALOS / PRISM satellite images. During the manual delineation, other data sources of satellite images were also consulted, including historical aerial photographs, historical topography maps, ASTER satellite images, and high resolution satellite images in Google Earth (QuickBird or SPOT), for general guidance when cloud or shadow in the main image sources make direct visual interpretation of glacier boundaries hard. The manual editing was conducted with the assumption that the upper boundaries of glaciers experienced little change, thus the editing was mainly conducted in lower boundaries and tongues of glaciers. Upper boundaries of glaciers were only edited when multiple sources all suggest existence of changes.

To enable tracking the evolution of glacier extent across different time periods, two properties were assigned to each glacier: the unique ID (UID) and the previous ID (PID). The UID is generated for each glacier as the string representation of the geometry center point within the glacier boundary polygon. Spatial overlay analysis between glacier boundaries in current and previous time period was conducted to assign values to the PID property in glacier polygons in current time period. The PID for a glacier is either the UID of the same glacier in previous time period, or the UID of a larger glacier in previous time period that has separated between the two periods, or a list of UIDs of glaciers that has merged to form the glacier in current time period.

3.2.2 Topographic parameter derivation

For each glacier, a set of topographic parameters were calculated, including area, perimeter, minimum elevation, mean elevation, maximum elevation, hypsometry, slope and aspect. The hypsometry for a glacier is computed as a list of area at each 100 m elevation zone, while the slope of a glacier is calculated as the average slope at all 100 m grid points within the glacier. The average slope method is used instead of the traditional method of calculating the slope as the arctangent of the maximum elevation differences within the glacier over the length of the glacier, since it is easier to implement, and has been shown to provide close and robust estimation of the slope of glacier calculated using the traditional method (**Paul and Svoboda, 2009; Frey et al., 2014**). The aspect of glacier is calculated as the direction of the line starting from the lowest elevation point of the glacier to the geometry center within the glacier.

3.3 DEM comparison

3.3.1 SRTM DEM correction

It is known that the C-Band frequency radar signal used by the SRTM sensor can penetrate snow and ice, resulting in an underestimation of glacier surface elevation. It is shown that the penetration can be up to 9 m for dry snow, and 1 - 2 m for exposed ice (**Rignot et al., 2001**). To compensate the penetration effect, the SRTM v1 DEM used in this study was corrected with specific methods before comparing with other sources of DEM.

In the IGM, the correction scheme developed for the Akshiirak mountain massif was used (**Surazakov and Aizen, 2006**), since these two massifs are both in the Tien Shan region and have similar climatic regimes with little precipitation in winter during the SRTM

acquisition time. It is assumed that a 1 m radar signal penetration happens on exposed clean ice glacier surface. The penetration increases linearly with increasing elevation from 1 m at the upper boundary of the exposed clean ice zone, to 9 m at the firn line. For places above the firn line, the penetration stays at 9 m. The upper boundary for the clean ice zone was estimated at 4235 m, determined by manual interpretation of Landsat ETM+ images. The firn line was estimated at 4500 m, as the average of mean elevation of all glaciers in the IGM in early 2000s. Corrections were applied on SRTM DEM in the IGM to offset the radar signal penetration in different elevation bands on glacier surface accordingly.

A different correction scheme was designed for the FGM, since the amount of winter precipitation in Pamir cannot be ignored. For areas from glacier tongue to glacier equilibrium line altitude (ELA) estimated as mean glacier elevation, the radar penetration is estimated as the sum of snow cover thickness and penetration in underlying ice (1 m). The thickness of snow cover was calculated using winter precipitation and winter precipitation lapse rate derived from the Fedchenko Station at 4169 m and the Altyn Mazar Station at 2782 m. For areas from glacier ELA to 5200 m, it is assumed that the radar signal penetration increases to 9 m linearly, and stays at the 9 m maximum penetration for higher elevation. The critical elevation of 5200 m is picked up based on analysis of snow pits data conducted during a field research in 2009 (**Aizen et al., 2009**).

3.3.2 Co-registration correction

It is important to co-register different DEMs for accurate comparison of surface elevation, as horizontal shifts between DEMs can lead to large vertical offsets. The analytical sinusoidal function method developed by Nuth and Kaab (**2011**) was used in this study to co-register different DEMs, as this method has sound theoretical background, is easy to

implement and has been proven to provide robust results (**Nuth and Kaab, 2011; Pieczonka, et al., 2013; Shangguan et al., 2014**).

For each pair of DEMs being compared, a sinusoidal function (**Eq 5.1**) was fitted on data in selected ice-free regions, linking difference of elevation, aspect and slope together.

$$\frac{dh}{\tan(\alpha)} = a \cdot \cos(b - \phi) + c \qquad \textbf{Equation 5.1}$$

where dh is the difference of elevation, α is the slope, ϕ is the aspect, while a and b are parameters to be fitted. Then the horizontal shifting vector is calculated as:

$$\Delta_x = abs(a) * \sin(b) \qquad \textbf{Equation 5.2}$$

$$\Delta_y = abs(a) * \cos(b) \qquad \textbf{Equation 5.3}$$

The results of the shifting vectors were reported in **Table 5.3-a** and **Table 5.4-a** for the FGM and the IGM, respectively. All resulting DEMs were resampled to 100 m horizontal resolution before comparison, to accommodate the roughest resolution DEM (the SRTM DEM and the DEM derived from topographic maps) used in this study.

3.3.3 Correction by slope group

Elevation differences between co-registered DEMs were calculated in selected ice-free regions. Mean differences and Normalized Median Absolute Deviance (NMAD) (**Höhle et al., 2009; Pieczonka et al., 2013**) were calculated to provide estimations of bias and uncertainty of the comparison, respectively, for the whole selected ice-free region, as well as each 5 ° slope group. Mean shift method were used to compensate the bias for the comparison at each slope group. The NMAD is used as the representation of uncertainty for DEM comparisons in this study since it provides more robust estimation of dispersion for

distribution known to have outliers compared with standard error (**Höhle et al., 2009**). It is found that for both the FGM and the IGM, the bias varies across different slope groups slightly, while the uncertainty goes up with increasing slope (**Table 5.3-b and Table 5.4-b**).

3.3.4 Estimation of glacier surface elevation and volume changes

For each sub-region within the FGM and the IGM, the change of glacier surface elevation was estimated in the ablation zone, defined as areas below the equilibrium line which is calculated as the average of the mean elevations of glaciers within the sub-region (**Nesje and Dahl, 2000; Cuffey and Paterson, 2010**). It is shown in the previous section that the uncertainty of DEM comparison goes up with slope, and the uncertainties are at a high level for places with slope steeper than 45°, thus only places with slope less than 45° were included in calculation. Mean surface elevation difference for grid points within the ablation zone with valid elevation data in the two time periods being compared was calculated for representing the surface elevation change, while the average NMAD was calculated to estimate the uncertainty of the surface elevation change. Then the glacier volume change for the ablation zone in each sub-region was estimated by multiplying the mean surface elevation change with the total area of ablation zone within the sub-region.

4 Results

4.1 Glacier extent and volume changes in the Fedchenko Glacier Massif

4.1.1 Characteristics of glacier distribution in the FGM

The characteristics of general glacier distribution by sub-region and by different topographic parameters (slope, aspect and area class) in the FGM were investigated based on

the glacier boundary polygons and CGIAR SRTM DEM representing the situation in 2000. A quantitative description of the spatial distribution of glaciers in the FGM could provide information necessary for hydrological / land surface modelling in this high mountainous area.

There are 1230 glaciers in FGM (without the Fedchenko glacier), with a total area of 1812.5 km^2. The Fedchenko glacier was excluded from the analysis, since it has an area of 687.4 km^2 which accounts for 27.5% of total glacier area in FGM and has the ability to modify the distribution of glaciers by different parameters significantly. The number of glaciers varies across different sub-regions from 234 in the sub-region ② and the sub-region ⑥ to 98 in sub-region ④ (**Figure 5.03-a**). The area of glaciers varies from 445.0 km^2 in the sub-region ⑤, accounting for 24.5% of total glacier area in the FGM, to 145.4 km^2 in the sub-region ⑥, accounting for only 8.0% of total glacier area (**Figure 5.03-e**). The sub-region ⑤ Upper Vanch and Upper Garmo Basins is located to the west of major FGM mountain ridges (**Figure 5.01-b**), which is in favor of the development of glaciers, since the major moisture source were brought to the FGM by westerlies. The sub-region ⑥ Middle Vanch and Middle Garmo Basins, though also located to the west of the FGM, has mountains with much lower elevation than other sub-regions, resulting in having a large number of small glaciers.

The number of glaciers decreases with increasing glacier area. There are 554 glaciers with area smaller than 0.1 km^2, accounting for 45.0% of the total number of glaciers in FGM, while only 215 glaciers with area greater than 5 km^2 exist (**Figure 5.03-b**). In contrast, the area of small glaciers only accounts for a small percentage of the total glacier area in the

FGM, while the total area for glaciers with area greater than 5 km^2 is 1622.8 km^2, accounting for 89.5% of the total glacier area in FGM (**Figure 5.03-f**).

The distribution of the number of glaciers by slope in general resembles the normal distribution, with a peak of 265 glaciers in the slope group 30° – 35°. There are 1055 glaciers with slope in the range of 15° to 40°, accounting for 85.8% of total glaciers in FGM (**Figure 5.3-c**). The distribution of glacier area by slope is right-skewed, with the glaciers in the slope group 15° - 20° and 20° - 25° having a total area of 1276.5 km^2, accounting for 70.4% of total area in FGM (**Figure 5.03-g**).

The number of glaciers for different aspect direction varies from 369 for east facing glaciers to 263 for south facing glaciers (**Figure 5.03-d**). The glacier area for different aspect direction varies from 507.9 km^2 for east facing glaciers to 380.9 km^2 for south facing glaciers (**Figure 5.03-h**). Glaciers with south aspect are much less in number and smaller in area compared with other aspect group, because of the stronger melting with higher incoming solar radiation (**Kutuzov et al., 2009; Kriegel, et al., 2013**).

4.1.2 Changes of glacier extent in the FGM

4.1.2.1 Changes in number of glaciers and area of glaciers

The area of glaciers in the FGM decreased continuously from 2558.8 km^2 in 1975, to 2499.9 km^2 in 2000, and to 2479.2 km^2 in 2007. The overall shrinkage of glacier area in the FGM is 79.6 km^2 between 1975 and 2007, or 3.1% of the total glacier area in 1975 (**Figure 5.04-1-a**). The Fedchenko Glacier, as the largest glacier in the glacier massif, retreated continuously in a rate slower than the whole FGM, with the glacier area of the Fedchenko Glacier decreased 2.04 km^2 between 1975 and 2007, or 0.3% of the glacier area in 1975. In

contrast to the decrease of glacier area, the number of glaciers in the FGM increased continuously from 1168 in 1975, to 1231 in 2000, and to 1269 in 2007, due to split of retreating glaciers (**Figure 5.04-1-a**). Such a decrease of glacier area in companion with an increase of the number of glaciers can be observed in all 7 sub-regions (**Figure 5.04-1-b to Figure 5.04-1-h**). Analysis of the relationship between percentage of glacier area changes with glacier area, slope and aspect shows that small glaciers tend to have stronger area shrinkage in both 1975 – 2000 and 2000 – 2007 compared with large glaciers (**Figure 5.04-2**). The percentage of glacier area change does not depend on slope (**Figure 5.04-3**) and aspect (**Figure 5.04-4**).

Along with the glacier retreat, the regional ELA in the FGM goes up continuously during the research period, from 4858 m in 1975, to 4868 m in 2000, and to 4883 m in 2007. Such an increase of ELA occurs in all sub-regions, area classes, slope groups and aspect directions (**Figure 5.05**).

4.1.2.2 Retreating glaciers

Although most glaciers in the FGM retreated with decreased area, there are a number of advancing glaciers. Excluding the advancing glaciers, the total area shrinkage between 1975 and 2000 is 61.8 km^2, accounting for 2.6% of total area of the retreating glaciers in 1975. The area shrinkage varies across different sub-regions, from the highest 14.7 km^2 in sub-region ② to the lowest 3.4 km^2 in the sub-region ⑦ (**Figure 5.06-1-a**). The largest glacier shrinkage is observed in the sub-region ② (5.7%) and sub-region ⑥ (5.6%), while the smallest retreating in the sub-region ① (0.8%) (**Figure 5.06-1-b**). Between 2000 and 2007, the total glacier area decreased by 27.2 km^2 (2.2% of total glacier area), excluding the

advancing glaciers. The glacier area shrinkage varies from 7.8 km^2 in the sub-region ⑤ (3.4%) to the 1.6 km^2 in the sub-region ④ (1.1%) (**Figure 5.06-1-a and Figure 5.06-1-b**).

Comparison of the glacier shrinkage across different sub-regions shows that the sub-region ⑥, as located in the outer area of the FGM, with large numbers of small glaciers located at low elevation experience stronger glacier area shrinkage than other sub-regions. In contrast, the sub-region ① with the largest glaciers in the FGM loss only 0.8% of its glacier area between 1975 and 2007.

Comparison of glacier shrinkage speeds in 1975 – 2000 and in 2000 – 2007 reveals the accelerated glacier retreat in the FGM. The shrinkage speed is 2.4 km^2 / year between 1975 and 2000, and increased to 3.4 km^2 / year between 2000 and 2007. Such an acceleration can be observed in all sub-regions, with the most conspicuous acceleration of retreating happened in the sub-region ⑤ (0.46 km^2 / year) and the sub-region ⑦ (0.24 km^2 / year), while the sub-region ① had the smallest acceleration (0.01 km^2 / year) (**Figure 5.06-1−c**).

4.1.2.3 Advancing glaciers

There are 35 glaciers with increasing area between 1975 and 2000 in the FGM, and the total increased area is 3.0 km^2. The number of advancing glaciers varies from 13 in the sub-region ① to 1 in the sub-region ④ and in the sub-region ⑥. The sub-region ⑤, exhibiting several large surging glaciers, has the highest advanced area of 2.1 km^2 between 1975 and 2000. In comparison, the advanced areas in the sub-region ③, ④ and ⑥ are negligible (less than 0.1 km^2) (**Figure 5.06-2**).

There are more advancing glaciers (76), and larger advanced areas (6.5 km^2) between 2000 and 2007, compared with the period between 1975 and 2000. All sub-regions, except

sub-region ②, experienced increases of both the number of advancing glaciers and advanced area. With 16 advancing glaciers and an increased advanced area of 0.95 km^2, the sub-region ⑥ is the sub-region with the strongest increase of advancing phenomenon (**Figure 5.06-2**).

4.1.3 Change of glacier surface elevation and volume in the FGM

Between 1975 and 2000, the mean decrease of glacier surface elevation is 10.61 ± 6.60 m for areas below the ELA in the FGM. The magnitude of glacier surface elevation change varies across different sub-regions, with the strongest decrease in the sub-region ② (18.26 ± 7.06 m), and the smallest in the sub-region ⑤ (1.52 ± 6.72 m) (**Figure 5.07-1-a**). Between 2000 and 2007, the mean decrease of glacier surface elevation in the FGM is 0.28 ± 5.47 m. The sub-region ① experienced the strongest glacier surface elevation decrease among the 7 sub-regions with a magnitude of 6.10 ± 4.81 m, while the sub-region ⑤, ⑥ and ⑦ have experienced insignificant decrease of glacier surface elevation. In contrast, the sub-region③ witnessed a slight increase of glacier surface elevation (10.68 ± 5.58 m), while the sub-region ② and ④ experienced insignificant increase of glacier surface elevation (**Figure 5.07-1-b**). The speed of the glacier surface elevation decrease in the sub-region ①, ⑤, ⑥ and ⑦, during the time period between 2000 and 2007, is slightly higher than the speed in 1975 – 2000 (**Figure 5.07-1-c and Figure 5.07-1-d**). The total loss of ice volume is estimated as 9.24 ± 3.11 m^3 between 1975 and 2007 for glacier areas below regional ELA in the FGM: 8.99 ± 2.41 m^3 in 1975 – 2000, and 0.25 ± 1.97 m^3 in 2000 – 2007 (**Figure 5.07-2**).

4.1.4 Change of glacier surface elevation on selected profiles in the FGM

Patterns of glacier surface elevation change vary considerably in the FGM. Three profiles were presented as show cases (**Figure 5.01-b, Figure 5.08 to Figure 5.10**). The first one is for the main body of the Fedchenko Glacier (**Figure 5.08-a and Figure 5.08-b**), which experienced continuous surface elevation decrease in both 1975 – 2000 and 2000 – 2007. Between 1975 and 2000, the maximum magnitude of surface elevation decrease is ~45 m, observed in the glacier tongue area (elevation ~2950 m). The magnitude goes down with increasing elevation and increasing distance to the glacier tongue, with the minimum surface elevation decrease of ~10 m observed at the area around 8,800 m upstream to the glacier tongue (elevation ~3300 m). Then the magnitude of surface lowering increases to ~40 m at 15, 000 m from the glacier tongue (elevation ~3550 m), and remains relatively stable around ~30 m for the subset of glacier with distance to the glacier tongue in the range of 15, 000 m – 32, 500 m (elevation 3550 – 4150 m). Between 2000 and 2007, the magnitude of surface lowering increases from ~10 m at the tongue area to ~20 m at 10,000 m upstream, and stays stable around ~10 m further upstream to about 24,000 m. Then the surface lowering decreases with increasing elevation to around 0 m (**Figure 5.09-a**). Comparison of the surface elevation lowering between the two time periods shows that the rates of surface lowering in two periods are similar around 1.17 m / year for the low elevation areas near the glacier tongue (distance to glacier tongue < 5, 000 m, elevation < 3200 m). The rates of surface lowering are also similar in high elevation areas (distance to glacier tongue > 25, 000 m, elevation > 3900 m), with mean values of 1.39 m / year and 1.21 m / year for the time periods 1975 – 2000 and 2000 – 2007, respectively. In the middle zone with distance to glacier tongue between 5,000

m and 25, 000 m, the magnitude surface elevation lowering in 2000 – 2007 is always stronger than in 1975 – 2000 (**Figure 5.10-a**).

The second profile is for the Medvezhiy Glacier (**Figure 5.08-c and Figure 5.08-d**). This glacier is known to have experienced a series of surging events in 1963, 1973, 1988 and 2001, with one major surging event in 1973 (**Dyurgerov et al., 1985; Raymond, 1987; Kotlyakov et al., 1997; Kotlyakov et al., 2008**). Between 1975 and 2000, the tongue of the glacier, created during the previous surge in 1973, retreated quickly for 2100 m, with a maximum surface lowering of 111.6 m (**Figure 5.9-b**). In higher elevation (elevation > 3150 m, distance to tongue > 3, 100 m), mass of ice accumulated with a maximum surface elevation increase of 112.1 m, as movement of ice from accumulation zone dammed by the ice in lower elevation deposited during the previous surging event. Between 2000 and 2007, there is little change of surface elevation for the Medvezhiy Glacier (**Figure 5.09-b and Figure 5.10-b**).

The third profile is for the Geographical Society glacier (**Figure 5.08-e and Figure 5.08-f**), which was identified as an unstable glacier though no surging event has happened by a study based on air photographs and satellite images before 1991 (**Kotlyak et al., 1997**). Between 1975 and 2000, the surface elevation has little changes, or slight increase for certain small areas, similar as the situation for the Medvezhiy Glacier in the time period between 2000 and 2007. A surging event happened between 2000 and 2007, with glacier tongue advanced for 870 m, and large volume of ice dumping form high elevation part to the low elevation part (**Figure 5.09-c and Figure 5.10-c**).

4.2 Glacier extent and volume changes in the Inylchek Glacier Massif

4.2.1 Characteristics of glacier distribution in the IGM

The general glacier distribution characteristics in the IGM were described based on data reflecting the situation in early 2000s. There are 236 glaciers, covering a total area of 750.9 km^2, with the South Inylchek Glacier (516.0 km^2) and the North Inylchek Glacier (139.5 km^2) as the two largest glaciers in this glacier massif. There are similar numbers of glaciers in the two sub-regions: 123 glaciers in sub-region ① and 113 glaciers in sub-region ② (**Figure 5.11-a and Figure 5.11-e**).

Most glaciers (88.9%) have an area less than 1 km^2, while 24 glaciers have an area in the range of 1 - 5 km^2, and only the South and North Inylchek glaciers having areas greater than 5 km^2 (**Figure 5.11-b and Figure 5.11-f**). The distribution of numbers of glaciers by slope resembles the normal distribution, with the peak of 62 in the slope group 30 - 35°, and most glaciers having an average slope less than 45° (**Figure 5.11-c)**. The distribution of glacier area by slope is extremely right skewed (**Figure 5.11-g**), as the South Inylchek and North Inylchek glaciers having mean slopes of 19.9° and 22.0°, respectively. The number of glaciers for different aspect direction varies from 74 for west direction to 44 for east direction. The west direction has the largest total glacier area, due to the fact that both South and North Inylchek glaciers are facing west. The east direction is the aspect direction with the second largest glacier area of 35.5 km^2, while the north and east directions having similar glacier areas (~19 km^2) (**Figure 5.11-d and Figure 5.11-h**).

4.2.2 Changes of glacier extent in the IGM

The total glacier area decreased from 753.6 km^2 in 1976, to 750.9 km^2 in 2000 and to 747.2 km^2 in 2007. The overall decrease of glacier area in the IGM is 6.5 km^2 between 1976 and 2007, or 0.86% of the total glacier area in 1976 (**Figure 5.12-1-a**). In comparison, the number of glaciers increased from 219 to 236 between 1976 and 2000, and then, between 2000 and 2007, did not changed in number. Both sub-regions in the IGM experienced continuous decreases of glacier areas in 1976 - 2000 and 2000 - 2007, and increases of number of glaciers between 1976 and 2000 (**Figure 5.12-1-a and Figure 5.12-1-b**). The area of the South Inylchek Glacier decreased from 517.7 km^2 in 1976 to 515.1 km^2 in 2007, or 0.50 % of the area in 1976, while the decrease of glacier area for the sub-region ① is 4.9 km^2, or 0.86 % of the area in 1976. The area of North Inylchek Glacier decreased from 149.6 km^2 in 1976 to 148.7 km^2 in 2007, or 0.57 % of the area in 1976, while the decrease of area for the sub-region ② is 1.6 km^2, or 0.84% of the area in 1976.

Similar to the FGM, percentage of glacier area shrinkage does not depend on slope (**Figure 5.12-3**) or aspect (**Figure 5.12-4**), while small glaciers tend to have larger percentage of area shrinkage (**Figure 5.12-2**). In accordance with the glacier retreats, ELA for the IGM moved up from 4483 m in 1976, to 4489 m in 2000 and 4500 m in 2007 (**Figure 5.13**).

There is only one case of advancing glacier in the IGM, the North Inylchek Glacier between 1976 and 2000, with the glacier tongue advanced for ~ 1900 m. The speeds of glacier retreat between 1976 and 2000 are ~0.20 km^2 / year for both sub-region ① and ②. Glacier retreat accelerated for the period between 2000 and 2007 with increased speed of glacier retreat of 0.26 km^2 / year and 0.62 km^2 / year for the sub-region ① and the sub-region ②, respectively (**Figure 5.14**).

4.2.3 Change of glacier surface elevation and volume in the IGM

Between the 1970s and 2000, the mean decrease of surface elevation is 26.46 ± 18.34 m for areas below ELA in the IGM. The magnitude of surface elevation decrease is 24.40 ± 18.01 m for sub-region ① and 32.68 ± 19.41 m for sub-region ②. Between 2000 and 2007, the mean decrease of surface elevation is 5.86 ± 5.41 m in the IGM: 5.16 ± 5.35 m in sub-region ① and 7.37 ± 5.55 m in sub-region ②. The speed of surface elevation decrease is faster in the period between the 1970s and 2000 than in the period between 2000 and 2007, and faster in sub-region ② than in sub-region ① (**Figure 5.15-1**). The estimated total loss of ice volume for glacier areas below ELA is 14.72 ± 5.19 m^3 between the 1970s and 2007, including 13.81 ± 4.36 m^3 in 1970s - 2000 and 0.90 ± 0.83 m^3 in 2000 - 2007 (**Figure 5.15-2**).

4.2.4 Change of glacier surface elevation on selected profiles in the IGM

Profiles of surface elevation changes on the South and North Inylchek glaciers were presented as show cases of glacier surface elevation changes in the IGM (**Figure 5.16**). In South Inylchek Glacier (**Figure 5.17-a**), between 1970s and 2000, the magnitude of surface elevation decrease is smaller in the tongue area (elevation < 3160 m, distance to glacier tongue < 6, 500 m) than in upper areas, in general less than 20 m, due to the protection of moraines (**Hagg et al., 2008**). The magnitude of surface elevation decrease rises up sharply from ~20 m to ~60 m in a small elevation range of 3160 m to 3260 m (distance to tongue in the range from 6,500 m to 10,000 m), then fluctuates around 30 m to 60 m in upper areas of the profile under examination. Between 2000 and 2007, the magnitude of surface elevation change is small. Small decrease of surface elevation less than 10 m can be found in areas below 3590 m (distance to glacier tongue < 21,000 m). For glacier areas above 3590 m, there

are minor increase of surface elevation of less than 6 m. Comparison of the rate of surface elevation changes (**Figure 5.18-a**) shows that in glacier tongue areas protected by moraine (distance to glacier tongue < 6,500 m), the rates of surface elevation change are similar in both 1970s - 2000 (0.85 m / year) and 2000 - 2007 (0.94 m / year). In upper areas of the North Inylchek Glacier, the decreasing rate is much higher in 1970s - 2000 than in 2000 - 2007.

The North Inylchek Glacier (**Figure 5.17-b**) experienced a major surge of the glacier tongue between 1970s and 2000, with the surface elevation change profile shows an increase of surface elevation in the glacier tongue areas (elevation < 3580 m, distance to glacier tongue < 7,300 m), with maximum increase of ~ 50 m. As large volumes of ice deposited from high elevation areas to glacier tongue areas, areas with elevation higher than 3580 m (distance to glacier tongue > 7, 300 m) experienced decreases of surface elevation. The magnitude of surface elevation decrease goes up with increasing elevation, and stays around 140 m for areas above 3770 m (distance to elevation > 15,300 m). Between 2000 and 2007, there exists small nonsignificant change of surface elevation. Areas below 3790 m (distance to glacier tongue < 16, 000 m) tends to have decrease of surface elevation with a maximum magnitude of ~ 20 m, while higher elevation areas tend to have increase of surface elevation, with a maximum magnitude of ~ 9 m.

5 Discussion

5.1 Glacier changes related to regional climate changes in the FGM

The glacier area shrinkage observed in the FGM during the research period is mainly related with the increase of summer air temperature. Between 1951 - 1976 and 1976 - 2010, the long-term mean annual and summer air temperature increased significantly at the Altyn

Mazar, Fedchenko, and Garm stations, while no significant changes of annual and seasonal precipitation found (**Chapter 2**).

Between 1975 and 2000, summer air temperature in these three stations showed small decreases, while winter precipitation showed insignificant increases (**Figure 5.19-1 to 5.19-3**). The climate regime in this period is relatively favorable for glacier development, though it did not compensate the general increase of summer ablation caused by the increase of summer air temperature since mid-1970s (**Khromova et al., 2006; Chapter 2**), resulting in the observed continuous decreases of glacier surface elevation, loss of glacier mass and retreat of most glaciers in the FGM.

Between 2000 and 2007, summer air temperature slightly increased at the Altyn Mazar, Fedchenko, and Garm stations, while winter precipitation increased only at the Altyn Mazar and Garm stations (**Figure 5.19-1 to Figure 5.19-3**). The increase of winter accumulation lead to the smaller rate of surface elevation decreasing between 2000 and 2007 in the FGM, compared with the period 1975 to 2000. Glaciers in several sub-regions even experienced slightly increase of surface elevation in this period. At the same time the glaciers continued to shrink in area with a faster rate than the rate in the former period, which is most probably due to the increase (though small) of summer air temperature. Increased winter snow accumulation and intensification of summer ablation might contribute to the dynamics of surging glaciers in the period 2000 - 2007, compared with the former period (1975-2000).

5.2 Glacier changes related to regional climate changes in the IGM

The observed retreat of glacier area and decrease of glacier surface elevation in the IGM can be attributed to the increase of summer air temperature, and decrease of summer

precipitation. Between 1951 - 1976 and 1977 - 2010, significant increase of summer air temperature and decrease of summer precipitation was observed at both stations, the Tien Shan and Koilu (**Chapter 2**).

The summer air temperature in the Tien Shan station increased significantly between 1976 and 2000, with a rate of 0.26 °C / 10a (Figure 19-4) while summer precipitation at the Tien Shan and the Koilu stations decreased significantly, with rates of -36.02 mm / 10a (Figure 19-6) and -24.58 mm / 10a (Figure 19-5), respectively. Increase of summer air temperature has a strong effect on mass balance of the glaciers with mainly summer accumulation (**Aizen et al., 1996; Fujita & Ageta, 2000**), leading to: (1) an increased amount of energy available for snow and ice melt; (2) a decreased proportion of solid precipitation (snow) in glacier accumulation zone; (3) lower albedo of glacier surface due to both (1) & (2), which result in more glacier and snow melt. The long-lasting negative mass balance of the glaciers in the IGM in this period, caused by the increase of summer air temperature and deficit of summer precipitation, led to the much stronger glacier area shrinkage and glacier surface elevation lowering for glaciers in the IGM than the glaciers in the FGM.

Between 2000 and 2007, summer air temperature in the Tien Shan Station had insignificant increase, in contrast with the Koilu Station where increase in air temperature was significant with a rate of 0.83 °C / 10a, though it should be noticed that the Koilu station is located at low elevation, where increase of air temperature tends to be stronger (**Chapter 2**) than high elevation glacier areas. Summer precipitation at the Tien Shan and the Koilu stations had insignificant decreases between 2000 and 2007, though both stations experienced strong increases of summer precipitation in the sub-period between the late 1990s and the early 2000s (**Figure 5.19-4 and Figure 5.19-5**). The climate condition was more favorable

for glaciers in the period 2000 – 2007 compared with the period 1976 - 2000, resulting in decelerated rates of surface elevation decrease in 2000 - 2007 (**Figure 5.15-1**). Since glacier extent is a slow respondent to the change of glacier mass balance, especially in large glaciers like the Inylchek Glacier, area of glacier continued to shrink during 2000 - 2007.

5.3 Regional differences of glacier changes

In general, the accelerated glacier area loss in the FGM, is in line with previous studies based on selected glaciers in Central Pamir. Khromova, et al. (**2006**) showed the accelerated trend of glacier shrinkage in Central and Eastern Pamir since the end of the 1970s to 2001, based on the areas of 5 glaciers and the terminus positions of 44 glaciers, which were derived from historical glacier surveys and satellite images. The largest one of the 5 selected glaciers have an area of ~25 km^2 in 1978. The area of the selected glaciers decreased 18.4% from 1978 to 2001, which is within the range of glacier area shrinkage between 1975 and 2000 found in this study for glaciers with similar areas. Zhang et al. (**2014**) studied the area changes of 287 glaciers in the Fedchenko Basin, from 1992 to 2000 and from 2000 to 2006 based on ETM+ and ALOS AVNIR-2 images. The glaciers analyzed include all glaciers in the sub-region ① and some glaciers in sub-region ② and ⑦ in this chapter. They reported a decrease of glacier area between 1992 and 2000, with a rate of -0.09% / year, and an increase of glacier area between 2000 and 2006, with a rate of 0.7% / year. The decreasing rate in the former period is stronger than the decreasing rate of glacier area between 1975 and 2000 in the sub-region 1 (-0.76% or -0.03% / year) as presented in this chapter. The increase of glacier areas in the latter period is in contradiction with the glacier area shrinkage between 2000 and 2007 found in this chapter. As Zhang et al. (**2014**) reported that most of the glacier area expansion occurred in upper elevations, it is possible that the increased areas of seasonal snow

cover in 2006, due to the increase of winter precipitation, were misclassified as glacier, leading to a false signal of glacier area increase.

Glacier surface elevation changes in the FGM or in other glacier systems in Central Pamir have not been fully studied before. This chapter provides the first quantification of glacier surface elevation change estimation between 1975 and 2000, while Gardelle et al. (**2013**) provides a region-wide estimation of glacier mass balance changes over the Pamir-Karakoram-Himalaya between 1999 and 2011, using SRTM and SPOT5 data. For Western Pamir and part of Central Pamir, Gardelle et al. (**2013**) reported slight increase of glacier surface elevation in the accumulation zone, while in the ablation zone, no elevation changes can be observed (-0.02 ± 0.13 m / year). The results are in accordance with the glacier surface elevation changes under the regional ELA between 2000 and 2007 presented in this chapter. The Fedchenko Glacier has attracted special attention, about its volume and the historical changes of its ice volume as a solid storage of water resources. Lambrecht et al. (**2014**) studied the area and volume changes of the Fedchenko Glacier's main trunk, based on historical topographic maps in 1928 and 1958, as well as SRTM DEM in 2000 and D-GPS survey in 2009. It was reported that the main trunk of the Fedchenko Glacier is in near balance situation. The glacier area decreased 1.4% between 1928 and 2000, while the loss of ice volume was ~5km^3. The surface elevation changes along the main flow-line of the Fedchenko Glacier main trunk in 2000 - 2009 as reported by Lambrecht et al. (**2014**), is similar to the profile of glacier surface elevation change between 2000 and 2007 presented in this chapter.

Major findings of the glacier changes in the IGM, including the accelerated retreat of glacier area, between 1976 - 2000 and 2000 - 2007, and the lesser lowering of glacier surface

elevation in 2000 - 2007 than in 1970s - 2000, can be supported by the results of several independent studies, utilizing different types of data and focusing on different periods (**Osmonov et al., 2013; Shangguan et al., 2014; Pieczonka & Bolch, 2015**).

The glacier ice volume loss is much stronger in the IGM than in the FGM, as the mean glacier surface elevation lowering in the IGM is more than twice of the mean surface lowering in the FGM. Such differences are in accordance with the differences of climate conditions in the two glacier massifs, as the climate condition in the FGM was more comparable for glaciers than the climate conditions in the IGM. The glacier area loss in the FGM and the IGM are within the same range, with the IGM experienced stronger retreat. The sub-region ① of the FGM, containing 150 glaciers with a total area of 855.1 km^2 in 1975, including the Fedchenko Glacier, can be treated as a counterpart of the IGM, which contains 219 glaciers with a total area of 753.6 km^2 in 1976. The glacier area loss of 0.81% from 1975 to 2007 in the sub-region ① of the FGM, is comparable to the glacier area loss of 0.86% in the IGM between 1976 and 2007. The IGM in the boundary of Sarydjaz River Basin (SJRB), can be compared with the FGM, since both have similar number and area of glaciers. The FGM has experienced smaller glacier area loss (2.4% between 1975 and 2007 or 0.075% / year) than IGM (3.7% between 1990 and 2010, or 0.176% / year) (**Osmonov, et al., 2013**). Both the FGM and the IGM have much smaller glacier area loss than glaciers in the outer zones of the Central Tien Shan and Central Pamir (**Table 5.5**).

6 Conclusion

This chapter investigated the changes of glacier area and surface elevation in the Fedchenko Glacier Massif and the Inylchek Glacier Massif. The results show that glaciers in

both glacier massifs have experienced continues glacier area loss in the period of 1975/1976 to 2000 and 2000 to 2007, with stronger area loss rate in the latter period. In contrast, the surface elevation lowering in both glacier massifs decelerated between the two periods.

In the FGM, the number of glaciers increased from 1168 in 1975 to 1269 in 2007, while the area of glaciers decreased from 2558.8 km^2 in 1975 to 2479.2 km^2 in 2007, with the lost area of 79.6 km^2 accounting for 3.1% of the area in 1975. The glacier area loss rate increased from 2.27 km^2 / year between 1975 and 2000, to 2.59 km^2 / year between 2000 and 2007. Larger glaciers tend to have less area loss, for example, in 2007 the Fedchenko Glacier has lost only 0.3% of its area in 1975. The number of surging glaciers also increased from 35 in 1975 - 2000, to 76 in 2000 - 2007. The mean decrease of glacier surface elevation is 10.61 ± 6.60 m between 1975 and 2000, and is 0.28 ± 5.47 m between 2000 and 2007, for areas below the regional ELA in the FGM. The total loss of ice volume is estimated as 9.24 ± 3.11 m^3 between 1975 and 2007 for glacier areas below regional ELA. The glacier area shrinkage and surface elevation lowering can be attributed to the general increase of air temperature, especially summer air temperature since the mid-1970s, which leads to stronger glacier ablation. The decelerate glacier surface elevation lowering in 2000 - 2007 can be attributed to the recent increase of winter precipitation.

In the IGM, the total glacier area decreased from 753.6 km^2 in 1976 to 747.2 km^2 in 2007, with the loss area accounting for 0.86% of the area in 1976, while the number of glaciers increased from 219 to 236. The glacier area loss rate increased from 0.10 km^2 / year between 1975 and 2000, to 0.46 km^2 / year between 2000 and 2007. Larger glaciers tend to have less area loss, as the South Inylchek Glacier and North Inylchek Glacier, lost ~0.5% of their areas between 1976 and 2007. The estimated total loss of ice volume is 14.72 ± 5.19 m^3

between the 1970s and 2007, including 13.81 ± 4.36 m^3 between 1970s - 2000 and 0.90 ± 0.83 m^3 between 2000 and 2007. The glacier area shrinkage and the surface elevation lowering are related with the increase of summer air temperature and decrease of summer precipitation. The decelerate glacier surface elevation lowering in 2000 - 2007 can be attributed to the increase of summer precipitation since the late 1990s.

Comparison of the two glacier mountain massifs shows that the magnitude of glacier surface elevation lowering in the IGM was more than twice as the magnitude in the FGM, which can be attributed to the more favorable climate conditions for glaciers in the FGM than in the IGM. The magnitudes of glacier area shrinkage in these two glacier massifs are comparable, with stronger magnitude in the IGM than in the FGM. The magnitudes of glacier shrinkage in both glacier massifs are much smaller than glaciers in outer zones of mountain systems in Central Asia.

Tables

Table 5.1a Data sources used in Fedchenko Glacier Massif[17]

Time period	Data source	Original IDs	Acquisition time	Resolution	Accuracy	Usage
1970s	KH9 satellite images	DZB1210-500134L005001_5 DZB1210-500134L006001_6	1975-07-13	6 m	horizontal: 6.27 m; vertical: ~ 6 m in flat regions, ~ 20 m in mountainous regions	represent both glacier surface elevation and boundary
early 2000s	LANDSAT ETM+ images	LE71510332000237SGS00 LE71520332000260SGS00	2000-08-24 2000-09-16	15m, 30 m	horizontal: ~15 m	represent glacier boundary
	SRTM v1 DEM	SRTM3N39E073V1, SRTM3N39E072V1,SRTM3N38E071V1, SRTM3N39E071V1,SRTM3N38E073V1,SRTM3N38E072V1	2000-02-11	3 arc sec, ~90 m	vertical: ~ 16 m	represent glacier surface elevation
late 2000s	ALOS / PRISM satellite images	ALPSMN031242815, ALPSMB031242870; ALPSMN031242820, ALPSMB031242875; ALPSMN031242825, ALPSMB031242880 ALPSMW087402825, ALPSMB087402880; ALPSMW087402820, ALPSMB087402875; ALPSMW087402815, ALPSMB087402870; ALPSMW087402810, ALPSMB087402865	2006-08-26 2007-09-15	2.5 m	horizontal: ~4 m in flat regions, ~8 m in mountainous regions; vertical: ~5 m in flat regions, ~18 m in mountainous regions	represent both glacier surface elevation and boundary

Table 5.1b Data sources used in Inylchek Glacier Massif

Time period	Data source	Original IDs	Acquisition time	Resolution / Scale	Accuracy	Usage
1970s	Topographic maps	K44-064, a, b ,g, v	1976	1:50,000	horizontal: ~12.5 m; vertical: ~20 m	represent glacier surface elevation
		K44-065, a, b ,g, v	1977 - 1980			
	KH9 satellite images	DZB1211-500142L007001_7	1976-01-12	6 m	horizontal: ~6 m in flat regions, ~10 m in mountainous regions	represent glacier boundary
		DZB1211-500142l008001_8				
		DZB1209-500081L001001_1	1974-11-16			
		DZB1209-500081L002001_2				
early 2000s	LANDSAT ETM+ images	LE71470312002230SGS00	2002-08-18	15m, 30 m	horizontal: ~15 m	represent glacier boundary
	SRTM v1 DEM	SRTM3N42E079V1	2000-02-11	3 arc sec, ~90 m	vertical: ~16 m	represent glacier surface elevation
late 2000s	ALOS / PRISM satellite images	ALPSMB088712805	2007-09-24	2.5 m	horizontal: ~4 m in flat regions, ~8 m in mountainous regions; vertical: ~5 m in flat regions, ~18 m in mountainous regions	represent both glacier surface elevation and boundary
		ALPSMW088712750				
		ALPSMB037512805	2006-10-08	2.5 m		
		ALPSMN037512750				

Table 5.2 Definition of the `CA_Albers` coordinate system

Group	Parameter	Value
Datum		
	Name	WGS84
	Major semi-axis (m)	6,378,137
	Ellipsoid flattening	0.003352811
Projection		
	Type	Albers conical equal area
	First parallel (degree)	47
	Second parallel (degree)	38
	Central meridian (degree)	85
	Latitude of origin (degree)	0
	False easting (m)	3,000,000
	False northing (m)	0

Table 5.3-1 Shifting vector used for aligning DEMs in the FGM

DEM former	DEM latter	shift of x (m)	shift of y (m)	mean dh (m)	NMAD (m)	comment
KH9 DEM	SRTM DEM	NA	NA	10.2	8.0	no shift needed
SRTM DEM	ALOS / PRISM DEM	45.3	-40.4	-3.1	7.3	shift vector was applied on ALOS / PRISM DEM

Table 5.3-2 Uncertainty of DEM comparisons in different slope groups in the FGM

slope (degree)	KH9 vs SRTM		SRTM vs ALOS /PRISM	
	mean dh (m)	NMAD (m)	mean dh (m)	NMAD (m)
0 - 5	4.0024	4.8491	-1.4669	3.0671
5 -10	7.9386	6.9385	-2.5334	5.0076
10 - 15	9.8228	7.0691	-3.7985	5.3894
15 - 20	10.5858	6.9805	-3.4677	5.8094
20 - 25	10.9457	7.0835	-3.9781	6.4861
25 - 30	11.0384	7.4541	-3.9066	7.0049
30 - 35	10.9224	8.1543	-2.8780	7.6270
35 - 40	10.5236	9.3274	-1.4570	9.0703
40 - 45	9.7986	11.9756	-1.8437	12.9263
45 - 50	9.7960	15.9203	-6.9876	19.5247
50 - 55	8.4491	23.1273	-18.1569	31.7765
55 - 60	12.5958	39.0511	-37.3897	49.1531
60 - 65	9.7158	82.5317	-61.9238	96.8196
65 - 70	212.9607	151.6763	-8.5725	187.3475

Table 5.4-1 Shifting vector used for aligning DEMs in the IGM

DEM former	DEM latter	shift of x (m)	shift of y (m)	mean dh (m)	NMAD (m)	comment
Topography map DEM	SRTM DEM	18.7	-29.2	24.8	32.8	shift vector was applied on TOPO DEM
SRTM DEM	ALOS / PRISM DEM	-30.2	56.7	-0.5	10.3	shift vector was applied on ALOS / PRISM DEM

Table 5.4-2 Uncertainty of DEM comparisons in different slope groups in the IGM

slope (degree)	TOPO vs SRTM		SRTM vs ALOS /PRISM	
	mean dh (m)	NMAD (m)	mean dh (m)	NMAD (m)
0 - 5	8.3231	15.2529	-1.4684	4.3909
5 -10	19.1251	22.9987	2.8139	4.4998
10 - 15	25.0745	25.2947	1.0632	5.8896
15 - 20	25.6379	29.7502	0.5701	6.8541
20 - 25	25.7280	34.1528	0.4922	8.2297
25 - 30	28.0126	34.5865	0.0943	10.2402
30 - 35	27.2168	35.6936	-0.2734	11.6428
35 - 40	26.0838	37.0449	0.0598	13.9966
40 - 45	27.7441	35.9144	-1.8243	19.2959
45 - 50	31.5426	34.4500	-7.8053	24.2822
50 - 55	31.7997	35.0946	-30.6113	33.1626
55 - 60	24.4931	55.3142	-69.1799	43.8164

Table 5.5 Summary of glacier area loss in Tien Shan

start year	end year	region	loss of glacier area	sources
1977	2003	Kyrgyz region	12%	Aizen et al., 2007
1963	2000	Kyrgyz region	28%	Niederer et al., 2007
1955	1999	Ili-Kungoy regions	16 - 32%	Bolch, 2007
1970s	2000s	Pskem region	19%	Narama et al., 2010
1970s	2000s	At-Bashy region	12%	
1970s	2000s	SE-Fergana region	9%	

Figures

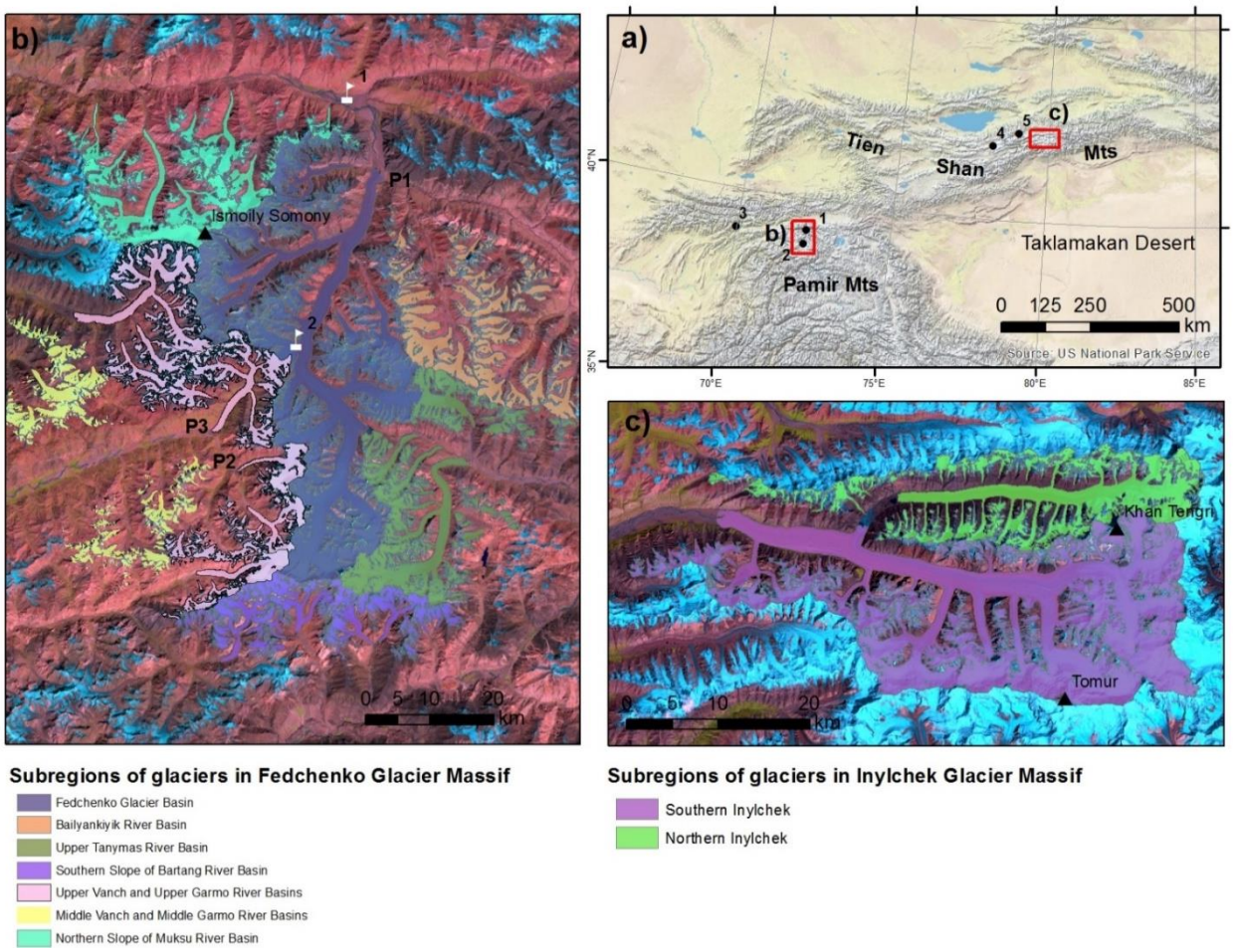

Figure 5.01 Maps of the research areas

a) Location of the FGM and the IGM in CA

b) Fedchenko Glacier Massif; base image: Landsat ETM+ imagery in 2000; overlay: glacier boundaries in 2000; P1, P2 and P3 indicate selected glaciers with profiles of surface elevation change analyzed

c) Inylchek Glacier Massif; base image: Landsat ETM+ imagery in 2000; overlay: glacier boundaries in 2000

Points show meteorological stations used in this study: 1. Altyn-Mazar, 2. Fedchenko Glacier, 3. Garm, 4. Tien Shan, 5. Koilu

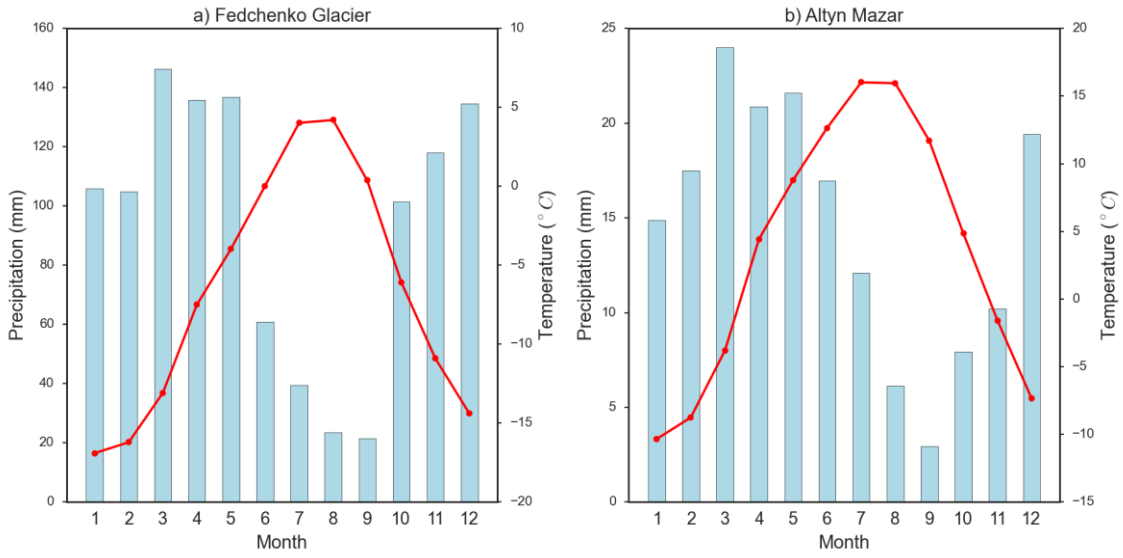

Figure 5.02-1 Long-term mean monthly air temperature and precipitation in stations within the Fedchenko Glacier Massif

a) Fedchenko Glacier and b) Altyn Mazar

Based on data from 1960 to 1990

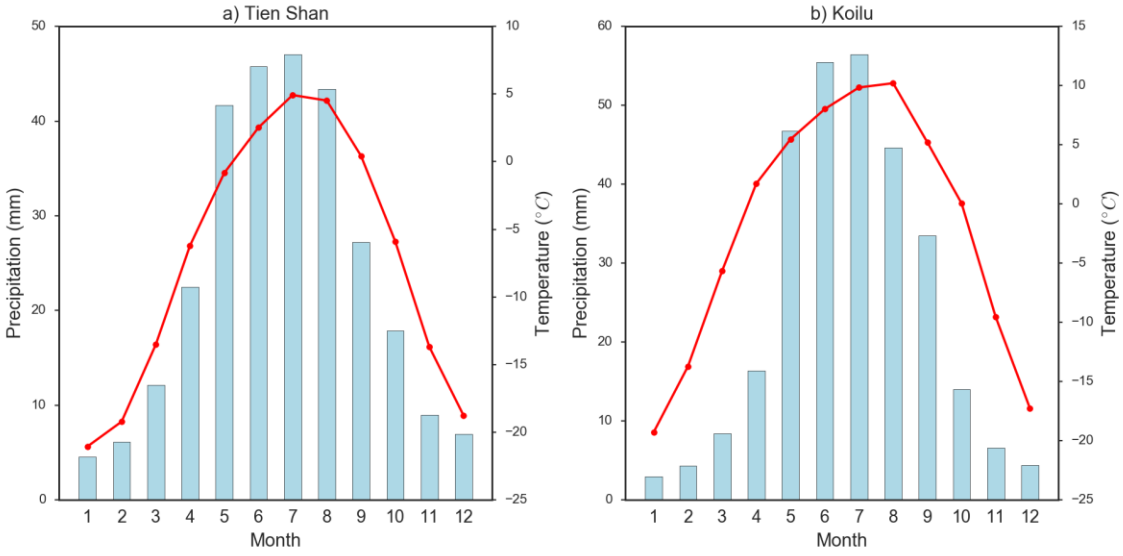

Figure 5.02-2 Long-term mean monthly air temperature and precipitation in stations near the Inylchek Glacier Massif

a) Tien Shan and b) Koilu

Based on data from 1960 to 1990

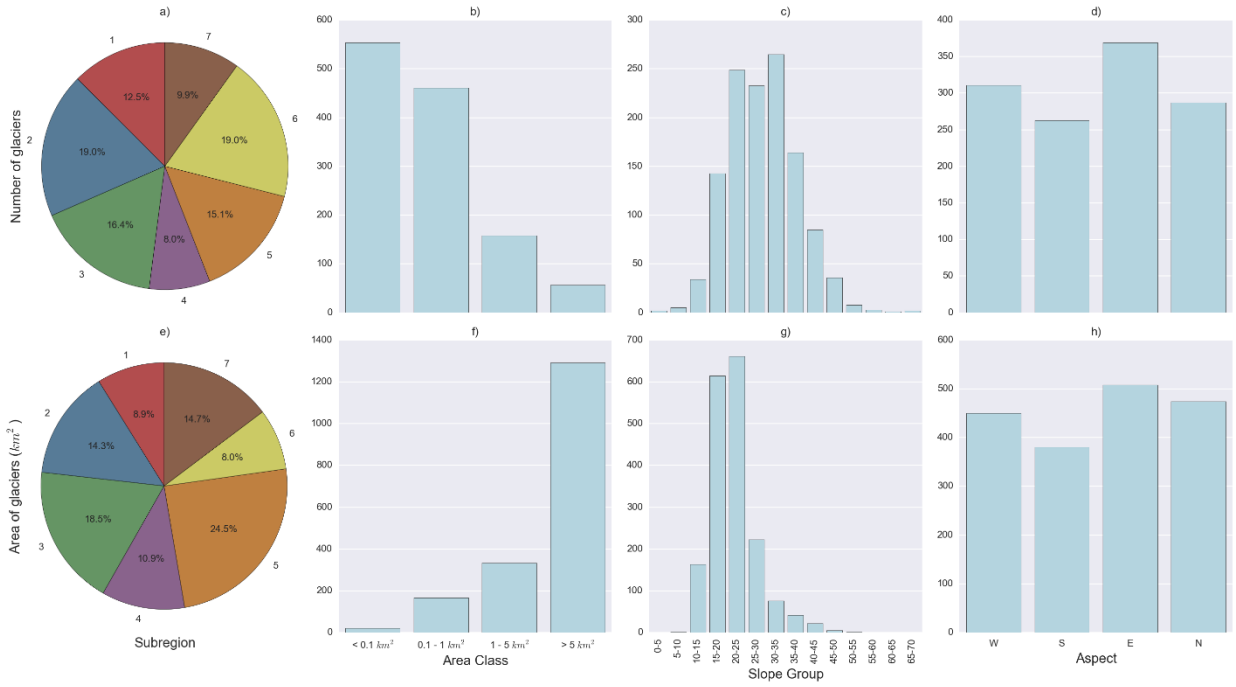

Figure 5.03 Distribution of glacier number (a - d) and area (e – h) by sub-region (a & e), area class (b & f), slope group (c & g) and aspect (d & h) in 2000 in the Fedchenko Glacier Massif

NOTE: The Fedchenko Glacier was not included in the analysis. It has an area of 687.4 km^2, with a mean slope of 15.5°, and a North exposition.

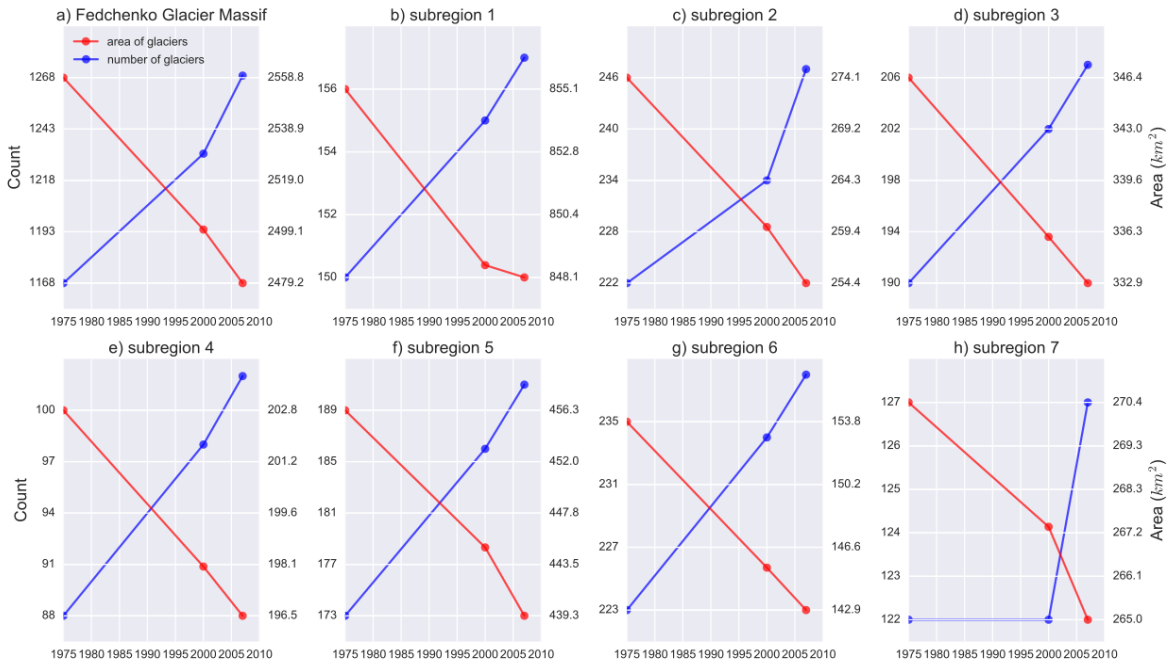

Figure 5.04-1 Glacier area and number in 1975 - 2000 and 2000 - 2007 in the Fedchenko Glacier Massif (a), and in each sub-region (b – h)

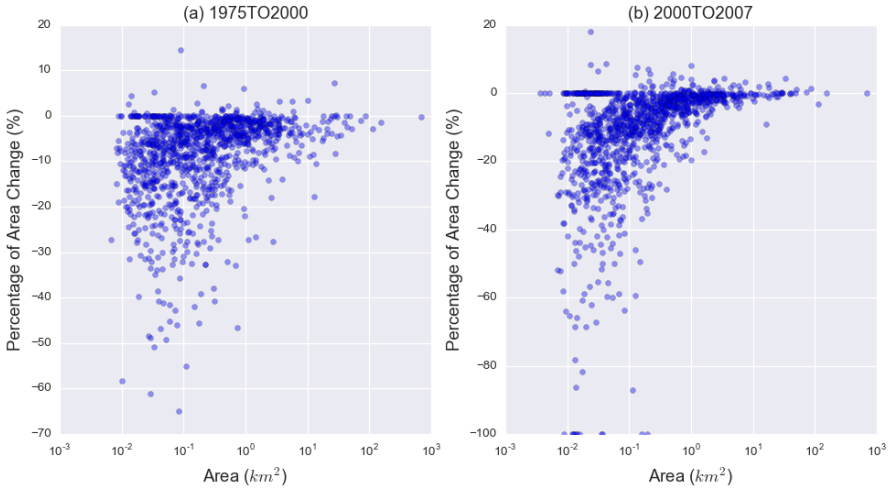

Figure 5.04-2 Percentage of glacier area change in 1975 - 2000 and 2000 - 2007 in the Fedchenko Glacier Massif against area

NOTE: the x-axis of area is in log scale.

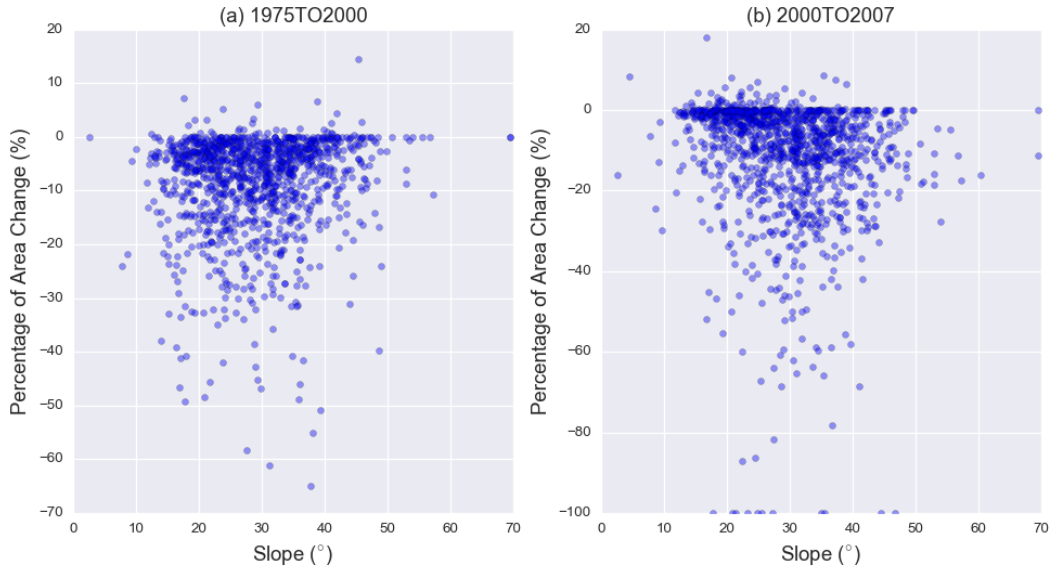

Figure 5.04-3 Percentage of glacier area change in 1975 - 2000 and 2000 - 2007 in the Fedchenko Glacier Massif against slope

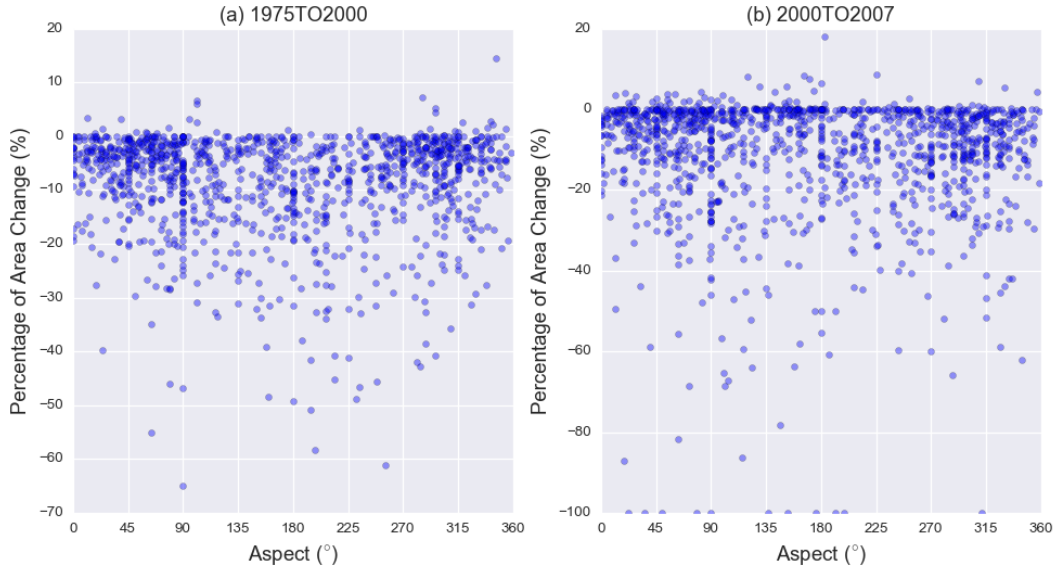

Figure 5.04-4 Percentage of glacier area change in 1975 - 2000 and 2000 - 2007 in the Fedchenko Glacier Massif against aspect

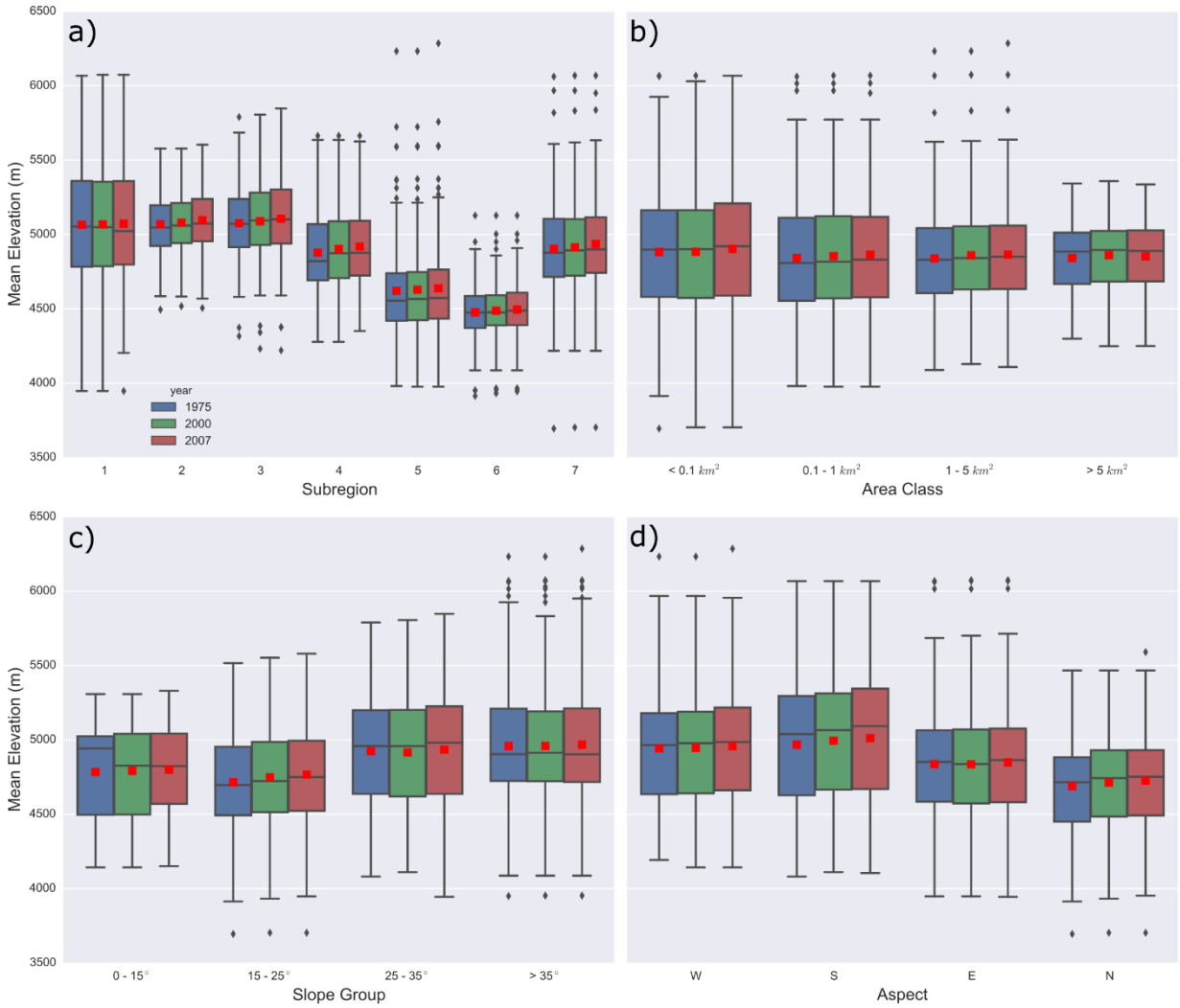

Figure 5.05 Changes of mean elevation of glaciers in the Fedchenko Glacier Massif by sub-regions (a), area class (b), slope group (c) and aspect (d)

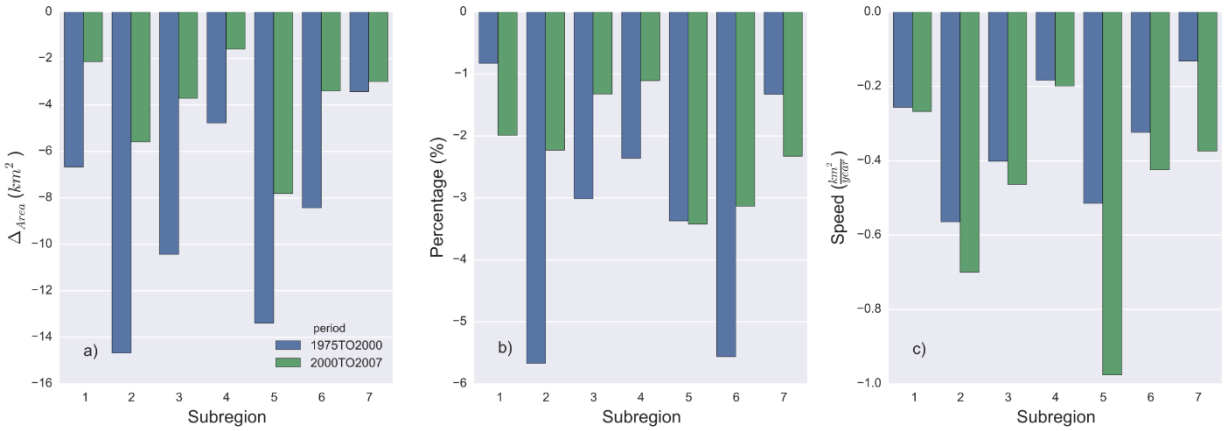

Figure 5.06-1 Glacier retreating in sub-regions of the Fedchenko Glacier Massif

a) decreased area, b) percentage of decreased area, c) retreating speed

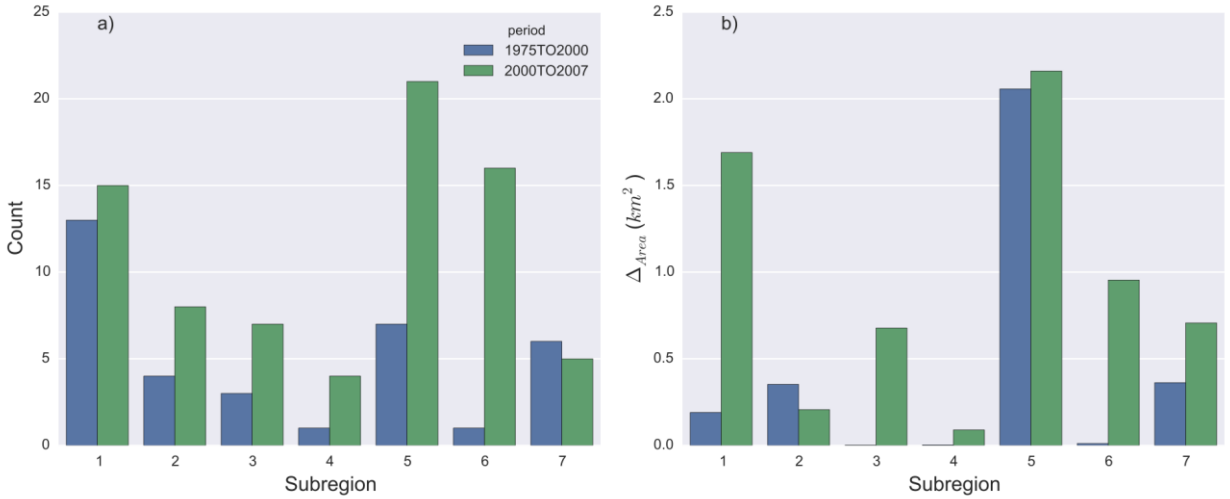

Figure 5.06-2 Advancing glaciers in sub-regions of the Fedchenko Glacier Massif

a) number of advancing glaciers b) increased area

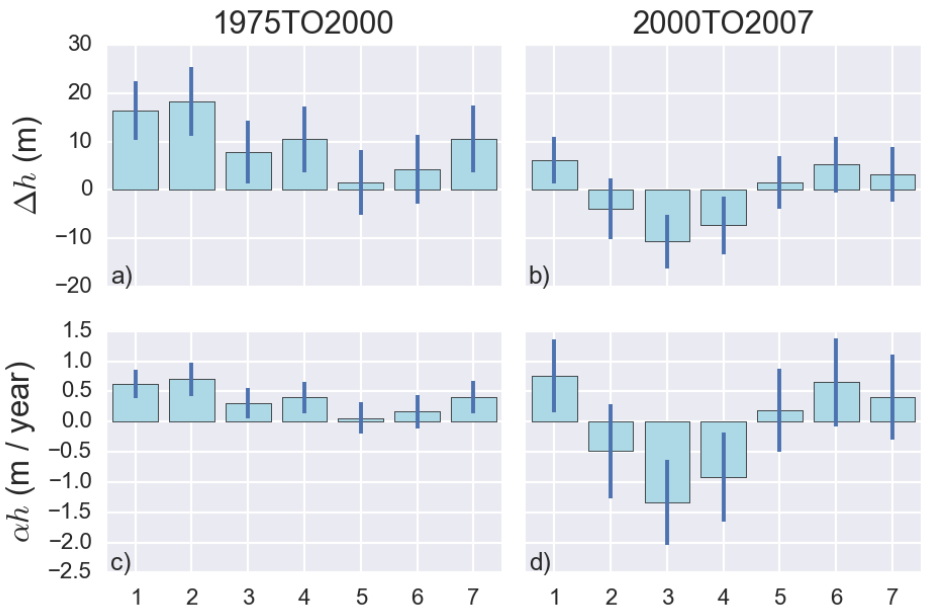

Figure 5.07-1 Glacier surface elevation changes in the Fedchenko Glacier Massif by sub-regions

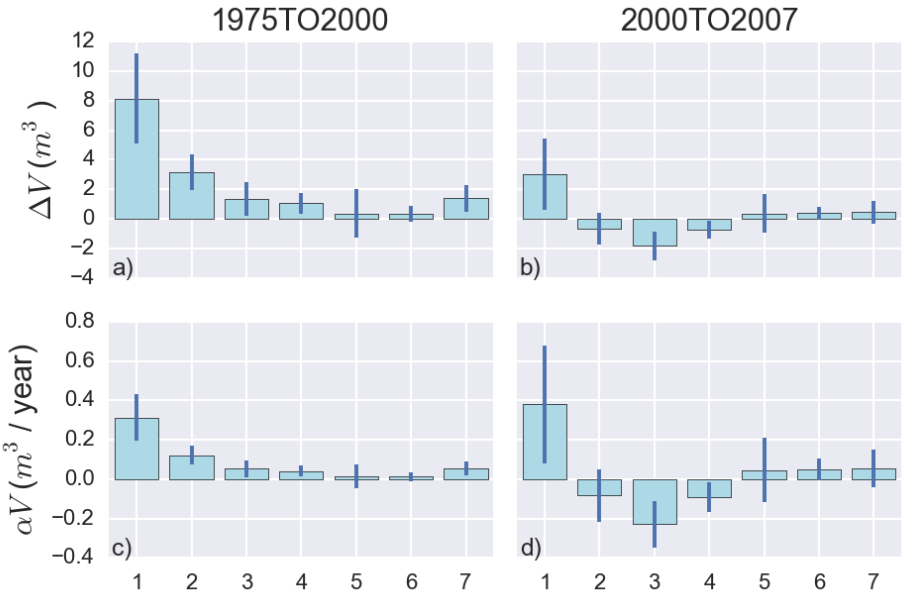

Figure 5.07-2 Glacier volume changes in the Fedchenko Glacier Massif by sub-regions

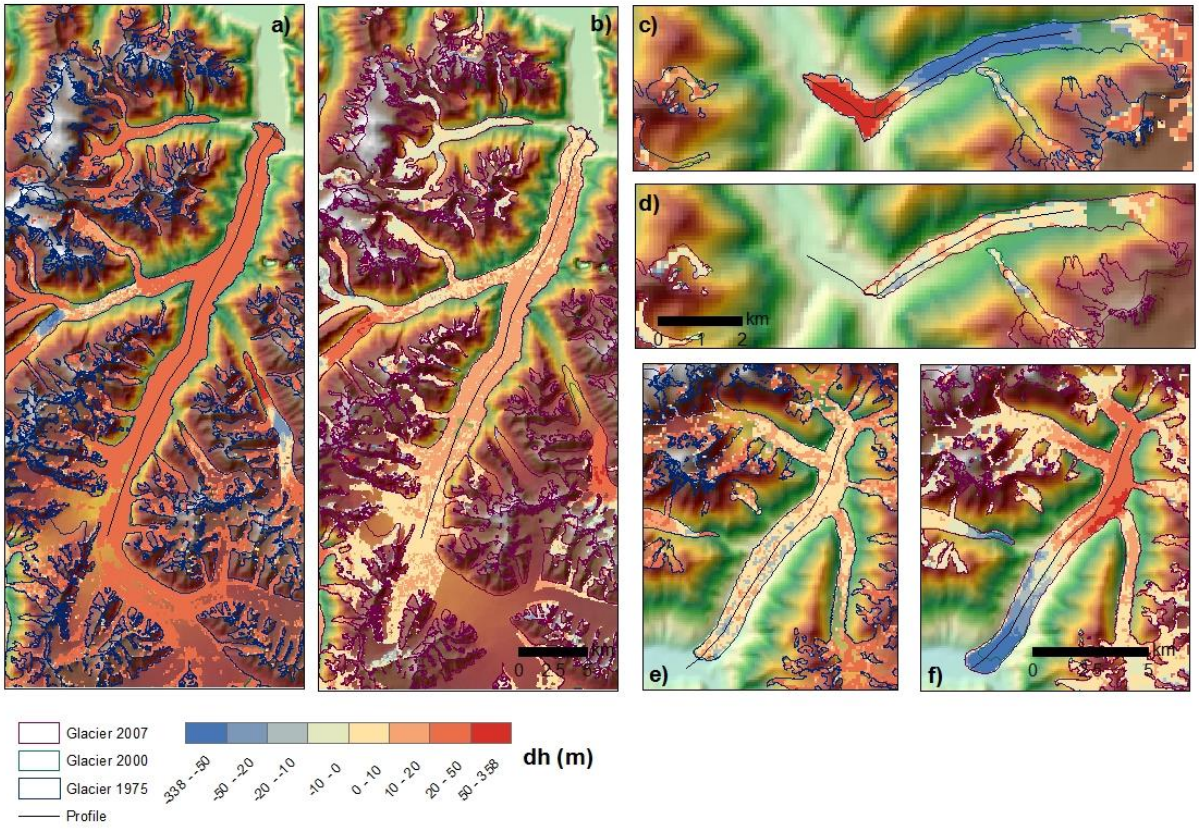

Figure 5.08 Glacier surface elevation changes in selected glaciers in the Fedchenko Glacier Massif

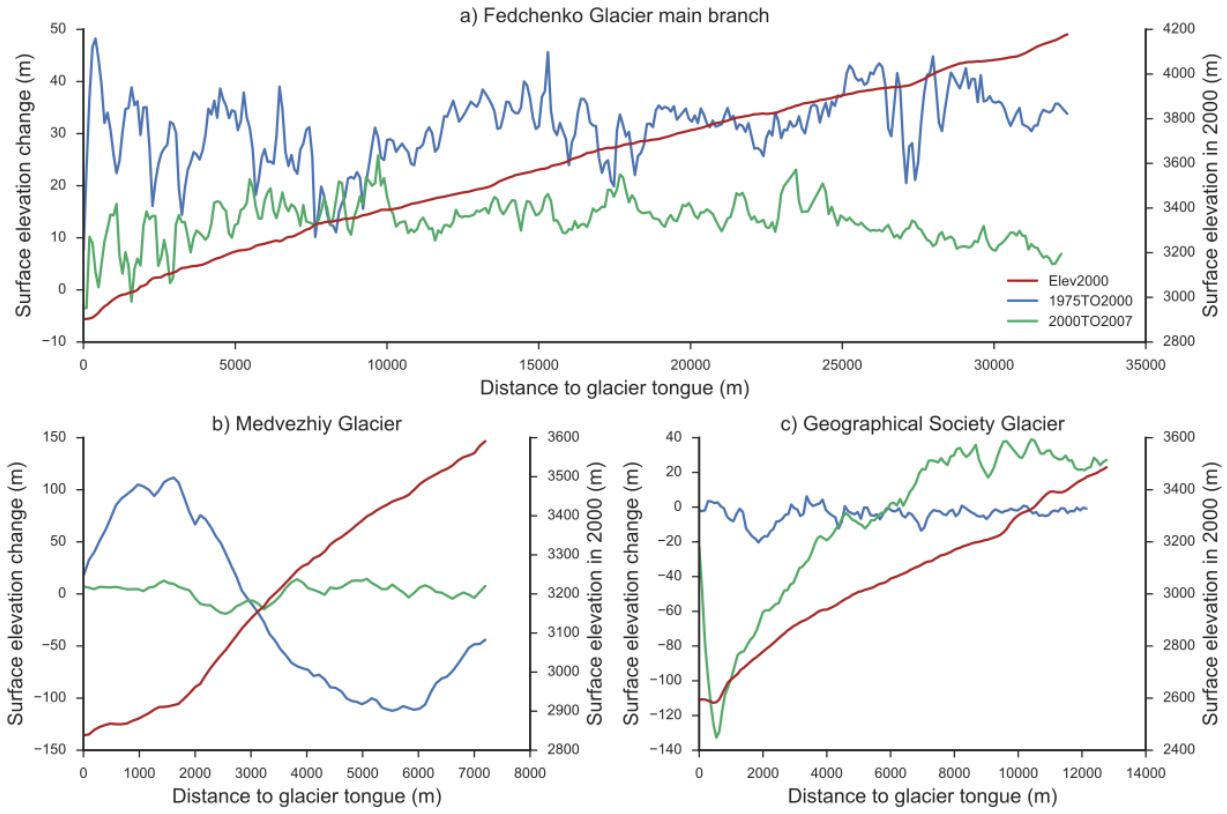

Figure 5.09 Profiles of glacier surface elevation change in selected glaciers in the Fedchenko Glacier Massif

a) Fedchenko Glacier main branch, P1 in Figure 5.1, Figure 5.8-a and Figure 5.8-b

b) Medvezhiy Glacier, P2 in Figure 5.1, Figure 5.8c and Figure 5.8-d

c) Geographical Society Glacier, P3 in Figure 5.1, Figure 5.8-e and Figure 5.8-f

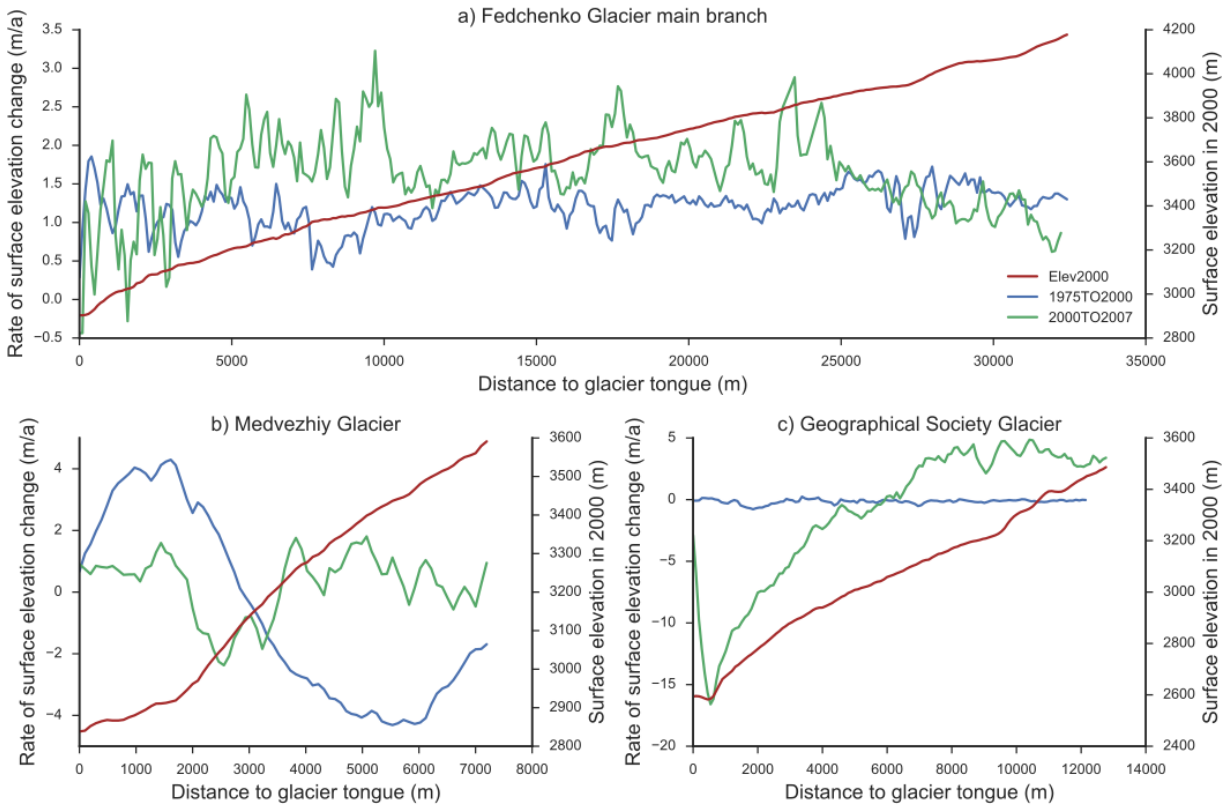

Figure 5.10 Profiles of rates of glacier surface elevation change in selected glaciers in Fedchenko Glacier Massif

a) Fedchenko Glacier main branch, P1 in Figure 5.1, Figure 5.8-a and Figure 5.8-b

b) Medvezhiy Glacier, P2 in Figure 5.1, Figure 5.8c and Figure 5.8-d

c) Geographical Society Glacier, P3 in Figure 5.1, Figure 5.8-e and Figure 5.8-f

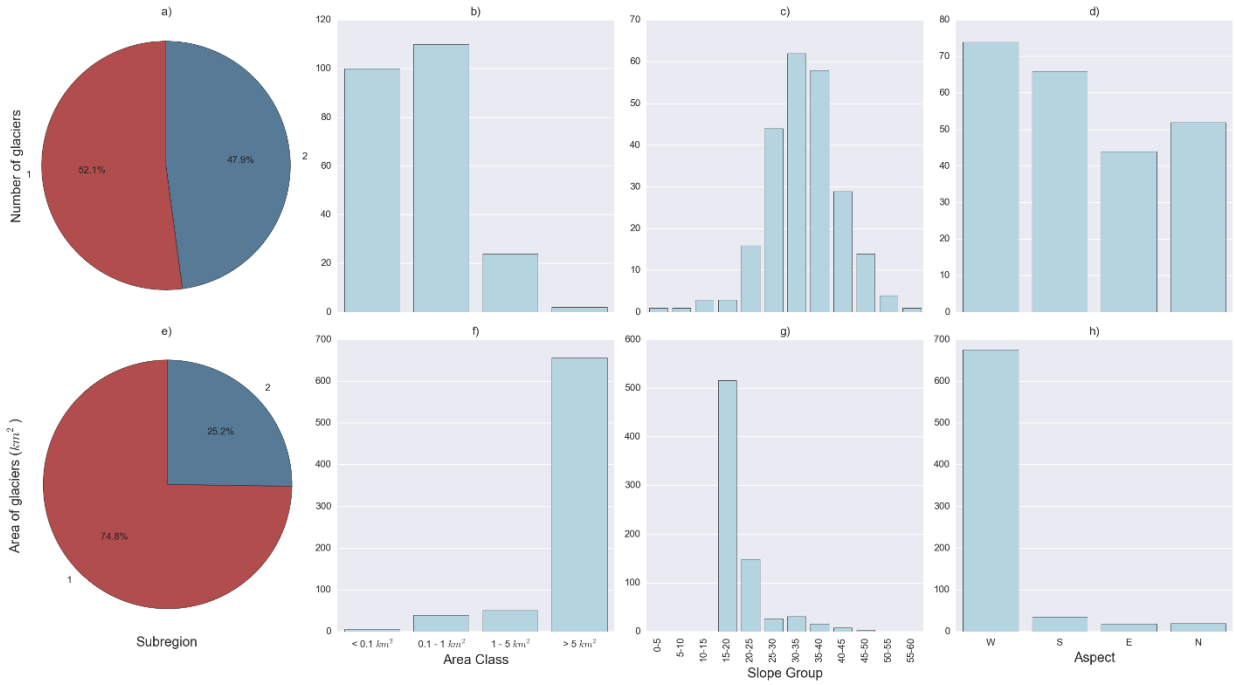

Figure 5.11 Distribution of glacier number (a - d) and area (e – h) by sub-region (a & e), area class (b & f), slope group (c & g) and aspect (d & h) in 2000 in the Inylchek Glacier Massif

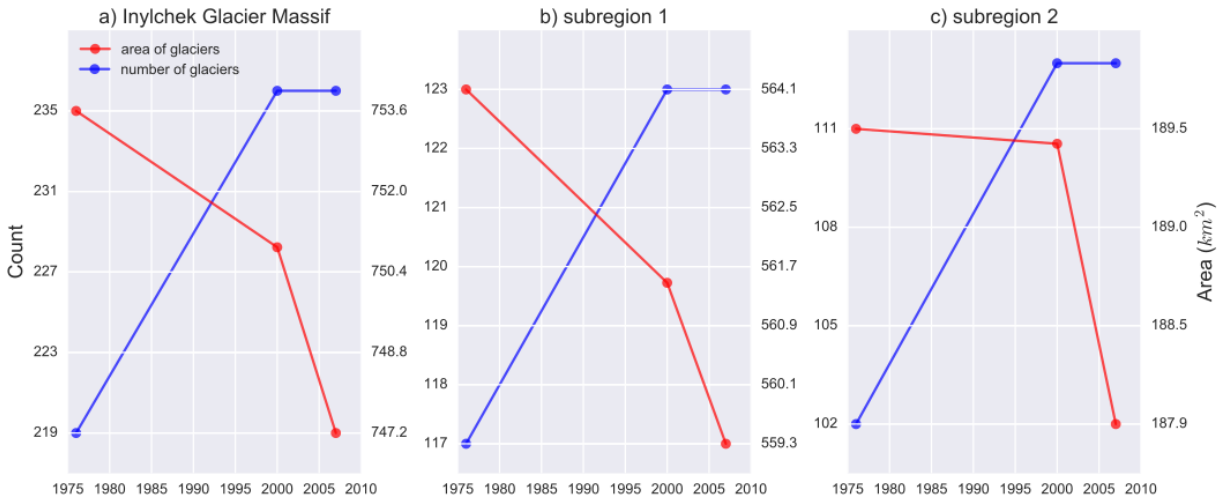

Figure 5.12-1 Glacier area and number in 1976 – 2000 and 2000 - 2007 in the Inylchek Glacier Massif (a), and in each sub-region (b – c)

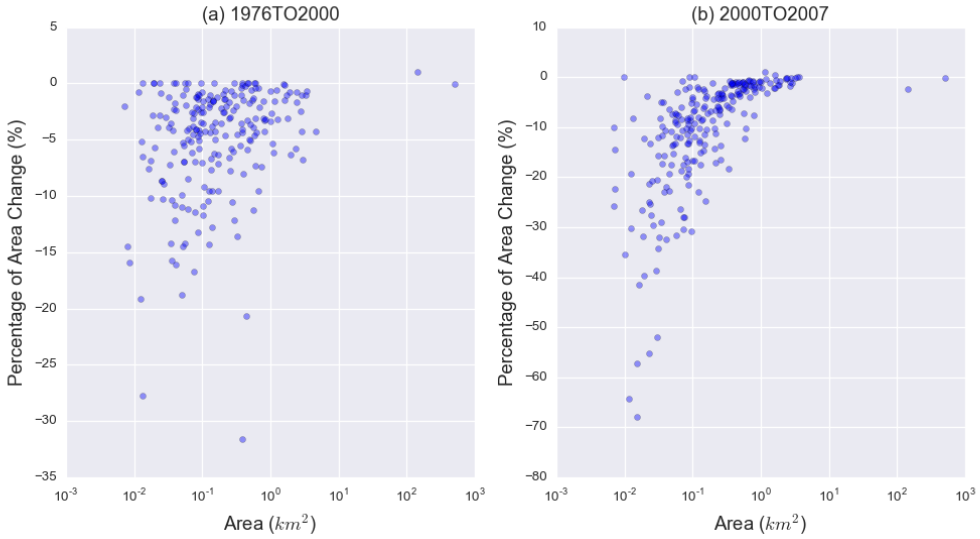

Figure 5.12-2 Percentage of glacier area change in 1976 - 2000 and 2000 - 2007 in the Inylchek Glacier Massif against area

NOTE: the x-axis of area is in log scale

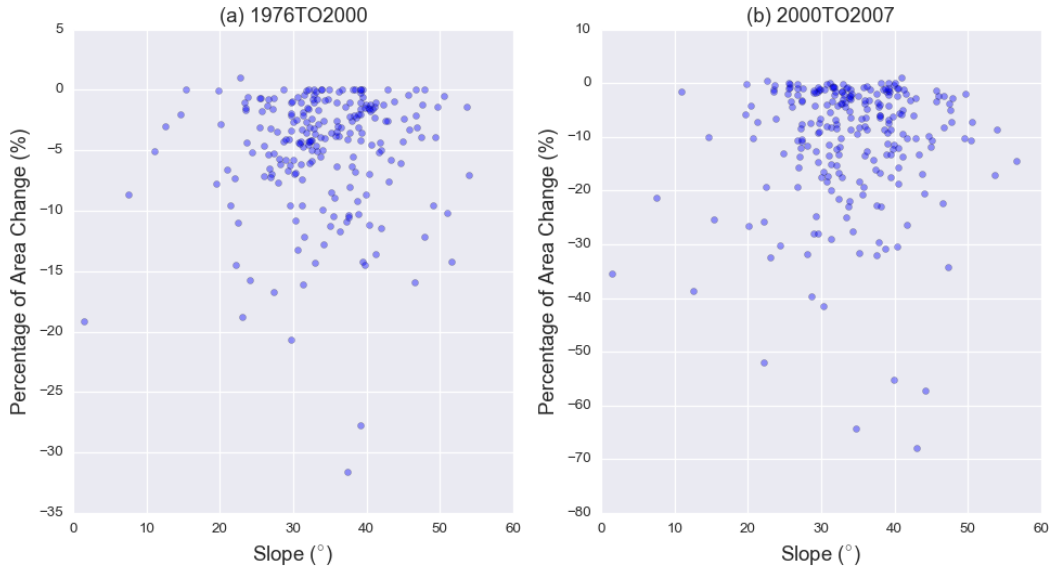

Figure 5.12-3 Percentage of glacier area change in 1976 - 2000 and 2000 - 2007 in the Inylchek Glacier Massif against slope

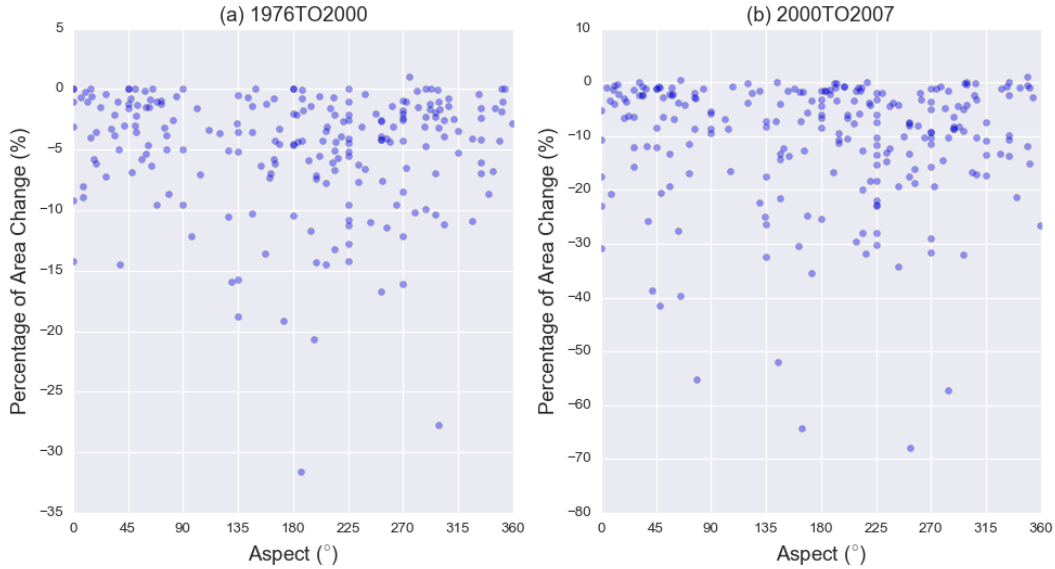

Figure 5.12-4 Percentage of glacier area change in 1976 - 2000 and 2000 - 2007 in the Inylchek Glacier Massif against aspect

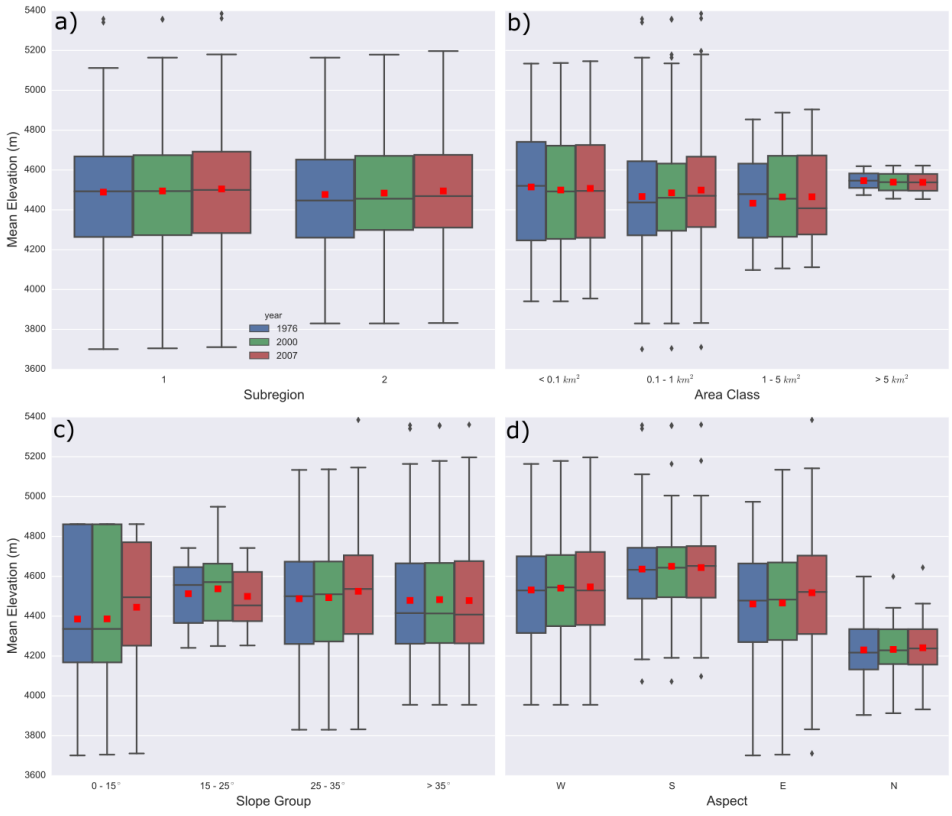

Figure 5.13 Changes of mean elevation of glaciers in the Inylchek Glacier Massif by sub-regions (a), area class (b), slope group (c) and aspect (d)

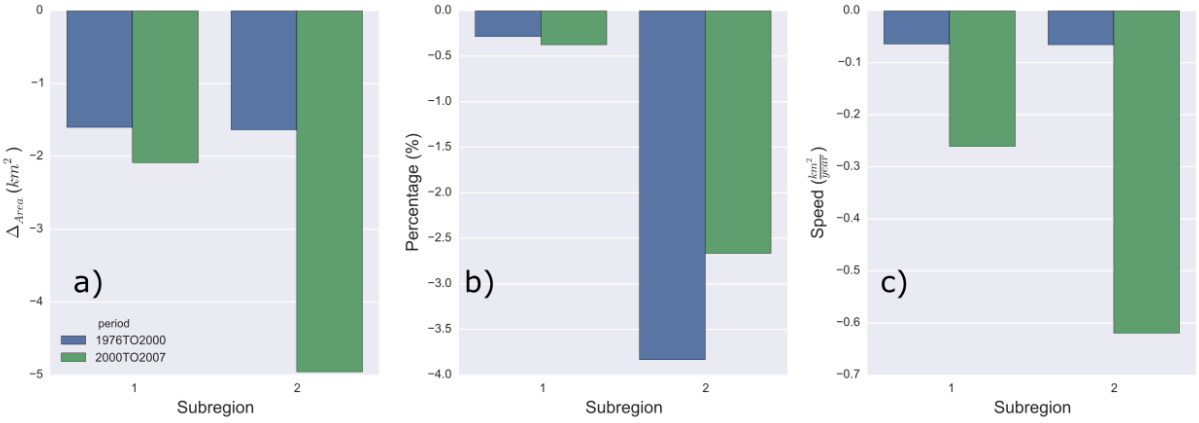

Figure 5.14 Glacier retreating by decreased area, percentage of decreased area and retreating speed in sub-regions of the Inylchek Glacier Massif

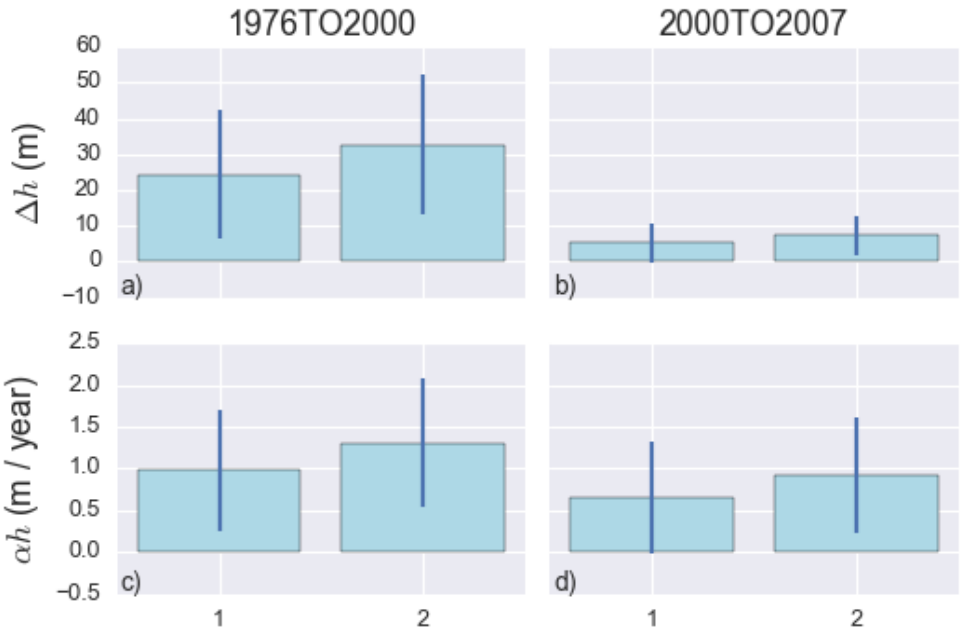

Figure 5.15-1 Glacier surface elevation changes in the Inylchek Glacier Massif by sub-regions

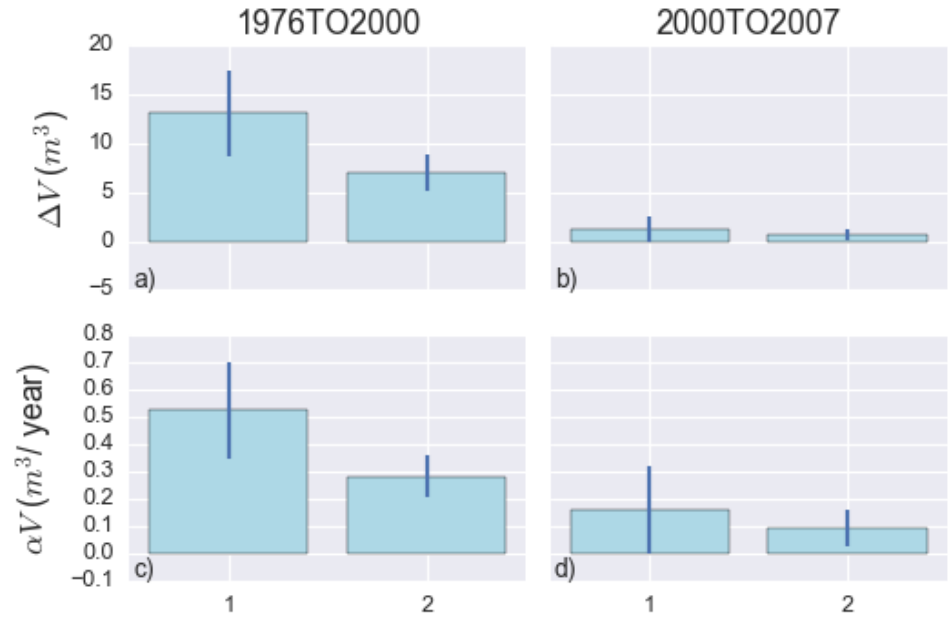

Figure 5.15-2 Glacier volume changes in the Inylchek Glacier Massif by sub-regions

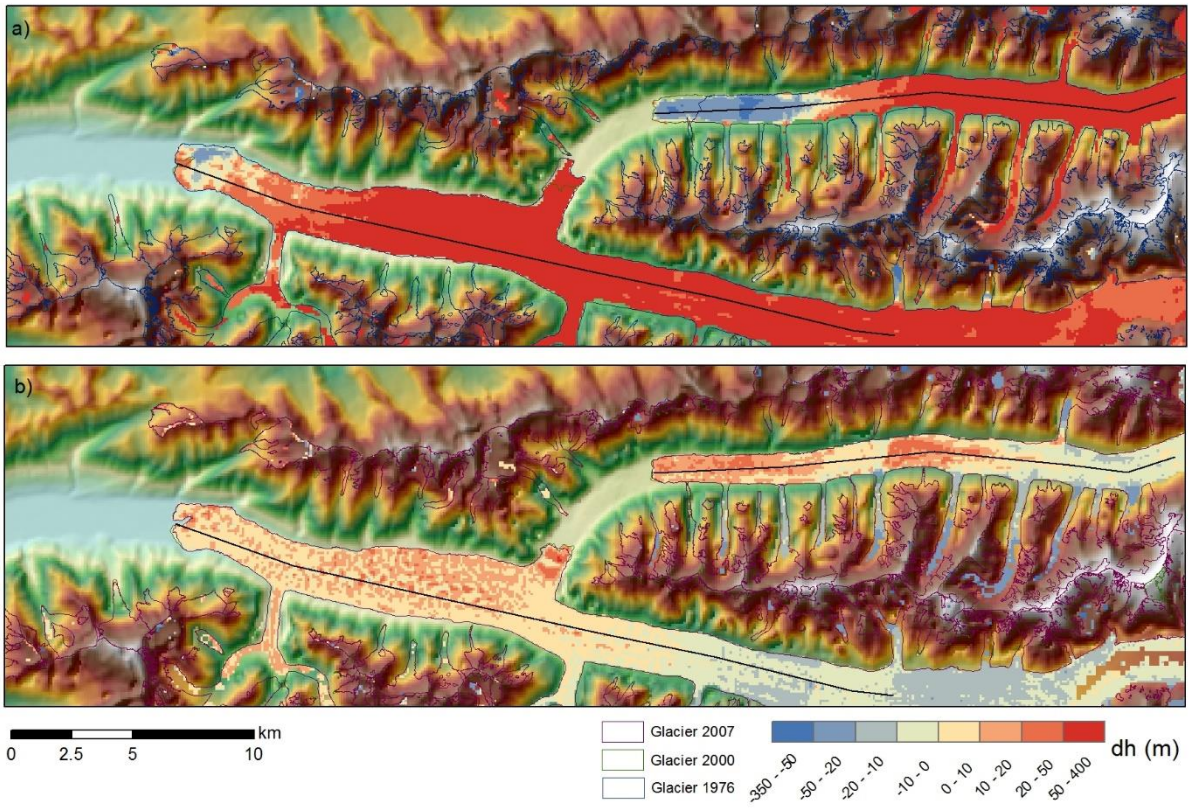

Figure 5.16 Glacier surface elevation changes in selected glaciers in the Inylchek Glacier Massif

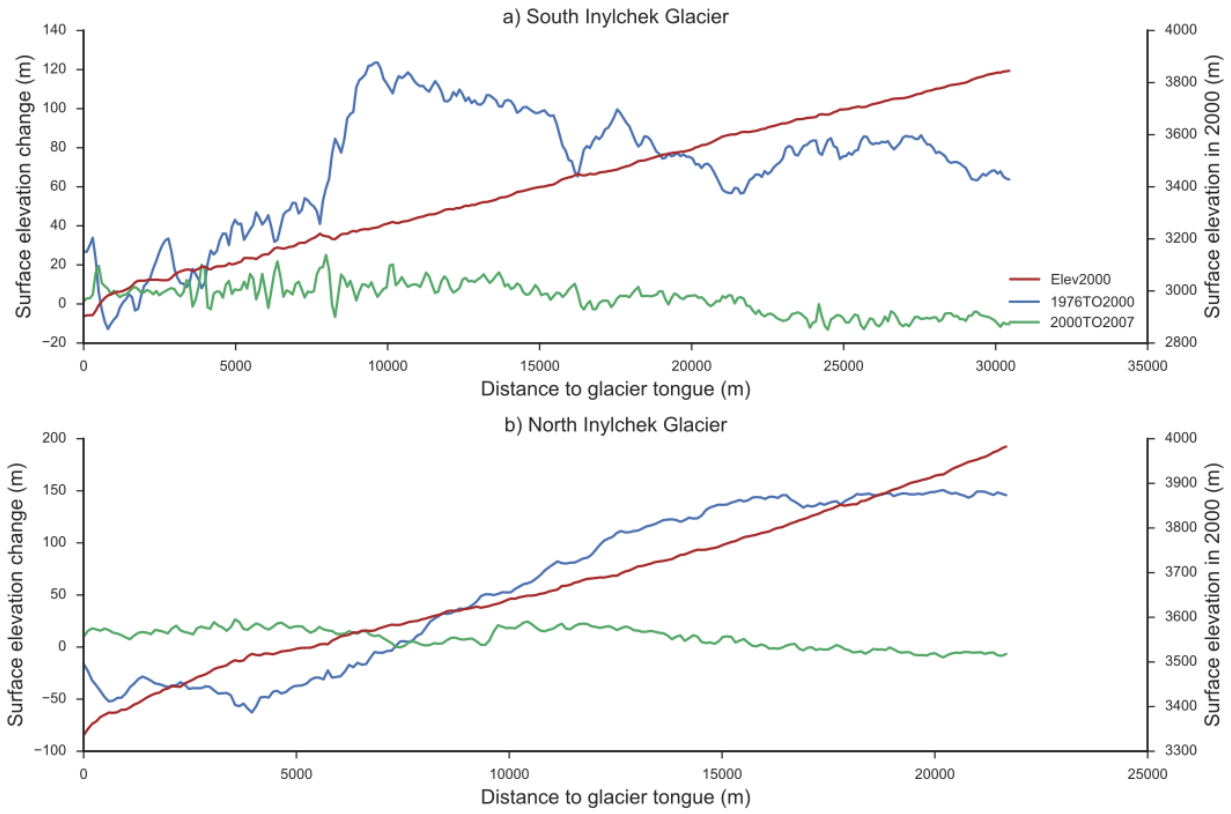

Figure 5.17 Profiles of glacier surface elevation change in selected glaciers in the Inylchek Glacier Massif

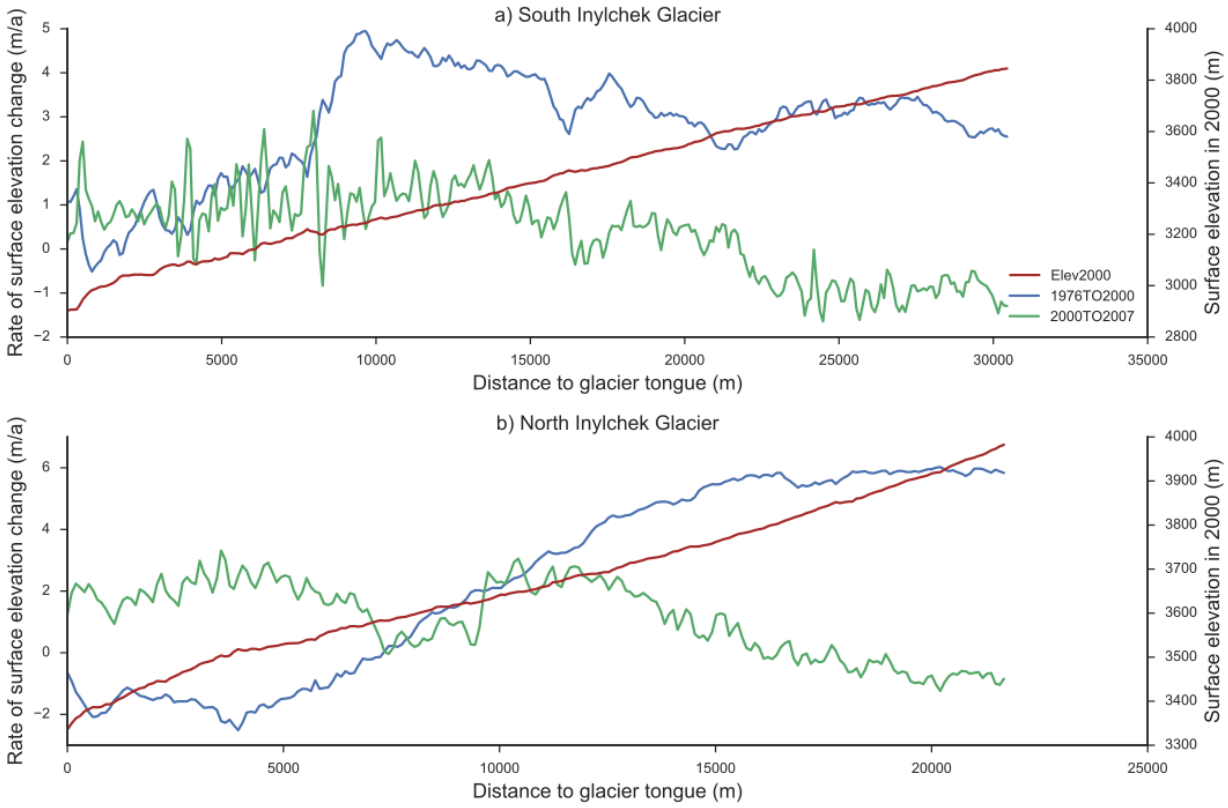

Figure 5.18 Profiles of rates of glacier surface elevation change in selected glaciers in the Inylchek Glacier Massif

Figure 5.19-1 Annual, winter and summer air temperature and precipitation in the Altyn-Mazar station

Figure 5.19-2 Annual, winter and summer air temperature and precipitation in Fedchenko Glacier station

Figure 5.19-3 Annual, winter and summer air temperature and precipitation in the Garm station

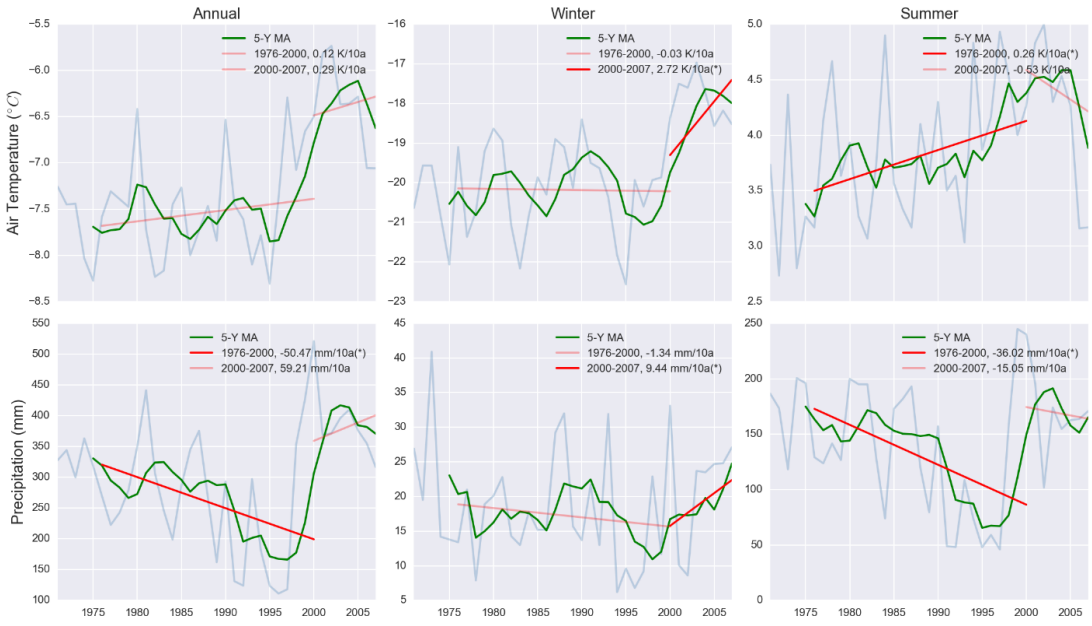

Figure 5.19-4 Annual, winter and summer air temperature and precipitation in the Tien Shan station

Figure 5.19-5 Annual, winter and summer air temperature and precipitation in the Koilu station

References

Aizen, V. B., Aizen, E. M., & Melack, J. M. (1996). Precipitation, melt and runoff in the northern Tien Shan. Journal of Hydrology, 186(1-4), 229–251.

Aizen, V., & Aizen, E. (1997). Hydrological cycles on the north and south peripheries of mountain-glacial basins of central Asia. *Hydrological Processes*, *11*(November 1995), 451–469. http://doi.org/10.1002/(SICI)1099-1085(199704)11:5<451::AID-HYP448>3.3.CO;2-D

Aizen, V., & Aizen, E. (1993). Glacier runoff estimation and simulation of streamflow in the peripheral territory of Central Asia. *IAHS Publications-Publications of the International Association of Hydrological Sciences*, *218*(218), 167–180. Retrieved from http://scholar.google.com/scholar?hl=en&btnG=Search&q=intitle:Glacier+Runoff+Estimation+and+Simulation+of+Streamflow+in+the+Peripheral+Territory+of+Central+Asia#0

Aizen, V., Aizen, E., & Kuzmichenok, V. (2007). Simulation and stochastic forecasting of water cycle components in Central Asian alpine basins. *Global and Planetary Change*, (56), 341 – 358. Retrieved from http://scholar.google.com/scholar?hl=en&btnG=Search&q=intitle:SIMULATION+AND+STOCHASTIC+FORECASTING+OF+WATER+CYCLE+COMPONENTS+IN+CENTRAL+ASIAN+ALPINE+BASINS#1

Aizen, V. B., Aizen, E. M., Dozier, J., Melack, J. M., Sexton, D. D., & Nesterov, V. N. (1997). Glacial regime of the highest Tien Shan mountain, Pobeda-Khan Tengry massif. *Journal of Glaciology*, *43*(145), 503–512.

Aizen, V. B., Aizen, E. M., & Kuzmichenok, V. a. (2007). Geo-informational simulation of possible changes in Central Asian water resources. *Global and Planetary Change*, *56*(3-4), 341–358. http://doi.org/10.1016/j.gloplacha.2006.07.020

Aizen, V. B., Aizen, E. M., & Kuzmichonok, V. a. (2007). Glaciers and hydrological changes in the Tien Shan: simulation and prediction. *Environmental Research Letters*, *2*(4), 045019. http://doi.org/10.1088/1748-9326/2/4/045019

Aizen, V. B., Aizen, E. M., & Melack, J. M. (1995). Climate, snow cover, glaciers , and runoff in the Tien Shan, Central Asia. *Water Resources Bulletin*, *31*(6), 1113–1129.

Aizen, V. B., Kuzmichenok, V. a., Surazakov, A. B., & Aizen, E. M. (2007). Glacier changes in the Tien Shan as determined from topographic and remotely sensed data. *Global and Planetary Change*, *56*(3-4), 328–340. http://doi.org/10.1016/j.gloplacha.2006.07.016

Aizen, V. B., Mayewski, P. a., Aizen, E. M., Joswiak, D. R., Surazakov, A. B., Kaspari, S., … Finaev, A. (2009). Stable-isotope and trace element time series from Fedchenko glacier

(Pamirs) snow/firn cores. *Journal of Glaciology*, *55*(190), 275–291. http://doi.org/10.3189/002214309788608787

ASPRS. (1990). Asprs Accuracy Standards for Large-Scale Maps, 1068–1070.

Bernauer, T., & Siegfried, T. (2012). Climate change and international water conflict in Central Asia. *Journal of Peace Research*, *49*, 227–239. http://doi.org/10.1177/0022343311425843

Bindschadler, R. A., Dowdeswell, J., Hall, D., & Winther, J. G. (2001). Glaciological applications with Landsat-7 imagery: Early assessments. *Remote Sensing of Environment*, *78*, 163–179. http://doi.org/10.1016/S0034-4257(01)00257-7

Bolch, T. (2007). Climate change and glacier retreat in northern Tien Shan (Kazakhstan/Kyrgyzstan) using remote sensing data. *Global and Planetary Change*, *56*(1-2), 1–12. http://doi.org/10.1016/j.gloplacha.2006.07.009

Bolch, T., Peters, J., Yegorov, A., Pradhan, B., Buchroithner, M., & Blagoveshchensky, V. (2011). Identification of potentially dangerous glacial lakes in the northern Tien Shan. *Natural Hazards*, *59*, 1691–1714. http://doi.org/10.1007/s11069-011-9860-2

Chevallier, P., Pouyaud, B., Mojaïsky, M., Bolgov, M., Olsson, O., Bauer, M., & Froebrich, J. (2013). River flow regime and snow cover of the Pamir Alay (Central Asia) in a changing climate. *Hydrological Sciences Journal*, *6667*(November 2013), 1–16. http://doi.org/10.1080/02626667.2013.838004

Cuffey, K. M., & Paterson, W. S. B. (2010). *The Physics of Glaciers*. Academic Press. Retrieved from http://www.amazon.com/Physics-Glaciers-Fourth-Kurt-Cuffey/dp/0123694612/ref=sr_1_sc_1?ie=UTF8&qid=1323191756&sr=8-1-spell

Dolgushin, L., & Osipova, G. (1989). *Ledniki [Glaciers]* (2nd Editio). Moscow: Misl.

Dyurgerov, M. B., Aizen, V. B., & Buynitskiy, A. B. (1985). Nakopleniye massy v oblasti pitaniya led- 20 nika Medvezh'yego za periody mezhdu yegopodvizhkami [Mass accumulation in the accumulation area of Medvezhiy Glacier during its quiescence periods]. *Materialy Glyatsiologicheskikh Issledovanii*, *54*, 131 – 135.

ENGEL, Z., ŠOBR, M., & YEROKHIN, S. A. (2012). Changes of Petrov glacier and its proglacial lake in the Akshiirak massif, central Tien Shan, since 1977. *Journal of Glaciology*, *58*(208), 388–398. http://doi.org/10.3189/2012JoG11J085

Finsterwalder, R. (1932). *Geodotutishe, topographische und glziologische Ergebnisse, "Wissenschaftliche Ergebnisse der Alai-Pamir Expedition 1928 Report."*

Frey, H., Machguth, H., Huss, M., Huggel, C., Bajracharya, S., Bolch, T., … Stoffel, M. (2014). Estimating the volume of glaciers in the Himalayan–Karakoram

region using different methods. *The Cryosphere*, *8*(6), 2313–2333. http://doi.org/10.5194/tc-8-2313-2014

Fujita, K., & Ageta, Y. (2000). Effect of summer accumulation on glacier mass balance on the Tibetan Plateau revealed by mass-balance model. *Journal of Glaciology*, *46*(153), 244–252. http://doi.org/10.3189/172756500781832945

Gardelle, J., Berthier, E., Arnaud, Y., & Kääb, a. (2013). Region-wide glacier mass balances over the Pamir-Karakoram-Himalaya during 1999–2011. *The Cryosphere*, *7*(4), 1263–1286. http://doi.org/10.5194/tc-7-1263-2013

Glazirin, G. E. (2010). A century of investigations on outbursts of the ice- dammed lake Merzbacher (central Tien Shan). *Austrian Journal of Earth Sciences*, *103*, 171–179.

Gorvunov, N. P., G., D. I., & Scherbakov, L. I. (1929). *Pamirskaya expediciya 1928 goda [Pamir expedition 1928] In Trudi Expedicii, Vip. 1, Obschii otchet [Proceedings of the Expedition, Vol. 1, General Report] (in Russian)*. Leningrad.

Grudzinskiy, M. A. (1959). Zvezdochka glacier (in Russian). In *Victory Peaks* (pp. 167 – 214). Moscow: Geographical literature Publishing.

Hagg, W., Braun, L. N., Kuhn, M., & Nesgaard, T. I. (2007). Modelling of hydrological response to climate change in glacierized Central Asian catchments. *Journal of Hydrology*, *332*(1-2), 40–53. http://doi.org/10.1016/j.jhydrol.2006.06.021

Hagg, W., Hoelzle, M., Wagner, S., & Klose, Z. (2011). Estimation of future glaciation and runoff in the Tanimas basin, Eastern Pamirs. *Hydrology and Earth System Sciences Discussions*, *8*(1), 1507–1540. http://doi.org/10.5194/hessd-8-1507-2011

Hagg, W., Mayer, C., Lambrecht, A., & Helm, A. (2008). Sub-Debris Melt Rates on Southern Inylchek Glacier, Central Tian Shan. *Geografiska Annaler, Series A: Physical Geography*, *90*(1), 55–63. http://doi.org/10.1111/j.1468-0459.2008.00333.x

Hausler, H., Scheibz, J., Leber, D., Kopecny, A., Echtler, H., Wetzel, H. U., & Moldobekov, B. (2011). Results From the 2009 Geoscientific Expedition To the Inylchek Glacier, Central Tien Shan (Kyrgyzstan). *Austrian Journal of Earth Sciences*, *104*(2), 47–57.

Höhle, J., & Höhle, M. (2009). Accuracy assessment of digital elevation models by means of robust statistical methods. *ISPRS Journal of Photogrammetry and Remote Sensing*, *64*(4), 398–406. http://doi.org/10.1016/j.isprsjprs.2009.02.003

Hutchinson, M. F. (1989). A new procedure for gridding elevation and stream line data with automatic removal of spurious pits. *Journal of Hydrology*, *106*(3-4), 211–232. http://doi.org/10.1016/0022-1694(89)90073-5

Hutchinson, M. F., Xu, T., & Stein, J. A. (2011). Recent Progress in the ANUDEM Elevation Gridding Procedure. *Geomorphometry.org*, 19–22.

Iawata, S. (2009). Mapping Features of Fedchenko Glacier, the Pamirs, Central Asia from Space. *Geographical Studies*, *84*, 33–43. http://doi.org/10.1038/173805e0

Kargel, J. S., Abrams, M. J., Bishop, M. P., Bush, A., Hamilton, G., Jiskoot, H., … others. (2005). Multispectral imaging contributions to global land ice measurements from space. *Remote Sensing of Environment*, *99*(1-2), 187–219. Retrieved from http://linkinghub.elsevier.com/retrieve/pii/S0034425705002154

Kaser, G., Grosshauser, M., & Marzeion, B. (2010). Contribution potential of glaciers to water availability in different climate regimes. *Proceedings of the National Academy of Sciences of the United States of America*, *107*(47), 20223–20227. http://doi.org/10.1073/pnas.1008162107

Kattelmann, R. (2003). Glacial lake outburst floods in the Nepal Himalaya: A manageable hazard? *Natural Hazards*, *28*(1), 145–154. http://doi.org/10.1023/A:1021130101283

Kaulbars, A. V. (1875). Materiali po geographii Tien Shanya sobrannie vo vremya puteshestviya [Data on Tien Shan geography collected during the journey] (in Russian). *Proc. Russ. Geogr. Soc.*, *5*, 253 – 539.

Khromova, T. E., Osipova, G. B., Tsvetkov, D. G., Dyurgerov, M. B., & Barry, R. G. (2006). Changes in glacier extent in the eastern Pamir, Central Asia, determined from historical data and ASTER imagery. *Remote Sensing of Environment*, *102*(1-2), 24–32. http://doi.org/10.1016/j.rse.2006.01.019

Korjenevskiy, N. L. (1934). Overview of the sutdy of glaciers in Central Asia from 1907 to 1932 (in Russian). *Izvestiya RGO (Processding of the Russian Geographical Society)*, *V*(III), 345.

Kotlyakov, V. M., Osipova, G. B., & Tsvetkov, D. G. (1997). Fluctuations of unstable mountain glaciers: scale and character. *Annals of Glaciology*, *24*, 338–343. Retrieved from <Go to ISI>://000071281900059

Kotlyakov, V. M., Osipova, G. B., & Tsvetkov, D. G. (2008). Monitoring surging glaciers of the Pamirs, central Asia, from space. *Annals of Glaciology*, *48*, 125–134. http://doi.org/10.3189/172756408784700608

Kriegel, D., Mayer, C., Hagg, W., Vorogushyn, S., Duethmann, D., Gafurov, A., & Farinotti, D. (2013). Changes in glacierisation, climate and runoff in the second half of the 20th century in the Naryn basin, Central Asia. *Global and Planetary Change*, *110*, 51–61. http://doi.org/10.1016/j.gloplacha.2013.05.014

Kutuzov, S., & Shahgedanova, M. (2009). Glacier retreat and climatic variability in the eastern Terskey–Alatoo, inner Tien Shan between the middle of the 19th century and beginning of the 21st century. *Global and Planetary Change*, *69*(1-2), 59–70. http://doi.org/10.1016/j.gloplacha.2009.07.001

Lambrecht, A., Mayer, C., Aizen, V., Floricioiu, D., & Surazakov, A. (2014). The evolution of Fedchenko glacier in the Pamir, Tajikistan, during the past eight decades. *Journal of Glaciology*, *60*(220), 233–244. http://doi.org/10.3189/2014JoG13J110

Langwagen, V. V. (1908). Ledniki hrebtovAleksandrovskogo, Zailiiskogo i Kungei Alatau [Glaciers on the Alexandrovskiy, Zailiiskiy and Kumgei Alatau] (in Russian). *Izv. Rus. Geograf. Obshch.*, *43*, 43 – 132.

Li, J., Li, Z., Ding, X., Wang, Q., Zhu, J., & Wang, C. (2014). Investigating mountain glacier motion with the method of SAR intensity-tracking: Removal of topographic effects and analysis of the dynamic patterns. *Earth-Science Reviews*, *138*, 179–195. http://doi.org/10.1016/j.earscirev.2014.08.016

Maling, D. H. (1992). *Coordinate systems and Map Projections* (2nd Editio). Oxford, England: Pergamon Press.

Martin, C. F. (2005). ICESat range and mounting bias estimation over precisely-surveyed terrain. *Geophysical Research Letters*, *32*(21), 5–8. http://doi.org/10.1029/2005GL023800

Mihalcea, C., Brock, B. W., Diolaiuti, G., D'Agata, C., Citterio, M., Kirkbride, M. P., … D'Agata, C. (2008). Using ASTER satellite and ground-based surface temperature measurements to derive supraglacial debris cover and thickness patterns on Miage Glacier (Mont Blanc Massif, Italy). *Cold Regions Science and Technology*, *52*(3), 341–354. http://doi.org/10.1016/j.coldregions.2007.03.004

Mushketov, I. V. (1896). Investigation of glaciers Russia (in Russian). *Izvestiya RGO (Processding of the Russian Geographical Society)*, *V*(III), 487.

Narama, C., Kääb, A., Duishonakunov, M., & Abdrakhmatov, K. (2010). Spatial variability of recent glacier area changes in the Tien Shan Mountains, Central Asia, using Corona (~1970), Landsat (~2000), and ALOS (~2007) satellite data. *Global and Planetary Change*, *71*(1-2), 42–54. http://doi.org/10.1016/j.gloplacha.2009.08.002

Narama, C., Shimamura, Y., Nakayama, D., & Abdrakhmatov, K. (2006). Recent changes of glacier coverage in the western Terskey-Alatoo range , Kyrgyz Republic , using Corona and Landsat. *Annals of Glaciology*, *43*(October 2002), 223–229. http://doi.org/10.3189/172756406781812195

Nesje, A., & Dahl, S. O. (2000). *Glaciers and Environmental Change*. Arnold. Retrieved from http://books.google.com/books?id=LPIcQY1YPLwC&pgis=1

Ng, F., Liu, S., Mavlyudov, B., & Wang, Y. (2007). Climatic control on the peak discharge of glacier outburst floods. *Geophysical Research Letters*, *34*(21), L21503. http://doi.org/10.1029/2007GL031426

Niederer, P., Bilenko, V., Ershova, N., Hurni, H., Yerokhin, S., & Maselli, D. (2007). Tracing glacier wastage in the Northern Tien Shan (Kyrgyzstan/Central Asia) over the last 40 years. *Climatic Change*, *86*(1-2), 227–234. http://doi.org/10.1007/s10584-007-9288-6

Nobakht, M., Motagh, M., Wetzel, H. U., Roessner, S., & Kaufmann, H. (2013). The inylchek glacier in Kyrgyzstan, Central Asia: Insight on surface kinematics from optical remote sensing imagery. *Remote Sensing*, *6*, 841–856. http://doi.org/10.3390/rs6010841

Nuth, C., & Kääb, a. (2011). Co-registration and bias corrections of satellite elevation data sets for quantifying glacier thickness change. *The Cryosphere*, *5*(1), 271–290. http://doi.org/10.5194/tc-5-271-2011

Osipova, G. B., & Tsvetkov, D. G. (1991). Kinematics of the surface of a surging glacier (comparison of the Medvezhiy and Variegated Glaciers). *Glaciers-Ocean-Atmosphere Interactions*, (208), 345–358.

Osmonov, A., Bolch, T., Xi, C., Kurban, A., & Guo, W. (2013). Glacier characteristics and changes in the Sary-Jaz River Basin (Central Tien Shan, Kyrgyzstan) – 1990–2010. *Remote Sensing Letters*, *4*(8), 725–734. http://doi.org/10.1080/2150704X.2013.789146

Paul, F., Barrand, N. E., Baumann, S., Berthier, E., Bolch, T., Casey, K., … Winsvold, S. (2013). On the accuracy of glacier outlines derived from remote-sensing data. *Annals of Glaciology*, *54*(63), 171–182. http://doi.org/10.3189/2013AoG63A296

Paul, F. (2003). *The New Swiss Glacier Inventory 2000 Application of Remote Sensing and GIS*. University of Zurich.

Paul, F., & Svoboda, F. (2009). A new glacier inventory on southern Baffin Island, Canada, from ASTER data: II. Data analysis, glacier change and applications. *Annals of Glaciology*, *50*(53), 22–31. http://doi.org/10.3189/172756410790595921

Pieczonka, T., & Bolch, T. (2015). Region-wide glacier mass budgets and area changes for the Central Tien Shan between ~1975 and 1999 using Hexagon KH-9 imagery. *Global and Planetary Change*, *128*, 1–13. http://doi.org/10.1016/j.gloplacha.2014.11.014

Pieczonka, T., Bolch, T., Junfeng, W., & Shiyin, L. (2013). Heterogeneous mass loss of glaciers in the Aksu-Tarim Catchment (Central Tien Shan) revealed by 1976 KH-9 Hexagon and 2009 SPOT-5 stereo imagery. *Remote Sensing of Environment*, *130*, 233–244. http://doi.org/10.1016/j.rse.2012.11.020

Potere, D. (2008). Horizontal positional accuracy of google earth's high-resolution imagery archive. *Sensors*, *8*(12), 7973–7981. http://doi.org/10.3390/s8127973

Racoviteanu, A. E., Williams, M. W., & Barry, R. G. (2008). Optical Remote Sensing of Glacier Characteristics: A Review with Focus on the Himalaya. *Sensors*, *8*(5), 3355–3383. http://doi.org/10.3390/s8053355

Ratcek, V. I. (1954). Glaciation of Peak Pobeda massif (in Russian). In *Geographical collection* (pp. 59 – 81). Moscow, Leningrad.

Raup, B., Kaab, A., Kargel, J., Bishop, M., Hamilton, G., Lee, E., … Khalsa, S. (2007). Remote sensing and GIS technology in the Global Land Ice Measurements from Space (GLIMS) Project. *Computers & Geosciences*, *33*(1), 104–125. http://doi.org/10.1016/j.cageo.2006.05.015

Raup, B., Racoviteanu, A., Khalsa, S. J. S., Helm, C., Armstrong, R., & Arnaud, Y. (2007). The GLIMS geospatial glacier database: A new tool for studying glacier change. *Global and Planetary Change*, *56*(1-2), 101–110. http://doi.org/10.1016/j.gloplacha.2006.07.018

Raymond, C. (1987). How do glaciers surge? A review. *Journal of Geophysical Research*, *92*(1), 9121–9134. Retrieved from http://www.agu.org/pubs/crossref/1987/JB092iB09p09121.shtml

Reuter, H. I., Nelson, A., & Jarvis, A. (2007). An evaluation of void-filling interpolation methods for SRTM data. *International Journal of Geographical Information Science*, *21*(9), 983–1008. http://doi.org/10.1080/13658810601169899

Rickmers, W. (1965). The Pamir Glaciers. *Geographical Journal*, *131*(2), 217–220. Retrieved from http://www.jstor.org/stable/10.2307/1793796

Rickmers, W. (1913). *The duab of Turkestan*. Cambridge, United Kingdom: Cambridge University Press.

Rignot, E., Echelmeyer, K., & Krabill, W. (2001). Penetration depth of interferometric synthetic-aperture radar signals in snow and ice. *Geophysical Research Letters*, *28*(18), 3501–3504. http://doi.org/10.1029/2000GL012484

Schetinnikov, A. (1998). *Morfologiya i rezhim lednikov Pamiro-Alaya [Morphology and regime of the Pamir-Alai glaciers]*. Tashkent: Central Asia Hydrometeorological Institute.

Schulz, V. (1962). *Lednik Fedchenko Vip 1 [Fedchenko Glacier vol 1]*. Tashkent: Nauka.

Schutz, B. E., Zwally, H. J., Shuman, C. a., Hancock, D., & DiMarzio, J. P. (2005). Overview of the ICESat Mission. *Geophysical Research Letters*, *32*(21), 1–4. http://doi.org/10.1029/2005GL024009

Shangguan, D., Bolch, T., Ding, Y., Kröhnert, M., Pieczonka, T., Wetzel, H.-U., & Liu, S. (2014). Elevation changes of Inylchek Glacier during 1974–2007, Central Tian Shan,

Kyrgyzstan derived from remote sensing data. *The Cryosphere Discussions*, *8*(3), 2573–2610. http://doi.org/10.5194/tcd-8-2573-2014

Siegfried, T., Bernauer, T., Guiennet, R., Sellars, S., Robertson, A. W., Mankin, J., … Yakovlev, A. (2012). Will climate change exacerbate water stress in Central Asia? *Climatic Change*, *112*, 881–899. http://doi.org/10.1007/s10584-011-0253-z

Sorg, A., Bolch, T., Stoffel, M., Solomina, O., & Beniston, M. (2012). Climate change impacts on glaciers and runoff in Tien Shan (Central Asia). *Nature Climate Change*, *2*(10), 725–731. http://doi.org/10.1038/nclimate1592

Surazakov, a. B., & Aizen, V. B. (2006). Estimating volume change of mountain glaciers using SRTM and map-based topographic data. *IEEE Transactions on Geoscience and Remote Sensing*, *44*(10), 2991–2995. http://doi.org/10.1109/TGRS.2006.875357

Surazakov, A., & Aizen, V. (2010). Positional accuracy evaluation of declassified Hexagon KH-9 mapping camera imagery. *Photogrammetric Engineering & Remote Sensing*, *76*(5), 603–608.

Toutin, T. (2008). ASTER DEMs for geomatic and geoscientific applications: a review. *International Journal of Remote Sensing*, *29*(7), 1855–1875. http://doi.org/10.1080/01431160701408477

Unger-Shayesteh, K., Vorogushyn, S., Farinotti, D., Gafurov, A., Duethmann, D., Mandychev, A., & Merz, B. (2013). What do we know about past changes in the water cycle of Central Asian headwaters? A review. *Global and Planetary Change*, *110*, 4–25. http://doi.org/10.1016/j.gloplacha.2013.02.004

Glacier Inventory of the USSR. (1979). *Catalogue of Glaciers in the USSR. Middle Asia and Kazakhstan*. Leningrad: Hydrometeo Publishing.

Vorob'ev, S. P. (1935). Atlas lednikov Narino-Khantengrinskoi expedicii, Tien Shan, Verhov'e Bol'shogo Narina [Atlas of glaciers from the Narin-Khan Tengri expedition] (in Russian). *Trudi Lednikovih Expedicii*, *2*(187-8).

Xie, Z., ShangGuan, D., Zhang, S., Ding, Y., & Liu, S. (2013). Index for hazard of Glacier Lake Outburst flood of Lake Merzbacher by satellite-based monitoring of lake area and ice cover. *Global and Planetary Change*, *107*, 229–237. http://doi.org/10.1016/j.gloplacha.2012.05.025

Zabirov, R. D. (1955). *Oledenenie Pamira [Pamir Glaciation] (in Russian)*. Moscow, Russia: Geographgiz.

Zhang, Q., Kang, S., & Chen, F. (2014). Glacier Variations in the Fedchenko Basin, Tajikistan, 1992-2006: Insights from Remote-sensing Images. Mountain Research and

Development, 34(1), 56–65. Retrieved from
http://www.bioone.org/doi/abs/10.1659/MRD-JOURNAL-D-12-00074

Chapter 6 Conclusion

This study aimed at quantifying the cryosphere changes in central Asia for the past ~20 to 40 years as consequences of regional climate changes using remote sensing and in-situ observation data. The study was conducted within an integrated research program on glaciers, snow, climate and hydrology of central Asia carried out by the glacier-climatic research group at the University of Idaho. Major findings of this study are summarized below.

1 Climate in CA

To assess the climate changes throughout central Asia (CA), a comprehensive climate dataset was compiled from several sources. All station data were quality-controlled and then merged, resulting in a data collection containing 457 stations. An iterative method based on Principal Component Analysis was developed to fill gaps in station time series from 1951 to 2010, resulting in gap filled time series in 369 and 381 stations for monthly air temperature and precipitation, respectively. A gridded monthly climate dataset for CA, including air temperature, precipitation, and other climate statistics, was created using Geographically Weighted Regression based methods for interpolation.

Analysis of the climate dataset shows that CA experienced a change of climate regime in 1976 / 1977, with 73% stations in CA experienced a significant increase of air temperature between 1951 – 1976 and 1977 – 2010. Spatially interpolated difference of annual air temperature between the two periods has a range from -0.41°C to 1.13°C, with an area-weighted mean increase of 0.70°C for the whole CA. Stronger increase of air temperature happened in lower elevation areas and higher northern latitude areas. Two main centers of increasing air temperature (up to 1 °C) are areas surrounding the Aral Sea and the

northeastern part of the Kazakh Steppe. High elevation areas in Tien Shan and Pamir experienced a much smaller increase of annual air temperature than other regions, or even a slight decrease of air temperature though not significant.

The annual precipitation did not change significantly throughout CA between 1951 – 1976 and 1977 – 2010, with a small area-weighted mean of 3 mm and a range from -80 mm to 45 mm for the difference between average annual precipitations in the two periods. Spatial interpolation results show that there are more areas (67.2% of the area in CA) with increasing precipitation. Strong increases of precipitation greater than 30 mm mainly occurred in Pamiro-Alai, Western Pamir, and Central Pamir, associated with increases of winter precipitation. The most significant decreases of precipitation occurred in the alpine regions of Tien Shan, especially in Central Tien Shan and Inner Tien Shan during summer.

2 Seasonal snow cover in CA

To assess the spatial distribution patterns and historical changes of seasonal snow cover in CA, a long-term snow cover dataset was developed from AVHRR and MODIS satellite data. An aggregated rating based snow identification scheme was designed to generate accurate snow cover classification from all available AVHRR level 1b raw data over CA. A correction method based on long-term snow probability in small sub-regions has been developed for generating corrected 8-day AVHRR snow cover, which is comparable to 8-day MODIS snow. The daily AVHRR snow cover data showed high accuracy, by validation against historical ground based snow survey data and the daily MODIS snow cover data. The comparison of the corrected 8-day AVHRR snow cover with 8-day MODIS cloud / gap free snow indicates high comparability between snow data from corrected AVHRR and MODIS.

A series of long-term snow cover statistics, describing snow cover area, duration, and timing, were derived from the AVHRR snow cover dataset for the time period from 1986 to 2008. Analysis of long-term mean snow cover statistics shows that the area weighted mean of long-term snow covering days ($\overline{SCD}$) for the whole CA is 95.2 ± 65.7 days, with most places have $\overline{SCmax}$ greater than 95% before Jan 26th. High elevation mountainous areas above 3000 m in Altai, Tien Shan and Pamir, which account for about 2.8% of total area in CA, have $\overline{SCD}$ greater than 240 days and $\overline{DSCmax}$ before Jan 5th. Regression analysis showed that elevation is the most important factor determining the distribution of $\overline{SCD}$ among elevation, latitude and relative location to major mountains.

The Mann-Kendal test and the Theil-Sen regression methods have been applied to analyze the spatial heterogeneous trends of change of SCD, snow cover onset date (SCOD), and snow cover melt date (SCMD). Area weighed mean SCD in the whole CA does not exhibit a significant trend of change from 1986 to 2008. Increase of SCD was observed in the northeastern Kazakh Steppe. Low elevation areas below 2000 m in Central Tien Shan, and Eastern Tien Shan, as well as mid-elevation areas from 1000 m to 3000 m in Western Tien Shan, Pamiro-Alai and Western Pamir, also experienced increase of SCD, associated with both earlier SCOD and later SCMD. Decrease of SCD was observed in mountainous areas of Altai, Tien Shan and Pamir, and vast areas in plains surrounding the Aral Sea. Such decreases of SCD were mainly associated with earlier SCMD, which can be attributed to the significant increase of spring air temperatures in the research period.

3 Glacier in selected massifs in CA

To assess glacier changes in CA, the Fedchenko Glacier Massif (FGM) and the Inylchek Glacier Massif (IGM) were selected as representative massifs for Central Pamir and Central Tien Shan, respectively. Glacier boundaries and surface elevations for the two selected glacier massifs in three periods (1975/1976, 2000 and 2007) were derived from military topography maps, declassified KH9 imageries, SRTM DEM, Landsat ETM/ETM+ images and ALOS / PRISM images.

In the FGM, the area of glaciers decreased from 2558.8 km^2 in 1975 to 2479.2 km^2 in 2007, with the lost area of 79.6 km^2 accounting for 3.1% of the area in 1975. The glacier area loss rate increased from 2.27 km^2 / year in 1975 - 2000, to 2.59 km^2 / year in 2000 - 2007. The number of surging glaciers increased from 35 in 1975 - 2000, to 76 in 2000 - 2007. The mean decrease of glacier surface elevation is 10.61 ± 6.60 m in 1975 - 2000, and is 0.28 ± 5.47 m in 2000 - 2007, for areas below the regional ELA in the FGM. In the IGM, the total glacier area decreased from 753.6 km^2 in 1976 to 747.2 km^2 in 2007, with the loss area accounting for 0.86% of the area in 1976. The glacier area loss rate increased from 0.10 km^2 / year between 1975 and 2000, to 0.46 km^2 / year between 2000 and 2007. The mean decrease of surface elevation is 26.46 ± 18.34 m for areas below ELA between the 1970s and 200,0 and is 5.86 ± 5.41 m between 2000 and 2007.

Analysis of the changes of glacier area and surface elevation in both glacier massifs shows that glaciers in both glacier massifs have experienced continuous glacier area loss in the period of 1975/1976 to 2000 and 2000 to 2007, with larger glaciers tend to experience less area loss, and stronger area loss rate in the latter period. In contrast, the surface elevation

lowering in both glacier massifs decelerated between the two periods, which can be attributed to the increase of precipitation during the latter period (increase of winter precipitation for the FGM and increase of summer precipitation for the IGM). The magnitude of glacier surface elevation lowering in the IGM was much stronger than in the FGM, which can be attributed to the more favorable climate conditions for glaciers in the FGM. The magnitudes of glacier area shrinkage in these two glacier massifs are comparable, and much smaller compared with glaciers in outer zones of mountain systems in CA.

Appendix A

Table 1 Meteorological stations in central Asia

ID	name	lon (deg)	lat (deg)	alt (m)	temporal range		selected	
					T	P	T	P
1	Abakan	91.32	53.77	254	1960 - 2014	1966 - 2014	TRUE	TRUE
2	AbramovGlacier	71.57	39.63	3960	1967 - 1998	1967 - 1998	TRUE	TRUE
3	Adamovka	60.35	52.43	309	1936 - 2014	1966 - 2014	TRUE	TRUE
4	Agalyk	66.97	39.53	1240	Not Available	1985 - 1999	FALSE	TRUE
5	Ahochi	78.45	40.94	1984	1957 - 2000	1957 - 2000	TRUE	TRUE
6	Ak-Bulak	55.63	51.02	143	1928 - 2014	1966 - 2014	TRUE	TRUE
7	Akaltyn	68.73	40.36	269	1957 - 1991	1957 - 1996	TRUE	TRUE
8	Akbaital	65.19	42.35	281	1951 - 2000	1951 - 2000	TRUE	TRUE
9	Akkavak	69.5	41.42	566	Not Available	1967 - 1999	FALSE	TRUE
10	Akkurgan	69.08	40.58	335	Not Available	1966 - 1999	FALSE	TRUE
11	Akrabat	66.82	38.26	1561	1950 - 1999	1950 - 1999	TRUE	TRUE
12	AkSai	76.32	40.88	3135	1952 - 1998	1952 - 1998	TRUE	TRUE
13	Aksenger	76.3	43.4	643	1960 - 2010	1960 - 2010	TRUE	TRUE
14	Aksu	80.14	41.1	1105	1953 - 2000	1954 - 2000	TRUE	TRUE
15	Aksuat	82.7	47.8	546	1940 - 2010	1941 - 2010	TRUE	TRUE
16	AkTash(Kyrg)	73.11	42.5	2157	1951 - 1988	1961 - 1990	TRUE	TRUE
17	AkTash(Uzb)	69.8	41.7	1154	Not Available	1956 - 1996	FALSE	TRUE
18	Akterek	76.7	42.24	1618	1980 - 2005	1982 - 2005	TRUE	TRUE
19	Akterekgava	72.78	41.32	1735	Not Available	1942 - 1990	FALSE	TRUE
20	Aktjubinsk	57.15	50.28	219	1904 - 2012	Not Available	TRUE	FALSE
21	Aktogai	79.6	46.9	364	1961 - 2010	1961 - 2010	TRUE	TRUE
22	Ala'erh	81.03	40.3	1012	1958 - 2000	1958 - 2000	TRUE	TRUE
23	Ala-Buka	71.5	41.4	1250	Not Available	1963 - 1990	FALSE	TRUE
24	AlaArcha	74.47	42.48	2946	1958 - 1973	Not Available	TRUE	FALSE
25	Alabel	73.07	42.24	3206	1961 - 1987	1960 - 1989	TRUE	TRUE
26	Alakol	81.5	46	360	1965 - 2010	1965 - 2010	TRUE	TRUE
27	Alashankou	82.58	45.18	285	1957 - 2000	1956 - 2000	TRUE	TRUE
28	Aleksandrov-G	48.55	50.15	23	1929 - 2014	1966 - 2014	TRUE	TRUE
29	Almalyk	69.6	40.84	507	1979 - 1999	1979 - 1999	TRUE	TRUE
30	Almaty	76.93	43.23	847	1879 - 2012	1879 - 2010	TRUE	TRUE
31	Almaty1172	77	43.18	1172	1915 - 2003	Not Available	TRUE	FALSE
32	Alplager	74.48	42.57	2130	1957 - 2005	1957 - 2005	TRUE	TRUE
33	Altai	96.25	46.4	2181	1954 - 2012	Not Available	TRUE	FALSE
34	Altay-Bayan-Oligy	89.5	48.3	2624	1970 - 1983	Not Available	TRUE	FALSE
35	Altyaryk	71.52	40.43	440	Not Available	1951 - 1999	FALSE	TRUE
36	AltynMazar	72.24	39.19	2782	1933 - 1997	1932 - 1997	TRUE	TRUE
37	Amankutan	66.94	39.31	1420	1932 - 1964	1933 - 1999	TRUE	TRUE

38	AndersRiver	83.64	37.95	1263	1960 - 1998	1960 - 1998	TRUE	TRUE
39	Andizhan	72.35	40.78	498	1900 - 1999	1900 - 1996	TRUE	TRUE
40	Angren(Kyrg)	70.78	41.55	2287	1931 - 1996	1931 - 1997	TRUE	TRUE
41	Angren(Uzb)	70.18	41	942	1949 - 2002	1949 - 2002	TRUE	TRUE
42	Anxi	95.77	40.53	1171	1939 - 1988	Not Available	TRUE	FALSE
43	AnzobskyPereval	68.87	39.08	3398	1940 - 2007	1940 - 2007	TRUE	TRUE
44	AralskoeMore	61.67	46.82	65	1905 - 2012	1906 - 2000	TRUE	TRUE
45	Arpa	74.82	40.77	2904	1961 - 1990	1953 - 1988	TRUE	TRUE
46	Ashbagat	58.33	37.96	224	1892 - 2012	1892 - 2000	TRUE	TRUE
47	Assy	78.3	43.3	2216	1952 - 2010	1952 - 2010	TRUE	TRUE
48	Astrahan'	48.05	46.28	-23	1837 - 2012	Not Available	FALSE	FALSE
49	Atbasar	68.37	51.82	304	1901 - 2012	Not Available	TRUE	FALSE
50	Atbashi	75.77	41.17	2027	1961 - 1995	1927 - 1995	TRUE	TRUE
51	Ayagoz	80.5	47.9	653	1936 - 2010	1936 - 2010	TRUE	TRUE
52	Ayaguz(town)	80.45	47.93	653	Not Available	1896 - 1989	FALSE	TRUE
53	Bachu	78.57	39.8	1117	1953 - 2000	1953 - 2000	TRUE	TRUE
54	Bahmazar	67.85	39.48	1000	Not Available	1974 - 1999	FALSE	TRUE
55	Baicheng	81.9	41.79	1229	1959 - 2000	1958 - 2000	TRUE	TRUE
56	Bairam-ali	62.17	37.61	238	1889 - 2012	1891 - 2000	TRUE	TRUE
57	Baisun	67.2	38.21	1241	1933 - 1999	1933 - 1999	TRUE	TRUE
58	Baityk(China)	90.57	45.36	1654	1957 - 2000	1957 - 2000	TRUE	TRUE
59	Baityk	74.5	42.65	1579	1914 - 2005	1913 - 2005	TRUE	TRUE
60	Bakhty	82.72	46.66	221	1927 - 2010	1927 - 2010	TRUE	TRUE
61	Balguntay	86.33	42.67	1753	1957 - 1990	Not Available	TRUE	FALSE
62	Balhash	75.08	46.8	350	1932 - 2012	1932 - 1999	TRUE	TRUE
63	Balkhash	75.01	46.88	416	1936 - 2003	Not Available	TRUE	FALSE
64	Barabinsk	78.37	55.33	119	1900 - 2014	1966 - 2014	TRUE	TRUE
65	Barnaul	83.52	53.43	183	1838 - 2014	1966 - 2014	TRUE	TRUE
66	Baruunturuun	94.4	49.65	1232	1961 - 2012	Not Available	TRUE	FALSE
67	Bashkizilsai	69.85	41.38	1277	1968 - 1999	1968 - 1999	TRUE	TRUE
68	Batken	70.83	40.06	1047	1980 - 2011	2005 - 2011	TRUE	TRUE
69	Bayan-Ol	92.1	49.8	934	1943 - 1983	Not Available	TRUE	FALSE
70	Bayanbulak	84.15	43.03	2458	1957 - 2000	1958 - 2000	TRUE	TRUE
71	Bazardzhoy	67.24	39.97	880	Not Available	1953 - 1998	FALSE	TRUE
72	Bekabad	69.24	40.22	300	1978 - 1998	1951 - 1999	TRUE	TRUE
73	BigAlmatyLake	76.98	43.06	2515	1932 - 2010	1932 - 2010	TRUE	TRUE
74	BijskZonal'naja	84.93	52.68	222	1941 - 2014	1966 - 2014	TRUE	TRUE
75	Bishkek(Frunze)	74.53	42.86	755	1896 - 2005	1895 - 2000	TRUE	TRUE
76	Blinkovo	70.13	42.23	1122	Not Available	1906 - 1991	FALSE	TRUE
77	Bogarnoe	67.45	39.94	748	1931 - 1999	1931 - 1999	TRUE	TRUE
78	Brichmulla	70.1	41.62	894	Not Available	1939 - 1987	FALSE	TRUE
79	Bukhara	64.43	39.8	230	Not Available	1961 - 1995	FALSE	TRUE
80	Bulakbashi	71.58	41.98	440	Not Available	1973 - 1992	FALSE	TRUE
81	Bulgan-Hovd	91.6	46.1	1739	1963 - 1983	Not Available	TRUE	FALSE

82	Bulunkul	72.94	37.72	3741	1950 - 2007	1991 - 2007	TRUE	FALSE
83	Bustonabad	69.65	38.68	1983	1948 - 2007	1948 - 2007	TRUE	TRUE
84	Buzaubai	62.47	41.75	96	1950 - 2003	1951 - 1999	TRUE	TRUE
85	Celinograd	71.37	51.13	347	1881 - 1990	Not Available	TRUE	FALSE
86	ChaarTash	73.77	41.16	2748	1960 - 1992	1960 - 1992	TRUE	TRUE
87	Chabankazgan	63.17	41.4	217	1949 - 1993	1951 - 1993	TRUE	TRUE
88	Chaek	74.42	41.88	1547	1961 - 2011	1980 - 2011	TRUE	TRUE
89	Chakhcharan	65.3	34.5	2230	1977 - 1992	Not Available	TRUE	FALSE
90	Chambil	66.48	39	494	Not Available	1950 - 1991	FALSE	TRUE
91	Chardzhou	63.6	39.09	193	1894 - 2012	1895 - 2000	TRUE	TRUE
92	Charshanga	66.02	37.52	266	1952 - 2003	Not Available	TRUE	FALSE
93	Charvak	70	41.6	974	1916 - 2001	1916 - 2002	TRUE	TRUE
94	Chatirkul	75.33	40.59	3532	1961 - 1988	1961 - 1990	TRUE	TRUE
95	Chatkal	71.31	41.9	1937	1933 - 2005	1933 - 1995	TRUE	TRUE
96	Cheleken	53.13	39.41	0	Not Available	1912 - 1991	FALSE	TRUE
97	Chimbai	59.78	42.93	64	1926 - 2012	1930 - 2000	TRUE	TRUE
98	Chimkent	69.65	42.33	583	Not Available	1919 - 1999	FALSE	TRUE
99	Chimkurgan	66.24	38.85	448	1960 - 1999	1960 - 1999	TRUE	TRUE
100	Chinaz	68.41	40.55	265	Not Available	1927 - 1999	FALSE	TRUE
101	Chirakchi	66.54	39.04	510	Not Available	1927 - 1999	FALSE	TRUE
102	CholponAta	77.04	42.62	1645	1929 - 2010	1929 - 2011	TRUE	TRUE
103	Chonaryk	73.75	42.06	1308	1943 - 1984	1943 - 1989	TRUE	TRUE
104	Chonashu	78.95	42.42	2791	1969 - 2011	1969 - 2011	TRUE	TRUE
105	Chonkyzylsu	78.2	42.19	2573	1951 - 2005	1948 - 2005	TRUE	TRUE
106	Chuguchak	83	46.73	535	1940 - 2000	1954 - 2000	TRUE	TRUE
107	Chust	71.23	41	680	Not Available	1936 - 1995	FALSE	TRUE
108	Dabancheng	88.32	43.35	1104	1956 - 2000	1956 - 2000	TRUE	TRUE
109	Dalverzin	69.28	40.42	293	1928 - 1999	1928 - 1999	TRUE	TRUE
110	Dangara	69.34	38.09	642	1931 - 2007	1943 - 2007	TRUE	TRUE
111	Daraut-Kurgan	72.19	39.55	2470	1948 - 1990	1949 - 1990	TRUE	TRUE
112	Dashnabad	68.05	38.51	778	Not Available	1932 - 1998	FALSE	TRUE
113	Dehavz	70.22	39.45	2561	1928 - 2007	1934 - 2007	TRUE	TRUE
114	Dehkanabad	66.5	38.35	864	1933 - 1999	1935 - 1999	TRUE	TRUE
115	Denau	67.92	38.27	516	1931 - 1999	1931 - 1999	TRUE	TRUE
116	Derbent	67.02	38.21	1011	Not Available	1957 - 1999	FALSE	TRUE
117	Dir	71.83	35.85	1425	1969 - 1979	Not Available	TRUE	FALSE
118	Dolon	75.74	41.84	3040	1961 - 1988	1961 - 1990	TRUE	TRUE
119	Dombarovskij	59.55	50.75	277	1938 - 2014	1966 - 2014	TRUE	TRUE
120	Dukant	70.07	41.15	2001	1959 - 2001	1959 - 2002	TRUE	TRUE
121	Dunhuang	94.68	40.15	1140	1938 - 2012	Not Available	TRUE	FALSE
122	Durmen	69.42	41.37	472	Not Available	1970 - 1996	FALSE	TRUE
123	Dushanbe-Agro	68.77	38.56	790	1926 - 2011	1926 - 2007	TRUE	TRUE
124	DzhalalAbad	72.97	40.94	768	1947 - 2003	1947 - 2000	TRUE	TRUE
125	Dzhangeldy	63.33	40.85	207	1952 - 1993	1952 - 1997	TRUE	TRUE

126	Dzhaus	67.25	39.19	1174	Not Available	1942 - 1996	FALSE	TRUE
127	Dzhavshangoz	72.47	37.35	3450	1934 - 2007	1935 - 2007	TRUE	TRUE
128	Dzhergetal	71.21	39.22	1785	1942 - 1984	1913 - 1992	TRUE	TRUE
129	Dzhizak	67.84	40.11	385	1881 - 2003	1891 - 2000	TRUE	TRUE
130	Erbent	58.6	39.3	89	Not Available	1961 - 2000	FALSE	TRUE
131	Ersov	48.3	51.37	110	1902 - 2014	1966 - 2014	TRUE	TRUE
132	Erzin	95.12	50.27	1100	1950 - 2014	1966 - 2014	TRUE	TRUE
133	Faizabad	69.32	38.55	1215	1951 - 2007	1942 - 2007	TRUE	TRUE
134	Fedchenko	72.07	40.56	466	Not Available	1929 - 1996	FALSE	TRUE
135	FedchenkoGlacier	72.22	38.84	4169	1935 - 1995	1935 - 1994	TRUE	TRUE
136	Fergana	71.75	40.38	578	1881 - 2012	1891 - 2000	TRUE	TRUE
137	FortShevchenko	50.26	44.54	-25	1848 - 2012	1891 - 2000	TRUE	TRUE
138	Fuhai	87.46	47.1	493	1958 - 2000	1957 - 2000	TRUE	TRUE
139	Furmanovo	49.48	49.67	10	1926 - 2012	Not Available	TRUE	FALSE
140	Fuyun	89.52	46.98	807	1961 - 2000	1961 - 2000	TRUE	TRUE
141	Gallyaaral	67.58	40.03	572	1933 - 1999	1933 - 1999	TRUE	TRUE
142	Gandjina	68.57	37.95	740	1954 - 2008	1954 - 2008	TRUE	TRUE
143	Garm	69.95	39	1316	1935 - 2008	1934 - 2008	TRUE	TRUE
144	Gasan-Kuli	53.97	37.46	-25	1926 - 2012	1926 - 2000	TRUE	TRUE
145	Gaudan	58.4	37.63	1488	1899 - 1990	1961 - 1990	TRUE	TRUE
146	Gorgan	54.47	36.82	155	1961 - 2012	Not Available	TRUE	FALSE
147	Govialt	95	47.6	1488	1965 - 1983	Not Available	TRUE	FALSE
148	Govialt1917	96.8	44.9	1917	1960 - 1983	Not Available	TRUE	FALSE
149	Gulcha	73.45	40.32	1561	1938 - 1992	1938 - 1997	TRUE	TRUE
150	Gur'ev	51.93	47.09	-27	1881 - 2012	1892 - 2000	TRUE	TRUE
151	Gushari	68.82	38.88	1359	1946 - 1984	1945 - 1990	TRUE	TRUE
152	Guzar	66.26	38.62	523	1927 - 1999	1927 - 1999	TRUE	TRUE
153	Haburabad	70.72	38.63	3238	1951 - 1990	1960 - 1990	TRUE	TRUE
154	Haidarkan	71.34	39.93	1993	1935 - 1990	1932 - 1990	TRUE	TRUE
155	Hami	93.52	42.82	739	1951 - 2012	Not Available	TRUE	FALSE
156	Hazarnovo	67.15	39.02	998	Not Available	1936 - 1999	FALSE	TRUE
157	Herat	62.22	34.22	964	1961 - 2009	Not Available	TRUE	FALSE
158	Hoboksar	85.72	46.78	1282	1953 - 2000	1954 - 2000	TRUE	TRUE
159	Horog	71.53	37.49	2064	1898 - 2009	1899 - 2007	TRUE	TRUE
160	Hotan	79.93	37.13	1375	1942 - 2012	Not Available	TRUE	FALSE
161	Hovaling	69.98	38.36	1458	1950 - 1994	1949 - 2007	TRUE	TRUE
162	Hovd	91.57	48.02	1405	1936 - 2012	Not Available	TRUE	FALSE
163	Humrogi	71.33	38.28	1737	1955 - 2007	1991 - 2007	TRUE	FALSE
164	HW(headIliR)	86.18	42.44	1739	1958 - 2000	1957 - 2000	TRUE	TRUE
165	Ili	77.4	44.1	455	Not Available	1933 - 1989	FALSE	TRUE
166	Irgiz	61.25	48.63	117	1863 - 2000	1891 - 1999	TRUE	TRUE
167	Irht	72.62	38.16	3290	1939 - 2007	1939 - 2007	TRUE	TRUE
168	Irkeshtam	73.9	39.67	2819	Not Available	1891 - 1976	FALSE	TRUE
169	Irtyssk	75.45	53.35	94	1935 - 2012	Not Available	TRUE	FALSE

170	Isambai	68.35	38.05	564	1951 - 2007	1951 - 2007	TRUE	TRUE
171	Isfana	69.52	39.84	1295	1950 - 2011	1950 - 2005	TRUE	TRUE
172	Isfara	70.63	40.12	847	1931 - 1994	1936 - 2005	TRUE	TRUE
173	Ishkashim	71.6	36.73	2520	1951 - 2007	1934 - 2007	TRUE	TRUE
174	Iskanderkul	68.39	39.06	2204	1930 - 2007	1930 - 2007	TRUE	TRUE
175	IssikBulak	81.02	44.97	1355	1958 - 2000	1957 - 2000	TRUE	TRUE
176	Issyk	77.47	43.37	1098	1937 - 2010	1937 - 2010	TRUE	TRUE
177	Itagar	72.92	42.17	2136	1980 - 2011	1980 - 2011	TRUE	TRUE
178	Jajlju	87.6	51.77	482	1941 - 2014	1966 - 2014	TRUE	TRUE
179	Jaslyk	57.5	44.1	128	1966 - 1993	1966 - 1996	TRUE	TRUE
180	Javan	69.05	38.32	663	1951 - 2007	1961 - 2007	TRUE	TRUE
181	Jimunai	85.87	47.44	984	1961 - 2000	1960 - 2000	TRUE	TRUE
182	JingheRiver	82.89	44.59	320	1953 - 2000	1953 - 2000	TRUE	TRUE
183	KabaRiver	86.41	48.05	529	1957 - 2000	1957 - 2000	TRUE	TRUE
184	KabulAirport	69.22	34.55	1791	1954 - 2010	Not Available	TRUE	FALSE
185	Kal'	71.45	40.88	384	Not Available	1935 - 1999	FALSE	TRUE
186	Kalai-Khumb	70.79	38.46	1260	1951 - 2007	1951 - 2007	TRUE	TRUE
187	Kalmykovo	51.83	49.03	-1	1925 - 2003	1924 - 1999	TRUE	TRUE
188	Kalpin	79.05	40.51	1161	1960 - 2000	1959 - 2000	TRUE	TRUE
189	Kamchik	70.52	41.1	2145	1983 - 1999	1969 - 1999	TRUE	TRUE
190	Kamen'-na-Obi	81.27	53.82	127	1941 - 2014	1966 - 2014	TRUE	TRUE
191	Kangurt	69.52	38.25	778	1934 - 1988	1951 - 1988	TRUE	TRUE
192	Kara-Tjurek	86.5	49.94	2600	1941 - 2014	1940 - 2014	TRUE	TRUE
193	Karabalta	73.83	42.79	814	1980 - 2011	1980 - 2010	TRUE	TRUE
194	Karabatkak	78.27	42.16	3328	1956 - 2005	Not Available	TRUE	FALSE
195	Karaganda	73.12	49.8	554	1936 - 2012	1932 - 2000	TRUE	TRUE
196	Karakalpakia	56.83	44.95	130	1966 - 1993	1966 - 1996	TRUE	TRUE
197	Karakia	66.75	40.11	600	Not Available	1948 - 1991	FALSE	TRUE
198	Karakudzhur	76.31	41.92	2800	1961 - 1988	1935 - 1990	TRUE	TRUE
199	Karakul(Uzb)	63.85	39.5	196	Not Available	1961 - 1995	FALSE	TRUE
200	Karakul	73.56	39.01	3935	1933 - 2007	1934 - 2007	TRUE	TRUE
201	Karamay	84.85	45.62	450	1956 - 2012	1956 - 2000	TRUE	TRUE
202	Karasu	72.93	40.78	1100	1980 - 2005	1980 - 2005	TRUE	TRUE
203	Karatash	67.5	40.17	963	Not Available	1977 - 1999	FALSE	TRUE
204	Karavan	71.72	41.47	1280	1942 - 1987	1943 - 1990	TRUE	TRUE
205	Karkaralinsk	75.53	49.42	851	Not Available	1891 - 1993	FALSE	TRUE
206	Karsakpai	66.74	47.83	504	1926 - 1994	1926 - 1994	TRUE	TRUE
207	Karshi	65.77	38.82	375	Not Available	1927 - 1991	FALSE	TRUE
208	Kashi(Kashgar)	75.99	39.46	1293	1951 - 2012	1951 - 2000	TRUE	TRUE
209	Kassansai	71.53	41.25	891	1933 - 1987	1933 - 1995	TRUE	TRUE
210	Katon-Karagai	85.63	49.17	1081	1932 - 2010	1898 - 2010	TRUE	TRUE
211	Kattagan	67.09	38.98	1000	Not Available	1933 - 1991	FALSE	TRUE
212	Kattakurgan	66.3	39.89	515	1913 - 1999	1901 - 1999	TRUE	TRUE
213	Kaunchi	69	41.08	340	1927 - 1999	1927 - 1999	TRUE	TRUE

214	Kaynar	77.4	49.2	840	1950 - 2010	1950 - 2010	TRUE	TRUE
215	Kazalinsk	62.12	45.77	66	1881 - 2012	1891 - 1999	TRUE	TRUE
216	Kazandzhik	55.52	39.25	33	Not Available	1928 - 2000	FALSE	TRUE
217	Kazarman	74.03	41.41	1266	1960 - 2002	1960 - 1998	TRUE	TRUE
218	Kegen	79.2	43	1845	1947 - 2010	1947 - 2010	TRUE	TRUE
219	Kerki	65.2	37.83	241	Not Available	1891 - 2000	FALSE	TRUE
220	Ketmen-Tyube	72.69	41.87	907	Not Available	1932 - 1990	FALSE	TRUE
221	Khiva	60.38	41.4	95	Not Available	1961 - 1995	FALSE	TRUE
222	King-Guzar	67.77	38.46	796	Not Available	1944 - 1999	FALSE	TRUE
223	Kirgizata	72.66	40.17	1766	Not Available	1940 - 1997	FALSE	TRUE
224	Kirovskoe	71.59	42.62	918	1961 - 1990	1961 - 1990	TRUE	TRUE
225	Kizilcha	70.42	41.21	2065	1958 - 1992	1958 - 1993	TRUE	TRUE
226	Kizyl-arvat	56.28	38.98	96	1883 - 2012	1883 - 2000	TRUE	TRUE
227	Kochkorka	75.73	42.21	1810	1942 - 1984	1942 - 1990	TRUE	TRUE
228	Kogaly	78.7	44.5	1410	1927 - 2010	1927 - 2010	TRUE	TRUE
229	Koilyu	78.97	42.21	2800	1951 - 1988	1951 - 1990	TRUE	TRUE
230	Kokand	70.93	40.56	399	1926 - 1999	1926 - 1999	TRUE	TRUE
231	Kokaral	69.23	40.69	340	1937 - 1999	1933 - 1999	TRUE	TRUE
232	Kokpekty	82.39	48.76	512	1894 - 2012	1891 - 1999	TRUE	TRUE
233	Kokshetay	69.38	53.28	229	1925 - 2012	Not Available	TRUE	FALSE
234	Koktobe	77.3	51.5	137	1970 - 2010	1970 - 2010	TRUE	TRUE
235	Komsomolabad	69.98	38.87	1259	1947 - 1989	1947 - 1989	TRUE	TRUE
236	Korla	86.13	41.75	932	1958 - 2012	1958 - 2000	TRUE	TRUE
237	Korona	74.55	42.51	4009	Not Available	1964 - 1975	FALSE	FALSE
238	Kosh-Agach	88.67	50	1759	1934 - 2014	1966 - 2014	TRUE	TRUE
239	Krasnojarsk	92.75	56.03	276	1891 - 2012	Not Available	TRUE	FALSE
240	Krasnovodsk	52.98	40.03	89	1883 - 2012	1883 - 2000	TRUE	TRUE
241	KrasnyiOctyabr	78.23	42.77	1608	Not Available	1933 - 1990	FALSE	TRUE
242	Kucha	82.99	41.72	1084	1951 - 2012	1951 - 2000	TRUE	TRUE
243	Kuigan	74.17	45.42	345	Not Available	1929 - 2003	FALSE	TRUE
244	Kujbysev(Bezencuk)	50.45	53.25	44	1935 - 1990	Not Available	FALSE	FALSE
245	Kulkuduk	63.3	42.52	333	1952 - 1991	1952 - 1991	TRUE	TRUE
246	Kulyab	69.78	37.91	604	1930 - 1992	1931 - 1990	TRUE	TRUE
247	Kumux	88.18	42.23	922	1959 - 2000	1959 - 2000	TRUE	TRUE
248	Kungrad	58.93	43.08	60	1951 - 2003	1951 - 2000	TRUE	TRUE
249	Kurgan-Tyube	68.86	37.82	426	1929 - 2007	1929 - 2007	TRUE	TRUE
250	Kurgan	65.4	55.47	74	1893 - 2011	Not Available	FALSE	FALSE
251	Kurshim	83.7	48.6	425	1936 - 2010	1936 - 2010	TRUE	TRUE
252	Kushka	62.35	35.29	57	1904 - 2003	1897 - 2000	TRUE	TRUE
253	Kushrabad	66.65	40.23	725	1957 - 1999	1957 - 1999	TRUE	TRUE
254	Kustanai	63.62	53.22	156	1902 - 2012	Not Available	TRUE	FALSE
255	Kuzedeevo	87.18	53.33	293	1956 - 2014	1966 - 2014	TRUE	TRUE
256	Kyzyl-orda	65.51	44.85	127	1891 - 2000	1891 - 1998	TRUE	TRUE
257	Kyzyl-Ozek	86	51.9	324	1941 - 2014	1966 - 2014	TRUE	TRUE

258	Kyzyl	94.5	51.72	626	1944 - 2014	1966 - 2014	TRUE	TRUE
259	Kyzyldzhar	74.24	40.31	2117	1964 - 1988	1961 - 1990	TRUE	TRUE
260	Kzyl-zhar	69.65	48.3	361	1937 - 2012	1937 - 1995	TRUE	TRUE
261	Lenghu	93.38	38.83	2734	1956 - 1990	Not Available	TRUE	FALSE
262	Leninabad	69.73	40.21	425	1881 - 2007	1891 - 2007	TRUE	TRUE
263	Leninogorsk	83.55	50.33	811	1934 - 2012	1934 - 2010	TRUE	TRUE
264	Lepsi	80.6	45.83	1012	1932 - 2010	1932 - 2010	TRUE	TRUE
265	Lotai	88.08	47.74	720	1938 - 2012	1954 - 2000	TRUE	TRUE
266	Luntai	84.25	41.78	976	1959 - 2000	1958 - 2000	TRUE	TRUE
267	Lyairun	70.9	38.9	2008	1962 - 1990	1960 - 1990	TRUE	TRUE
268	Lyakhsh	71.25	38.32	1998	1961 - 2007	1960 - 2007	TRUE	TRUE
269	Lyangar	66.65	39.33	510	Not Available	1974 - 1987	FALSE	TRUE
270	Madrushkent	69.67	39.45	2234	1933 - 2007	1933 - 2007	TRUE	TRUE
271	Madzherum	66.73	40.62	613	Not Available	1963 - 1999	FALSE	TRUE
272	Mangnai	90.85	38.25	2946	1958 - 2000	1958 - 2000	TRUE	TRUE
273	Marhamat	72.33	40.5	610	Not Available	1936 - 1999	FALSE	TRUE
274	Mashhad	59.63	36.27	980	1906 - 2012	Not Available	TRUE	FALSE
275	Mazar-I-Shari	67.2	36.7	378	1961 - 1992	Not Available	TRUE	FALSE
276	Mazongshan	97.03	41.8	1770	1957 - 2012	Not Available	TRUE	FALSE
277	Medeo	77.04	43.17	1511	Not Available	1931 - 1960	FALSE	TRUE
278	Minchukur	66.93	38.65	2132	1951 - 1999	1951 - 1999	TRUE	TRUE
279	Minusinsk	91.7	53.72	254	1886 - 2014	1966 - 2014	TRUE	TRUE
280	Mointy	73.35	47.22	582	Not Available	1935 - 1991	FALSE	TRUE
281	Mubarek	69.15	39.25	285	1935 - 1999	1933 - 1999	TRUE	TRUE
282	Mugur-Aksy	90.43	50.38	1850	1964 - 2014	1966 - 2014	TRUE	TRUE
283	Muinak	59.04	43.76	68	1951 - 1993	1933 - 1994	TRUE	TRUE
284	Muminabad	70.03	38.11	1240	1951 - 2007	1991 - 2007	TRUE	FALSE
285	Muratsai	74.49	42.58	2287	Not Available	1958 - 1991	FALSE	FALSE
286	Murgab	73.96	38.16	3576	1894 - 2007	1894 - 2007	TRUE	TRUE
287	Mynzhilky	77.08	43.09	3009	1936 - 2010	1935 - 2010	TRUE	TRUE
288	Namangan	71.59	40.99	474	1924 - 2003	1891 - 2001	TRUE	TRUE
289	Naryn	75.98	41.43	2039	1885 - 2012	1886 - 2005	TRUE	TRUE
290	Narynkol	80.17	42.73	1806	1947 - 2010	1947 - 2010	TRUE	TRUE
291	Nasretdinbek	71.92	40.7	428	1958 - 1999	1958 - 1999	TRUE	TRUE
292	Navoi	65.35	40.13	347	Not Available	1961 - 1995	FALSE	TRUE
293	Nenastnaja	88.82	54.75	1186	1933 - 2014	1966 - 2014	TRUE	TRUE
294	Neozhidannyj	89.07	53.28	527	1948 - 2014	1966 - 2014	TRUE	TRUE
295	Nishbash	70.18	40.94	1085	Not Available	1953 - 1999	FALSE	TRUE
296	NizhniyPyandge	68.56	37.2	329	1947 - 1990	1947 - 2007	TRUE	TRUE
297	Nookat	72.64	40.26	1357	1980 - 2011	1980 - 2011	TRUE	TRUE
298	Novorossiika	76.09	42.73	1524	1931 - 2000	1926 - 2000	TRUE	TRUE
299	Novouzensk	48.13	50.43	32	1900 - 2014	1966 - 2014	TRUE	TRUE
300	Nukus	59.61	42.45	75	1951 - 2003	1936 - 2000	TRUE	TRUE
301	Nuratasovhoz	65.69	40.57	484	1956 - 2003	1956 - 2000	TRUE	TRUE

302	Ogurcovo	82.95	54.9	131	1931 - 2014	1966 - 2014	TRUE	TRUE
303	Oigaing	71.51	42.01	2151	1963 - 1999	1962 - 2002	TRUE	TRUE
304	Olen'jaRechka	93.23	52.8	1404	1927 - 2014	1966 - 2014	TRUE	TRUE
305	Omno-Gobi	91.72	49.02	1590	1963 - 2012	Not Available	TRUE	FALSE
306	Omsk	73.38	55.02	121	1876 - 2014	1967 - 2014	TRUE	TRUE
307	Orenburg	55.1	51.68	115	1832 - 2014	1966 - 2014	TRUE	TRUE
308	OrlovskiiPoselok	86.49	48.7	1095	Not Available	1909 - 1993	FALSE	TRUE
309	Osh	72.8	40.53	1016	1881 - 1997	1891 - 1996	TRUE	TRUE
310	Paitug	72.17	40.9	503	Not Available	1938 - 1987	FALSE	TRUE
311	Panfilov	80	44.18	643	1911 - 2012	1891 - 2010	TRUE	TRUE
312	Pap	71.11	40.88	442	1948 - 1999	1948 - 1999	TRUE	TRUE
313	Papan	73	40.3	1400	Not Available	1947 - 1991	FALSE	TRUE
314	Pendjikent	67.61	39.49	1008	1931 - 2007	1915 - 2007	TRUE	TRUE
315	Pereljub	50.33	51.87	72	1934 - 2014	1966 - 2014	TRUE	TRUE
316	Petropavlovsk	69.15	54.83	142	1890 - 2011	Not Available	TRUE	FALSE
317	PochaAta	74.89	45.42	1500	1928 - 2005	Not Available	TRUE	FALSE
318	Podgornoe	79.47	43.33	1273	1934 - 2010	1930 - 2010	TRUE	TRUE
319	Pokrovka	78	42.35	1740	1950 - 2000	1951 - 2000	TRUE	TRUE
320	Przhevalsk	78.38	42.5	1716	1879 - 2011	1883 - 2011	TRUE	TRUE
321	Pskem	70.37	41.91	1256	1933 - 2003	1933 - 2002	TRUE	TRUE
322	Pushan	78.28	37.62	1372	1959 - 2000	1959 - 2000	TRUE	TRUE
323	Qinghe	90.38	46.67	1218	1958 - 2000	1957 - 2000	TRUE	TRUE
324	Qitai	89.58	43.99	794	1951 - 2000	1951 - 2000	TRUE	TRUE
325	Quemo	85.55	38.13	1248	1953 - 2000	1953 - 2000	TRUE	TRUE
326	Rebriha	82.33	53.08	218	1956 - 2014	1966 - 2014	TRUE	TRUE
327	Repetek	63.18	38.57	29	1913 - 1990	1912 - 1990	TRUE	TRUE
328	Rubcovsk	81.2	51.58	216	1925 - 2014	1966 - 2014	TRUE	TRUE
329	Ruoqiang	88.17	39.03	888	1953 - 2012	1953 - 2000	TRUE	TRUE
330	Rushan	71.56	37.95	1966	1951 - 2007	1947 - 2007	TRUE	TRUE
331	RusskajaPoljana	73.88	53.78	127	1960 - 2014	1966 - 2014	TRUE	TRUE
332	Rybach'e	76.18	42.46	1622	1931 - 2000	1911 - 2005	TRUE	TRUE
333	Sabzevar	57.67	36.22	941	1971 - 2000	Not Available	TRUE	FALSE
334	Sadrinsk	63.65	56.07	89	1894 - 2012	Not Available	FALSE	FALSE
335	Sam	56.2	45.42	86	1946 - 2012	1951 - 2000	TRUE	TRUE
336	Samara(Bezen)	49.43	52.98	46	1852 - 2012	Not Available	FALSE	FALSE
337	Samarchuk	70	40.52	1031	Not Available	1948 - 1999	FALSE	TRUE
338	Samarkand	66.96	39.65	726	1891 - 2012	1891 - 2000	TRUE	TRUE
339	Sangiston	68.63	39.39	1502	1932 - 2007	1947 - 2007	TRUE	TRUE
340	Sanglok	69.23	38.27	2235	1948 - 2007	1948 - 2007	TRUE	TRUE
341	SanTash	78.87	42.73	2000	1963 - 1998	1963 - 1998	TRUE	TRUE
342	Sanzar	68.01	39.73	1313	1935 - 1999	1934 - 1999	TRUE	TRUE
343	SariTash	73.25	39.72	3153	1934 - 2005	1934 - 2005	TRUE	TRUE
344	Sarkand	79.9	45.4	764	1927 - 2010	1927 - 2010	TRUE	TRUE
345	Sarydzhas	79.69	43.07	1956	Not Available	1951 - 1965	FALSE	TRUE

346	Sazagan	66.72	39.53	800	Not Available	1937 - 1999	FALSE	TRUE
347	Seleznevka	83.48	49.6	396	1967 - 2010	1967 - 2010	TRUE	TRUE
348	Semei	80.2	50.4	195	1944 - 2010	1944 - 2010	TRUE	TRUE
349	Semipalatinsk	80.26	50.41	202	1891 - 2012	1901 - 2010	TRUE	TRUE
350	Semiyarka	78.4	50.9	148	1936 - 2010	1936 - 2010	TRUE	TRUE
351	Serahs	61.21	36.54	279	1903 - 2003	1902 - 2000	TRUE	TRUE
352	SevenWells	91.62	43.49	873	1952 - 2000	1952 - 2000	TRUE	TRUE
353	SevertsovaGlacier	67.64	39.11	2775	1959 - 1999	1960 - 1999	TRUE	TRUE
354	Shaartuz	68.13	37.32	379	1935 - 2007	1943 - 2007	TRUE	TRUE
355	Shache(Yarkand)	77.26	38.33	1230	1953 - 2000	1953 - 2000	TRUE	TRUE
356	Shahrisabs	66.83	39.07	624	1928 - 1999	1927 - 1999	TRUE	TRUE
357	ShahristanskiiPereval	68.54	39.55	3438	1934 - 2007	1928 - 2007	TRUE	TRUE
358	Shahrud	55.03	36.42	1345	1971 - 2000	Not Available	TRUE	FALSE
359	Shaimak	74.62	37.53	3840	1958 - 2007	1991 - 2007	TRUE	FALSE
360	Shelek	78.3	43.6	606	1933 - 2010	1933 - 2010	TRUE	TRUE
361	Shemonaiha	81.9	50.6	329	1936 - 2010	1936 - 2010	TRUE	TRUE
362	Sherabad	67.02	37.67	417	1928 - 1999	1927 - 1999	TRUE	TRUE
363	Shihez	86.05	44.32	443	1952 - 2000	1953 - 2000	TRUE	TRUE
364	Shurchi-mst	67.8	38	446	1951 - 1999	1959 - 1999	TRUE	TRUE
365	Shurchi-post	67.73	37.9	420	Not Available	1935 - 1999	FALSE	TRUE
366	Slavgorod	78.65	52.97	125	1941 - 2014	1966 - 2014	TRUE	TRUE
367	Soloneshnoe	84.33	51.63	409	1956 - 2014	1966 - 2014	TRUE	TRUE
368	Sorocinsk	53.13	52.43	122	1935 - 2014	1966 - 2014	TRUE	TRUE
369	Sosnovka	94.52	51.15	947	1965 - 2014	1966 - 2014	TRUE	TRUE
370	Sukok	69.79	41.25	1164	1959 - 1999	Not Available	TRUE	FALSE
371	Susamyr	73.95	42.19	2089	1935 - 2005	1936 - 2005	TRUE	TRUE
372	Syrdarya	68.68	40.81	264	Not Available	1961 - 1995	FALSE	TRUE
373	Takhiatash	59.57	42.34	76	Not Available	1953 - 1996	FALSE	TRUE
374	Talas	72.22	42.53	1217	1930 - 2005	1930 - 2000	TRUE	TRUE
375	Taldy-Kurgan	78.38	45.01	601	1930 - 2010	1930 - 2010	TRUE	TRUE
376	Tamdy	64.61	41.75	263	1932 - 2012	1932 - 2000	TRUE	TRUE
377	Tamga	77.56	42.16	1690	Not Available	1941 - 1987	FALSE	TRUE
378	Tangivoruh	70.55	39.85	1311	1948 - 1988	1943 - 1988	TRUE	TRUE
379	Tara	74.38	56.9	73	1887 - 2012	Not Available	FALSE	FALSE
380	Tashkent	69.3	41.33	477	1875 - 2012	1877 - 2001	TRUE	TRUE
381	Tashkurgan	75.2	37.81	3091	1957 - 2000	1957 - 2000	TRUE	TRUE
382	Tatarsk	75.97	55.22	110	1941 - 2014	1966 - 2014	TRUE	TRUE
383	Tavildara	70.51	38.71	1624	1932 - 1994	1949 - 1994	TRUE	TRUE
384	Tedzhen	60.51	37.38	188	1907 - 2003	Not Available	TRUE	FALSE
385	Tekeli	79	44.8	1722	1959 - 2010	1959 - 2010	TRUE	FALSE
386	TekeTor	74.51	42.52	3800	Not Available	1964 - 1975	FALSE	FALSE
387	Tepshe	74.5	42.56	2748	Not Available	1964 - 1975	FALSE	FALSE
388	Termez	67.33	37.27	309	1900 - 2012	1900 - 2000	TRUE	TRUE
389	TienShan	78.11	41.86	3611	1929 - 2005	1930 - 2005	TRUE	TRUE

390	TigrovyiMys	58.75	43.91	54	1951 - 1999	1953 - 1993	TRUE	TRUE
391	Tikenlik	87.72	40.63	848	1957 - 2000	1957 - 2000	TRUE	TRUE
392	Toitepa	69.22	41.04	388	Not Available	1976 - 1999	FALSE	TRUE
393	Tokmak	75.29	42.84	816	1980 - 2011	1941 - 2011	TRUE	TRUE
394	Toktogul	72.93	41.87	982	1952 - 2011	1952 - 2010	TRUE	TRUE
395	Toli	83.6	45.94	1076	1957 - 2000	1956 - 2000	TRUE	TRUE
396	Tomsk	84.92	56.5	139	1837 - 1990	Not Available	TRUE	FALSE
397	Tonhil-Govialtay	93.9	46.3	2470	1973 - 1983	Not Available	TRUE	FALSE
398	Topkaragay	74.49	42.51	2656	Not Available	1958 - 1991	FALSE	FALSE
399	TopkaragayGl	74.53	42.48	3870	Not Available	1964 - 1975	FALSE	FALSE
400	Torbat-Heydar	59.22	35.27	1333	1971 - 2000	Not Available	TRUE	FALSE
401	Tosontsengel	98.28	48.73	1723	1964 - 2012	Not Available	TRUE	FALSE
402	Troizk	61.62	54.08	192	1941 - 2014	1966 - 2014	TRUE	TRUE
403	Tuergate	75.39	40.51	3605	1959 - 2000	1959 - 2000	TRUE	TRUE
404	Turfan	89.2	42.93	24	1951 - 2000	1951 - 2000	TRUE	TRUE
405	Turgai	63.47	49.63	133	1900 - 2000	1900 - 1995	TRUE	TRUE
406	Turkestan	68.23	43.28	207	1882 - 2012	Not Available	TRUE	FALSE
407	Turtkul	61.01	41.5	106	Not Available	1891 - 1996	FALSE	TRUE
408	Tuyabuguz	69.4	40.93	404	1966 - 1999	1973 - 1999	TRUE	TRUE
409	TuykGl	74.53	42.47	3800	Not Available	1964 - 1975	FALSE	FALSE
410	Tyuya-ashuNorthern	73.81	42.36	3050	1953 - 1987	1953 - 1991	TRUE	TRUE
411	Tyuya-ashuSouthern	73.81	42.34	3284	1958 - 2005	1958 - 2005	TRUE	TRUE
412	Uch-Aral	80.93	46.17	397	1933 - 2010	1928 - 2010	TRUE	TRUE
413	Uchtobe	77.98	45.23	426	1934 - 2010	1913 - 2010	TRUE	TRUE
414	Ufa	55.83	54.72	104	1891 - 2012	Not Available	FALSE	FALSE
415	Uigi	89.93	48.93	1715	1959 - 2012	Not Available	TRUE	FALSE
416	Uil	54.64	49.07	128	1925 - 2012	1891 - 1999	TRUE	TRUE
417	Uliastai	96.85	47.75	1759	1937 - 2012	Not Available	TRUE	FALSE
418	Ulus	66.33	39.62	505	1956 - 1999	1956 - 1999	TRUE	TRUE
419	Ura-Tube	68.99	39.9	1024	1930 - 2007	1943 - 2007	TRUE	TRUE
420	Uralsk	51.28	51.25	37	1839 - 2012	Not Available	TRUE	FALSE
421	Urdzhar	81.62	47.09	470	1936 - 2010	1934 - 2010	TRUE	TRUE
422	Urgandzhar	74.42	42.56	3712	Not Available	1964 - 1975	FALSE	FALSE
423	Urgench	60.63	41.57	100	Not Available	1928 - 2000	FALSE	TRUE
424	Urumqi	87.62	43.78	894	1907 - 2012	1951 - 2000	TRUE	TRUE
425	Ust'-Gorelnik	77.07	43.14	1916	1936 - 1991	1937 - 1991	TRUE	TRUE
426	Ust'-Kamenogorsk	82.5	50.02	278	1911 - 2010	1911 - 2010	TRUE	TRUE
427	Ust'-Koksa	85.62	50.27	977	1941 - 2014	1966 - 2014	TRUE	TRUE
428	Ustie-R-Dzhulaisai	70.74	41	1079	Not Available	1953 - 1999	FALSE	TRUE
429	Ustie-R-Kurbankul	71.81	39.98	1451	Not Available	1947 - 1999	FALSE	TRUE
430	Ustie-R-Maidantal	70.6	42.15	1492	Not Available	1940 - 1999	FALSE	TRUE
431	Ustie-R-Obizarang	68	38.05	548	Not Available	1976 - 1999	FALSE	TRUE
432	Ustie-R-Ters	70.8	41.6	1759	1932 - 1992	1932 - 1995	TRUE	TRUE
433	Ustie-R-Tos	71.66	41.6	1543	1914 - 1997	1942 - 1990	TRUE	TRUE

434	UstieTersRiver	70.87	41.24	1766	1961 - 1990	Not Available	TRUE	FALSE
435	Usu	84.67	44.43	478	1953 - 2000	1953 - 2000	TRUE	TRUE
436	Uyuk	70.95	43.78	373	Not Available	1931 - 1991	FALSE	TRUE
437	Uzgen	73.29	40.78	1015	1980 - 2005	1980 - 2005	TRUE	TRUE
438	Uzynagash	76.3	43.2	814	1971 - 2010	1971 - 2010	TRUE	TRUE
439	VAlaArcha	74.45	42.44	3432	Not Available	1964 - 1991	FALSE	FALSE
440	Verhneural'sk	59.2	53.88	401	1904 - 2014	1966 - 2014	TRUE	TRUE
441	VerhniyGorelnik	77.06	43.13	2262	1937 - 1987	1937 - 1989	TRUE	TRUE
442	Wujiaqu	87.54	44.4	439	1958 - 2000	1959 - 2000	TRUE	TRUE
443	Wuqia	75.25	39.72	2175	1956 - 2000	1956 - 2000	TRUE	TRUE
444	Yangi-akchob	66.47	40.28	810	Not Available	1947 - 1999	FALSE	TRUE
445	Yanqi	86.57	42.08	1055	1951 - 2000	1951 - 2000	TRUE	TRUE
446	Yining	81.33	43.95	663	1951 - 2012	Not Available	TRUE	FALSE
447	Yiwu	94.7	43.27	1729	1958 - 1990	Not Available	TRUE	FALSE
448	Yumenzhen	97.03	40.27	1527	1952 - 1990	Not Available	FALSE	FALSE
449	Zaamin	68.4	39.96	626	1964 - 1992	1967 - 1992	TRUE	TRUE
450	ZapovednikMarkakol	86	48.8	1372	1983 - 2010	1983 - 2010	TRUE	TRUE
451	Zaysan	85.2	48	408	1912 - 2010	1891 - 2010	TRUE	TRUE
452	Zhalanash	78.7	43.1	1699	1959 - 2010	1959 - 2010	TRUE	TRUE
453	Zhalanashkol	82.1	45.6	377	1961 - 2010	1961 - 2010	TRUE	TRUE
454	Zhaosu	81.13	43.14	1851	1954 - 2000	1954 - 2000	TRUE	TRUE
455	Zilair	57.4	52.22	522	1941 - 2014	1966 - 2014	TRUE	TRUE
456	Zlatoust	59.67	55.2	538	1837 - 1875	Not Available	FALSE	FALSE
457	Zmeinogorsk	82.17	51.15	354	1902 - 2014	1966 - 2014	TRUE	TRUE

Appendix B

ELSEVIER LICENSE
TERMS AND CONDITIONS

Sep 11, 2015

This is a License Agreement between Hang ZHOU ("You") and Elsevier ("Elsevier") provided by Copyright Clearance Center ("CCC"). The license consists of your order details, the terms and conditions provided by Elsevier, and the payment terms and conditions.

All payments must be made in full to CCC. For payment instructions, please see information listed at the bottom of this form.

Supplier	Elsevier Limited The Boulevard,Langford Lane Kidlington,Oxford,OX5 1GB,UK
Registered Company Number	1982084
Customer name	Hang ZHOU
Customer address	1016 S. Deakin St. MOSCOW, ID 83843
License number	3706150868929
License date	Sep 11, 2015
Licensed content publisher	Elsevier
Licensed content publication	Remote Sensing of Environment
Licensed content title	Deriving long term snow cover extent dataset from AVHRR and MODIS data: Central Asia case study
Licensed content author	Hang Zhou,Elena Aizen,Vladimir Aizen
Licensed content date	September 2013
Licensed content volume number	136
Licensed content issue number	n/a
Number of pages	17
Start Page	146
End Page	162

Type of Use	reuse in a thesis/dissertation
Portion	full article
Format	both print and electronic
Are you the author of this Elsevier article?	Yes
Will you be translating?	No
Title of your thesis/dissertation	Diagnosis and Estimation of Cryospheric Changes in Central Asia
Expected completion date	Dec 2015
Estimated size (number of pages)	250
Elsevier VAT number	GB 494 6272 12
Permissions price	0.00 USD
VAT/Local Sales Tax	0.00 USD / 0.00 GBP
Total	0.00 USD
Terms and Conditions	

INTRODUCTION

1. The publisher for this copyrighted material is Elsevier. By clicking "accept" in connection with completing this licensing transaction, you agree that the following terms and conditions apply to this transaction (along with the Billing and Payment terms and conditions established by Copyright Clearance Center, Inc. ("CCC"), at the time that you opened your Rightslink account and that are available at any time at http://myaccount.copyright.com).

GENERAL TERMS

2. Elsevier hereby grants you permission to reproduce the aforementioned material subject to the terms and conditions indicated.

3. Acknowledgement: If any part of the material to be used (for example, figures) has appeared in our publication with credit or acknowledgement to another source, permission must also be sought from that source. If such permission is not obtained then that material may not be included in your publication/copies. Suitable acknowledgement to the source must be made, either as a footnote or in a reference list at the end of your publication, as follows:

"Reprinted from Publication title, Vol /edition number, Author(s), Title of article / title of chapter, Pages No., Copyright (Year), with permission from Elsevier [OR APPLICABLE SOCIETY COPYRIGHT OWNER]." Also Lancet special credit - "Reprinted from The Lancet, Vol. number, Author(s), Title of article, Pages No., Copyright (Year), with permission from Elsevier."

4. Reproduction of this material is confined to the purpose and/or media for which permission is hereby given.

5. Altering/Modifying Material: Not Permitted. However figures and illustrations may be altered/adapted minimally to serve your work. Any other abbreviations, additions, deletions and/or any other alterations shall be made only with prior written authorization of Elsevier Ltd. (Please contact Elsevier at permissions@elsevier.com)

6. If the permission fee for the requested use of our material is waived in this instance, please be advised that your future requests for Elsevier materials may attract a fee.

7. Reservation of Rights: Publisher reserves all rights not specifically granted in the combination of (i) the license details provided by you and accepted in the course of this licensing transaction, (ii) these terms and conditions and (iii) CCC's Billing and Payment terms and conditions.

8. License Contingent Upon Payment: While you may exercise the rights licensed immediately upon issuance of the license at the end of the licensing process for the transaction, provided that you have disclosed complete and accurate details of your proposed use, no license is finally effective unless and until full payment is received from you (either by publisher or by CCC) as provided in CCC's Billing and Payment terms and conditions. If full payment is not received on a timely basis, then any license preliminarily granted shall be deemed automatically revoked and shall be void as if never granted. Further, in the event that you breach any of these terms and conditions or any of CCC's Billing and Payment terms and conditions, the license is automatically revoked and shall be void as if never granted. Use of materials as described in a revoked license, as well as any use of the materials beyond the scope of an unrevoked license, may constitute copyright infringement and publisher reserves the right to take any and all action to protect its copyright in the materials.

9. Warranties: Publisher makes no representations or warranties with respect to the licensed material.

10. Indemnity: You hereby indemnify and agree to hold harmless publisher and CCC, and their respective officers, directors, employees and agents, from and against any and all claims arising out of your use of the licensed material other than as specifically authorized pursuant to this license.

11. No Transfer of License: This license is personal to you and may not be sublicensed, assigned, or transferred by you to any other person without publisher's written permission.

12. No Amendment Except in Writing: This license may not be amended except in a writing signed by both parties (or, in the case of publisher, by CCC on publisher's behalf).

13. Objection to Contrary Terms: Publisher hereby objects to any terms contained in any purchase order, acknowledgment, check endorsement or other writing prepared by you, which terms are inconsistent with these terms and conditions or CCC's Billing and Payment

terms and conditions. These terms and conditions, together with CCC's Billing and Payment terms and conditions (which are incorporated herein), comprise the entire agreement between you and publisher (and CCC) concerning this licensing transaction. In the event of any conflict between your obligations established by these terms and conditions and those established by CCC's Billing and Payment terms and conditions, these terms and conditions shall control.

14. Revocation: Elsevier or Copyright Clearance Center may deny the permissions described in this License at their sole discretion, for any reason or no reason, with a full refund payable to you. Notice of such denial will be made using the contact information provided by you. Failure to receive such notice will not alter or invalidate the denial. In no event will Elsevier or Copyright Clearance Center be responsible or liable for any costs, expenses or damage incurred by you as a result of a denial of your permission request, other than a refund of the amount(s) paid by you to Elsevier and/or Copyright Clearance Center for denied permissions.

LIMITED LICENSE

The following terms and conditions apply only to specific license types:

15. Translation: This permission is granted for non-exclusive world English rights only unless your license was granted for translation rights. If you licensed translation rights you may only translate this content into the languages you requested. A professional translator must perform all translations and reproduce the content word for word preserving the integrity of the article. If this license is to re-use 1 or 2 figures then permission is granted for non-exclusive world rights in all languages.

16. Posting licensed content on any Website: The following terms and conditions apply as follows: Licensing material from an Elsevier journal: All content posted to the web site must maintain the copyright information line on the bottom of each image; A hyper-text must be included to the Homepage of the journal from which you are licensing at http://www.sciencedirect.com/science/journal/xxxxx or the Elsevier homepage for books at http://www.elsevier.com; Central Storage: This license does not include permission for a scanned version of the material to be stored in a central repository such as that provided by Heron/XanEdu.

Licensing material from an Elsevier book: A hyper-text link must be included to the Elsevier homepage at http://www.elsevier.com . All content posted to the web site must maintain the copyright information line on the bottom of each image.

Posting licensed content on Electronic reserve: In addition to the above the following clauses are applicable: The web site must be password-protected and made available only to bona fide students registered on a relevant course. This permission is granted for 1 year only. You may obtain a new license for future website posting.

17. For journal authors: the following clauses are applicable in addition to the above:

Preprints:

A preprint is an author's own write-up of research results and analysis, it has not been

peer- reviewed, nor has it had any other value added to it by a publisher (such as formatting, copyright, technical enhancement etc.).

Authors can share their preprints anywhere at any time. Preprints should not be added to or enhanced in any way in order to appear more like, or to substitute for, the final versions of articles however authors can update their preprints on arXiv or RePEc with their Accepted Author Manuscript (see below).

If accepted for publication, we encourage authors to link from the preprint to their formal publication via its DOI. Millions of researchers have access to the formal publications on ScienceDirect, and so links will help users to find, access, cite and use the best available version. Please note that Cell Press, The Lancet and some society-owned have different preprint policies. Information on these policies is available on the journal homepage.

Accepted Author Manuscripts: An accepted author manuscript is the manuscript of an article that has been accepted for publication and which typically includes author-incorporated changes suggested during submission, peer review and editor-author communications.
Authors can share their accepted author manuscript:

immediately

- via their non-commercial person homepage or blog
- by updating a preprint in arXiv or RePEc with the accepted manuscript
- via their research institute or institutional repository for internal institutional uses or as part of an invitation-only research collaboration work-group
- directly by providing copies to their students or to research collaborators for their personal use
- for private scholarly sharing as part of an invitation-only work group on commercial sites with which Elsevier has an agreement

after the embargo period

- via non-commercial hosting platforms such as their institutional repository
- via commercial sites with which Elsevier has an agreement

In all cases accepted manuscripts should:

link to the formal publication via its DOI

bear a CC-BY-NC-ND license - this is easy to do

if aggregated with other manuscripts, for example in a repository or other site, be shared in alignment with our hosting policy not be added to or enhanced in any way to appear more like, or to substitute for, the published journal article.

Published journal article (JPA): A published journal article (PJA) is the definitive final record of published research that appears or will appear in the journal and embodies all value-adding publishing activities including peer review co-ordination, copy-editing, formatting, (if relevant) pagination and online enrichment.

Policies for sharing publishing journal articles differ for subscription and gold open access articles:

Subscription Articles: If you are an author, please share a link to your article rather than the full-text. Millions of researchers have access to the formal publications on ScienceDirect, and so links will help your users to find, access, cite, and use the best available version.

Theses and dissertations which contain embedded PJAs as part of the formal submission can be posted publicly by the awarding institution with DOI links back to the formal publications on ScienceDirect.

If you are affiliated with a library that subscribes to ScienceDirect you have additional private sharing rights for others' research accessed under that agreement. This includes use for classroom teaching and internal training at the institution (including use in course packs
and courseware programs), and inclusion of the article for grant funding purposes.

Gold Open Access Articles: May be shared according to the author-selected end-user license and should contain a CrossMark logo, the end user license, and a DOI link to the formal publication on ScienceDirect.

Please refer to Elsevier's posting policy for further information.

18. For book authors the following clauses are applicable in addition to the above: Authors are permitted to place a brief summary of their work online only. You are not allowed to download and post the published electronic version of your chapter, nor may you scan the printed edition to create an electronic version. Posting to a repository: Authors are permitted to post a summary of their chapter only in their institution's repository.

19. Thesis/Dissertation: If your license is for use in a thesis/dissertation your thesis may be submitted to your institution in either print or electronic form. Should your thesis be published commercially, please reapply for permission. These requirements include permission for the Library and Archives of Canada to supply single copies, on demand, of the complete thesis and include permission for Proquest/UMI to supply single copies, on demand, of the complete thesis. Should your thesis be published commercially, please reapply for permission. Theses and dissertations which contain embedded PJAs as part of the formal submission can be posted publicly by the awarding institution with DOI links back to the formal publications on ScienceDirect.